Development of gas systems for gaseous detector operation at HL-LHC

Mara Corbetta

N°d'ordre NNT :
2021LYSE1080

THESE de DOCTORAT DE L'UNIVERSITE DE LYON
opérée au sein de
l'Université Claude Bernard Lyon 1

Ecole Doctorale 52
PHYSIQUE ET ASTROPHYSIQUE DE LYON (PHAST)

Spécialité de doctorat : Physique

Soutenue publiquement le 30/04/2021, par :
Mara Corbetta

Développement de systèmes de gaz pour le fonctionnement des détecteurs gazeux au HL-LHC

Devant le jury composé de :

Laktineh Imad, Professeur, Université Claude Bernard Lyon	Président
Paganoni Marco, Professeur, Università degli Studi Milano-Bicocca	Rapporteur
Uribe-Estrada Cecilia, Professeure, BeneMérita Universidad Autonoma de Puebla	Rapporteure
Carloganu Cristina, Directrice de Recherche CNRS, Université Clermont Auvergne	Examinatrice
Fouz Iglesias Maria, Directrice de Recherche, Centro de Investigaciones Energéticas, Medioambientales y Tecnológicas (CIEMAT)	Examinatrice
Laktineh Imad, Professeur, Université Claude Bernard Lyon	Examinateur
Tytgat Michael, Ingénieur de Recherche, Ghent University	Examinateur
Grenier Gérald, Maître de Conférences, Université Claude Bernard Lyon 1	Co-Directeur de thèse
Mandelli Beatrice, Chercheure, European Organization for Nuclear Research (CERN)	Co-directrice de thèse
Guida Roberto, CERN Staff, European Organization for Nuclear Research (CERN)	Invité

ÉCOLE DOCTORALE DE PHYSIQUE
UNIVERSITÉ DE LYON

DOCTORAL THESIS

Development of Gas Systems for Gaseous Detector Operation at HL-LHC

Author:
Mara CORBETTA

Supervisors:
G. GRENIER
B. MANDELLI

Thesis submitted for the degree in Philosophiae Doctor
École doctorale de physique, PHAST
Université de Lyon 1
with CERN, Experimental Physics, Detector Technologies

Abstract

Development of Gas Systems for Gaseous Detector Operation at HL-LHC

PhD Thesis
Author: M. Corbetta
Supervisors: G. Grenier, B.Mandelli
École doctorale de physique (PHAST), Université de Lyon

After the highly remarkable results achieved in the first decades of operation of the CERN Large Hadron Collider (LHC), the accelerator complex is currently facing major upgrades, and the substantial increase in luminosity will pose major technical challenges also for the Experiments. A long consolidation and upgrade program is being realized during the Long Shutdown 2, concerning among others the Muon systems, composed of gaseous detectors for which a correct and stable gas mixture composition is a key requirement to guarantee good and stable long-term performance. As Greenhouse gases (GHGs) are widely used as gas mixture components in LHC gaseous detectors, their operation shall keep into account the latest CERN requirements in terms of reduction of GHGs emission and gas systems cost. This work delineates the development and upgrades of two different research lines put in place to contribute to the CERN strategies to minimize GHGs consumption. The first is the operation of gas systems with gas recirculation, in particular for the Triple-GEM detectors case, which performance was validated in a HL-LHC-like radiation environment, in terms of long-term stability, Muon detection efficiency and CF_4-based impurities production. A possible strategy to further limit GHG emission is the recuperation of valuable gas components after their usage in the detectors, with the aim of re-injecting them in the gas system. This thesis focuses in particular on the recuperation of two GHGs used in LHC Experiments gaseous detectors, CF_4 and $C_2H_2F_4$. The design and operation of CF_4 recuperation plants on the LHCb RICH2 and CMS CSC gas systems is discussed, showing how good recuperation efficiencies can be reached with a good purity of the recuperated CF_4. Furthermore, the development of a $C_2H_2F_4$ recuperation prototype plant is presented, which characterization proves a very high separation efficiency (80% - 95%) and an extremely good quality of the recuperated $C_2H_2F_4$.

Abstract

Développement de systèmes à gaz pour le fonctionnement des détecteurs gazeux au HL-LHC

Thèse de doctorat
Autrice: M. Corbetta
Encadrants: G. Grenier, B.Mandelli
École doctorale de physique (PHAST), Université de Lyon

Après les résultats très remarquables obtenus au cours des premières décennies par Large Hadron Collider (LHC) du CERN, le complexe d'accélérateurs fait actuellement l'objet d'importantes mises à niveau et l'augmentation substantielle de la luminosité posera également des défis techniques majeurs pour les Expériences. Un long programme de consolidation et de mise à niveau est en cours de réalisation pendant le Long Shutdown 2, concernant entre autres les systèmes à muon, composés de détecteurs à gaz pour lesquels une composition correcte et stable du mélange gazeux est une condition essentielle pour garantir de performances bonnes et stables à long terme. Les gaz à effet de serre (Greenhouse gases, GHGs) étant largement utilisés comme composants de mélanges gazeux dans les détecteurs à gaz du LHC, leur fonctionnement doit tenir compte des dernières exigences du CERN quant à la réduction des émissions de GHGs et du coût des systèmes à gaz. Ce travail de thèse s'inscrit dans deux axes de recherche portant sur le développement et la mise à jour de techniques pour contribuer aux stratégies du CERN visant à minimiser la consommation de GHGs. Le premier est le fonctionnement des systèmes à gaz avec recirculation de gaz, en particulier pour le cas des détecteurs Triple-GEM, dont les performances ont été validées dans un environnement de rayonnement de type HL-LHC, quant à la stabilité à long terme, l'efficacité de détection des muons et la production d'impuretés de mélanges à base de CF_4. Une stratégie possible pour limiter davantage les émissions de GHG est la récupération de composants de gaz précieux après leur utilisation dans les détecteurs, dans le but de les réinjecter dans le système de gaz. Cette thèse se concentre en particulier sur la récupération de deux GHGs utilisés dans les détecteurs gazeux des expériences LHC, le CF_4 et le $C_2H_2F_4$. La conception et l'exploitation des modules de récupération de CF_4 sur les systèmes de gaz RICH2 de LHCb et CSC de CMS sont discutées, montrant comment de bons rendements de récupération peuvent être atteints avec une bonne pureté du CF_4 récupéré. En outre, le développement d'une module prototype de récupération du $C_2H_2F_4$ est présenté, dont la caractérisation a prouvé une efficacité de séparation très élevée (80% - 95%) et une très bonne qualité du $C_2H_2F_4$ récupéré.

Summary

Development of Gas Systems for Gaseous Detector Operation at HL-LHC

PhD Thesis
Autor: M. Corbetta
Supervisors : G. Grenier, B.Mandelli
École doctorale de physique (PHAST), Université de Lyon

After the highly remarkable results achieved by the physics program of the CERN Large Hadron Collider (LHC) during Run 1 and Run 2, the accelerator complex is currently facing major upgrades to fulfill the requirements of the future LHC Physics. The main goal of the Long Shutdown 2 (LS2) was to improve the accelerator performance, with upgrades targeted to the short-term as well as preparatory works in view of the future High-Luminosity LHC (HL-LHC) period. During the HL-LHC phase, foreseen to start in 2025, the accelerator will deliver luminosity five times higher than the LHC original nominal value. Therefore, already after the LS2 upgrades, the substantial increase in luminosity will pose major technical challenges for the Experiments during Run 3. A long consolidation and upgrade program is being realized on all detector systems during the LS2, with the integration of new features and reinforcement of existing components.

In the framework of the LHC physics program, Muon detection is fundamental for a complete identification and characterization of collisions, since Muons represent a very clean probe for many events of interest. LHC Experiments are hence equipped with a Muon system, composed of gaseous detectors, that demand a correct and stable gas mixture composition as a basic requirement to guarantee good and stable long-term performance. Therefore, the gas distribution system represents one of the most critical infrastructures necessary for the operation of gaseous detector systems. Gaseous detectors at the LHC Experiments make use of different gases, some of which are classified as Greenhouse Gases (GHG). As a matter of fact, together with the requirements imposed by the accelerator upgrades, gaseous detectors operation shall keep into account the latest CERN requirements in terms of reduction of GHGs emission and gas systems cost. This work delineates the development and upgrades of two different research lines put in place to cope with gas systems requirements: the operation of gas systems with gas recirculation, in particular for the Triple-GEM detectors case, and the recuperation of valuable gas components after their usage in the gas systems, with focus on the recuperation process of Tetrafluoromethane (CF_4) and 1,1,1,2-Tetrafluoroethane ($C_2H_2F_4$ or R134a).

Since their initial design, LHC gas systems foresaw the possibility of re-using the gas mixture multiple times to limit gas emissions and gas system cost. The main strategy was to operate the gas system in recirculation mode, collecting the exhaust gas mixture and re-injecting it in the system after a purification process. Many LHC detector systems already adopted this mode of operation since Run 1, with very successful results.

Among other detectors belonging to the new generation of Micro Pattern Gaseous Detectors (MPGD), Gas Electron Multipliers (GEM) detectors have been more and more considered in the last years as tracking devices, in particular with the nowadays common Triple-GEM configuration. They are present in LHC Experiments Muon systems thanks to their ability to cope with the high-rate radiation environment of the future phases of the LHC. Triple-GEM detectors were successfully operated in the LHCb Muon System with a CF_4-based gas mixture in a gas recirculating system during Run 2, with a reduction of 90% in GHG emission with respect to Run 1. Nevertheless, as the future LHC phases foresee a much higher rate of background radiation, it is fundamental to validate Triple-GEM detectors operation with gas recirculation in a High Luminosity LHC-like radiation environment. A set of studies and characterization of Triple-GEM detectors performance was realized for operation with gas recirculation in a high rate radiation environment, at the CERN Gamma Irradiation Facility (GIF++).

Triple-GEMs operation was characterized at laboratory level for variations in CF_4 content in the standard gas mixture ($Ar/CO_2/CF_4$ 45/15/40), with parallel simulation to compare the experimental results with the theoretical behavior of the electron avalanches with a given gas mixture. Firstly, it was found that the simulation models quite well the amplification gain of the detector, which is used to quantify the effect of gas mixture variations on detector performance. The simulation and laboratory measurements showed that a significant variation in the gain is obtained per 1% of CF_4 variations, up to 10% with respect to the standard mixture value, confirming the fundamental requirement of an extremely stable gas mixture composition.

Triple-GEM detectors were then operated in a small replica of LHC gas systems at the GIF++ facility, to study their performance in a LHC-like configuration in presence of high-rate radiation. A long-term irradiation campaign was completed exposing Triple-GEM detectors to ^{137}Cs gamma emission, accumulating around 80 mC/cm^2 with detectors operated with recirculating gas fraction higher than 90%. Detectors response was found to be stable along the entire duration of the test, regardless of the gas recirculating fraction and the background radiation rate. Moreover, during the irradiation campaign the action of the purifier module for removing and stabilizing H_2O and O_2 concentration in the recirculating gas system was validated. Triple-GEM detectors exposed to radiation when operated in Ar/CO_2 gas mixture were also studied with the SEM technique, observing the GEM foils holes morphology after irradiation. It was found that a fraction of the GEM holes results to be damaged, with smudged outlines and distorted shapes. However, given the results of the long-term irradiation test, the damages to these holes are not sufficient to compromise amplification capabilities of the GEM foil.

Triple-GEMs Muon detection efficiency was also studied at the GIF++ facility, during a Test Beam campaign, operating the gas system both in open mode and with gas recirculation (90% recirculating fraction). The obtained results show how the operation of Triple-GEM detectors is equivalent in the two different gas system modes, thanks to the action of the purifier module. The detector under study could reach the maximum efficiency for both Ar/CO_2 70/30 and $Ar/CO_2/CF_4$ 45/15/40 gas mixtures with 90% gas recirculation. Furthermore, it was observed how Triple-GEM detectors efficiency is not compromised by high-rate gamma background.

Finally, Fluoride impurities production in CF_4-based mixture was studied for Triple-GEMs operated in high-radiation rate environments, at the GIF++ facility with 10×10 cm^2 detectors prototypes and in the LHCb experiment during Triple-GEMs operation of LHC Run 2. The production process characterization showed how the CF_4 content does not particularly affect the Fluoride production rate, at least for concentrations below 50%, and how a higher input gas flow rate contributes to the decrease of Fluoride produced in the chamber volume. Moreover, it was showed how both detectors electric field and irradiation intensity contribute to an increase in the Fluoride ion production, finding the same effect also in the LHCb experiment measurements. Lastly, the equivalence of operation with the gas system in open mode and in gas recirculation mode in relation to Fluoride impurities was verified in the GIF++ setup as well as in the LHCb full size gas system. It was found that the standard LHC purifier module is capable of trapping Fluoride ions produced in the detector volume, that are therefore not carried by the re-injected gas mixture.

Though many of the LHC gas systems are already operated with gas recirculation, recirculating 100% of the gas mixture is currently not feasible for many of those, for which the gas recirculating fraction have to be limited around 90%. Moreover, in other cases where 100% recirculation is possible, a set of causes could yield to the emission of a great amount of gas. A possible strategy to further limit gas emissions is to put in operation gas recuperation plants, already in use in some LHC gas systems, with the purpose of recuperating the most valuable mixture component at a good purity level. Nevertheless, recuperation plants introduce additional complexity in the gas systems and impose the need of a continuous gas mixture monitoring, as well as dedicated R&D studies to optimize recuperation plants for every specific case. The work presented in the second part of this thesis focuses on the recuperation of two Freon gases used in LHC Experiments gaseous detectors, CF_4 and R134a, both Greenhouse gases, with a Global Warming Potential of 7390 and 1430 respectively.

Among other Greenhouse gases, CF_4 is widely used by LHC gaseous detectors, in combination with Ar and CO_2. Membrane separation technology proved efficient in separating CF_4 from the others mixture components, though with limitations linked to its variable performance in relation to operation parameters such as the input flow rate. Moreover, it was proved that membrane efficiency strongly depends on the input gas mixture composition, favoring CF4 separation when its concentration is higher. The good knowledge developed on separation membranes allowed to design two different CF_4 recuperation plants making use of such technology.

A CF_4 recuperation plant was commissioned and put into operation in the LHCb RICH2 gas system, in which 100 m^3 of CF_4/CO_2 92/8 gas mixture are used. During the LS2, the RICH2 volume was emptied from its standard mixture and filled with CO_2, recuperating the exhaust mixture to extract and store good quality CF_4. The recuperation process allowed to store about 450 m^3 of CF_4, with Air/CO_2 contamination <1%, with a total recuperation efficiency around 60%. The knowledge acquired during the first months of operation of the plant allowed to design and realize different modifications to improve the CF4 recuperation system, that will be again used during the filling phase before Run 3, and to develop a new recuperation process for the CF_4/CO_2 gas mixture to be used during physics run operation.

The separation membrane technology has also been exploited for the CMS CSC CF_4

recuperation plant, already operational since Run 1. Membranes are used in combination with other separation methods, allowing to recuperate CF_4 from the CSC gas mixture ($Ar/CO_2/CF_4$ 40/50/10), with an average purity level of 95%. Though with oscillating performance in terms of efficiency, the plant is nowadays continuously operational. This allowed to reach in 2018 the design operation configuration, in which CF_4 is continuously recuperated from the CSC gas system exhaust and, in parallel, re-injected in the mixer module. Recuperated CF_4 is injected in combination with fresh CF_4 (50/50), in way to guarantee a significantly decreased supply gas consumption while maintaining the CSC mixture at a good quality level. This is realized thanks to a gas analysis system that allows a precise tuning of the mixer parameters through Gas Chromatograph analysis and real-time check on the gas mixture quality with a Single Wire Chambers monitoring system. Operational since 2016, the latter also allows continuous monitoring of the CSC gas mixture quality during normal operation, at the mixer output as well as at the return of the closed loop system, to verify the good quality of the recirculated gas.

Together with CF_4, another widely used Greenhouse gas is R134a, as it is the main component of the gas mixture of RPC detectors, operational in the ALICE, ATLAS and CMS Muon systems. Therefore, the design and development of an R134a recuperation plant was started in 2018, with the aim of separating R134a from the other mixture components (iC_4H_{10}, SF_6), to be able to re-use it in the RPC mixer module. Thanks to the experience gained through many tests and modifications of the prototype plant, the gas mixture thermodynamic properties were determined and an effective separation process could be designed, recuperating R134a through subsequent distillation processes. The characterization of the prototype plant showed very high separation efficiency (80% - 95%) and an extremely good quality of the recuperated R134a, with pollution levels around hundreds of ppm in iC_4H_{10} and Air. The obtained results are encouraging in view of further possible upgrades and a successful final commissioning of the recuperation plant.

Résumé

Développement de systèmes à gaz pour le fonctionnement des détecteurs gazeux au HL-LHC

Thèse de doctorat
Autrice: M. Corbetta
Encadrants: G. Grenier, B.Mandelli
École doctorale de physique (PHAST), Université de Lyon

Après les résultats remarquables obtenus par le programme de physique du Large Hadron Collider (LHC) du CERN pendant le Run 1 et le Run 2, le complexe d'accélérateurs fait actuellement l'objet d'importantes mises à niveau pour répondre aux exigences de la physique du futur LHC. L'objectif principal du Long Shutdown 2 (LS2) était d'améliorer les performances de l'accélérateur, avec des améliorations ciblées sur le court terme ainsi que des interventions préliminaires en vue du futur High Luminosity LHC (HL-LHC). Pendant la phase HL-LHC, prévue pour 2025, l'accélérateur fournira une luminosité cinq fois supérieure à la valeur nominale initiale du LHC. Par conséquent, même après les mises à niveau du LS2, l'augmentation substantielle de la luminosité posera des défis techniques majeurs pour les expériences pendant le Run 3. Un long programme de consolidation et de mise à niveau est en cours de réalisation pendant le LS2, avec l'intégration de nouvelles fonctionnalités et le renforcement des composants existants.

Dans le cadre du programme de physique du LHC, la détection des muons est fondamentale pour une identification et une caractérisation complète des collisions, car les muons représentent un indicateur très approprié pour de nombreux événements d'intérêt. Les expériences LHC sont donc équipées d'un système à suons, composé des détecteurs à gaz, qui nécessitent une composition correcte et stable du mélange de gaz comme condition de base pour garantir des performances bonnes et stables à long terme. Par conséquent, le système de distribution de gaz représente l'une des infrastructures les plus critiques nécessaires au fonctionnement de détecteurs à gaz. Les détecteurs à gaz des Expériences LHC utilisent différents gaz, dont certains sont classés comme gaz à effet de serre (Greenhouse gases, GHG). En effet, en plus des exigences imposées par les mises à niveau des accélérateurs, leur fonctionnement doit tenir compte des dernières exigences du CERN quant à la réduction des émissions de GHGs et du coût des systèmes à gaz. Ce travail de thèse s'inscrit dans le développement et la mise à niveau de deux axes de recherche différents mis en place pour faire face aux besoins des systèmes à gaz: le fonctionnement des systèmes avec recirculation, en particulier pour les détecteurs Triple-GEM, et la récupération de composants gazeux précieux après leur utilisation dans les systèmes à gaz, en mettant l'accent sur le processus de récupération du tétrafluorométhane (CF_4) et du 1,1,1,2-tétrafluoroéthane ($C_2H_2F_4$ ou R134a).

Depuis leur conception initiale, les systèmes à gaz du LHC prévoient la possibilité de réutiliser le mélange de gaz plusieurs fois pour limiter les émissions et le coût

du système. La stratégie principale était de recycler le gaz, en collectant le mélange gazeux à la sortie du système et en le ré-injectant dans le système après un processus de purification. De nombreux systèmes à gaz du LHC ont déjà adopté ce mode de fonctionnement depuis le Run 1, avec des résultats très positifs.

Parmi les autres détecteurs appartenant à la nouvelle génération de Micro Pattern Gaseous Detectors (MPGD), les détecteurs Gas Electron Multiplier (GEM) ont été de plus en plus considérés dans les dernières années comme des dispositifs de trajectographie, en particulier avec la configuration actuelle Triple-GEM. Ils sont présents dans les systèmes à muons des expériences LHC grâce à leur capacité de fonctionner correctement dans l'environnement à haut flux de radiations des futures phases du LHC. Des détecteurs Triple-GEM ont été utilisés avec succès, pendant le Run 2, dans le système à muons de LHCb avec un mélange de gaz à base de CF_4 couplé à un système de recirculation, avec une réduction de 90% des émissions de GHG par rapport au Run 1. Néanmoins, compte tenu du fait que les phases futures du LHC prévoient un taux de radiations ambiantes beaucoup plus élevé, il est fondamental de valider le fonctionnement des détecteurs Triple-GEM avec recirculation de gaz dans un environnement radiatif de type HL-LHC. Un ensemble d'études et de caractérisations des performances des détecteurs Triple-GEM a été réalisé à la Gamma Irradiation Facility du CERN (GIF ++), pour un fonctionnement avec recirculation de gaz dans un environnement à haut flux de rayonnement ionisants.

Le fonctionnement d'un Triple-GEM a été caractérisé au niveau du laboratoire par rapport aux variations de CF_4 dans le mélange de gaz standard ($Ar/CO_2/CF_4$ 45/15/40). En parallèle, des simulations ont été réalisées pour comparer les résultats expérimentaux avec le comportement théorique des avalanches d'électrons dans un mélange gazeux donné. Premièrement, il a été constaté que la simulation modélise d'une bonne manière le gain d'amplification du détecteur, indicateur qui est utilisé pour quantifier l'effet des variations du mélange gazeux sur les performances du détecteur. La simulation et les mesures en laboratoire ont montré qu'une variation significative du gain est obtenue pour 1% de variation du CF_4, jusqu'à 10% par rapport à la valeur de mélange standard, en confirmant l'exigence fondamentale d'une composition de mélange gazeux extrêmement stable.

Des détecteurs Triple-GEM ont ensuite été utilisés dans un modèle réduit des systèmes à gaz du LHC, pour étudier leurs performances dans une configuration de type LHC en présence de rayonnement à haut débit. Une campagne d'irradiation à long terme a été réalisée, exposant les détecteurs Triple-GEM à une source gamme de ^{137}Cs, accumulant une dose d'environ 80 mC/cm^2 avec des détecteurs fonctionnant avec une fraction de recirculation du gaz supérieure à 90%. La réponse des détecteurs s'est avérée stable pendant toute la durée du test, indépendamment de la fraction de recirculation de gaz et du taux de rayonnement de fond. De plus, lors de la campagne d'irradiation, l'action du module purificateur pour éliminer et stabiliser la concentration de O_2 et H_2O dans le système de recirculation de gaz a été validée. Des détecteurs Triple-GEM exposés au rayonnement lorsqu'ils fonctionnent avec un mélange gazeux Ar/CO_2 ont été étudiés avec la technique SEM, en observant la morphologie des trous des feuilles GEM après irradiation. Il a été constaté qu'une fraction des trous GEM était endommagée, avec des contours irréguliers et des figures déformées. Toutefois, compte tenu des résultats du test d'irradiation à long terme, les dommages causés sur ces trous ne sont pas suffisants pour compromettre les capacités d'amplification de la feuille GEM.

L'efficacité de détection des Muons des Triple-GEM a également été étudiée dans l'installation GIF ++, lors d'une campagne de tests en faisceaux, en opérant le système de gaz en mode ouvert mais aussi avec recirculation de gaz (fraction de recirculation de 90%). Les résultats obtenus montrent comment le fonctionnement des détecteurs Triple-GEM est équivalent dans les deux configurations de fonctionnement du système à gaz, grâce à l'action du module purificateur. Le détecteur à l'étude pourrait atteindre l'efficacité maximale pour les deux mélanges testés (Ar/CO_2 70/30 et $Ar/CO_2/CF_4$ 45/15/40) avec une recirculation de gaz à 90%. On a également observé comment l'efficacité des détecteurs Triple-GEM n'est pas compromise par un fond gamma à haut flux.

Enfin, la production d'impuretés dans un mélange à base de CF_4 a été étudiée pour des Triple-GEM fonctionnant dans des environnements à taux de radiations élevé, dans l'installation GIF ++ avec des prototypes de détecteurs de 10×10 cm^2 et dans l'expérience LHCb pour l'utilisation des Triple-GEM pendant le Run 2 du LHC. La caractérisation du processus de production a montré comment la concentration de CF_4 n'affecte pas particulièrement le taux de production de fluorure, au moins pour des concentrations inférieures à 50%, et comment un débit de gaz d'entrée plus élevé contribue à la diminution du fluorure produit dans le volume de la chambre. De plus, il a été montré comment le champ électrique et l'intensité d'irradiation des détecteurs contribuent à une augmentation de la production d'ions fluorure, relevant le même effet également dans les mesures sur l'expérience LHCb. Finalement, l'équivalence de fonctionnement avec le système de gaz en mode ouvert et en mode de recirculation de gaz par rapport aux impuretés de fluorure a été vérifiée dans l'expérimentation GIF++ ainsi que dans le système de gaz pour les GEM de LHCb. Il a été constaté que le module purificateur standard du LHC est capable de bloquer les ions fluorure produits dans le volume du détecteur, qui ne sont donc pas réintroduits par le mélange gazeux ré-injecté.

Bien que de nombreux systèmes à gaz du LHC fonctionnent déjà avec une recirculation de gaz, la recirculation de 100% du mélange gazeux n'est actuellement pas possible pour beaucoup d'entre eux, pour lesquels la fraction de recirculation de gaz doit être limitée à environ 90%. De plus, dans d'autres cas où une recirculation à 100% est possible, un ensemble de causes pourrait conduire à l'émission d'une grande quantité de gaz. Une stratégie possible pour limiter davantage les émissions de gaz consiste à mettre en service des modules de récupération, déjà utilisés dans certains systèmes à gaz du LHC, dans le but de récupérer le composant du mélange le plus précieux avec un bon niveau de pureté. Néanmoins, les modules de récupération introduisent une complexité supplémentaire dans les systèmes à gaz, imposent la nécessité d'une surveillance continue du mélange gazeux, ainsi que des études R&D dédiées pour optimiser les modules de récupération pour chaque cas spécifique. Les travaux présentés dans la deuxième partie de cette thèse portent sur la récupération de deux gaz fréon utilisés dans les détecteurs à gaz des Expériences LHC, le CF_4 et le R134a, tous deux gaz à effet de serre, avec un Global Warming Potential (GWP) de 7390 et 1430 respectivement.

Parmi les autres GHG, le CF_4 est largement utilisé par les détecteurs gazeux du LHC, en combinaison avec Ar et CO_2. La technologie de séparation par membrane s'est avérée efficace pour séparer le CF_4 des autres composants du mélange, en présentant toutefois des limitations liées à ses performances variables par rapport aux

paramètres de fonctionnement tels que le débit d'entrée. De plus, il a été prouvé que l'efficacité des membranes dépend fortement de la composition du mélange gazeux d'entrée, favorisant la séparation du CF_4 lorsque sa concentration est plus élevée. Les connaissances développées sur les membranes de séparation ont permis de concevoir deux différentes usines de récupération du CF_4 en utilisant cette technologie.

Un module de récupération du CF_4 a été développé et mis en service dans le système RICH2 de LHCb, dans lequel 100 m^3 de mélange gazeux CF_4/CO_2 92/8 sont utilisés. Lors du LS2, le volume du RICH2 a été vidé de son mélange standard et rempli de CO_2, récupérant le mélange émis pour en extraire et stocker le CF_4. Le processus de récupération a permis de stocker environ 450 m^3 de CF_4, avec une contamination de Air/CO_2 <1% et avec une efficacité de récupération totale autour de 60%. Les connaissances acquises au cours des premiers mois d'exploitation du module de séparation ont permis de concevoir et de réaliser différentes modifications pour améliorer le système de récupération du CF_4, qui sera à nouveau utilisé lors de la phase de remplissage avant le Run 3, et de développer un nouveau processus de récupération pour le mélange gazeux CF_4/CO_2 à utiliser pendant le Run 3.

La technologie des membranes de séparation a également été exploitée pour le module de récupération de CF_4 dans le système CSC de CMS, déjà opérationnel depuis le Run 1. Les membranes sont utilisées en combinaison avec d'autres méthodes de séparation, permettant de récupérer le CF_4 du mélange gazeux CSC ($Ar/CO_2/CF_4$ 40/50/10), avec un niveau de pureté moyen de 95%. Bien que présentant des performances oscillantes quant à l'efficacité, le module de récupération fonctionne aujourd'hui en continu. Cela a permis d'atteindre en 2018 l'objectuf de fonctionnement prévu à la conception, dans lequel le CF_4 est continuellement récupéré de l'échappement du système de gaz CSC et, en parallèle, réinjecté dans le module mélangeur. Le CF_4 récupéré est injecté en combinaison avec du CF_4 frais (50/50), de manière à garantir une consommation de gaz significativement diminuée tout en maintenant le mélange CSC à un bon niveau de qualité. Ceci est réalisé grâce à un système d'analyse de gaz qui permet un réglage précis des paramètres du mélangeur grâce à une analyse par chromatographie en phase gazeuse et un contrôle en temps réel de la qualité du mélange gazeux avec un système de surveillance des Single Wire Chambers. Opérationnel depuis 2016, ce dernier permet également de surveiller en continu la qualité du mélange gazeux CSC en fonctionnement normal, à la sortie du mélangeur ainsi qu'au retour du système en boucle fermée, pour vérifier la bonne qualité du gaz recirculé.

Un autre GHG largement utilisé est le R134a, car il est le composant principal du mélange gazeux des détecteurs RPC, en opération dans les systèmes à muons des expériences ALICE, ATLAS et CMS. Par conséquent, la conception et le développement d'un module de récupération du R134a ont été lancés en 2018, dans le but de séparer le R134a des autres composants du mélange (iC_4H_{10}, SF_6), pour pouvoir le réutiliser dans le module mélangeur. Grâce à l'expérience acquise avec de nombreux tests et modifications d'un module prototype, les propriétés thermodynamiques du mélange gazeux RPC ont été déterminées et un processus de séparation efficace a pu être conçu, récupérant le R134a grâce à des processus de distillation. La caractérisation du module prototype a montré une efficacité de séparation très élevée (80% - 95%) et une très bonne qualité du R134a récupéré, avec des niveaux de pollution de l'ordre de centaines de ppm (iC_4H_{10}, air). Les résultats obtenus sont encourageants compte tenu de nouvelles améliorations possibles et dans l'optique de la mise en

service du module de récupération dans les expériences.

Contents

List of Figures

List of Tables

Introduction

After the highly remarkable results achieved by the physics program of the Large Hadron Collider (LHC) during Run 1 and Run 2, the accelerator complex is currently facing major upgrades to fulfill the requirements of the future LHC Physics. The main goal of the Long Shutdown 2 (LS2) was to improve the accelerator performance, with upgrades targeted to the short-term as well as preliminary interventions in view of the future High-Luminosity LHC (HL-LHC) [1]. During the HL-LHC phase, foreseen to start in 2025, the accelerator will deliver a luminosity five times higher than the LHC original nominal value. Therefore, already after the LS2 upgrades, the substantial increase in luminosity will pose major technical challenges for the Experiments during Run 3. A long consolidation and upgrade program is being realized during the LS2 on all detectors systems, with the integration of new features and reinforcement of existing components.

In the framework of the LHC Physics program, Muon detection is fundamental for a complete identification and characterization of collisions, since Muons represent a very clean probe for many events of interest. LHC Experiments are hence equipped with a Muon system, composed of gaseous detectors, that require a correct and stable gas mixture composition as a basic requirement to guarantee good and stable long-term performance. Therefore, the gas distribution system represents one of the most critical infrastructures necessary for the operation of Muon systems [2]. Gaseous detectors at the LHC Experiments make use of different gases, some of which are classified as Greenhouse gases (GHG). Together with the requirements imposed by the accelerator upgrades, gaseous detectors operation shall keep into account the latest CERN requirements in terms of reduction of the GHGs emission and gas systems cost. Since their initial design, LHC gas systems foresaw the possibility of re-using the gas mixture multiple times. The main strategy was to operate the gas system in recirculation mode, collecting the exhaust gas mixture and re-injecting it in the system after a purification process. Many LHC detector systems already adopted this mode of operation since Run 1, with very successful results.

Among other detectors belonging to the new generation of Micro Pattern Gaseous Detectors (MPGD), Gas Electron Multipliers (GEM) detectors have been more and more considered in the last years as tracking devices, in particular with the nowadays common Triple-GEM configuration. They are present in LHC Experiments Muon systems thanks to their ability to cope with the high-rate radiation environment of the future Phases of the LHC. Triple-GEM detectors were successfully operated in the LHCb Muon System with a CF_4-based gas mixture in a gas recirculating system during Run 2, with a reduction of 90% in GHG emission with respect to Run 1. Nevertheless, as the future LHC Phases foresee a much higher rate of background radiation, it is fundamental to validate Triple-GEM detectors operation with gas recirculation in a High Luminosity LHC-like radiation environment. Chapter 3 will focus on the studies and characterization of Triple-GEM detectors performance realized in view of their operation in the HL-LHC environment.

A study was realized on Triple-GEM detectors response for variation of the standard $Ar/CO_2/CF_4$ gas mixture (45/15/40), in parallel with a Garfield++ simulation to compare theoretical predictions with the actual detector behavior. Triple-GEMs performance was then studied in relation to long-term operation stability and Muon detection efficiency at the CERN Gamma Irradiation facility (GIF++). Thanks to the ^{137}Cs gamma source available in the facility and the Muon beam delivered from the SPS, it was possible to validate Triple-GEMs operation with a small replica of an LHC gas recirculating system, in irradiation conditions that mimic what detectors will face in the future LHC Phases. Moreover, microscopic analysis were conducted on GEM foils used in the detectors for the irradiation tests with the Scanning Electron Microscopy (SEM) technique. Finally, as the main issue of operating gas systems with gas recirculation is the possible accumulation of impurities, the Fluoride-impurities production process from operation with CF_4-based gas mixture was characterized at the GIF++ facility, in relation to different detector operation conditions and in particular for high-rate irradiation, using an Ion Selective Electrode (ISE) station to quantify the Fluoride present in the gas mixture. The same measurement technique was also used to measure Fluoride-impurities produced in the LHCb GEM chambers during the last months of operation of the detectors during Run 2.

Though many of the LHC gas systems are already operated with gas recirculation, recirculating the 100% of the gas mixture is currently not feasible for many of the those, for which the gas recirculating fraction have to be limited around the 90%. Moreover, in other cases where 100% recirculation is possible, a set of causes could yield to the emission of a great amount of gas. A possible strategy to further limit gas emissions is to put in operation gas recuperation plants, already in use in some LHC gas systems, with the purpose of recuperating the most valuable mixture component at a good purity level. Nevertheless, recuperation plants introduce additional complexity in the gas systems and impose the need of a continuous gas mixture monitoring, as well as dedicated R&D studies to optimize recuperation plants for every specific case. The work presented in Chapter 4 focuses on the recuperation of two Freon gases used in LHC Experiments gaseous detectors, Tetrafluoromethane (CF_4 or R14) and 1,1,1,2-Tetrafluoroethane ($C_2H_2F_4$ or R134a), both Greenhouse gases, with a Global Warming Potential of 7390 and 1430 respectively.

Different gaseous detectors in LHC Experiments make use of CF_4, that can be efficiently separated and recuperated with the selective membranes technique, obtaining a product with sufficiently high purity. The separation by selective membranes is studied and characterized with focus on the specific case of CF_4 separation, in view of its application on the recuperation plants of the LHCb RICH2 and CMS CSC detector systems. The LHCb RICH2 detector is operated during physics runs with almost 100% recirculation, with a gas mixture of CF_4/CO_2 in fractions 92/8. During the LHC LS2 the detector volume was filled with 100% CO_2 to allow system maintenance, yielding to a massive emission of CF_4, considering the 100 m^3 detector volume and the many volume-exchanges necessary to reach the full mixture change. A CF_4 recuperation plant based on membrane separation was put into operation in 2019 during the CF_4 emptying procedure, optimizing its performance to reach a good recuperation efficiency. Afterwards, different upgrades were also realized to improve the recuperation operation for the CF_4 filling procedure to be done before Run 3, as well as for the future standard operation of the gas system during physics

runs. The selective membrane separation technique, in combination with others gas purification techniques, is also used in the CF_4 recuperation plant of the CMS CSC detectors system. Operated with 90% gas recirculation to compensate for impurities accumulation, the CSC gas system exhausts a significant amount of $Ar/CO_2/CF_4$ 40/50/10 gas mixture, which is hence sent to recuperation, obtaining as final product good quality CF_4, only polluted with small quantities of Ar and N_2. The recuperation plant is operational since 2012, and it nowadays operates in its original design configuration, with continuous CF_4 recuperation from the gas system exhaust and continuous injection of half fresh and half recuperated gas. To guarantee good mixture quality, the recuperated CF_4 re-injection process is monitored with gas analysis and with a Single Wire Proportional Chambers (SWPCs) monitoring system, operational on the system since 2015 to monitor the fresh and recirculated gas quality.

R134a is used as major component of the gas mixture of Resistive Plate Chambers (RPCs), operational in the Muon Systems of the ALICE, ATLAS and CMS Experiments. R134a is always present in the RPC gas mixture for at least the 90%, in combination with iC_4H_{10} and SF_6, and it is fundamental to limit its emission given the high volume of the RPC detectors systems. A prototype of R134a recuperation system was put in operation in 2018, with the aim of separating R134a from the other components of the exhaust RPC mixture and possible impurities, and re-use it in the mixer module in place of the fresh gas. The RPC mixture separation was studied from a theoretical point of view, as it presents some major challenges given the azeotropic behavior of R134a/iC_4H_{10} in their vapor-liquid phase equilibrium. The prototype was hence designed, tested and characterized, to make it ready for the final commissioning and realization in the different Experiments.

Chapter 1

High Energy Physics at the LHC

The aim of Particle Physics research is to determine the fundamental matter components, their properties and the way they interact with each other. The Standard Model (SM), describing elementary particles and their interaction, has been successfully tested by the Physics program taking place at the Large Hadron Collider (LHC), especially with the discovery of the Higgs boson. Nevertheless, the SM shows some limitations that give rise to the need of exploring new physics beyond it. This Chapter will illustrate the basics of elementary particles research and how it is approached at the LHC, together with the latest relevant results and future upgrade plans for the accelerator and Experiments.

1.1 The Standard Model of particle physics

The Standard Model (SM) contains the theoretical elements of modern Particle Physics, described through the gauge invariance principle in the framework of quantum field theory. In the SM, the fundamental constituent of matter are 12 elementary particles called fermions, identified by their spin equal to $1/2$. Fermions are divided into two types, leptons and quarks, each type divided in turn into three generations. Charged leptons are electrons e^-, muons μ^- and taus τ^-, with their associated neutrinos (ν_e, ν_μ and ν_τ). Quarks are divided into first (u, d), second (c, s) and third (t, b) generations. The stable matter is made of fermions of the first generation. Additionally, each fermion is associated to its anti-particle, with opposite quantum numbers.

Lepton	Charge	Mass [$1/c^2$]
e^-	-1	0.511 MeV
ν_e	0	$\leq$ 3 eV
μ^-	-1	105.66 MeV
ν_μ	0	$\leq$ 19 eV
τ^-	-1	1777 MeV
ν_τ	0	$\leq$ 18.2 eV

Quark	Charge	Mass [$1/c^2$]
u	+2/3	2.3 MeV
d	-1/3	4.8 MeV
c	+2/3	1.275 GeV
s	-1/3	95 MeV
t	+2/3	173.21 GeV
b	-1/3	4.18 GeV

TABLE 1.1: The fermions of the Standard Model with their charge and mass.

Fermions interact through the exchange of spin-1 particles, the so called gauge bosons, elementary particles themselves. These particles are associated to the fundamental interacting forces, and to the coupling constants that refer to their strength. The Electromagnetic interaction, described by Quantum Electro-Dynamics (QED), applies to all charged particles and it is mediated by the neutral boson γ. The Weak interaction is mediated by the charged bosons $W^\pm$ and Z, and it was unified with the Electromagnetic interaction by the ElectroWeak theory (EW). The strong interaction only

applies to quarks, it is carried by eight gluons that can interact with each other and it is described by the Quantum Chromo-Dynamics theory (QCD). Nevertheless, the EW theory does not foresee a mechanism that gives mass to fundamental particles. The Brout-Englert-Higgs mechanism was therefore introduced in order to generate the mass of heavy bosons, and it can be applied to fermions too. Since the W and Z bosons are massive while the photon is not, the EW symmetry is broken, yielding to the existence of an additional scalar boson with spin 0, the Higgs boson. Its interaction with ordinary particles generates their masses, while its own mass is an open parameter of the theory.

Many SM parameters were successfully measured in the last decades, in a very large energy range and with high precision. However, the SM cannot be considered an ultimate theory, as many aspects still do not find explanation in this model. It can somehow be seen as an approximation of a wider unified theory, which could include the description of aspects like the existence of the fourth elementary interaction (gravitation), the CP symmetry violation, the dark matter existence and many others. One of the possible models could be the Super Symmetry (SUSY) theory, in which each particle of the SM has a super-symmetric partner with the same quantum numbers but the spin, which differs by 1/2. None of the proposed theories has so far found strong proofs in experimental observation, and the search of a unified theory remains therefore open.

1.2 Overview of the physics at the LHC

The Large Hadron Collider (LHC) is a two-ring superconducting hadron accelerator and collider at the European Organization for Nuclear Research (CERN). Made of 27 km of superconducting magnets, laying 100 m underground, it allows the confinement and acceleration of two proton beams, running in opposite directions. It has been designed to provide enough statistics to fulfill the requirements of the CERN Physics program, oriented to precision measurements of the Standard Model as well as to the search of new physics.

The LHC can nominally provide a center-of-mass energy of 14 TeV for proton-proton collisions, created by 2808 bunches containing 1.15×10^{11} particles each, with a bunch spacing of 25 ns. Primary protons are obtained from Hydrogen, and they are accelerated in a first linear collider (LINAC), to be then injected in the chain of circular accelerators that allows the achievement of their maximum energy (6.5 TeV). Protons pass through the Proton Synchrotron (PS, 25 GeV), the Super Proton Synchrotron (SPS, 450 GeV) and finally are injected in the LHC. The design luminosity of the collider is 10^{34} cm^{-2} s^{-1}, with a foreseen integrated luminosity of 3000 fb^{-1} by 2030. The LHC is also capable of providing heavy ions beams, supplying pPb and PbPb collisions with a center-of-mass energy of 2.76 TeV and 5.02 TeV respectively. Figure 1.1 reports a schematic drawing of the LHC complex with the different accelerators and experiments.

The high center-of-mass energy allows the production of massive particles, and the high luminosity gives access to rare phenomena. Collisions happen in the four LHC Interaction Points, where the experiments are located. Two general purpose Experiments, ATLAS (A Toroidal Lhc ApparatuS) and CMS (Compact Muon Solenoid),

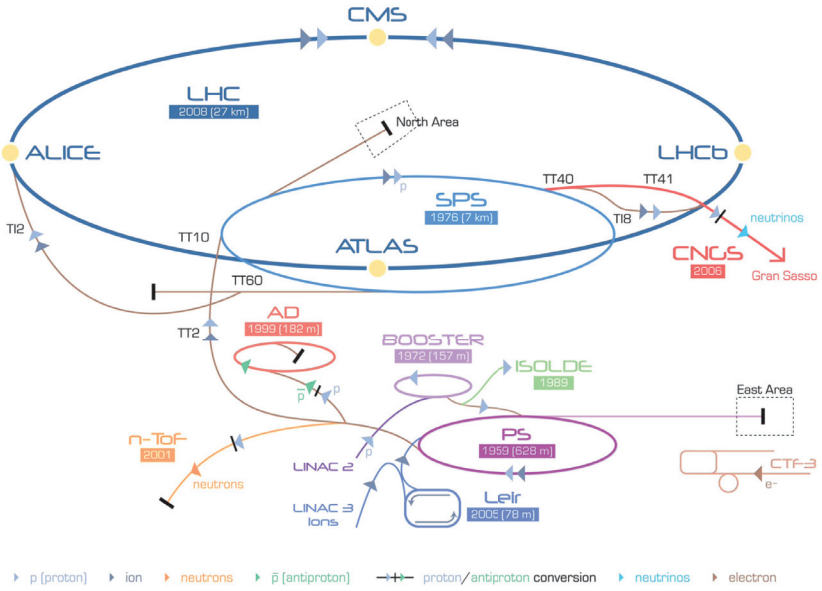

FIGURE 1.1: Schematic drawing of the LHC complex layout, with accelerators and experiments. [3]

were designed to explore all the possible aspects of the LHC physics, from heavy-ions collisions and forward physics to Higgs boson physics and direct search of new particles. The ALICE experiment (A Large Ion Collider Experiment) is specifically dedicated to heavy ions physics, while the LHCb Experiment has the aim to maximize the LHC potential in beauty and charm physics.

Though the final purpose is specific for each Experiment, the requirements on the detectors of which they are composed are quite the same. Their key aim is to identify charged and neutral particles and measure particles momentum with high resolution. In addition, they all need high granularity, to reduce the influence of overlapping events, and a fast and radiation-tolerant electronics for proper data acquisition. LHC Experiments can be described dividing their structure into three different categories:

- *Inner Detectors*:
  Located close to the collision points, they allow the tracking and momentum measurement of charged particles, as well as Interaction Point and vertices reconstruction.

- *Hadronic and Electromagnetic Calorimeters*:
  They measure the energy of hadrons, photons and electrons crossing their volume, based on the energy loss of emerging particles.

- *Muon systems*:
  Since Muons escape the electromagnetic calorimeter, a dedicated Muon system is used to detect them. Typically placed at the outermost layers of the experiments, it allows to unambiguously detect the signature of many relevant events.

As an example, the CMS structure is reported in Figure 1.2, showing the different layers of the Experiment and the relative detected particles.

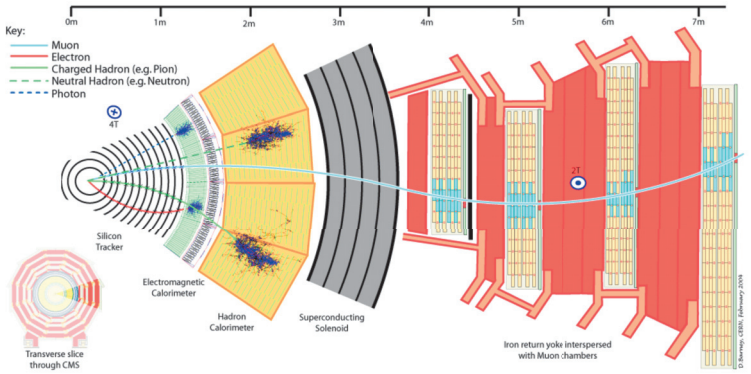

FIGURE 1.2: Transversal view of the CMS experiment, with the different layers of detectors and relative detected particles [4].

1.3 LHC physics achievements

In the first three-years Physics run of the LHC (Run 1, 2010-2013), the results achieved by the overall Physics program were highly remarkable. The LHC has been operated at up to 8 TeV of center-of-mass energy, delivering about 25 fb^{-1} with a peak luminosity of 7.7×10^{33} $cm^{-2}s^{-1}$ (in ATLAS and CMS). Within several relevant results, the major achievement was undoubtedly the observation of a new particle, with a mass of 125 GeV and Higgs-like properties. The discovery came from both ATLAS and CMS experiments, which identified the new particle as the Standard Model Higgs boson [5] [6]. The channels with the strongest Higgs sensitivity at the LHC are the vector-boson fusion and gluon-fusion, while the most significant decay processes are the di-photon, the ZZ to four leptons and the leptonic WW channels. For both ATLAS and CMS, the most relevant results were obtained in the ZZ and di-photon channels, which allowed the measurement of the Higgs boson mass with a very high precision. The discovery was determined by the 5-standard-deviation significance of the deviation from the background-only hypothesis. As reported in the plots of Figure 1.3, a signal excess was observed in the invariant mass distribution of the analyzed events, pointing to the precise mass value of 125 GeV.

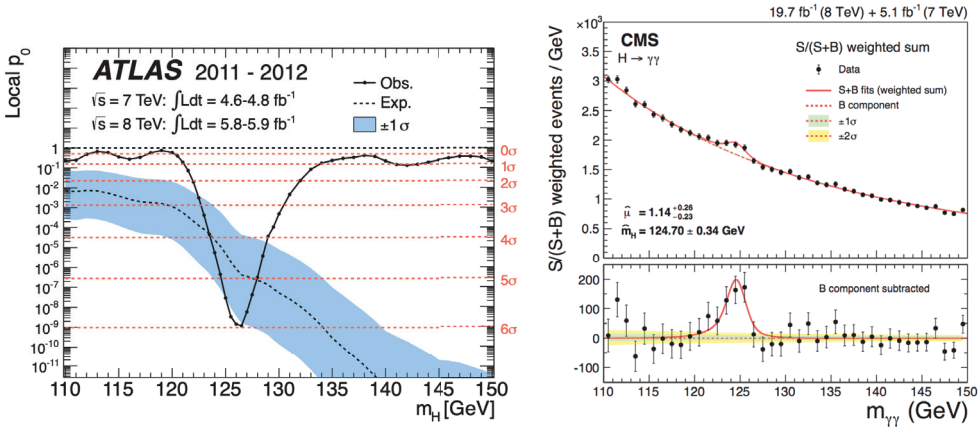

FIGURE 1.3: The observed local p_0 value as a function of m_H in the low mass range of ATLAS events (left) [5] and invariant mass distribution of a CMS di-photon event (right) [6].

Flavor physics studies of the LHCb experiment also accomplished notable results during Run 1. The very rare decay $B_s^0 \to \mu^+\mu^-$ was observed [7], with a branching ratio extremely consistent with the one calculated with the SM theory. Moreover, the first experimental evidence of direct CP violation was observed in B_s^0 decays [8]. Furthermore, very successful PbPb and pPb runs brought unprecedented results in heavy-ion physics, such as the detailed studies of jet quenching in PbPb collisions and di-jet production in pPb collisions.

After the conclusion of Run 1 in 2013, the first Long Shutdown (LS1) started, to consolidate the originally defective magnet interconnections, to allow the LHC to operate at the design energy of 14 TeV in the center-of-mass. In addition, a massive program of maintenance for the LHC and its injectors was put in place, including other repairs, consolidations, upgrades and cabling across the whole accelerator complex and the associated experimental facilities.

Run 2 of the LHC (2015-2018) was successfully completed largely achieving all goals set in terms of luminosity production [9]. The LHC produced 160 fb^{-1} of integrated luminosity at a beam energy of 6.5 TeV, for each of the two high-luminosity experiments, ATLAS and CMS. In 2018, the LHC was routinely operated with an average peak luminosity that was twice the design value, mainly thanks to the higher-than-design beam brightness from the injector chain.

Concerning the Higgs-physics, other decay channels were explored in addition to the ones that led to the Higgs discovery in 2012, the latter characterized by a high precision on the mass value but very low branching ratios. During Run 2, all of the main production and decay modes have been observed, establishing the Higgs coupling to fermions ($H \to \tau^+\tau^-$) and to quarks ($H \to b\bar{b}$), overcoming large background-rejection challenges [10].

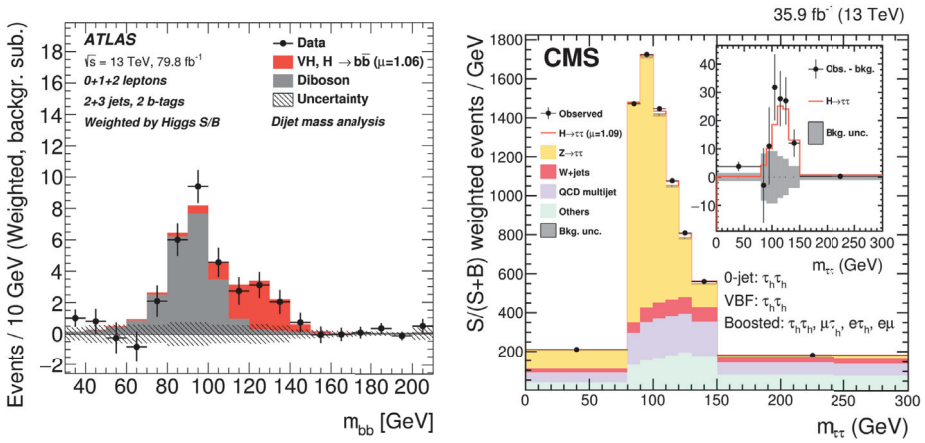

FIGURE 1.4: The di-b-jet mass distribution from the ATLAS $H \to b\bar{b}$ analysis (left) and the di-tau mass distribution from the CMS $H \to \tau^+\tau^-$ analysis (right). [10]

Though one of the primary goals of Run 2 was to progress on the search for the direct production of Beyond the Standard Model (BSM) physics, no significant excess of events over the SM expectation has been observed by ATLAS and CMS, despite the huge number of searches carried out. On the other hand, precise Standard Model measurements were concluded during Run 2 such as cross-sections, masses

and other SM parameters. The extremely precise cross-section measurements were allowed by the impressive precision of the luminosity measurements (2.5%), as the latter is used to normalize the cross-section value [10].

A number of important results were achieved by the LHCb experiment, such as the first observation of CP violation in charm particle physics [11], and the discovery of new penta-quarks [12], a stable baryon-meson configuration that could be described as a state of tightly bond cluster of five quarks. Concerning ALICE, Run 2 saw the first LHC run with XeXe collisions, opening new possibilities for collider physics [13]. Moreover, significant results were obtained concerning studies on quark-gluon plasma (QGP) thanks to PbPb collisions, which showed much narrower jets than the pp ones [14].

1.4 Future physics and LHC Upgrades

The LHC is currently reaching the delayed end of the LS2, foreseen for 2019-2020 and now extended up to 2021. The main goal of this Long Shutdown was to improve the accelerator for both short-term and long-term future, including preliminary upgrades leading to the High-Luminosity LHC (HL-LHC). The HL-LHC phase, foreseen to start in 2025, will see a luminosity increase of a factor five with respect to the LHC original nominal value. Figure 1.5 shows a luminosity prediction in the ATLAS Experiment during the next upgrades of the LHC.

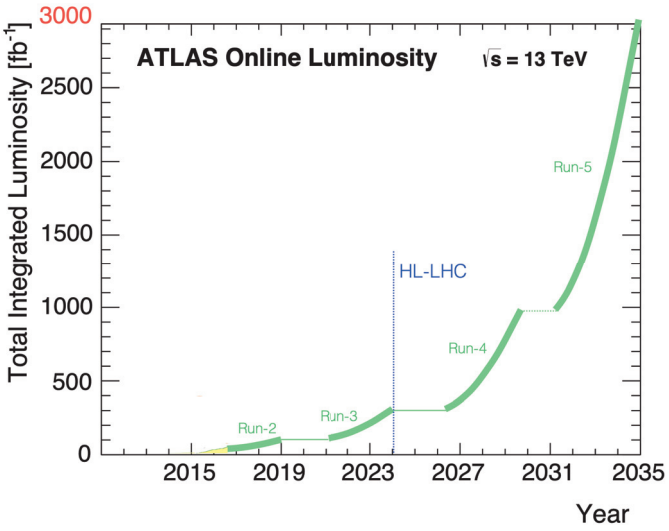

FIGURE 1.5: Trend of the total integrated luminosity foreseen for the ATLAS Experiment in the future phases of the LHC. [15]

The HL-LHC upgrades are also triggered by the fact that many critical components of the LHC will reach the end of their lifetime. To ensure safe operation at higher energies, hence requiring further magnets training, the electrical insulation of the dipole diodes bus-bars was reinforced [1]. Moreover, maintenance interventions were performed on the LHC cryomagnets, following a planning based on statistical analysis of the electrical faults. Among other interventions, a massive improvement program of the LHC injector chain was conducted. For the proton chain, this includes the replacement of Linac2 with Linac4 as well as all necessary upgrades to

the PS Booster (PSB), the PS and SPS, aimed at producing beams with the challenging HL-LHC parameters. In fact, to fulfill the HL-LHC requirement of integrated luminosity, the proton injectors are expected to produce proton beams with about double intensity and 2.4 times larger brightness [16].

Figure 1.6 reports the most recent long-term schedule established for the LHC, which locates the start of Run 3 in early spring of 2022. Already after the LS2 upgrades, the substantial increase in luminosity will pose major technical challenges for the Experiments during Run 3. The average pileup will rise, increasing the background levels, the average event size and the time it takes to reconstruct the events. Faster detectors and readout electronics are fundamental, as well as more sophisticated trigger systems, to fully exploit the Run 3 Physics, by efficiently identifying events signatures while keeping the transverse momentum resolutions at the current level. What is more, detectors will need to withstand a substantially increased radiation dose.

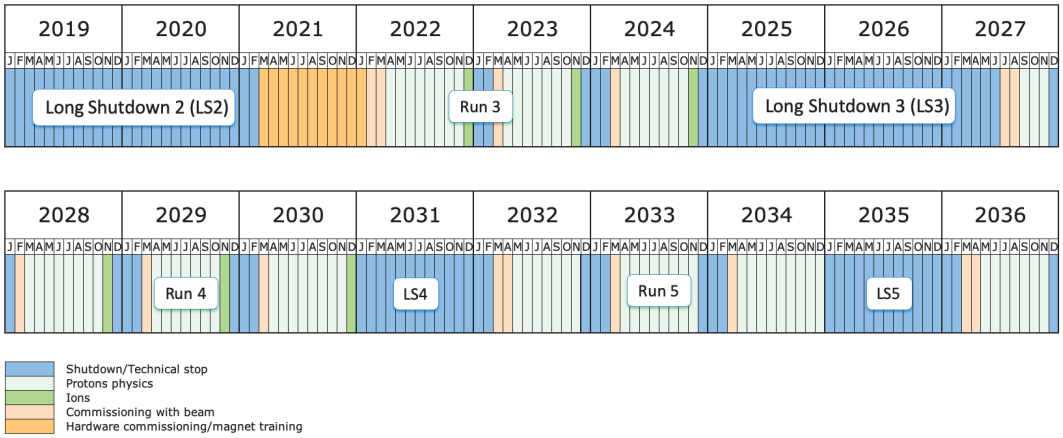

FIGURE 1.6: LHC long term schedule. [17]

A long consolidation and upgrade program saw its realization during the LS2 for all detectors systems, including improvements in the trigger and data acquisition systems, the front-end electronics and upgrades in detector themselves. In fact, while integration of new features and replacement of machine components will be the basis of the future collider performance, all Experiments showed the need of a complete renewal and reinforcement [18].

The ALICE Experiment has been equipped with a new Inner Tracking System (ITS), surrounding the new small-diameter beam pipe. The new ITS readout chips will also be employed by the Muon Forward Tracker (MFT). A new Fast Interaction Trigger detector (FIT) will replace the previous three trigger detectors, removing most of the unwanted signal. Finally, the Time Projection Chamber (TPC) readout was replaced, moving from Wire Chambers to four-layer Gas Electron Multiplier chambers (GEM), to cope with the increased interaction rate [19].

The ATLAS Experiment faced upgrades in its trigger and DAQ systems, reaching the 10 kHz as High-Level Trigger output [20]. The Liquid Argon and Tile calorimeters were as well improved in terms of electronics granularity, while the full Inner Tracker was subject to a major upgrade, making it efficiently operational for the next ten years [21]. The Muon System is currently progressing in the installation of the New Small Wheel [22], while a new high-granularity Timing detector is foreseen to

improve the ATLAS performance in the forward region [23].

Significant upgrades on the Level-1 Trigger of CMS were realized, leading to a performance widely acceptable for the HL-LHC phase. Both the end-cap and barrel calorimeters saw interventions to increase their granularity, as well as the installation of new back-end boards for ECAL and HCAL [24]. New Muon detectors sections are being installed (GEM [25]), as well as an additional MIP Timing Detector in the region close to the Interaction Point. The current tracker coverage was extended and the granularity increased thanks to improved Si-strip and pixels read-out [26].

As the LHCb Experiment fulfilled its original mandate with the end of Run 2, it is facing major upgrades on most of its systems, to be again efficiently operational under new luminosity conditions. The full electronics and data acquisition systems was replaced to handle the enormously increased data collection. Part of the MWPC Muon station will be replaced, to complete the full MWPC detector system replacement started in the LS1 [27]. The installation of the Scintillating Fiber tracker (Sci-Fi) is currently being finalized, guaranteeing small granularity and high spatial resolution in the region behind the dipole magnet [28]. The Vertex Locator (VELO), a silicon vertex detector, was also subject to improvements based on hybrid pixel sensors, to maintain its physics performance in the new operating condition [29].

Chapter 2

Muon Systems and Gaseous Detectors at the LHC

In the framework of the LHC physics program, Muon detection is fundamental for a complete identification and characterization of collisions, since Muons represent a very clean probe for many events of interest. In addition, they can provide trigger and veto for event selection. With a mass of 105.6 GeV, Muons can quite easily penetrate matter and they escape electromagnetic calorimeters. Each LHC Experiment is hence equipped with a Muon detector system, made of dedicated detectors capable of identifying and tracking these particles. This Chapter will start with a brief description of LHC Experiments Muon Systems, to give an overview of the framework of the different topics discussed in this thesis. As gaseous detectors are the designed detector type for Muon detection, their working principle will be illustrated with focus on Gas Electron Multipliers, as this type of detector will be the topic of the discussion of Chapter 3. Finally, the LHC Muon System infrastructure will be described, giving an introductory description of LHC gas systems design, to lay the basis for the discussion of the upgrade and development studies reported in Chapter 4.

2.1 LHC Experiments Muon Systems

In this Section a short overview on the LHC Experiments Muon Systems is given, illustrating their main requirements, their structure and the type of chambers installed, as they were originally designed and operated during Run 1 and Run 2. As in the current Long Shutdown (LS2) various detector systems upgrades are taking place, the last paragraph will illustrate the most important additions to the LHC Muon Systems and the key upgrades to the detectors currently installed.

ALICE [30]
In order to fulfill the ALICE physics program requirements, the Muon spectrometer is located downstream of the ALICE detector, covering the angular range $171^\circ < \theta < 178^\circ$. It consists of three absorbers, a Muon magnet, a trigger system and a tracking system, schematically reported in Figure 2.1. The absorbers allow to reduce the initial flux of primary hadrons by a factor 100, and they protect the detectors from low energy particles created in secondary interactions. The magnet generates a magnetic field (0.7 T) that allows to measure Muon momenta by tracking them along the field.

The trigger system (Muon Trigger system, MTR) allows to efficiently trigger high p_T Muons, exploiting the full luminosity potential of the LHC heavy ion beams. The

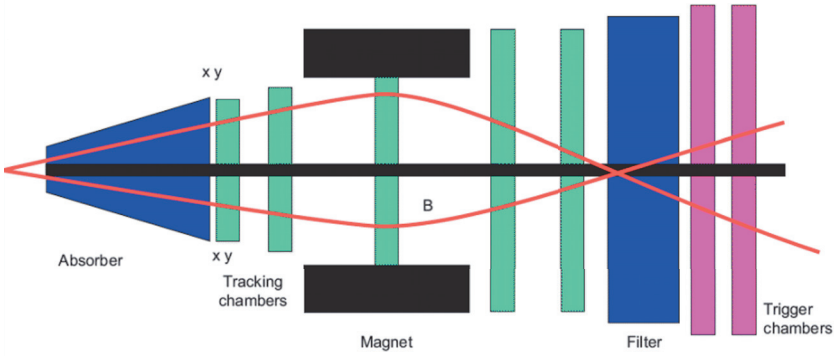

FIGURE 2.1: Schematic drawing of the ALICE Muon spectrometer [31]

system consists of 4 planes of 18 Resistive Plate Chamber detectors (RPCs) each, operating in avalanche saturated mode. Signals are collected by individual strips along the RPCs length and treated by a dual threshold discriminator. Information from the 4 trigger planes are processed by the local hardware cards, determining roughly the transverse momentum of the Muon track. Global hardware cards collect the full information from local cards and determine the trigger condition of the event in less than 700 ns. The Muon trigger delivers information to the central trigger processor for the generation of the ALICE Level-0 trigger.

The data collected by the tracking system (Muon Chambers system, MCH) allow to measure Muon transverse momentum in the bending plane by tracking Muons along the magnetic field. A momentum resolution of about 1% is achieved thanks to a spatial resolution in the bending plane better than 100 μm. The MCH is made of 5 stations with 2 detection planes consisting of 5 mm Drift Multi Wire Proportional chambers with bi-Cathode Pad read-out (CPV). Different pad densities are present, depending on the station position with regard to the pseudo-rapidity. The initial direction of the Muon is determined from its track parameters and the position of the interaction point, provided by the pixel internal tracking system (ITS) of ALICE .

ATLAS [32]
The ATLAS Muon spectrometer forms the outer part of the Experiment and it is designed to detect charged particles exiting the barrel and end-cap calorimeters. Its aim is to trigger on these particles in the region $|\eta|$ <2.4 and to measure particles momentum in the pseudorapidity range $|\eta|$ <2.7, with a momentum resolution of about 10% for 1 TeV tracks (equivalent to a z-axis resolution $\leq$ 50 μm). Precision tracking chambers in the barrel region are located between and on the eight coils of the superconducting barrel toroid magnet, while the end-cap chambers are in front and behind the two end-cap toroid magnets. The ϕ symmetry of the toroids is reflected in the symmetric structure of the Muon chamber system, consisting of eight octants, each subdivided in the azimuthal direction in two sectors with slightly different lateral extensions, a large and a small sector. The chambers in the barrel are arranged in three concentric cylindrical shells around the beam axis, while in the two end-cap regions Muon chambers form large wheels, perpendicular to the z-axis. Figure 2.2 reports the cross section of the Muon system on the plane transverse to the beam axis, with the overall layout of the Muon chambers.

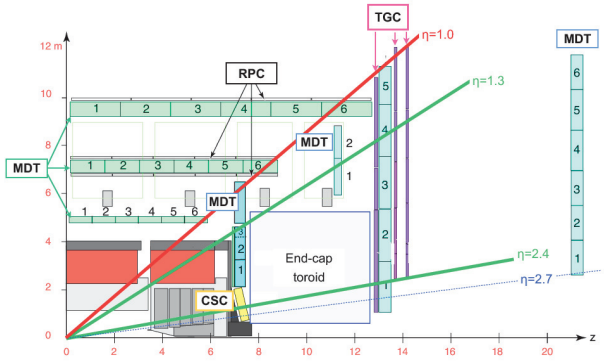

FIGURE 2.2: Schematic representation of the cross-section of the ATLAS Muon system.

The precision momentum measurement is performed by the Monitored Drift Tube chambers (MDTs), that cover the pseudorapidity range $|\eta|$ <2.7. The MDTs consist of three to eight layers of drift tubes, operated at an absolute pressure of 3 bar, which achieve an average resolution of 80 μm per tube, or about 35 μm per chamber. To reach such resolution, a high-precision optical alignment system monitors the positions and internal deformations of the MDT chambers. In the forward region (2< $|\eta|$ <2.7), Cathode Strip Chambers (CSC) are used in the innermost tracking layer due to their higher rate capability and time resolution. The CSCs are multi wire proportional chambers with cathode planes segmented into strips in orthogonal directions, allowing both coordinates to be measured from the induced-charge distribution. The resolution of a chamber is 40 μm in the bending plane and about 5 mm in the transverse plane. The difference in resolution between the bending and non-bending planes is due to the different readout pitch.

To satisfy the Muon tracks trigger requirements a system of fast trigger chambers is also present, capable of delivering track information within a few tens of nanoseconds after the passage of the particle. In the barrel region ($|\eta| < 1.05$), Resistive Plate Chambers (RPC) were selected for this purpose, while in the end-cap ($1.05 < |\eta| < 2.4$) Thin Gap Chambers (TGC) were chosen. Both chamber types deliver signals with a spread of 15–25 ns, thus providing the ability to tag the beam-crossing. The trigger chambers measure both coordinates of the track, one in the bending plane and one in the non-bending plane.

CMS [33]
The CMS Experiment structure is based on a super-conducting solenoid, that produces a 3.8 T magnetic field. The iron yoke is equipped with a Muon spectrometer for identification, triggering and momentum measurement. The system is divided into five separate wheels in the barrel, with four concentric layers of detectors. Both the positive and negative end-caps are instead instrumented with four independent disks. Figure 2.3 reports a schematic drawing of the CMS Muon spectrometer layout.

In the barrel, four concentric shells of Drift Tube chambers (DTs) are installed (η < 1.2), each shell made of 3 independent units, called superlayers (SL), and a thick honeycomb plate glued together. Each SL is composed by 4 layers of drift tubes, with all wires parallel. The two external SLs measure the Muon trajectory in the

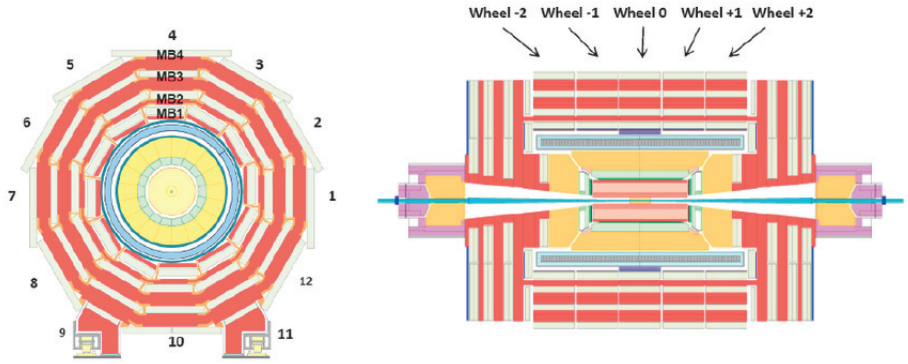

FIGURE 2.3: Schematic view of one of the five wheels of the Muon barrel system of the CMS Experiment in the x-y plane (left) and of the five wheels in the longitudinal view (right) [34].

CMS bending plane, while the third SL measures the z coordinate. The time needed by the primary electrons to reach the anode is measured and the spatial position of the track is calculated from the time measurement and the known time-to-distance relationship. The measurement spatial resolution reaches 100 μm in the ϕ coordinate and 150 μm in the z coordinate.

Resistive Plate Chambers are installed in both the barrel and end-cap as dedicated trigger detectors ($\eta < 1.6$). They guarantee a precise bunch crossing assignment of the Muon tracks thanks to their fast response and good time resolution. The barrel Muon station are equipped with two RPC layers for the innermost stations and one layer for the outer stations for a total number of 6 layers per sectors. The end-caps are instrumented with one RPC layer per station for a total of 4 layers. The location of the RPC stations can be found in Figure 2.5.

Finally, precise time and position measurements in the end-caps are provided by Cathode Strips Chambers ($0.9 < |\eta| < 2.4$). Each chamber is trapezoidal in shape and consists of six gas gaps, thus each chamber measures up to six space coordinates. The wire signal gives fast information with a spatial resolution of about 1 mm while a precise spatial measurement is achieved using the center of gravity of the charge distribution induced on the cathode strips.

LHCb [35]
The Muon detection system is fundamental in the LHCb Experiment since Muons are present in the final states of many CP-sensitive B decays, which the Experiment is capable of detecting thanks to its forward angular coverage of 10-300 mrad in the bending plane. The system provides fast information for high p_T Muon trigger at the earliest level of online event selection, as well as Muon identification for the high level trigger and offline analysis.

The Muon system is composed of five stations (M1-M5) of rectangular shape, placed along the beam axis, with a total of 1380 chambers covering an area of 435 m^2. Each station is equipped with 276 Multi Wire Proportional Chambers (MWPCs, 5 mm gas gap), except for the high rate region, where 12 double layers of Triple Gas Electron

Multipliers (GEMs) are installed. The stations consist of two mechanically independent parts, side A and C, that can be horizontally moved to access the beam pipe and the chambers for maintenance, and each of them is divided into four regions (R1-R4) with increasing distance from the beam axis (Figure 2.4).

Despite the good Triple-GEMs performance during Run 1 and Run 2, chambers were removed during the Long Shutdown 2 and the LHCb Muon system will only operate with MWPCs for Run 3, which at that point will be composed of fully renewed chambers thanks to the substitutions operated during LS1 and LS2. Further upgrades including μ-RWELL detectors (micro-Resistive WELL) are foreseen for the following runs in view of the operation of the LHCb Experiment with increased LHC luminosity [36].

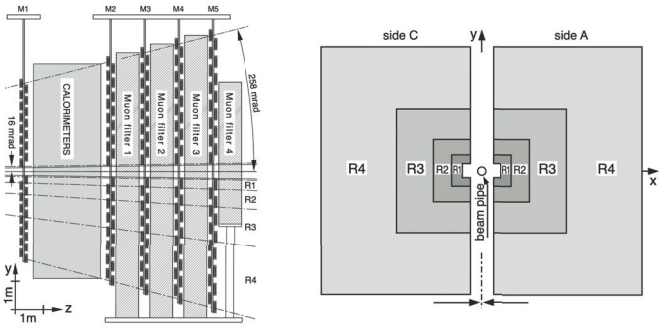

FIGURE 2.4: Side view of the LHCb Muon detector with the M1-M5 stations (left) and station layout with the four regions R1–R4 (right).

2.1.1 Muon Systems Upgrades

As illustrated in Section 1.4, a major upgrade of the LHC is being prepared (HL-LHC) to extend the sensitivity for new physics searches. The integrated luminosity will increase tenfold with respect to the original design values, with a foreseen integrated luminosity of 3000 fb^{-1} for the coming decade. The LHC upgrade will mainly affect the CMS and ATLAS Experiments, as they will experience the increased luminosity the most [37]. Within the many detector upgrades, a number of interventions was foreseen for the Muon Systems of these two Experiments, to keep up with the new LHC performance and fully exploit its physics potential. Some relevant examples of upgrades realized during the current LS2 and others foreseen future interventions are reported in the following.

CMS GEM [25]
The GEM (Gas Electron Multiplier) technology has proven to operate reliably at hit rates of the order of a few MHz/cm^2, easily adequate for CMS at the HL-LHC, in particular in the Triple-GEM configuration. Three sets of GEM detectors are foreseen for the CMS upgrade. During the current LS2, a first ring of two-layer Triple-GEM detectors were installed in the CMS end-cap, named GE1/1, placed close to the ME1/1 CSC chambers. Their acceptance in pseudorapidity reaches $|\eta|$= 2.15. They allow a better measurement of the track bending, significantly reducing mismeasured tracks, and they can also provide a backup for any problems that might arise in the ME1/1 system. The two-layers of GE2/1 chambers, that will be installed in the second end-cap station, partly overlap in pseudorapidity with the GE1/1

chambers, and extend the GEM detector acceptance in the pseudorapidity range 2.15< $|\eta|$ <2.4. Finally, the ME0 detectors will increase the acceptance of the Muon system to $|\eta|$=2.8, making use of the same Triple-GEM technology as GE1/1 and GE2/1, but in a six-layers configuration. They will provide a Muon trigger signal in the very forward region, and the ME0 hits will be used in the offline Muon reconstruction. An ME0 chamber provides up to six track points and therefore enough redundancy to reject neutron-induced backgrounds and to form Muon track segments in the L1 trigger. Figure 2.5 reports the layout of the CMS Muon detectors, including the new GE1/1, GE2/1 (red) and ME0 (orange) Triple-GEM detectors stations.

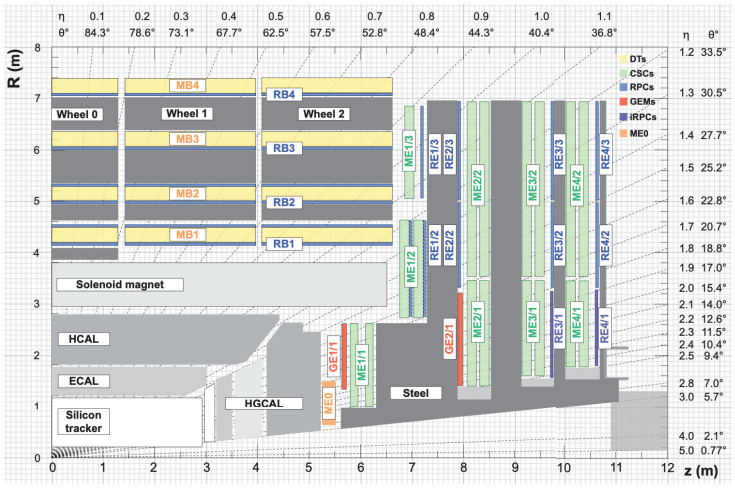

FIGURE 2.5: Schematic layout of the CMS Muon System, where are indicated the new Triple-GEM stations (GE1/1 and GE2/1 in red, ME0 in orange) and the iRPC stations (RE3/1 and RE4/1, in purple).

CMS Improved RPC [37]
For the CMS RPC system future upgrades, the addition of new detectors for the forward region is foreseen. The main motivation is to extend the geometrical acceptance of the RPCs from $|\eta|$=1.9 to 2.4 and to increase the redundancy in the end-cap region, as envisaged already in the original CMS Muon system design. The new stations will use an improved version of Resistive Plate Chambers, named iRPC, to sustain the high expected rates (2 kHz/cm^2), with a hit efficiency well above 95%. The higher rate capability with respect to the current RPC detectors will be achieved by shortening the recovery time of the electrodes and reducing the total charge produced in a discharge. To this purpose, the iRPCs use thinner electrodes and a narrower gas gap, both reduced from a thickness of 2 mm in the current design to 1.4 mm. Furthermore, the operational high voltage is lowered and the resulting loss in gas gain will be compensated by the higher signal amplification of improved front-end electronics. The lower charge produced per traversing particle will also reduce the integrated charge deposited and slow down aging processes. The baseline choice of material will remain HPL (High Pressure Laminate, also called bakelite), as for the present RPCs. The location of the new iRPC detector system can be seen in the CMS Muon system layout reported in Figure 2.5.

ATLAS Micromegas [22]

The first station of the ATLAS Muon end-cap system (Small Wheel) will be replaced in view of the high luminosity performance of the upgraded LHC. The New Small Wheel (NSW) will have to operate in a high background radiation region (15 kHz/cm^2) while reconstructing Muon tracks with high precision as well as supplying information for the Level-1 trigger. To fulfill such demanding requirements, the NSW will combine two chamber technologies: small-strip Thin Gap Chambers (sTGC) and Micromegas detectors (MM). In particular, the NSW will be the first LHC detector system exploiting the newly developed MM technology (Figure 2.6), part of the new generation of Micro Patter Gaseous Detectors (MPGD). The MM detectors have exceptional precision tracking capabilities due to their small gap (5 mm) and strip pitch (approximately 0.5 mm), crucial to maintain the current momentum resolution even in the future high-background environment. The NSW installation was planned to happen gradually between the LS2 and the first Run 3 year-end technical stop, but due to the LS2 extended duration it could be possible to have it fully ready for the beginning of Run 3.

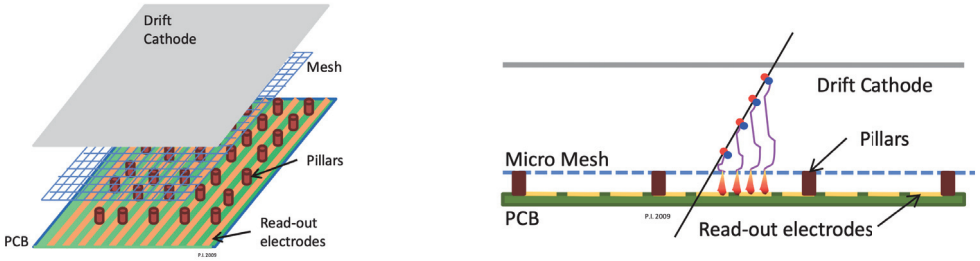

FIGURE 2.6: Schematic representation of the Micromegas detector layout (left) and its working principle (right).

2.2 Gaseous detectors

As illustrated in the previous Section, gaseous detectors are the basic element of Muon triggering and tracking systems. This Section will describe their basic working principles, ionization by charged particles and gas multiplication, to give an overview on the pulse generation process. The Single Wire Proportional Chambers (SWPCs) working principle will also be illustrated, such configuration being the basic one of gaseous chambers. Moreover, as SWPCs will be employed in the gas monitoring systems described in the following Chapters, a short overview will be given on the characterization of such detectors in relation to their performance under different gas-operation conditions. Finally, Gas Electron Multipliers being the focus topic of Chapter 3, their working principle will be illustrated, in particular for the Triple-GEM configuration.

2.2.1 Gaseous detectors working principle

When a fast charged particle passes through a gas, it can create ionized molecules along its path, resulting in an ion pair, i.e. a positive ion plus a free electron [38]. Ion pairs serve as the basic constituent of the electrical signal developed in gaseous detectors. When the incoming particle transfers a given minimum amount of energy

to the gas molecule, i.e. the ionization energy, the ionization process occurs. However, other energy-loss mechanisms may take place, such as excitation processes, in which an electron can be elevated to a higher bound state without being completely removed. For this reason, the W-value is defined as the average energy lost by the incident particle per ion pair formed, which is always greater than the simple ionization energy. The W-value generally depends on the gas involved, the type of radiation and its energy. Typical values are between 25 eV and 35 eV per ion pair. Assuming W to be constant for a given type of radiation, the energy deposit will be proportional to the number of ion pairs formed in the gas.

Positive ions and free electrons created by the incoming particle would take part in the random thermal motion, with the tendency of moving away from regions of high density. The process is much more pronounced for electrons, being their thermal velocity much higher. Of the many collision processes that normally take place between free electrons, ions and neutral gas molecules, the most significant ones for gaseous detector operation are charge transfer and recombination. Nevertheless, the influence of both phenomena is highly mitigated by the application of an external electric field, that favors charges mobility and collection. Electrostatic forces would tend to move the charges away from their point of origin, in a motion that consists in the superposition of their random thermal velocity and their drift velocity in the field direction, with positive ions and free electrons drifting in opposite directions. In both cases, their velocity is defined by $v = \mu \cdot E/p$ where E is the electrical field strength and p is the gas pressure. The mobility coefficient μ remains basically constant over wide ranges of electric field and pressure. Nevertheless, while its typical value for ions is around $1.5{\cdot}10^4$ m^2atm/V, for free electrons it has a value about 1000 times greater.

If the electric field applied in the gas volume is low, electrons and ions created by incident radiation would simply drift along the field lines to their collecting electrodes. However, when the applied field is increased, gas multiplication process starts to take place. Free electrons are easily accelerated by the applied field, gaining kinetic energy. When such energy is greater than the W-value of the gas molecules, secondary ionization can occur in the collision between free electrons and neutral gas molecules, generating additional ion pairs. The average energy gained by free electrons increases with increasing electric field intensity, imposing a threshold value of the field above which secondary ionization can take place (around 10^6 V/m). The electrons produced from secondary ionization will in turn be accelerated by the field, undergoing collisions during the subsequent drift and thus creating additional ionization pairs. The gas multiplication process takes the form of a cascade, the so called Townsend avalanche. Each free electron created can potentially create more free electrons, and the whole process can be described by the Townsend equation:

$$\frac{dn}{n} = \alpha \cdot dx$$

where α is the first Townsend coefficient. Such coefficient is equal to zero for electric field values below the ionization threshold, and increases with increasing field strength. Assuming a spatially constant field, α can be considered a constant in the equation, that gives then the exponential growth of the electron density for increasing distance as the avalanche progresses:

$$n(x) = n(0) \cdot e^{\alpha x}$$

Under proper conditions, the number of secondary ionization events can be kept proportional to the number of primary ion pairs formed. The proportionality factor, i.e. the total gas multiplication gain, can be calculated from the Townsend equation:

$$M = \frac{n}{n_0} \cdot e^{\alpha x}$$

As reported in Figure 2.7, it exists a region of the applied voltage, i.e. of the electric field in the gas volume, for which the collected charge begins to multiply, and the avalanche amplitude increases (proportional region). Over most of this region, the gas multiplication is linear, and the collected charge is then proportional to the number of original ion pairs created by the incident radiation. This region of true proportionality represents the usual operation mode of gas-filled proportional counters. If the applied voltage is further increased, non linear effects can be introduced, falling in a limited-proportionality region.

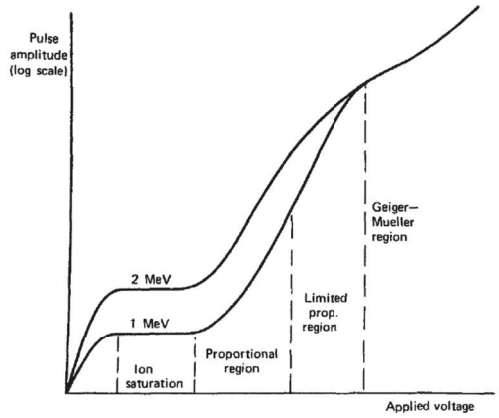

FIGURE 2.7: Regions of operation of gaseous detector, represented in terms of proportionality between the pulse amplitude and the applied voltage. [38]

Gaseous detectors generally aim to work in the proportional region as the proportionality between the final number of electrons with the number of ion pairs created leads directly to a proportionality also with the energy lost by the incoming charged particle. The collection of the multiplied charges allow therefore to have a measurement of such energy, together with the counting of the number of incoming particles. The charge collection takes place by the formation of a signal on the electrodes which in the most basic configurations are the same that allow to establish the electric field in the gas volume through a given voltage difference between the two. The signal generation rises from the induced charge on the electrodes by the movement of ions and electrons, where electrons are typically chosen as main collected charges thanks to their higher drift velocity. The induced charge variation along the time of displacement of the electron towards the electrode is described by the expression of $V(t)$, which therefore defines the time development of the signal depending on the specific electric field shape.

The most widely used gas to fill gaseous detectors is Argon, due to the optimal combination of its properties with a generally limited cost. It has in fact a very low electron attachment coefficient, that guarantees most of the free electrons to reach

the multiplication phase without interference. It should however be taken into account that, beside simple ionization, the collision between electrons and neutral gas molecules may give rise to excitation, without the creation of a secondary electron. The excited molecules decay to their ground state, through the emission of a visible or ultraviolet photon, that may create additional ionization elsewhere in the gas. These events are normally undesirable, since they may cause a loss of proportionality or the presence of spurious pulses. Moreover, they cause the avalanche to spread in space. It has been found that the addition of a certain amount of polyatomic gas, such as Carbon Dioxide (CO_2), can suppress the photon-induced effects by absorbing the photons in a mode that does not lead to further ionization (vibrational modes). The polyatomic component is then usually present in some percentage, together with the monatomic one, as a stabilizing additive (also called quencher). Another advantage in adding a quencher gas into the mixture is its influence on the free electrons motion. Being Argon a purely inelastic gas, electrons tend to collide with gas molecules and scatter in every direction, making the drift quite inefficient. A polyatomic gas as CO_2 is instead an inelastic gas, with many degrees of freedom (linear, rotational, roto-vibrational modes), which allow electrons to be much faster in reaching the anode.

2.2.2 Single Wire Proportional Chambers

Together with the parallel plates configuration, the most simple gaseous detector layout is the one of Single Wire Proportional Chambers (SWPCs). They have a cylindrical configuration, consisting of a sealed container, with conducting walls and a thin end-window. The cylindrical container acts as cathode, while a wire positioned along its axis acts as anode (Figure 2.8). The voltage polarity is realized in way to have electrons attracted towards the central axial wire, to facilitate their collection and signal formation. The electric field at a radius r in such geometry is given by:

$$E(r) = \frac{V}{r \cdot ln(b/a)}$$

where V is the applied voltage, a is the anode wire radius and b is the cathode inner radius. As electrons are attracted to the anode, with such field they will be drawn towards the high field region, in the immediate vicinity of the anode wire, where r is very small. The physical multiplication region only begins where the field becomes large enough to support avalanche formation, that for a minimum field value of 10^6 V/m corresponds to about 0.04 cm. In Figure 2.8 the electric field is plotted against the distance from the anode.
SWPCs can be an handful tool for monitoring purposes, as their performance is very sensitive to out-gassing and gas mixture variations, specifically to the presence of impurities even at the level of ppm [39]. As SWPCs monitoring systems operation will be discussed in the following Chapters, it will be here presented a brief summary of their characterization, realized at laboratory level to better understand their performance in relation to gas mixture variations. The characterization is obtained collecting with a basic electronic chain the X-ray signal induced by an ^{55}Fe radioactive source, estimating the SWPCs amplification gain from the mean value of the ^{55}Fe typical spectrum, for different compositions of the filling gas mixture.

SWPCs performance was tested for different compositions of the two most used gas mixtures, Ar/CO_2 and $Ar/CO_2/CF_4$. In the first case, the gas mixture composition

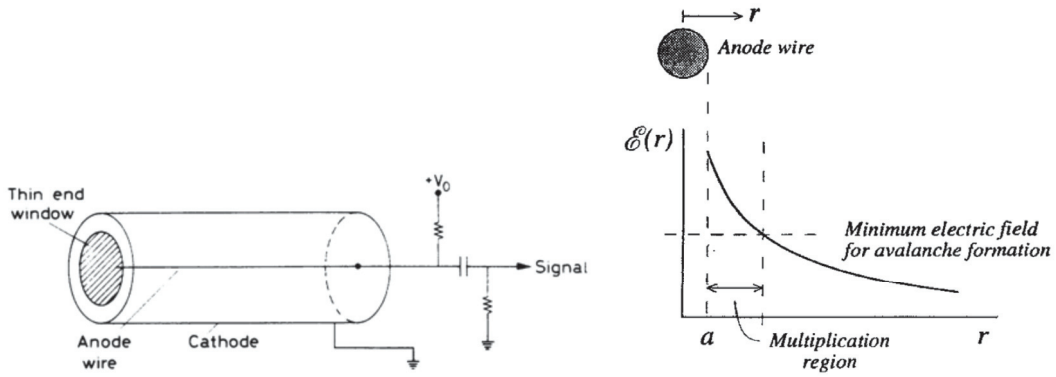

FIGURE 2.8: Geometrical layout of a SWPC (left) and trend of its electric field as a function of the radius r (right). [38]

was varied between the ratio 80/20 and 62.5/37.5, with 2.5% variations steps. For the CF_4-based mixture, the Ar/CO_2 ratio was kept constant at 3/1 while the CF_4 concentration was varied from 35% to 45% in 1% steps. Figure 2.9 reports the SWPC normalized amplification gain in relation to the variations of the gas mixture components, for a fixed High Voltage value. In the first case, the gain shows a decrease of about the 10% for an increase of 1% of CO_2 in the gas mixture, with a higher impact for lower values of CO_2 content. The gain trend for CF_4 concentration variations is found to be consistently linear on the range of tested concentration, with about a 5% gain loss per 1% of CF_4 increase. These results show how the SWPCs are particularly sensitive even to small changes in the gas mixture components concentrations, that can therefore be easily spotted by looking at SWPCs performance variations.

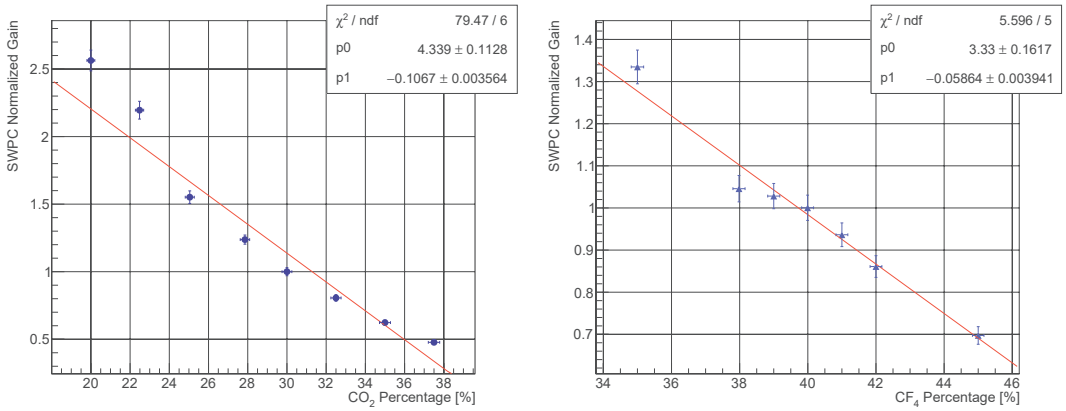

FIGURE 2.9: SWPCs normalized amplification gain as a function of CO_2 concentration in the Ar/CO_2 gas mixture (left) and as a function of CF_4 variations for the mixture $Ar/CO_2/CF_4$ with Ar/CO_2 ratio fixed at 3/1 (right).

SWPCs behavior was also characterized in relation to the presence of pollutants in their filling gas. The test was realized with the Ar/CO_2 70/30 gas mixture, polluted with variable concentrations of O_2 (0-1150 ppm) and N_2 (0-50000 ppm), typical gas systems impurities. Figure 2.10 reports the SWPCs normalized amplification gain in relation to the impurities concentrations in the mixture. Results show how the amplification gain exponentially decreases with the increase of O_2 concentration, with

a gain drop of 20% in the range 0-500 ppm. On the other hand, detector performance results to be quite stable up to N_2 concentration of 1%, while after this value the amplification gas linearly drops down to -70% for N_2 concentration of 5%. This characterization will allow to have precise references on the variations of SWPCs performance when O_2 and N_2 are present in the gas mixture.

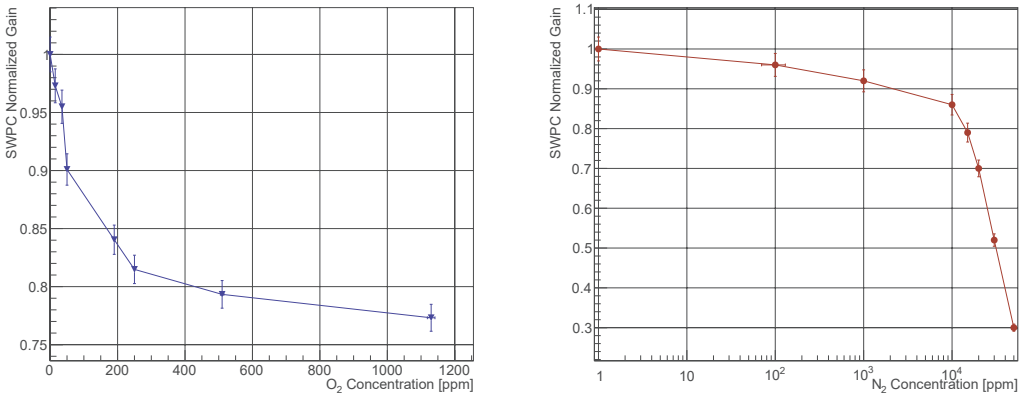

FIGURE 2.10: SWPC normalized amplification gain for variations of the concentration of O_2 (left) and N_2 (right).

2.2.3 Triple-GEM Detectors

Gas Electron Multipliers (GEMs) belong to the wider class of Micro-Pattern Gaseous Detectors (MPGDs), mainly developed to overcome the limits of Multi Wire Proportional Chambers (MWPCs) in term of efficiency at high particle rates and limited operating life span. The first GEM layout was proposed by F. Sauli in 1997, and it was widely studied and improved since then. GEM detectors are nowadays an affirmed technology, employed in many different applications [40].

The GEM electrode is a thin polymer foil, metal-coated on both sides, perforated with a high density of holes. The typical foil is based on a 50 μm thick Kapton foil, with two 5 μm layers of Copper-coating on the opposite sides. Holes have normally a diameter of 70 μm, with 140 μm pitch. The foil manufacturing is based on a double-mask process: the pattern of the holes is engraved by conventional photolithography on the metal of both sides of the foil, and holes are then opened with a Kapton-specific solvent. Dissolving the unprotected polymer on both sides creates holes with a double-conical shape, with the diameter in the center of the insulator slightly smaller than at the metal surface.

A basic single-layer GEM detector is formed by a GEM foil, inserted in a gas volume, between a drift foil and a patterned read-out foil. Each hole acts as an individual proportional amplifier for the primary electrons created by the ionization produced by incoming radiation in the upper drift region. Applying a potential difference between the top and the bottom GEM electrodes, a dipole field develops in the holes, focusing there the electrons. If the field intensity is high enough, the multiplication process will occur inside the holes. Electrons produced in the upper region will drift towards the holes and they will acquire sufficient energy to cause ionizing collisions with the molecules of the gas. A fraction of the electrons in the avalanche will leave

the multiplication region and transfer into the lower section of the structure, where they can be collected by an electrode. The amplification gain reached with a single foil configuration is around 10^2-10^3, for an electric field of 2 kV/cm (ΔV=500 V) and the typical GEM gas mixture Ar/CO_2 70/30. Figure 2.11 reports a schematic drawing of a single-layer GEM detector and the typical electric field lines shape in the GEM holes.

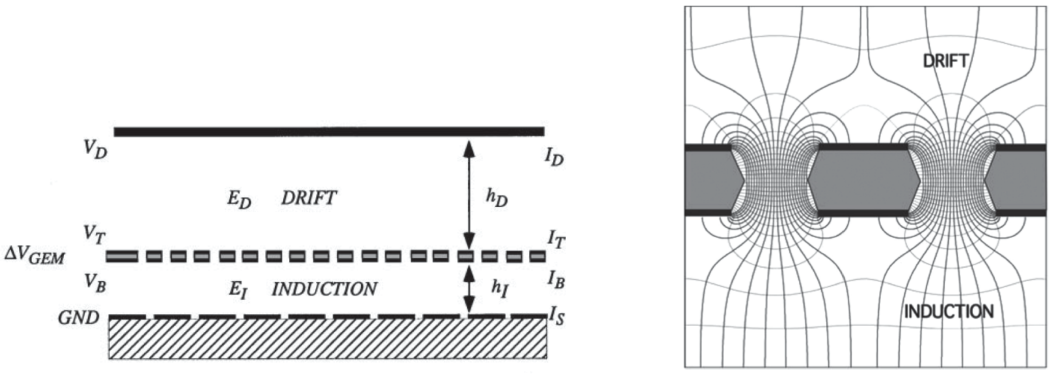

FIGURE 2.11: Single-layer GEM detector configuration (left) and graphic representation of the typical GEM foil holes with the electric field lines (right). [38]

The negative signal on the anode is generated by the collection of electrons, making the device potentially very fast and minimizing space charge effects. The purely electronic signal is generated by the movement of the negative charges in the induction gap. The size and shape of the signal depend on the induction field, that creates faster and narrower signals when it has an higher intensity. Ions do not participate to the signal induction: they slowly drift back towards the top GEM electrode and the drift foil. The signal generated by the movement of positive charges is totally shielded by the GEM foil, therefore no ion tail is contained in the typical GEM signal.

A unique feature of GEM devices is that the fraction of the amplified electrons transferring to the gas gap following the first electrode can be injected and multiplied in a second foil. The advantage of a multiple structure is that an acceptable gain can be obtained with each foil operated at a lower voltage, therefore with less probability of discharges. Triple-GEM detectors are composed by three identical GEM electrodes, separated by gas-filled gaps. The typical spacing between foils is 3-2-2-1 mm or 3-1-2-1 mm, referring to the drift space, two transfer gap and induction gap respectively (Figure 2.12). The combination of three GEM foils allows to operate each of them at less than 400 V reaching a total amplification gain up to 10^5.

Voltage can either be supplied with a dedicated line for each foil, or with a single voltage source and a resistive distribution chain. In the latter case, the resistive circuit can be either realized with a series of resistors or with a single ceramic voltage divider [41]. More details on Triple-GEM detectors assembling procedure, testing and characterization, in particular for the 10×10 cm^2 detector prototype used in the studies presented in this thesis, can be found in reference [42].

The gas mixture typically used for Triple-GEM detectors is Ar/CO_2, in the proportion 70/30, which however results in a relatively low time resolution due to the limited drift velocity (0.005 cm/ns, [43]). To accomplish requirements on a better time

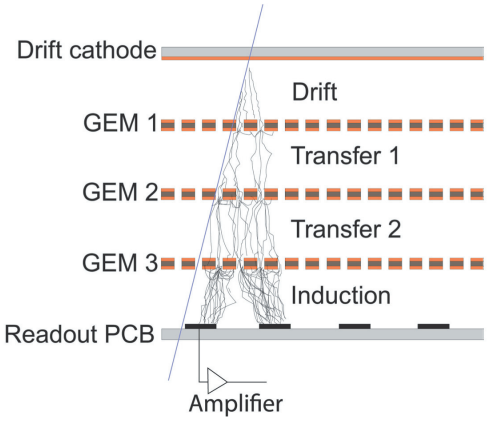

FIGURE 2.12: Schematics of the Triple-GEM detector configuration. [40]

resolution, the addition of CF_4 has been tested, leading to a gas mixture with a drift velocity increased of a factor two, particularly advantageous for operation in high rate environments and to resolve very close events. The optimal gas mixture composition was assessed on $Ar/CO_2/CF_4$ in fractions 45/15/40. As it will be discussed in the following Chapter (Section 3.6), the usage of CF_4 in the Triple-GEM gas mixture implies a series of consequences concerning the possible impurities created in the detector volume when operated in high-rate environments, because of the chemical reactivity of fluorinated compounds liberated in the electron avalanches.

2.3 The LHC Gas Systems

As the gas mixture is the key element of gaseous detectors operation, a correct and stable mixture composition is a basic requirement for good and stable long-term performance. Therefore, regardless the location and scope of gaseous detectors in LHC Experiments, the gas distribution system represents one of the most critical infrastructures to build and maintain [2]. The basic function of the gas system is to mix the different gas components in the appropriate proportion and to deliver the mixture to the corresponding detectors. More than 30 dedicated gas systems are currently operational at CERN, over the four LHC Experiments as well as on non-LHC detector systems.

The LHC gas systems have been implemented following a modular design, in way to be able to adapt to each detector system requirements while maintaining a basic common structure to optimize building, commissioning and maintenance operations. Each of the modules complies to a specific function, and it is associated with a Programmable Logic Controller (PLC) unit, an industrial PC with basic functionalities for managing and monitoring the unit. The control software for the gas system runs in the PLC, which is connected to each gas system module through a Profibus protocol [44] in way to collect I/O information. The control software is based on the WinCC-OA SCADA tool, which is capable of creating the description of a device in terms of a data point, with data point elements representing its parameters. Relevant parameters can be stored in a database, and consulted through a custom graphical user interface. Such interface also allows to actively control the device, and more

globally the gas system module with all its elements and in terms of interactions between two modules.

In the LHC Experiments, the gas system modules are located over three different levels: the surface room (SG), the underground service room (US) and the experimental cavern (UX). All the units that need an immediate access are located in the SG, together with the primary gas supply. Following a route of few hundred meters, gas connections are brought underground to the US, which provides gas pre-distribution into several channels, as well as part of the gas system parameters regulation. The effective detailed distribution to each detector is instead done in the UX, from the service balcony gas racks. Figure 2.13 reports a schematic representation of the basic configuration of an LHC gas system, with the location of the single modules, briefly described in the list below.

Primary Gas Supply:
Each gas is provided by two independent supply sources, one in use and one in stand-by, that can compensate when there is a failure in the other one and during replacement of the storage tanks.

Mixer Module:
Primary gases are used to prepare the gas mixture for each detector. Mixer modules have up to four input lines, equipped with Mass Flow Controllers (MFCs), controlled via the software control system to set the correct concentration of each component of the gas mixture. In particular, for each fresh gas, two MFCs are installed with different volume flow ranges, in way to adapt to the needs of the gas systems in different moments of operation (run, fill, purge). The gas mixture is prepared with high precision, with less than 1% uncertainty on the concentration value of each gas component. A mixing volume allows to properly mix the gas mixture components before it is sent to the following modules.

Gas Distribution:
Several steps are needed to distribute the gas mixture to each detector, with specific gas volume flow and pressure. Pre-distribution modules are located in the US, and they are related to different detector sectors of the Experiment. They can be grouped with common regulation parameters, and then be split into smaller modules for specific sections of the detector sector. The gas is sent from the US to the UX, where the final distribution modules are located, and each pre-line is split into several smaller lines, to distribute the gas with the required granularity. The UX modules are designed with simplified electronic and manual systems which do not require access during LHC operation, while the others distribution levels can still be accessed and controlled during LHC runs if necessary. The gas mixture coming from the exhaust of the chambers is re-grouped into return modules.

Pump Module:
Once the gas has flown from the UX into the return modules, the union of the full return gas volume is sent to the pump module, that compresses the gas to an higher pressure in way to send it back to the surface. In general, more pumps are present in a single module, to have a backup available or increase the compressing rate.

Exhaust Module:
The gas returning to the surface modules can either be fully exhaust to atmosphere

or sent back to recirculation, depending on the mode of operation (see the following Section 2.3.2). The return gas passes through the exhaust module, where volume flow and pressure regulations allow to manage the gas emission in relation to the gas system parameters which are subject to specific requirements, for example the chamber pressure stability.

Purifier Module:
If the return gas is re-injected in the system, a purifier module allows to act on some of the impurities typically accumulated along the gas path, in the gas system elements or directly in the detectors volume. Impurities can indeed accumulate due to leaks, gas supply quality and detector permeability, or in some cases they can directly be created inside the detector volume due to chemical reactions happening between the gas molecules and detectors material when subject to irradiation. The most common impurities are N_2, O_2 and H_2O, but only the last two can be easily removed through adsorption filters [45]. The purifier module consists of two 24-liters cartridges, filled with suitable material that interacts with the specific impurity. Molecular sieves are used for H_2O removals (for example MS5Å, 130 g(H_2O)/kg) and metallic catalysts for O_2 absorption (for example $NiAl_2O_3$, 15/50 g(H_2O/O_2)/kg). As the active materials is subject to saturation, its usage is bound to regeneration cycles realized by heating the columns. The presence of two columns hence allows to have one column in use while the other is regenerated, avoiding to interrupt the purification process.

Gas Analysis Module:
The gas analysis module allows a continuous monitoring of the gas mixture quality in the critical gas system points (after mixer, exhaust, after purifier). Normally, O_2, H_2O and InfraRed (iC_4H_{10}, CO_2) analyzers are present, to measure the concentration of impurities and relevant mixture components. In some cases, the analysis module has an integrated system to perform Gas Chromatograph analysis on selected sample lines, in way to obtain a more complete measurement of all the gas mixture components. The Gas Chromatograph analysis system is discussed in details in Section 2.3.1.

2.3.1 Gas analysis with Gas Chromatograph

Gas Chromatography (GC) is a laboratory analysis technique that allows to separate and quantify in terms of concentration the different components of a given gas mixture. For what concerns gas analysis in the LHC Experiments gas systems, the instrument of choice is generally a micro-GC [46] [47], a compact Gas Chromatograph created by the integration of micro-fabricated components. The basic elements of the instrument are a micro injector, one or more analytical columns and dedicated Thermal Conductivity Detectors (TCDs). The advantage of this type of device is to have analytical columns that are much shorter than the ones of a standard Chromatograph, allowing to perform analysis in the time span of some minutes. The working principle of the micro-GC will be briefly described in this Section, followed by the discussion of the GC-based analysis setups of the LHC Experiments with relevant examples.

The gas mixture under analysis is injected into the micro-GC through a micro injector, along with a pure known gas, the so-called carrier gas. Usual carrier gases are Ar, He or N_2, depending on the specific properties of the column type of choice

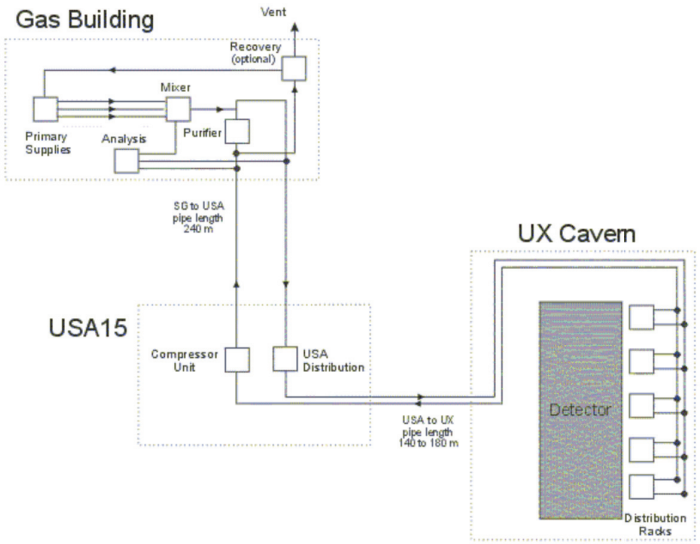

FIGURE 2.13: Schematic representation of the basic modules of an LHC gas system.

and the analyzed mixture. As the gas enters the column, all the components are still mixed and spatially close to each other. The separation is realized thanks to the material that coats the surface inside the column, as different components react with different intensities with the material, in particular through Van der Waals forces. Therefore, some of the components will be more delayed in their flow through the column with respect to others, separating in this way the original gas mixture in terms of arrival times at the output of the column, where the TCD is located.

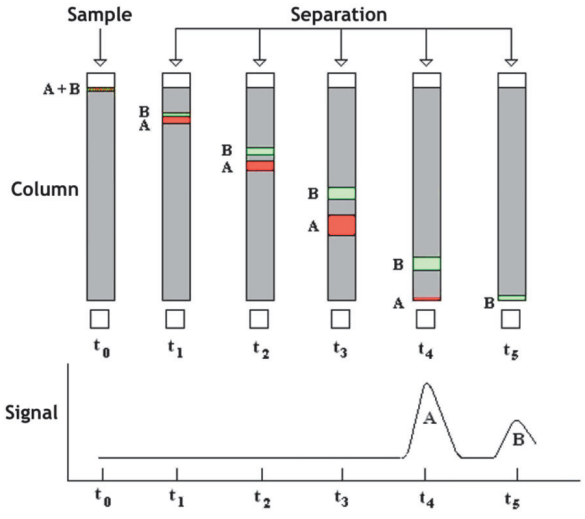

FIGURE 2.14: Schematic representation of the separation process inside a microGC column.

Many separation columns exist, and their choice mainly depend on the nature of the mixture components to be analyzed. The columns typically used for LHC gas system analysis are the following:

- *PPlotU*:
  made of Divinylbenzene/Ethylen-glycoldimethacrylate, designed to separate C1 to C4 hydrocarbons, CO_2, CH_4, H_2O, H_2S, SO_2, N_2O.
- *MolSieve*:
  5Å zeolite molecular sieve, designed to separate H_2, CO, methane, N_2, O_2 and some noble gases.
- *OV1*: made of 100% Polydimethylsiloxane, designed to separate hydrocarbons from C_4 to C_{12}, BTEX, and VOC.

Together with the column coating type, many parameters can be varied to optimize the component separation such as the column length, the carrier gas and its pressure, the injector and column temperature.

The TCD is capable of sensing changes in thermal conductivity of the column stream, and compares it to the reference flow of the carrier gas. The detector consists of a pair of electrically heated filaments in a temperature-controlled cell, that change their resistance according to the different thermal conductivity of the gas stream components. The change in resistance is then measured with a Wheatstone bridge circuit (Figure 2.15), which produces a voltage signal. One way of the Wheatstone bridge is reserved to the carrier gas, while the second way is reserved to the analytical column flow. When the analytical flow is pure carrier gas, the bridge is balanced and no signal is produced. When the analytical flow contains other components, the heat capacities of the sample molecules cause fluctuations in the filament temperature. The bridge is hence unbalanced and a voltage signal is produced.

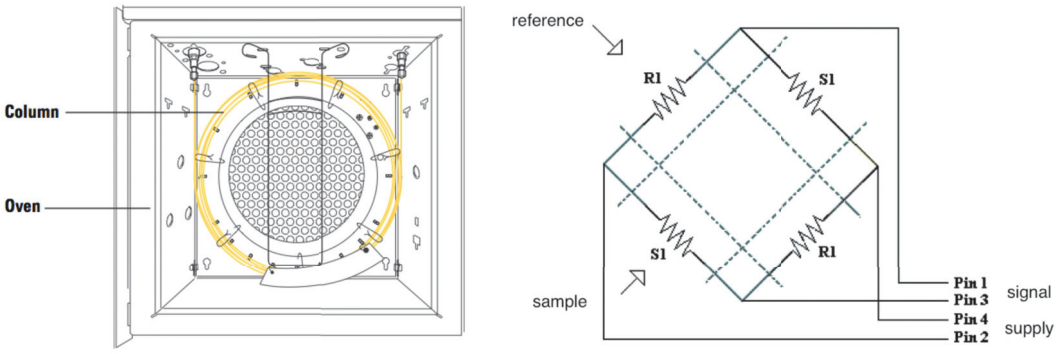

FIGURE 2.15: Drawing of a microGC column section (left) and schematics of the Wheatstone bridge mechanism (right). [46]

The TCD signal is amplified by the electronics and the final chromatogram is obtained, as trend in time of the measured voltage variations. Being the mixture components separated in time by the column, to each component will correspond a voltage variation (peak) in the chromatogram. Figure 2.16 reports an example of a chromatogram, where there CMS CSC gas mixture was analyzed. The analysis refers to the PPU column, where the three mixture components, $Ar/CO_2/CF_4$ are present and the peaks are well separated.

Once the chromatogram is obtained, it is processed offline to calculate the concentration of the separated components. The peak area is indeed proportional to the component concentration in the sample mixture, which can hence be determined simply

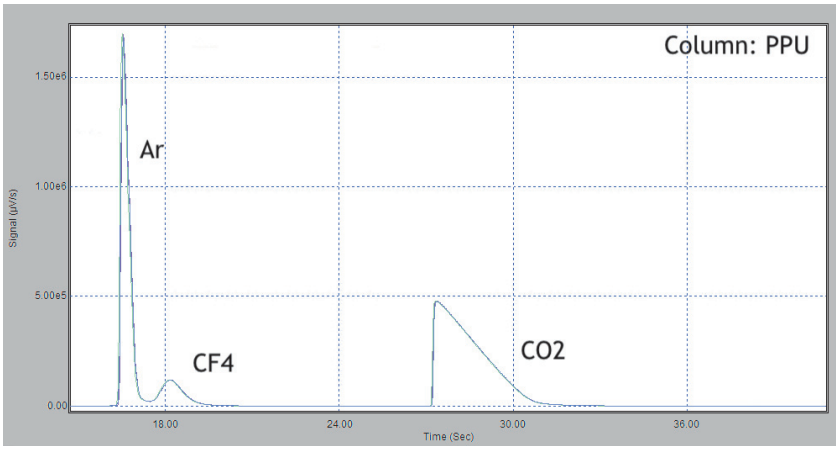

FIGURE 2.16: Chromatogram of the CMS CSC gas mixture from the PPU analysis column.

through calibration procedures. The microGC can detect concentrations down to few ppm, with a proportionality area-concentration that is linear for concentrations in the range 0-20%, but flattens above the 20-30%. Figure 2.17 reports the calibration measurements realized for the CMS CSC gas mixture, in particular the one concerning the CF_4 concentration. The plot shows the trend of the conversion factor variation obtained measuring the area of CF_4 peaks in reference mixtures of increasing nominal CF_4 content (5% - 100%). It can be seen how the trend is approximately linear for lower concentration values, but then the curve slope progressively decreases. It is therefore fundamental to have a calibration with a reference mixture in which the concentration of the relevant component is as close as possible to the one of the sample mixture, to avoid inaccuracies in the concentration calculation.

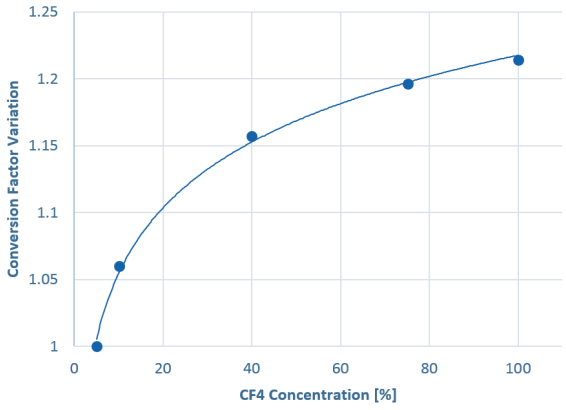

FIGURE 2.17: Example of CF_4 calibration curve, obtained analyzing mixtures with known CF_4 concentration.

Concerning the microGC analysis systems operational on LHC gas systems, CMS and LHCb boast the most complete analysis setup. A microGC is permanently installed in the Analysis module, connected to 14 and 17 lines respectively. During physics runs, relevant sample lines are analyzed once every two weeks, providing a constant monitoring of the gas mixture composition and quality, that is made available on an online webpage to detectors users. This type of gas mixture monitoring

allows to spot mixer malfunctioning, leaks and other problems at the distribution level, as well as to verify the proper functioning of the Purifier module. As an example, the analyses of the CMS CSC gas system are reported in Figure 2.18. The chromatograms are relative to the MolSieve column, especially useful to detect and quantify O_2 and N_2, well separated into two distinct peaks. It can be seen how the mixture composition at mixer level is very pure, while impurities are measured in the sample returning from the system, which is then purified of the accumulated O_2 by the action of the Purifier material.

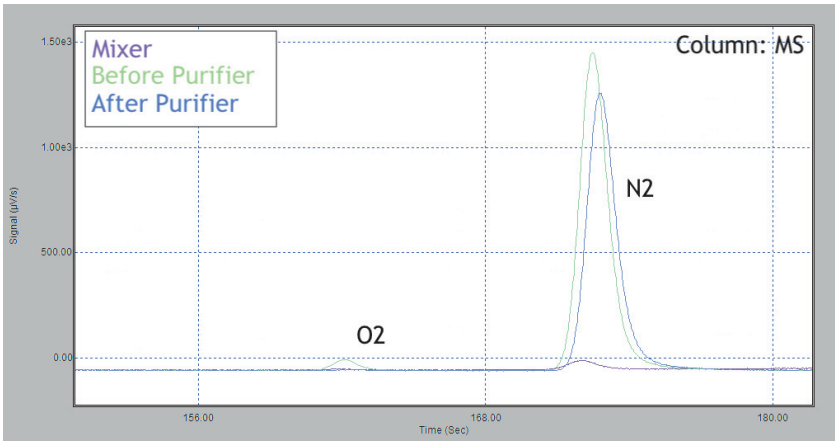

FIGURE 2.18: Chromatogram of the CMS CSC gas mixture in three different analysis points, from the MolSieve column.

For the CMS Experiment, an underground microGC analysis station is also available to monitor the return gas mixture quality when it is still separated in flows coming from single sectors of the gas distribution, to spot problems of specific sets of chambers. A microGC analysis station is also installed at the Gamma Irradiation Facility (GIF++, Section 3.1.5), where it is used to monitor the gas mixture quality of Muon chambers before and after irradiation. Moreover, aside stable microGC analysis setups, portable alternatives are available to be displaced where necessary.

An example in which the portable microGC was used is the fill procedure of the ALICE Time-Of-Flight (TOF) detector, realized during the LS2. The TOF detector is operated with R134a/SF_6 93/7 gas mixture, but during maintenance periods the detector is operated in back-up mode with pure R134a. At the moment of re-filling the detector volume with the correct mixture in preparation for Run 3, the SF_6 flow is put back in the mixer module. To speed up the procedure and lower the total SF_6 consumption, the volume flow was set at a higher value than what is normally necessary to maintain the 7% concentration. Figure 2.19 reports the trend of the SF_6 concentration measured with the microGC at the exhaust of the TOF gas system, along the progressive days of filling procedure. The trend is superposed to the expected filling concentration, calculated considering the mixture flow rate and the detector volume. Such calculation was repeated for different settings of the mixer, calculating the total SF_6 volume necessary to reach the desired concentration in relation to the time scale available for the operation, and the most convenient one in terms of SF_6 consumption was picked. Thanks to the microGC measurement procedure, it was possible to closely monitor the filling of the detector, limiting the total volume of potentially wasted SF_6 by stopping the high-flow injection as soon as the exhaust concentration reached the correct value.

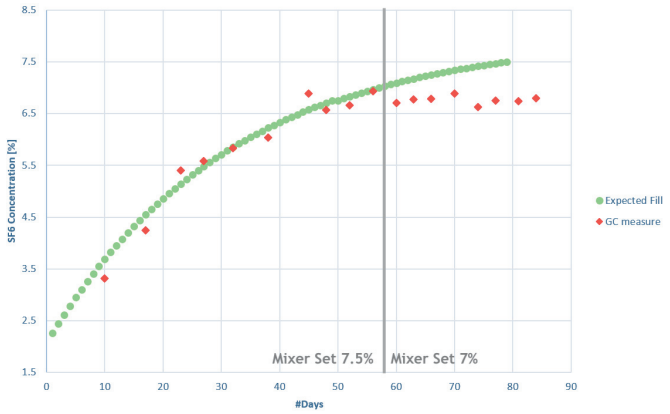

FIGURE 2.19: Trend of the SF_6 concentration at the exhaust of the TOF gas system during the filling procedure, with the expected fill trend for the mixer set at 7.5%.

In the context of this thesis, microGC analysis were widely used to characterize and verify the quality of gas mixture employed in different applications, using each time the most convenient microGC analysis setup available.

2.3.2 Gas Systems operation and gas emission

In the simplest gas system, the gas mixture is sent underground to gas distribution and to the chambers, and once it is brought back at the surface it is exhausted to atmosphere (open mode). Nonetheless, already in the first phases of LHC gas systems design, the possibility of re-using the gas mixture multiple times was taken into account in case of large detector volumes or usage of expensive gases to limit their consumption. When a gas system is operated in recirculation mode, the gas mixture is collected after being used in the detector, passed through the Purifier module to undergo purification processes and then it is re-injected in the system. Figure 2.20 reports a schematic representation of the closed loop gas system, where gas is recirculated.

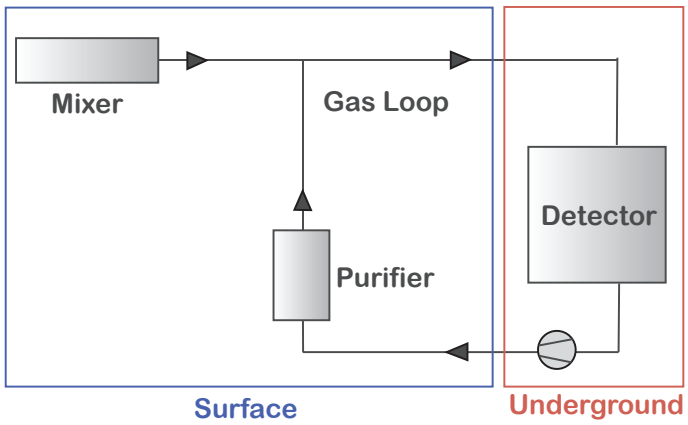

FIGURE 2.20: Drawing of the closed loop configuration of an LHC gas system.

Operating the gas systems in closed loop configuration allows to re-use a great fraction of the gas mixture, as most of the systems where it is employed are capable of recirculating a total gas volume equal to the 90% of the system volume at minimum. In this way, gas systems operational costs can be reduced by 90% or more. Nevertheless, it should be noticed that such operation mode implies a greater level of complexity of the gas system, as volume flows and pressures need to be constantly regulated. Moreover, since the gas mixture is only partially renewed at every loop, the accumulation of impurities along the gas path is inevitable. It is therefore of fundamental importance to validate detector operation for systems operated in such configuration, as it will be widely discussed for Triple-GEM detectors in Chapter 3.

Even when gas systems are operated in closed loop, a given amount of gas mixture volume will be exhausted to the atmosphere, either to compensate for the freshly injected fraction, because of gas system and detectors leaks or due to detector maintenance works (fill, purge, hardware intervention). Moreover, given the need of some types of Muon systems detectors to operate with gas mixtures based on Greenhouse gases (GHGs), this implies that to some extent GHGs will be emitted in the atmosphere during gas systems operation.

A Greenhouse gas (GHG) is defined as a gas that, when in atmosphere, absorbs and emits radiation within the thermal infrared range. GHGs are the main responsible of the Greenhouse effect which, despite originally being a Earth's natural phenomenon, has been strongly enhanced by the emissions caused by human activities, such as the burning of fossil fuels and the forests clearing. The main GHGs currently in Earth's atmosphere are water vapor, CO_2 and methane. Nevertheless, many of the human originated contributions could have much higher impact despite being present in lower quantities. A measure of how much heat a GHG traps in the atmosphere in a fixed time span is the Global Warming Potential (GWP) index. The GWP defines how much energy the emission of 1×10^3 kg of a gas would absorb over a period of time, relative to the emission of 1×10^3 kg of CO_2. The GWP index strongly depends both on the radiation absorption spectrum in the infrared (radiative activity) and on the lifetime of the gas in the atmosphere. In particular, hydro-fluorocarbons (HFCs), hydro-chlorofluorocarbons (HCFCs), and sulfur hexafluoride (SF_6) are called high GWP gases as they trap thousands or tens of thousands times more heat than CO_2.

LHC gaseous detectors are often characterized by large detector volumes (up to 100 m^3 per system), and this translates into a very high consumption of gas, which in the GHGs case means an elevate operating cost as well as high emissions in the atmosphere. The gas consumption optimization has been a design criteria for reducing operational costs since the beginning, but the GHG issue has boosted this need in relation to the new set of environmental restrictions concerning the use of fluorine based gases. The European regulation of 2014 [48] calls for restricting the use of fluorinated gases to one-fifth of their consumption in 2014 by 2030. Moreover, as a consequence of such restriction, GHGs are becoming less and less available for purchase and at greater prices. As CERN is willing to comply with these constraints, the gas mixtures of certain detectors must be adapted, or the emission of Greenhouse gases into the atmosphere must be substantially reduced. Concerning LHC Experiments emissions, as reported in Figure 2.21, the most significant portion is represented by the R134a component of the RPCs mixture, present on the ATLAS and CMS Experiments, which accounts for the 80% of the total GHG emission. The

cause of such contribution from RPC systems mainly comes from gas leaks at detectors level, which repair is made particularly difficult by the inaccessible location of most of the chambers. A great effort is ongoing during the LS2 to repair such leaks and reduce as much as possible the RPCs emission contribution.

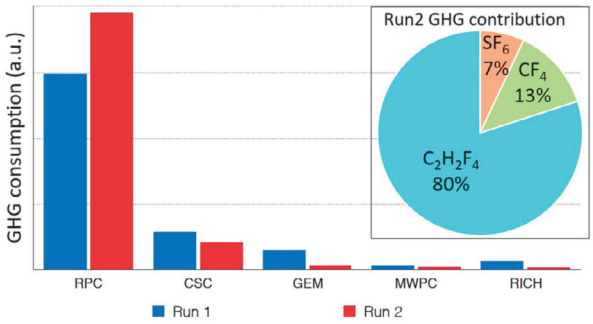

FIGURE 2.21: GHG emissions divided by type of detectors for Run 1 and Run 2. [49]

Taking all these factors into account, CERN is taking steps to reduce GHGs emission and gas systems cost, following different strategies [50]:

- *Optimization of current technologies*:
  The optimization of currently operating technologies allows to improve gas systems performance beyond their original design requirements and to overcome possible issues raised during the first years of operation. For example, the CMS RPC gas system was forced to work with gas recirculation rates around 80%-90% during Run 2, due to leaks present at the detector level. LS2 gave the precious occasion to repair such leaks and therefore increase the gas recirculating fraction. Other improvements were implemented in the last years or are currently under commissioning, such as the installation of automatic regulation valves to mitigate valve-opening effect on detectors pressure, or the introduction of additional pressure sensors, on which the flow regulation is based, mounted on simple gas volumes (so called dummy chambers) located at the same height of real chambers.

- *Gas recuperation systems*:
  Gas recuperation allows to collect the gas mixture that would normally be exhausted to atmosphere and recuperate the most valuable GHG component, to potentially re-use it in the system. Gas recuperation plants introduce more complexity in the gas system operation and maintenance, and they require dedicated R&D studies depending on the specific gas mixture components to separate. Different recuperation systems were developed since the start of LHC gas systems operation, as for example the nC_5H_{12} recuperation for ATLAS TGC and the C_4F_{10} recuperation for LHCb RICH1. The work of this thesis will cover on Chapter 4 the recuperation of CF_4 for LHCb RICH2 and CMS CSC, and the R&D studies on the recuperation prototype of R134a for RPCs (ATLAS, CMS).

- *Alternative gases*:
  An additional research line is focused on long-term replacement of the GHGs that are currently used for gaseous detectors operation. Environmentally friendly

alternatives are being searched for R134a, SF_6 and CF_4. In particular, as different compounds have been developed in industry to replace R134a as refrigerant, these candidates are being looked into as possible replacements in the RPCs gas mixture. The aim is to find a new eco-friendly mixture that is able to reproduce the same detector performance as it is observed with the current gas mixture. Though encouraging results have been obtained with the use of mixture containing HFO-1234ze and a neutral gas, a final satisfactory solution was not still achieved and further R&D studies will be needed [51] [52].

- *GHG disposal*:
  When it is not possible to re-use or recuperate the gases, a last option could be their disposal. Systems for the disposal of GHG have been developed by industry, but GHGs are normally very stable compounds hence very difficult to treat. The option of GHGs abatement systems on LHC Experiment is nowadays discarded, as it would come at great infrastructure cost and complexity, as well as it would lack on addressing the GHGs unavailability and price increase.

Chapter 3

Gas-related Triple-GEM detector studies

In the last years, Gas Electron Multipliers (GEM) detectors have been more and more considered as tracking devices, in particular with the nowadays common Triple-GEM configuration. They are present in LHC Experiments Muon systems thanks to their ability to cope with the high-rate radiation environment of the future Phases of the LHC (Chapter 1). Triple-GEM detectors are also implemented in various other applications, such as beam diagnostics, medical imaging and nuclear reactors [53] [54].

Triple-GEM detectors are usually operated with Ar/CO_2 or $Ar/CO_2/CF_4$ gas mixtures (Chapter 2) and, as for all gaseous detectors, quality and stability of the gas mixture composition are fundamental to guarantee optimal and safe long-term operation. Previous studies have characterized Triple-GEMs behavior in relation to Ar/CO_2 gas mixture composition variations [42], showing that a precise regulation of components concentration is fundamental to have a stable response of the detector. A similar study is carried on to characterize Triple-GEM detectors response for variation of the standard $Ar/CO_2/CF_4$ gas mixture (45/15/40). Experimental characterization is carried on in parallel with a Garfield++ [55] simulation to compare theoretical predictions with the actual detector behavior.

While R&D studies on GHG alternatives will continue in the next years, more and more LHC gas systems are operated with gas recirculation (Chapter 2). Triple-GEM detectors were successfully operated in the LHCb Muon System with a CF_4-based gas mixture in a gas recirculating system during LHC Run 2, with a reduction of 90% in GHG emission with respect to Run 1. Nevertheless, as the future LHC phases foresee a much higher rate of background radiation, it is fundamental to validate Triple-GEM detectors operation with gas recirculation in a High Luminosity LHC-like radiation environment. Triple-GEMs performance was therefore studied in relation to long-term operation stability and Muon detection efficiency at the CERN Gamma Irradiation facility (GIF++). Thanks to the ^{137}Cs gamma source available in the facility and the Muon beam delivered from the SPS, it was possible to validate Triple-GEMs operation with a small replica of an LHC gas recirculating system [56], in irradiation conditions that mimic what detectors will face in the future LHC phases. Moreover, microscopic analysis were conducted on GEM foils used in the detectors for the irradiation tests after the operation with Ar/CO_2. The analysis was realized with the Scanning Electron Microscopy (SEM) technique, that allowed to obtain detailed images of the condition of GEM foil holes after being exposed to high-rate radiation. Modifications in the holes shape were spotted, but only in a fraction of the thousands of holes present on a single multiplication foil, which remains therefore fully

operational without significant decrease of electron amplification capabilities.

The main issue of operating gas systems with gas recirculation is the possible accumulation of impurities, created at detector level or gathered from gas system components. Common impurities are O_2 and H_2O, which can easily be quantified and removed from the standard gas system Purifier module, as also verified during the high-rate irradiation campaign. Nevertheless, as other Freon gases, CF_4 is subject to break up processes in the electron avalanche when exposed to radiation. Fluorine-based gas impurities can be created in such way in the irradiated gas volume, and they could accumulate due to gas recirculation, possibly accelerating aging phenomena that would compromise the longevity and performance of Triple-GEM detectors. The Fluoride-impurities production process in Triple-GEMs was therefore characterized at the GIF++ facility, in relation to different detector operation conditions and in particular for high-rate irradiation, using an Ion Selective Electrode (ISE) station to quantify the Fluoride present in the gas mixture. The same measurement technique was also used to measure Fluoride-impurities in the LHCb GEM chambers during the last months of operation during Run 2. The campaign showed coherent results with what was obtained in the GIF++ characterization, showing how radiation is a key factor in the CF_4 break up process, but also that the gas recirculation mode can be safe for Triple-GEMs operation thanks to the capability of the Purifier module to trap the Fluoride-impurities created in the detector volume.

3.1 Experimental setup

The following paragraphs describe the elements of the experimental setup that are common to the various tests illustrated in this Chapter, starting from the detector itself then moving to the gas system, electronics and data acquisition systems. The basic characterization of the Triple-GEM detector is described, as it is normally performed before every test to verify detectors condition. Finally, the Gamma Irradiation Facility (GIF++) is described, as the studies in high-rate irradiation conditions were carried on in such facility.

3.1.1 10×10 cm^2 Triple-GEM Prototype

All the studies described in this chapter are realized using 10×10 cm^2 Triple-GEM detector prototypes, provided by the CERN PCB workshop. The detector assembly procedure is carried on in a certified clean room, to avoid any possible contamination of the parts in direct contact with the filling gas. The assembly kit includes three 50 μm Kapton GEM foils, with a two-side Copper-clad of 5 μm. The holes have a 70 μm diameter, with 140 μm pitch. The drift foil, without holes, is 50 μm think in Kapton, with the Copper-clad only on one side. The foils are stack one on top of the other between a readout PCB board and a top cover plate, with fiberglass spacers of 3-1-2-1 mm respectively, according to the layout represented in Figure 3.1. The spacers and foils frame are made of EM-470 FR4 base material from EMC, and covered with polyurethane NUVOWERN, as well as the 20×20 cm^2 frame that contains the foils stack. The foils and readout board are cleaned in several steps, including baths with $KMnO_4$, H_2SO_4, Chromic acid and final rinse with de-ionized water. The foils are kept in place by four nylon screws at the corners, which are then sealed from the outside with Araldite-2011 glue, to prevent any gas leak. The complete gas box is composed by the readout plane at the bottom, the epoxy frame on the sides and the

cover plate on top. Two Viton O-rings on the top and bottom of the frame ensure the tightness of the box, sealed by metallic screws all around the perimeter. Filling gas is supplied and exhausted by two fast-connectors installed on two opposite side of the epoxy frame, allowing to connect plastic pipes of 4 mm OD (Figure 3.2).

Voltage is supplied to the GEM foils through connections predisposed on the readout board, which are manually welded to the foils copper flaps. Each foil supply input is then connected either to a resistor chain or to a custom-made ceramic voltage divider [41], in way to have a single High Voltage supply line. The resistor configuration is reported in Figure 3.3, together with a picture of the ceramic divider. The resistors chain or ceramic divider allow to split the High Voltage, supplying the required voltage to each foil (between 300 V and 400 V).

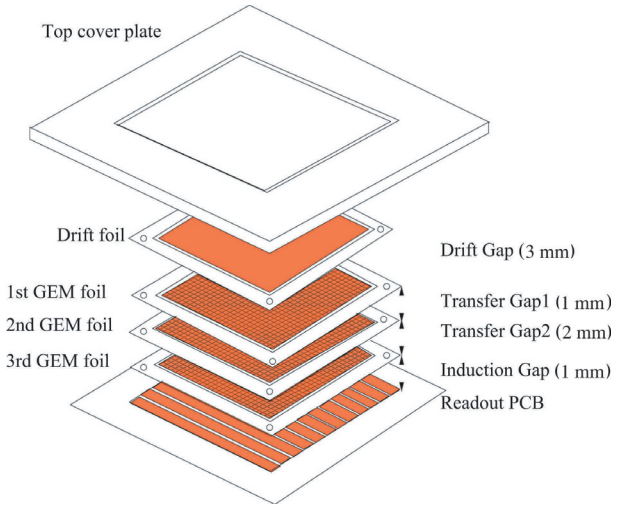

FIGURE 3.1: Schematics of the Triple-GEM detector assembly. [57]

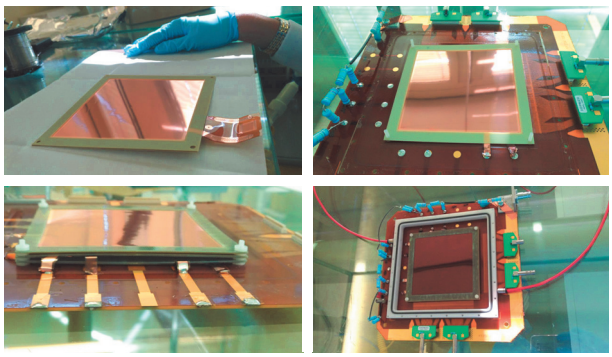

FIGURE 3.2: Different phases of the detector assembly procedure.

3.1.2 Gas System

Triple-GEM detector prototypes are operated with dedicated gas systems. For the tests carried on at laboratory level, a basic system was built to prepare the desired gas mixture and flush the chambers in open mode. Three Mass Flow Controllers (MFCs, Bronkhorst F210CM) are connected to the fresh gases supply panel (Ar, CO_2, CF_4), and remotely controlled by a dedicated software (FlowDDE, FlowView from

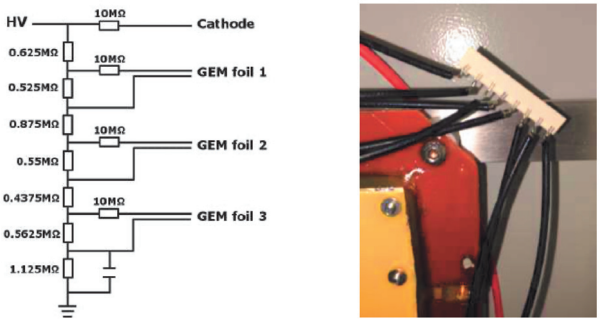

FIGURE 3.3: Resistors configuration (left) of the ceramic-voltage divider (right).

Bronkhorst) that is used to set the desired flow of each component. A mixing volume is placed after the MFCs, in way to allow the primary component to properly mix before being injected in the chambers. A rotameter and a MEMS flow sensor (Micro ElectroMechanical System, OMRON D6FP0001A1, 0-0.1 LPM) allow to regulate and precisely measure the gas flow, which is sent to the Triple-GEM with a plastic pipe (4 mm OD, Polyurethane Hydrolysis resistant, FESTO) through the dedicated connectors on the gas box. Two sensors are installed on the exhaust line of the Triple-GEM to measure O_2 and H_2O concentrations in the output gas (0 ppm - 25% O2X1, GE Infrastructure Sensing and $\pm$ 60° Dewpoint Transmitter, Vaisala DMT242). Temperature and atmospheric pressure are monitored with dedicated sensors (Electrotherm with Pt100). An ADC Data Logger (PicoLog ADC-24) collects the output signals from all the sensors, allowing to record and monitor relevant parameters.

For the studies carried on at the GIF++ facility, detectors are operated in a more complex gas system, a small replica of LHC gas systems [56]. In such system, detectors can be operated either in open mode, i.e. constantly injecting fresh gas mixture, or with recirculating gas. The mixing part is equivalent to the one built for the laboratory tests, but in this case the mixing volume output is split into different lines to supply more chambers. Rotameters allow the flow regulation of the total fresh gas from the mixer and of each supply line. About 100 m of inox piping connect the gas rack to the actual detectors input, as the latter are placed inside the irradiation bunker. The exhausts lines are brought back to the gas rack and merged into a single line, on which an O_2 and a H_2O sensors are placed. When the system is operated in open mode, a bubbler installed after the analyzers allows to exhaust the gas mixture to air. For operation with gas recirculation, a Pump module allows to send a fraction of the exhaust gas back to the input of the chambers, where it is integrated with the desired fraction of fresh mixture. Between the Pump module and the re-injection point, a standard Purifier module for O_2 and H_2O removal is installed. It is composed by three 1 liter cartridges, two of them used in parallel. The first is filled with Molecular Sieve 5Å (MS5A), used for H_2O removal (130 g(H_2O)/kg). The other contains the catalyst $NiAl_2O_3$, efficient in removing both H_2O and O_2 (15/50 g(H_2O/O_2)/kg) [58]. The third cartridge contains a mix of the two materials, allowing to keep the system running when regeneration is needed for the other two, (about once a year). Relevant gas parameters (pressure, flow rate) and environmental parameters (temperature, atmospheric pressure) are measured with dedicated sensors, recorded together with the O_2 and H_2O sensors output with an ADC Data Logger (PicoLog ADC-24), for a continuous monitoring of the system. A schematic

representation of the GIF++ gas system is reported in Figure 3.4.

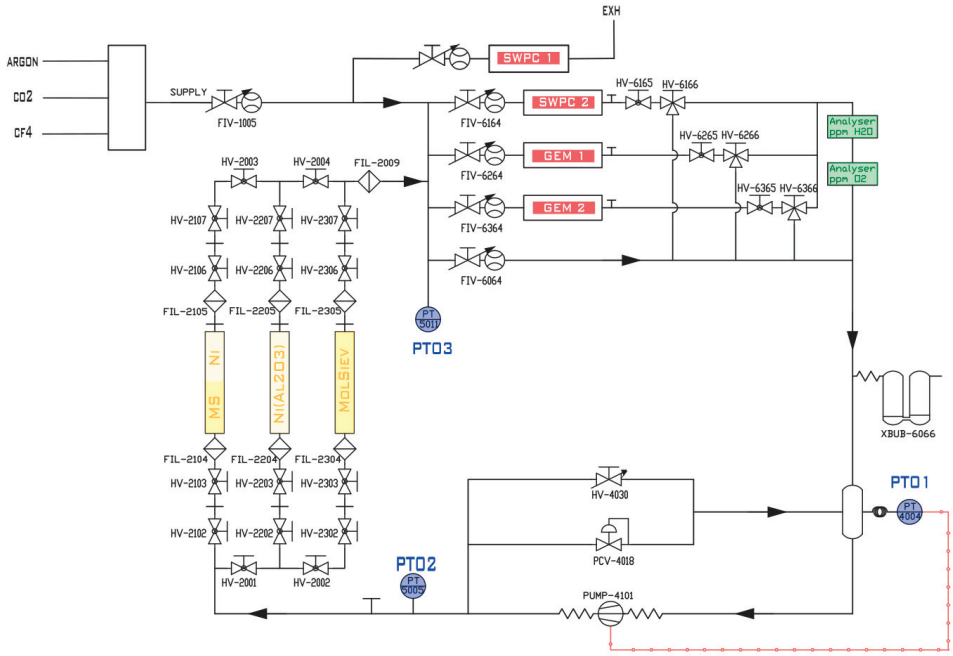

FIGURE 3.4: Schematics of the GIF++ gas system, with the gas distribution, gas analyzers, Pump and Purifier modules.

3.1.3 Electronics and Data Acquisition Systems

Different kinds of electronics and acquisition systems were used for the Triple-GEM detectors, depending on the scope of the specific test or measurement.

The standard acquisition system, used both in the laboratory and at GIF++, has the aim of characterizing the detectors behavior through both detector current and signal, induced by γ irradiation. Detector current is measured through the standard 10×10 cm^2 readout board [59]. The board is composed of two sets of 256 parallel metal strips engraved on the two sides of a thin Kapton foil. For each set of 256 strips, two 128-pin connectors allow to sum-up the signal from 128 readout strips. The current output of one of these connectors is readout with a PicoAmperometer (RBD Instrument 9103), therefore accounting for half of the current collected by the readout plane. The PicoAmperometer is capable of measuring DC currents from picoamps to milliamps, and its output is connected via USB to a PC to read and store collected data. The dedicated software (Actuel, RBD Instruments) allows to save in text format the measured current values with the relative timestamp. Detector signal was collected instead connecting a lemo cable to the bottom of the third GEM foil. The signal is collected by a pre-amplifier (CAEN A1422 Charge Sensitive Preamplifier), that produces a voltage pulse proportional in amplitude to the integrated charge of the detector signal. Signal amplification and optimization of the signal-to-noise ratio is realized with an amplifier (ORTEC 474 Timing Filter Amplifier), which output is recorded to be processed offline using a multichannel ADC device (CAEN Waveform Desktop Digitizer, DT57242).

During the Test Beam campaign, as Muon signals had to be detected with γ irradiation acting as background, the data acquisition system was changed to the Scalable Readout System (SRS), a general purpose multi-channel readout system, provided by the RD51 collaboration [60]. Detector signal is read via four APV25 hybrids [61], 128-channel analogue pipeline chips designed for the readout of microstrip detectors. Each channel of the APV25 is composed of a low noise amplifier, an analogue pipeline and a deconvolution readout circuit. The output signal is transmitted to the SRS, that allows to collect and online-process detector signal through a dedicated DAQ software. The SRS trigger signal is obtained with the coincidence of the trigger signal supplied by the facility and the signal of a 4×4 cm^2 scintillator placed in front of the detector surface. A calibration run is done before every acquisition, to allow the optimization of S/N performed by the SRS. Detector signal is recorded as collected charge distribution in the 25 ns time window of the acquisition (Figure 3.5). The maximum deposited charge and the time of such maximum are stored in ROOT [62] files for offline processing, together with position tags that allow to reconstruct signal location on the 256 strips of each of the readout planes. Detector current is monitored connecting the PicoAmperometer to the bottom of the third GEM foil, as the microstrip connectors were already occupied by the APV25 chips.

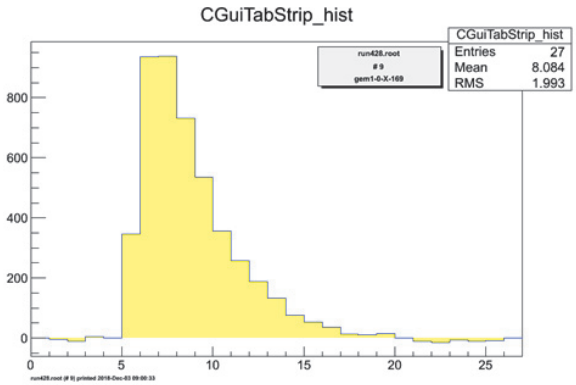

FIGURE 3.5: Typical waveform acquired by the SRS APV25.

3.1.4 Triple-GEM Detectors Characterization

Before testing Triple-GEM detectors in different operation conditions, a basic characterization was done irradiating the chambers with ^{55}Fe X-rays. The same characterization, in the form of High Voltage scan, was also used for gas mixture characterization tests. Moreover, such scans were repeated in-between different tests as a check of the chambers status.

Detectors are irradiated with ^{55}Fe sources, with activity between 15 and 35 MBq. When the photons emitted by the radioactive source have enough energy, they extract primary electrons from gas molecules, that after the three GEM multiplication stages produce a detectable pulse. Detector signal (Figure 3.6) is collected and processed through the basic acquisition system, to obtain a pulse height spectrum. The typical ^{55}Fe spectrum is reported in Figure 3.6. It is composed by a main peak, corresponding to the 5.9 keV primary electron extracted, and by the so-called escape peak. The latter is related to the relaxation of the gas atom K-shell and emission of

a photo-electron of energy 2.7 keV, i.e. the difference between the transferred energy (5.9 keV) and the K-shell binding energy (3.2 keV). Being the emission monoenergetic, events follow a Gaussian distribution that can be fitted to obtain the mean and width values of the peak. The mean value of the ^{55}Fe main peak is taken as a reference for the detector amplification gain, as its value in ADC counts is directly proportional to the number of electrons at the readout plane.

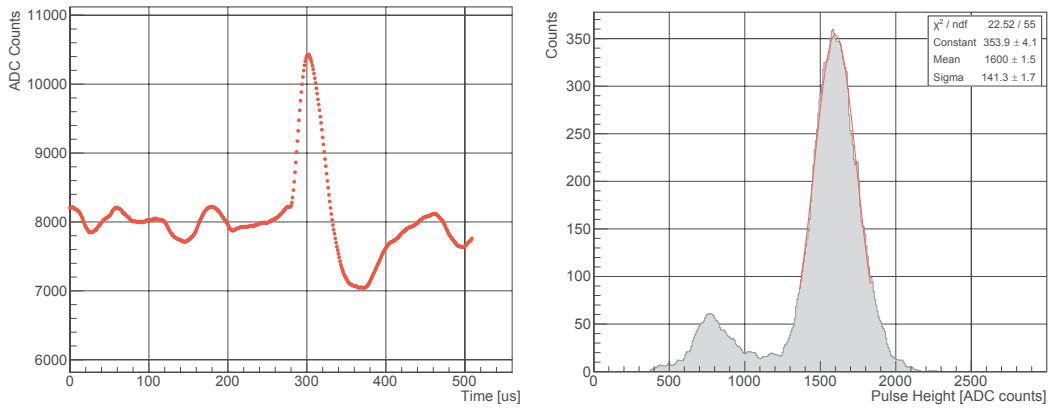

FIGURE 3.6: Triple-GEM waveform obtained with ^{55}Fe irradiation (left) and signal height distribution (right), corresponding to the typical ^{55}Fe spectrum.

In parallel to detector signal, also the current is measured and used to estimate the actual multiplication gain of the detector. The total effective gain is calculated as follows:

$$Gain_{tot} = \frac{I_{GEM}}{N_{pairs} \cdot Flux \cdot Area \cdot \epsilon \cdot e}$$

where I_{GEM} is the measured current, N_{pairs} is the number of electrons extracted per incoming photon (3-5), $Flux \cdot Area$ is the source activity, ϵ is the detection efficiency and e is the electron charge (1.6×10^{-19} C).

High Voltage scans are performed progressively increasing the total supply voltage of the detector, corresponding to an increase of single foil voltage as:

$$V_{foil} = \frac{HV_{tot} \times R_{foil}}{\sum R_i}$$

Being the voltage of the three foils very similar, *Foil Voltage* will be used in the following to indicate the average voltage applied to the three foils. The total High Voltage spans in different ranges, depending on the gas mixture in use (3.3-3.7 kV for Ar/CO_2 70/30 and 4-4.5 kV for $Ar/CO_2/CF_4$ 45/15/40).

The ^{55}Fe main peak mean value and the detector current are recorded for each HV step, together with the counting rate of the chamber registered by the ADC Desktop Digitizer (the number of detected pulse shapes per time unit). The latter is used to reconstruct a sort of efficiency curve, where full efficiency is said to be reached when the counting rate reaches a plateau. The chamber working point is set to be at the HV 100 V after the 90% efficiency point. The same rule will be applied in all the following tests to select the detector working point. An example of curves collected in the High Voltage scan is reported in Figure 3.7, where the Triple-GEM was operated

with Ar/CO_2 70/30 gas mixture. It can be seen that the amplification gain, both as ^{55}Fe main peak position and detector current, is exponentially increasing with applied voltage. The total amplification gain reaches values around 1-5 $\times$ 10^4 when the X-ray counting rate plateau is reached (HV around 3600 V), which corresponds to the typical gain value at which Triple-GEM are operated. [40]

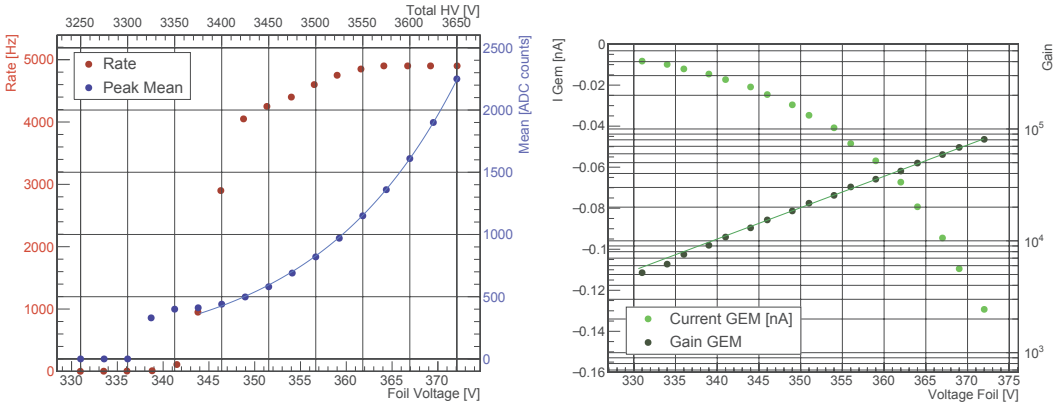

FIGURE 3.7: High Voltage scan trends of ^{55}Fe main peak position and detector counting rate (left), measured detector current and calculated amplification gain (right).

3.1.5 Gamma Irradiation Facility (GIF++)

Tests requiring irradiation with high-rate gamma radiation were carried on at the CERN Gamma Irradiation Facility (GIF++), a dedicated test zone for large-area Muon chambers, for performance characterization and aging tests [63]. The facility, operational since 2015, provides irradiation with a source of ^{137}Cs (662 keV photons), apt to mimic the high radiation rate of the HL-LHC phase.

The GIF++ area is composed by the irradiation bunker, a preparation zone and a two-floor area that hosts the gas systems and the electronic services. The bunker is delimited by 1.6 m thick concrete blocks, creating a shielded area only accessible when the ^{137}Cs source is in OFF position . The preparation area is available for preliminary test on detectors before moving them into the irradiation area. A picture of the irradiation bunker with some installed setups is reported in Figure 3.8, where the Triple-GEM gas R&D setup is also marked.

The ^{137}Cs source spectrum is composed by primary 662 keV photons and scattered photons with lower energy. This isotope was chosen for its long half-life (approximately 30 years) which can give a more uniform photon rate over time. Moreover, its spectrum very well resembles the typical neutron-induced background present in LHC experiments. The activity of the source is 13.5 TBq (measured in March 2016), making it capable of delivering approximately 1 Gy/h at a distance of 1 meter. The ^{137}Cs source is located at the center of the irradiation bunker, inside an irradiator column equipped with two $\pm$ 37 $^\circ$ panoramic collimators, which allow to cover with irradiation a large part of the bunker area. The source itself is embedded between two Tungsten blocks, which assure the source OFF status when it is sent in the so-called garage position, at the bottom of the support tube. The source is moved on the top of the tube to bring the irradiator in the source ON status. The collimators

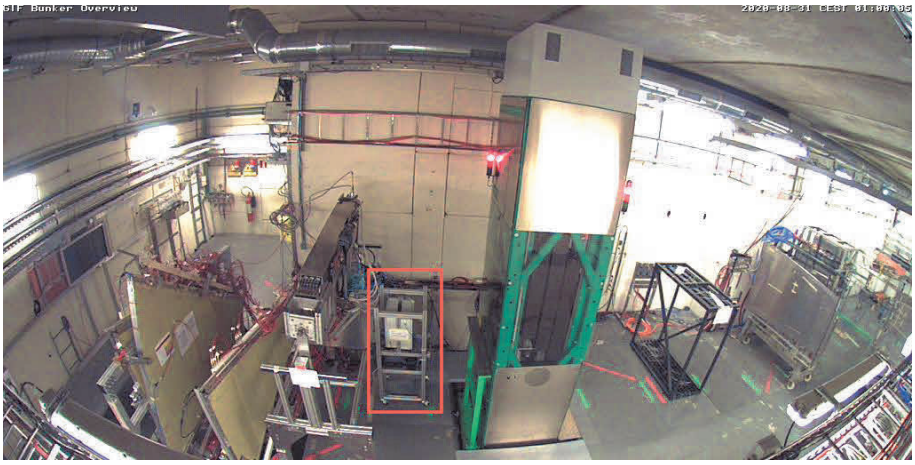

FIGURE 3.8: GIF++ irradiation bunker, with the Triple-GEM gas R&D setup marked in red.

also make possible that the current intensity only depends on the z-coordinate, i.e. on the distance from the irradiator, as it is shown in the simulated current plot in Figure 3.9. Thanks to the bunker structure, two independent irradiation zones are created, named upstream and downstream, referring to their position with respect to the gamma source.

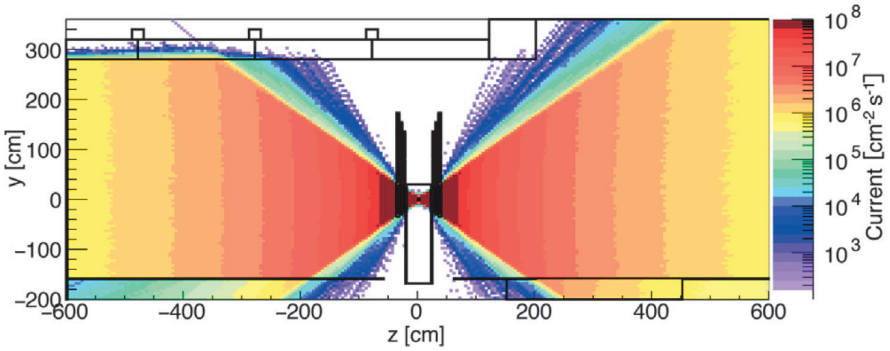

FIGURE 3.9: Simulation of the photon current intensity in the area of the GIF++ irradiation bunker [64].

The irradiator structure is also equipped with two independent 3x3 arrays of absorption filters, convex filters made out of paint coated lead, one per irradiation zone, in way to attenuate gamma irradiation independently on the two sides. The filters can be arranged through a control system to fine tune the photon flux according to 24 nominal attenuation factors. The attenuation factor can be selected with different combinations of the three filters. The nominal reduction factor of each filter is given in Table 3.1. A total attenuation between 1 and 46415 can be selected, with nearly equidistant steps on a logarithmic scale. It has however to be taken into account that the nominal attenuation factor of the filters is the attenuation of the 662 keV photons, and that the effective attenuation for photons of lower energy can be slightly different from the nominal values.

A Control System based on a WinCC Open Architecture project, hosted in the CERN Control Centre (CCC), allows to manage the irradiator status, bunker access status and environmental conditions of the facility. All the relevant information regarding

Plane:	A	B	C
Pos. 1	1	1	1
Pos. 2	10	1.47	2.15
Pos. 3	100	100	4.64

TABLE 3.1: Nominal attenuation factors of each absorption filter of the GIF++ ^{137}Cs source. [65]

GIF++ is made accessible to the users through the DIP, an information distribution service that allows real-time data sharing.

In order to allow the operation of many gaseous detector setups, the GIF++ is equipped with a gas system infrastructure. Primary supply of the commonly used gases is available to the users, such as Ar, CO_2, N_2, He, SF_6, $C_2H_2F_4$, iC_4H_{10} and CF_4. Gas racks are installed in the service area to allow the preparation of gas mixtures, and about 50 m of gas lines connect the primary supply to the panels installed inside the irradiation bunker. The gas system safety is guaranteed by the gas analysis system, which measures the flammability level of mixture components, as well as Oxygen and water vapor. More specific analyses on components concentration are allowed by a Gas-Chromatograph that is permanently available in the facility.

Finally, GIF++ facility can profit of approximately six to eight weeks per year of beam time as main user, being located on the H beam line (Figure 3.10). A Muon beam is generated as secondary beam from the primary SPS proton beam, on a production target. The decay of Pions and Kaons produced in the primary target generates the Muon beam. Beam line users are allowed to set the nominal momentum of beam particles, from a minimum of 10 GeV/c to a maximum of 400 GeV/c. The spill structure follows the one of the SPS, with a spill every 30 seconds. The intensity of the beam can reach 10^4 Muons per spill, but it is limited by radiation protection aspects. The lateral distribution of the Muon beam depends on several factors, but generally the core of the beam covers a surface of 10×10 cm^2, where about half of the particles is contained. The other half is spread over a footprint of about 1 m^2.

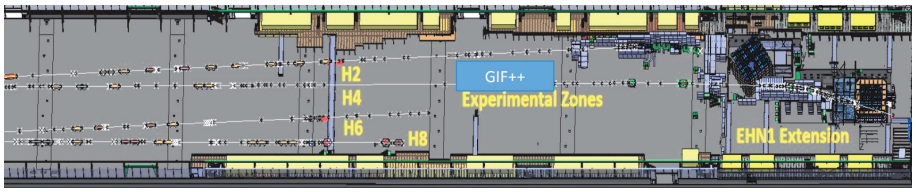

FIGURE 3.10: CERN North Area beam lines, with GIF++ located on the H4 line.

3.2 CF_4-mixture variations

Gas mixture composition is a key element in determining Triple-GEM detector performance, and its stability is fundamental for safe and reliable operation. Together with the standard Ar/CO_2 70/30 gas mixture, $Ar/CO_2/CF_4$ 45/15/40 is widely used to improve time resolution performance of Triple-GEMs. It is therefore studied the influence of variations in the standard CF_4-based mixture, evaluating the impact of the different mixture components on detector performance at laboratory level.

The test is carried on in parallel with a Garfield++ simulation to compare the actual measured detector performance with theoretical gas mixture behavior.

3.2.1 Experimental Setup

The experimental study was carried on with the basic setup and acquisition described in Sections 3.1.2 and 3.1.3. The schematics of the experimental setup is reported in Figure 3.11. The mixer part serves as gas mixture components regulation, and the simple acquisition chains allow to measure detector signal and current from the irradiation of the detector with ^{55}Fe (activity 15 MBq).

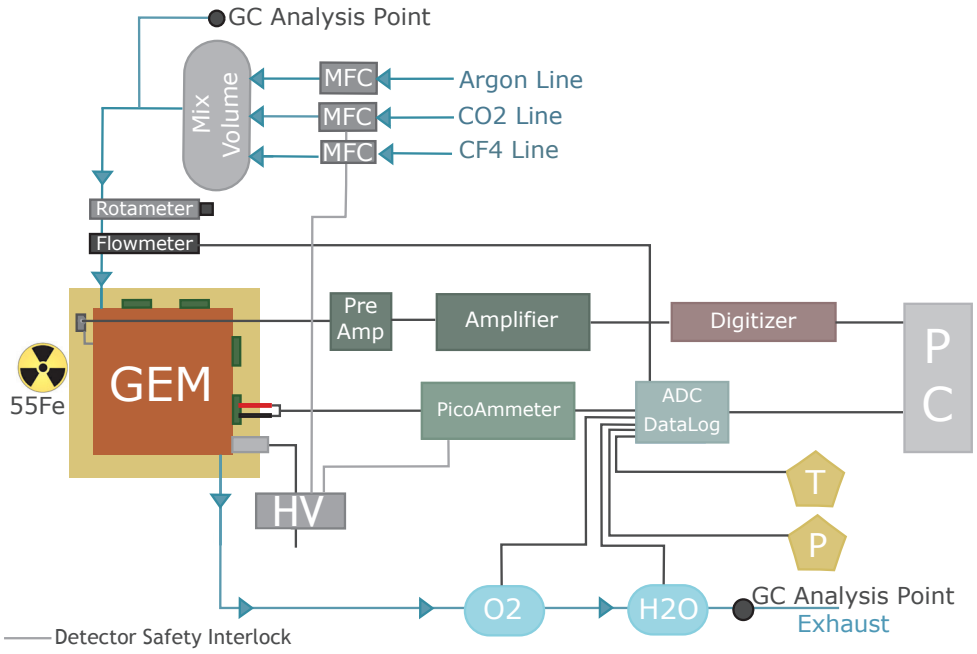

FIGURE 3.11: Schematic representation of the laboratory experimental setup.

Gas mixture composition was varied following different criteria, as in general the concentration instability could occur in any of the mixer lines. Firstly, the CO_2 fraction was kept constant, while varying Ar and CF_4 in steps of 2%, and then the Ar fraction was kept constant, varying CO_2 and CF_4 in steps of 2%. Finally, the CF_4 concentration was varied in steps of 1% while keeping the ratio Ar/CO_2 constant to the one of the reference gas mixture, i.e. Ar/CO_2 3/1. The tables below summarize the gas mixtures under test (Table 3.2). For every mixture composition tested, a High Voltage scan was performed by increasing the total voltage applied to the Triple-GEM and measuring detector current, mean peak position of the ^{55}Fe spectrum and counting rate, as described in the detector characterization section.

3.2.2 Simulation Tools

Triple-GEM performance with different CF_4-based gas mixtures was analyzed through a computer simulation. The simulation was composed of sections developed in GEANT4 [66] and Garfield++ [55], and ANSYS APDL [67] was used to model the structure of the three foils and the electric field. The ANSYS model includes the

CO_2 Constant		
Ar %	**CO_2 %**	**CF_4 %**
51	15	34
49	15	36
47	15	38
45	15	40
43	15	42
41	15	44
39	51	46

Ar Constant		
Ar %	**CO_2 %**	**CF_4 %**
45	23	32
45	21	34
45	19	36
45	17	38
45	15	40
45	13	42
45	11	44
45	9	46
45	7	48

Ar/CO_2		
Ar %	**CO_2 %**	**CF_4 %**
48.75	16.25	35
48	16	36
47.25	15.75	37
46.5	15.5	38
45.75	15.25	39
45	15	40
44.25	14.75	41
43.5	14.5	42
42.75	14.25	43
42	14	44
41.25	13.75	45

TABLE 3.2: Summary of the gas mixtures tested at experimental level and in the simulation.

drawing of the physical basic element of the detector, i.e. a section with two quarter-of-hole, which is repeated at the 1-2-1 mm distance which characterizes the gap configuration of the Triple-GEM prototype used in the experimental setup. The materials of each element are defined (Kapton and Copper) and voltage differences are set on each copper layer, in way to reproduce the voltage distribution across the three GEM foils. Figure 3.12 reports the drawing of the basic element and the variation of the intensity of the voltage across the foils in color-scale. The output of the ANSYS model is then used as an input of the Garfield++ application for geometry and electric field.

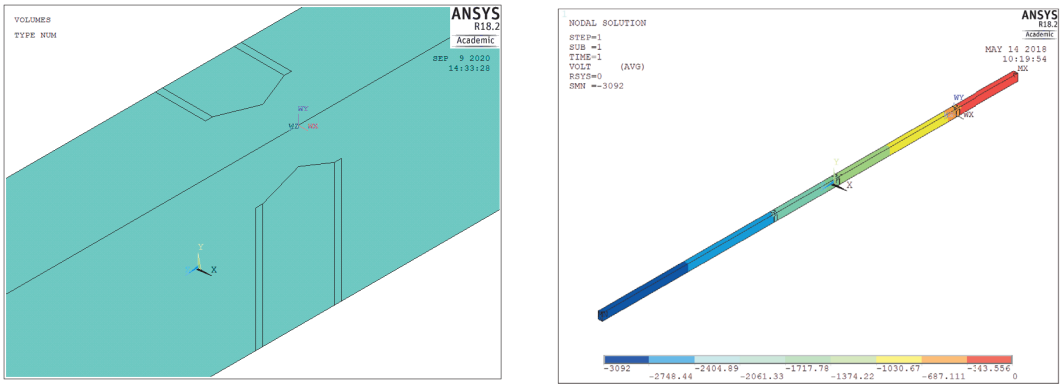

FIGURE 3.12: Pictures of the GEM foil hole basic element (left) and the triple foil structure with the voltage across the foils in color-scale (right) .

The GEANT4 physical toolkit is used to simulate the primary ionization process by ^{55}Fe photons, to have electrons with defined position and momentum as a Garfield++ starting point. The GEANT4 geometry represents the first stage of the process, and it consists of the physical space between the ^{55}Fe source (a point-source at given distance) and the first gas-gap encountered by photons. It is also simulated the detector box window crossed by photons, made by an aluminum foil (10 μm), followed by the drift foil (Kapton foil of 50 μm and Copper covering of 5 μm). The physical space of the simulation terminates just before the first GEM foil, i.e. at 3 mm distance from the drift foil. Figure 3.13 shows a schematics of the simulation structure in relation

to the process geometry, showing the separation between the GEANT4 section and the Garfield++ one.

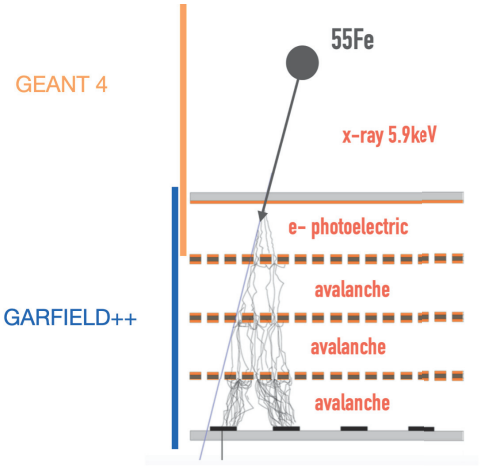

FIGURE 3.13: Schematics of the geometry layout of the simulation, with the separation between GEANT4 and Garfield++ sections.

The gas mixture of tunable composition fills the drift gap. Voltage difference in the gap is neglected as the ionization process does not depend on the electric field and the characteristics of electrons are saved before they can be affected by the field. The GEANT4 application in fact does not simulate how electrons hit the first GEM foil, it only takes care of the photon-electron conversion process saving the initial characteristics of the electron right after its creation. The electron properties are stored in a ROOT file (x, y, z coordinates, projections of momentum, energy, time, id of the parent particle and PDG code), which is given as an input file to the Garfield++ application.

The Garfield++ application takes care of computing the electron avalanche process through the gas gaps and the GEM foils. As showed in Figure 3.13, it covers the process from the first gem foil to the readout. It gives as output the properties of electrons formed in the avalanche, such as final position on the readout plane. Figure 3.14 reports an example of the data obtained for the electrons in the avalanche, for the standard mixture composition $Ar/CO_2/CF_4$ 45/15/40. On the left plot it is reported the z-distribution of the electrons final position, i.e. along the direction perpendicular to the gem foils area. It can be seen how at each foil some of the electrons are stopped, and only a fraction of them can reach the readout board. The scatter plot on the right shows the x-y distribution of the electrons position at the level of the third gem foil (z= -0.2 cm). It clearly shows the round shape of the avalanche projection on the plane perpendicular to its development direction, as well as the circular crown of the gem foils hole. From the latter feature it can be deduced that the electrons that are stopped at the foils level are in great fractions ending up around the hole diameter, where the electric field lines are more concentrated.

The full simulation process was repeated for each gas mixture tested, with about 10k events at the Garfield++ application starting point. The effective amplification gain for a given gas mixture was calculated as the mean value of the distribution of the number of electrons reaching the read-out plane for every primary electron released in the drift volume. Such value was used to compare the simulation performance to the experimental results.

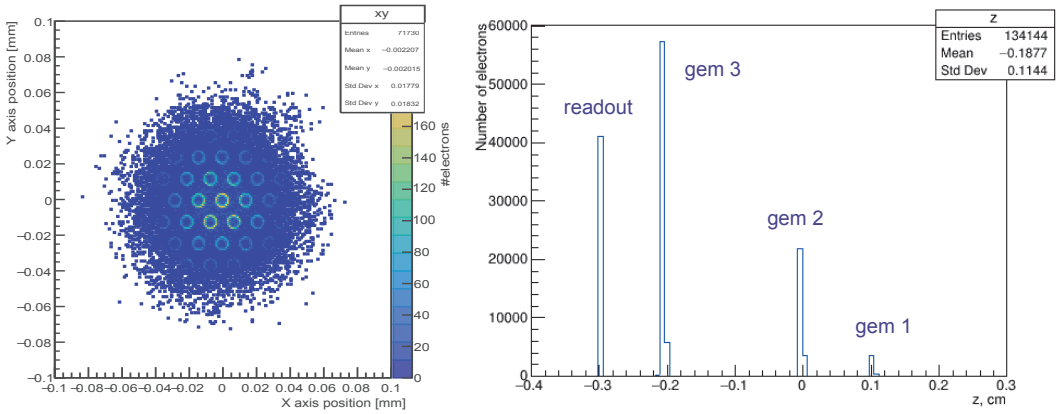

FIGURE 3.14: Distribution of the x-y position of electrons created in the avalanche across a gem foil (left) and z-axis distribution of their final position (right).

3.2.3 Results

Figures 3.15 and 3.16 report the trends of the Triple-GEM amplification gain as a function of the CF_4 concentration in the gas mixture, for the three sets of gas mixture tested. On the plots it is shown the gain value obtained from experimental measurements and simulation, both normalized with respect to the value obtained with the standard concentrations 45/15/40. The first relevant conclusion that can be drawn from the trends in the reported plots is that experimental and simulated results are generally coherent with each other. The discrepancy obtained for some of the points could be traced back to the fact that the amplification gain calculated in the simulation does not take into account the possible effects of readout electronics on the detector signal.

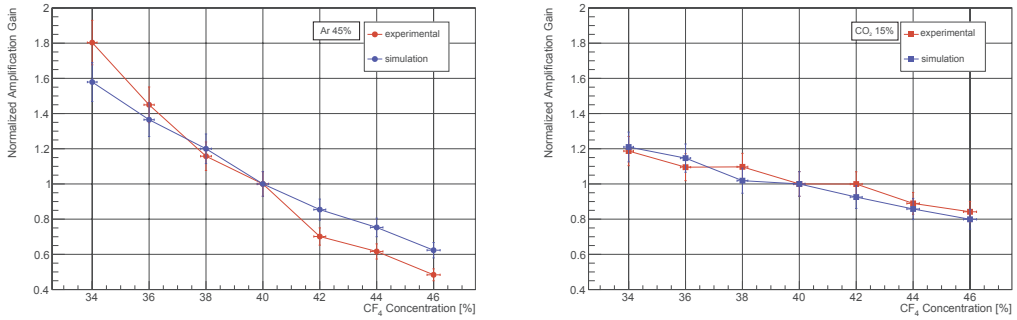

FIGURE 3.15: Triple-GEM normalized value of amplification gain as a function of CF_4 concentration in the gas mixture, with constant Ar fraction (left) and with constant CO_2 fraction (right).

In the first two data sets, constant Ar and constant CO_2 (Figure 3.15), the amplification gain shows a linear decrease for increasing CF_4 concentration, but the slope is found to be more significant when the Ar concentration is kept constant. In this case there is about 10% in gain variation per 1% of CF_4, while for constant CO_2 fraction the gain variation is only 3%. These results confirm the expectation of CO_2 being the main quencher element in the mixture, while Ar and CF_4 have similar properties, though Ar remain the main ionization component. When the Ar/CO_2 ratio is kept constant (Figure 3.16), an increase of 1% of CF_4 causes about 8% of amplification gain drop. In this case the increase of CF_4 implies a decrease of both Ar and CO_2,

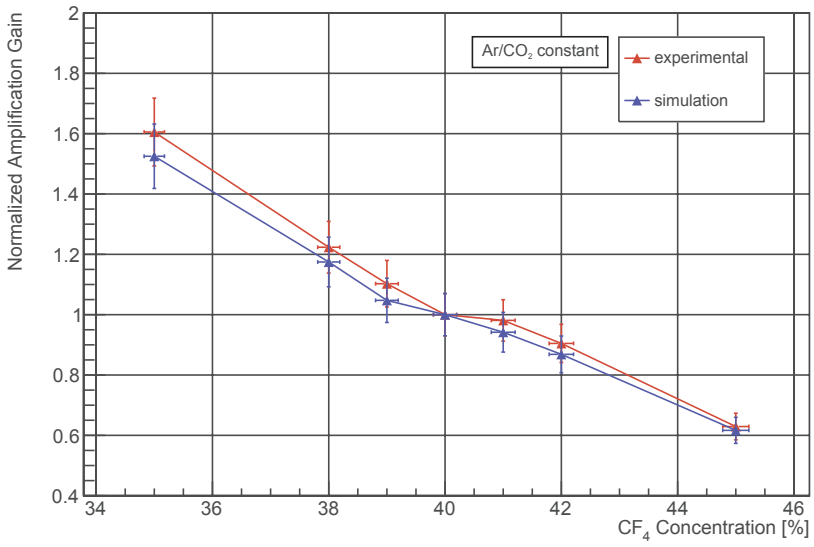

FIGURE 3.16: Triple-GEM normalized value of amplification gain as a function of CF_4 concentration in the gas mixture, with the ratio Ar/CO_2 constant at 3/1.

where the CO_2 decrease effects prevails and causes a diminished ionization process.

The overall results confirm the importance of high precision and stability of the gas mixture composition, given the non-negligible effects of the variation in the gas mixture components concentration variations on Triple-GEM detectors performance.

3.3 Long-term high-rate irradiation with gas recirculation

The performance of Triple-GEM detectors in a LHC-like gas system was studied at the GIF++ facility, in way to validate their long-term operation when exposed to high-rate radiation.

3.3.1 Experimental setup and methods

Two 10×10 cm^2 Triple-GEM detectors were installed at the GIF++ facility (Section 3.1.5), placed in front of the ^{137}Cs source, at 1 m distance (Figure 3.17), irradiated at various gamma rates, from 4.5 $\times$ 10^6 Hz/cm^2 to 50 $\times$ 10^6 Hz/cm^2. Detectors were operated in the small replica of LHC gas system described in Section 3.1.2, with the standard acquisition system for gamma irradiation (Section 3.1.3). Figure 3.18 shows a schematic representation of the experimental setup, with the gas system path and the data acquisition system.

Together with the standard gas analyzers, an extra gas monitoring system was added to the setup. As reported in the setup schematics, two Single Wire Proportional Chambers (SWPCs) were added in the gas system. One of the chambers was placed along the fresh gas mixture line, while the other was placed in parallel to the Triple-GEMs, therefore fed with the recirculating gas mixture. The SWPCs were both physically placed inside the GIF++ bunker, but outside the irradiation cone and with lead bricks shielding, in way not to be invested by the ^{137}Cs radiation. The SWPCs were

instead irradiated with small ^{55}Fe sources (activity of about 12 MBq), allowing a continuous monitoring of their performance through the readout of gamma-induced signal. Their electronic chain was the same as for the Triple-GEMs signal, as well as the characterization through High Voltage scans and offline signal analysis with the ^{55}Fe typical spectrum (Section 3.1.4). As Single Wire Chambers are very sensitive in their response to variations in gas mixture quality, they represent a very useful tool to monitor the purity of fresh and especially recirculated gas, allowing to spot gas mixture problems and verify the possible origin of Triple-GEMs performance variations.

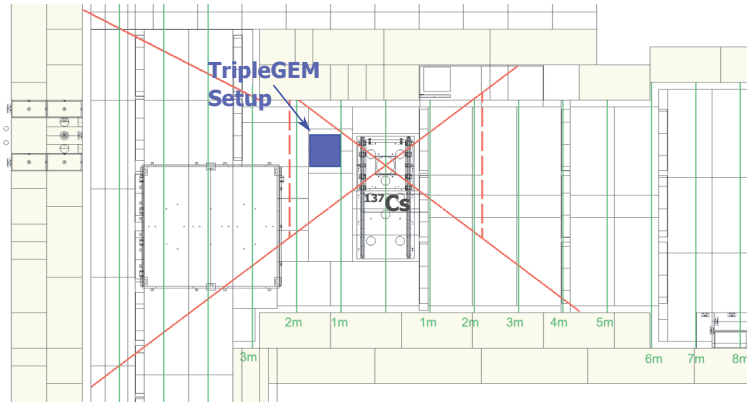

FIGURE 3.17: Top view of the GIF++ irradiation bunker, with the location of the Triple-GEM gas R&D setup marked in the downstream area.

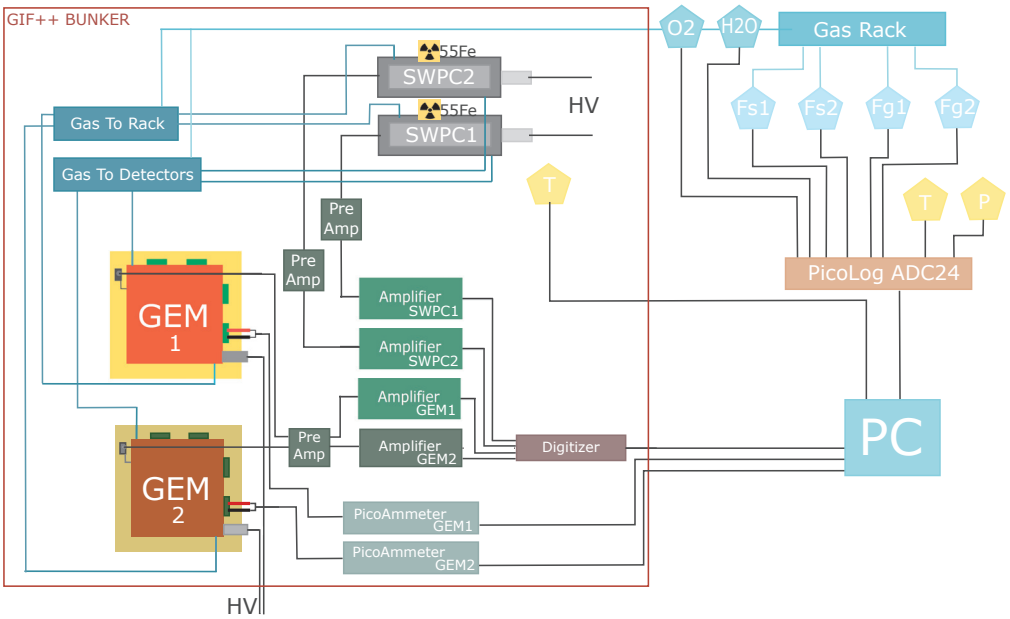

FIGURE 3.18: Schematics of the Triple-GEM setup installed at the GIF++. Detectors and data acquisition electronics are located inside the irradiation bunker (left), while the main gas system parts, High Voltage supply and other electronics are located outside (right).

Long-term performance of Triple-GEM detectors was tested during a two-years campaign, mainly focusing on operation with $Ar/CO_2/CF_4$ 45/15/40 gas mixture, with

an initial period of operation with Ar/CO_2 70/30 gas mixture. Each gas mixture was tested first in open mode, then with recirculating gas, progressively increasing the recirculating fraction (70%, 90%, 95%). Throughout the irradiation campaign, the ^{137}Cs source was operated with different attenuation filters (ABS 15, 10, 1), allowing to study Triple-GEM detectors behavior under background irradiation of different intensities. Triple-GEM detectors were operated at a working point yielding to an amplification gain of about 10^4 at the beginning of the campaign, and the correspondent High Voltage supply was kept constant for the entire duration of the test. Triple-GEM detectors operation stability was monitored via continuous acquisition of detector current. The measured value was corrected offline for temperature and atmospheric pressure variations, given the dependence of amplification gain on $exp(T/p)$ [68]. During the weekly access to the GIF++ bunker (^{137}Cs source off), detector performance is tested with high voltage scans irradiating the chambers with ^{55}Fe X-rays (activity 35 MBq). The mean value of the ^{55}Fe main peak is used as a weekly check for the Triple-GEM detector amplification gain along the duration of the campaign.

3.3.2 Purifier module validation

During the irradiation campaign, the efficiency of the Purifier module installed in the GIF++ gas system was tested for H_2O and O_2 removal. H_2O and O_2 concentrations were measured before irradiation with the gas system at 50% gas recirculation, bypassing the Purifier module. The H_2O concentration in such condition was measured to be around 2000 ppm, while the O_2 concentration around 200 ppm. Moreover, such concentrations were found to be oscillating depending on the gas flow rate and environmental parameters variation. For the irradiation campaign the Purifier module was put back in the gas system. Figure 3.19 shows the impurities concentration during the period of operation with $Ar/CO_2/CF_4$ gas mixture. Concentrations of H_2O and O_2 are kept around 50 ppm (typical LHC gas system concentrations [69]) during the full period, showing how the gas purity of open mode operation is also maintained with gas recirculation. Measured impurities showed oscillations of 4% and 1% respectively. These variations are acceptable for stable operation, as it was shown that they would affect Triple-GEM detectors amplification gain for less than 0.5% [70]. It could then be concluded that the Purifier module successfully contributes to the removal of accumulated impurities, allowing operation with low and very stable concentrations of H_2O and O_2.

3.3.3 Single Wire Chambers gas monitoring

The Single Wire Chambers monitoring system confirmed the capability of the gas system to deliver a gas mixture with stable composition, as well as the efficiency of the action of the gas Purifier module. Figure 3.20 reports the trend of the SWPCs amplification gain along the irradiation campaign, showing their response to freshly injected gas mixture (SWPC1) and recirculated gas (SWPC2). The plot shows that for both detectors a very good stability was achieved for the full period, and in particular that the chamber operated with recirculated gas has equivalent performance to the one operated with fully fresh gas, allowing to conclude that the gas system is delivering also in the long-term a gas mixture of good quality and stability.

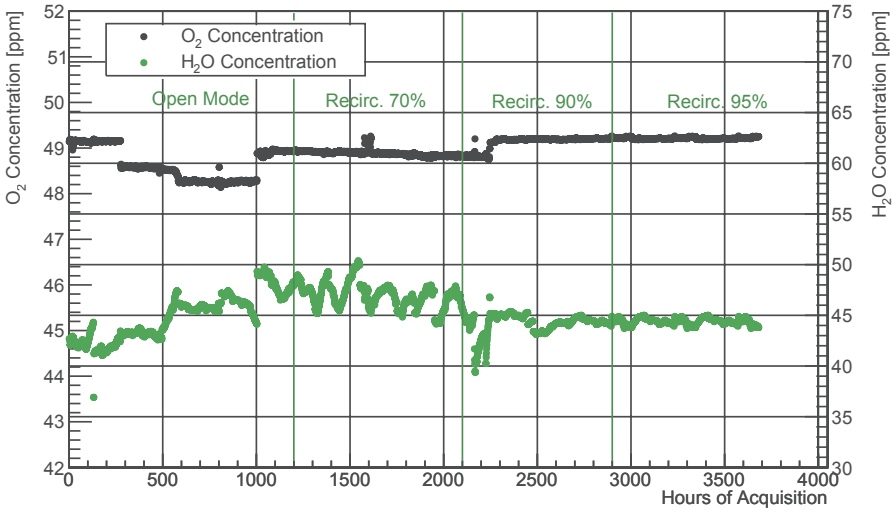

FIGURE 3.19: H_2O and O_2 concentrations in the long-term irradiation campaign period with $Ar/CO_2/CF_4$ gas mixture, for different gas recirculating fractions.

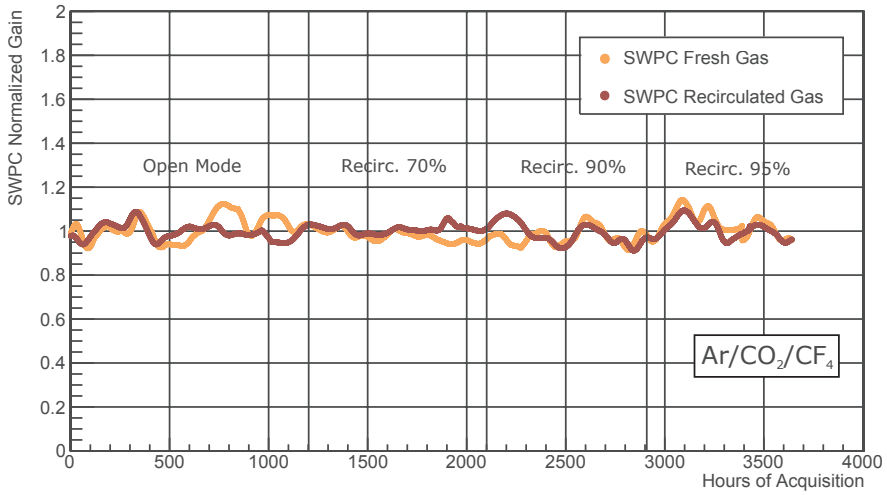

FIGURE 3.20: Amplification gain trend of the two SWPCs, monitoring the performance of fresh and recirculated gas mixture, with $Ar/CO_2/CF_4$ 45/15/45 gas mixture.

3.3.4 Results

Triple-GEM detectors operation was monitored continuously along the irradiation campaign measuring detector current, proportional to the chamber amplification gain. Figure 3.21 and Figure 3.22 show the trend of detector current during the periods of operation with Ar/CO_2 70/30 and $Ar/CO_2/CF_4$ 45/15/40 gas mixtures respectively, with different gas recirculating fractions, marked on the plots. For simplicity, only the trend of one of the two detectors is reported, as they showed very similar results. From the reported trends, it can be seen that Triple-GEMs performance is found to be stable, with average gain oscillations of 5% around the initial value. In some periods larger oscillations are recorded (10%-15%), but they can be traced back to large environmental parameters variation. In particular, given the

impossibility of stabilizing environmental temperature in the facility, it showed oscillations up to 10 °C in short time periods (day/night). Such variations do not allow a proper correction of the measured detector current for the $exp(T/p)$ dependence, as it is only efficient when relatively small oscillations occur.

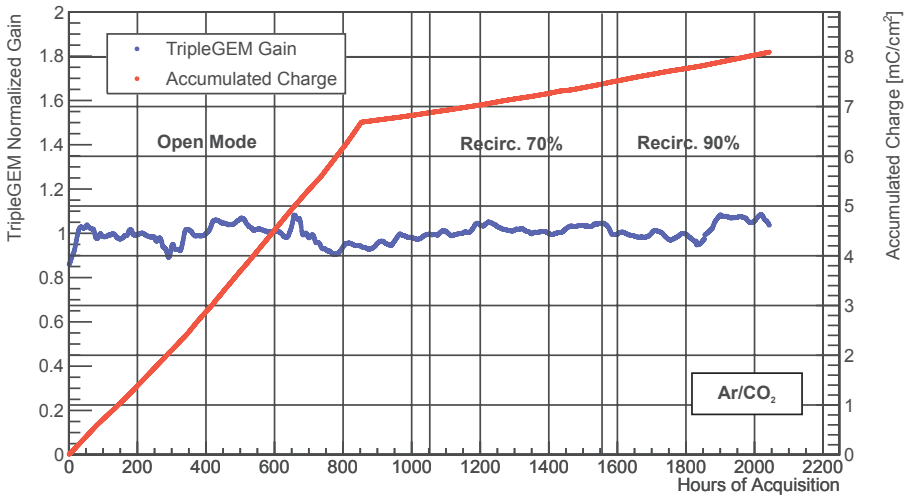

FIGURE 3.21: Normalized amplification gain, corrected for T/Patm variations, and charge accumulation during operation in gas recirculation (Ar/CO_2).

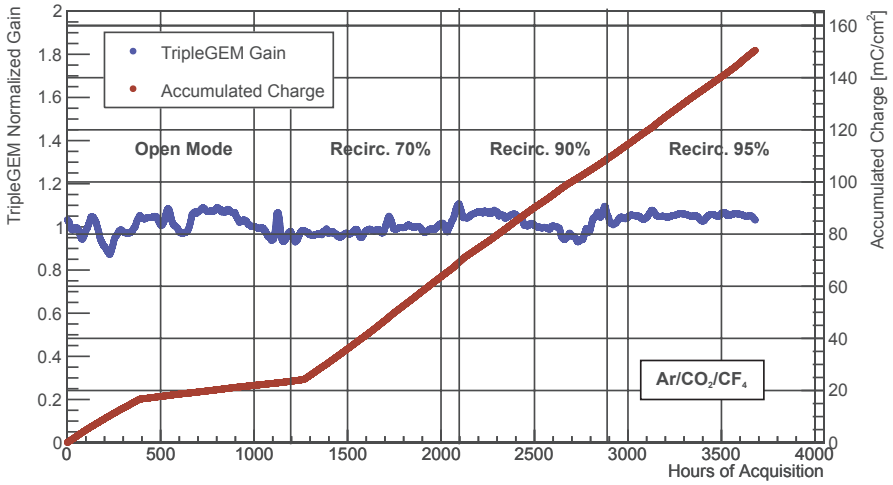

FIGURE 3.22: Normalized amplification gain, corrected for T/Patm variations, and charge accumulation during operation in gas recirculation ($Ar/CO_2/CF_4$).

The figure also reports the progressively accumulated charge due to the exposition to high-rate radiation. The Triple-GEMs accumulated charge was calculated from the measured detector current (I_{GEM}) as follows:

$$qAcc = \frac{2 \times I_{GEM}[nA] \times Times[s]}{100cm^2 \times 10^9}$$

where 100 cm^2 is the total irradiated area of the chamber. The different slope of the curves represents different accumulation rates, given by the different irradiation source intensities. Different absorption filters were indeed applied to the ^{137}Cs source along the irradiation campaign, due to other users requests. This allowed to test Triple-GEM detectors performance with different aging speeds, which could in principle give different outcomes. More than 150 mC/cm^2 were accumulated along the campaign for each detector, of which about 80 mC/cm^2 during operation with $Ar/CO_2/CF_4$ gas mixture and gas recirculating fraction higher than 90%. As an example, an accumulated charge of 80 mC/cm^2 corresponds to 13 times the accumulated charge of 10 years of operation in CMS during the HL-LHC Phase (Ar/CO_2 gas mixture, CMS GE1/1 region [4]).

It is therefore concluded that the overall stability of Triple-GEMs performance is maintained regardless of the gas recirculating fraction and the irradiation rate, guaranteeing stable detector performance during operation in gas recirculating systems with recirculating fractions up to 95%.

Moreover, the weekly performance monitoring realized with ^{55}Fe irradiation is found to be aligned with the results of ^{137}Cs irradiation. Figure 3.23 shows the amplification gain trend obtained from ^{137}Cs detector current for the entire irradiation campaign, together with the trend of the weekly scans, in which the amplification gain is estimated from the main peak of the ^{55}Fe spectrum obtained measuring detector signal. It can be seen how the two variables, normalized to their initial value, are following each other, showing equivalence between the two measurements of Triple-GEM detectors amplification gain.

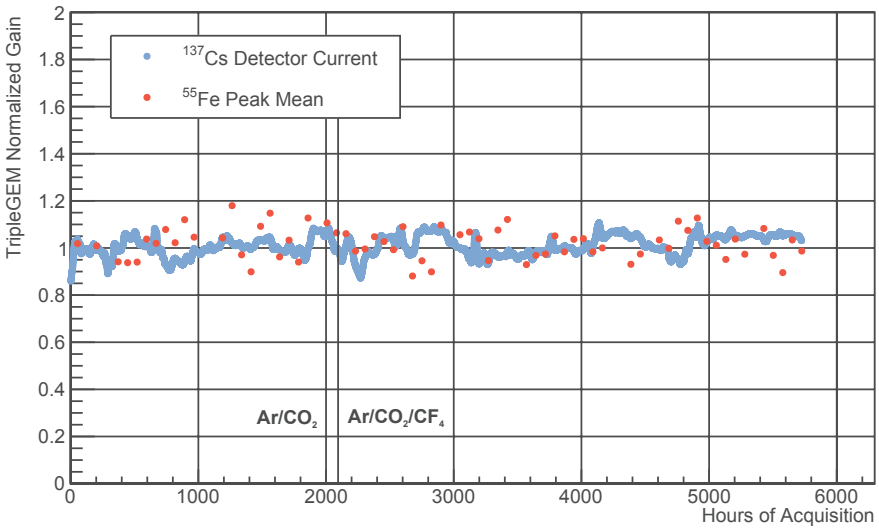

FIGURE 3.23: Triple-GEM detector normalized gain trend obtained from ^{137}Cs detector current monitoring and from weekly ^{55}Fe acquisition, during the entire long-term irradiation campaign.

3.4 Studies on GEM holes radiation damage

Though no clear sign of aging phenomena affecting Triple-GEM detectors performance emerged in the studies presented in the previous section, a microscopy analysis was realized on some samples taken from GEM foils that were used in Triple-GEM detectors operated in high-rate radiation with gas recirculation. In particular, the sample was taken at the end of the period of operation with Ar/CO_2 gas mixture, after the accumulation of about 8 mC/cm^2. A short description of the SEM imaging technique will follow before the presentation of the obtained results.

3.4.1 Scanning Electron Spectroscopy (SEM)

The analysis were realized in the laboratories of the CERN EN-MME-MM department [71], where a Scanning Electron Microscope is available. The Scanning Electron Microscopy (SEM) is an imaging technique based on the employment of an electron beam that is directed at the specimen under observation [72]. The SEM is mainly used to study surfaces and external morphology of objects, providing images that are rather similar in appearance to those formed by human eye. Figure 3.24 reports a schematic diagram of the SEM main components.

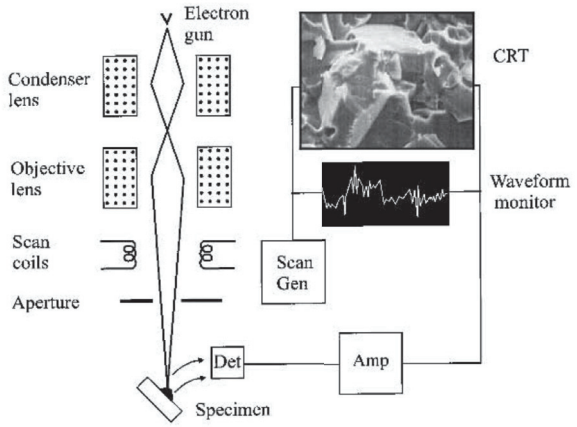

FIGURE 3.24: Schematic diagram of the components of the Scanning Electron Microscope [72].

The electron source is usually the thermionic emission of a tungsten filament. Emitted electrons are accelerated to energies between 1 keV and 30 keV, and the beam is de-magnified by condenser lenses until it reaches a diameter of 2-10 nm when hitting the specimen. The beam position on the sample is controlled digitally, in way for it to scan in a raster fashion over a rectangular area. Thanks to the interaction of primary electrons with the specimen, a secondary and back-scattering electron signal is produced, mainly by inelastic scattering. If primary electrons have penetrated more than a fraction of micrometer, they will not be back-scattered out of the sample, and that is the reason why only surface information can be gathered with the SEM technique. In most cases, the main signal is the one of secondary electrons, detected by a scintillator-photomultiplier system (Everhart-Thornley detector). Detected signal is collected and recorded in relation to the primary beam location , allowing to create a distribution map of the emission intensity, i.e. the specimen amplified image. The magnification factor can range from 10 up to 10^6, as it only depends on the ratio between the raster dimension on the sample and the one of the display device.

The smaller is the sample area that is scanned, the higher the amplification factor of the image.

3.4.2 Results

GEM foils were scanned with the SEM simply placing them in the sample position, as the instrument can fit the full 10×10 cm^2 foil. The actual area that can be scanned is much smaller, therefore the foil was progressively moved and rotated to obtain images from different locations of the foil surface. Figure 3.25 reports a picture showing the sample stand where the GEM foil is lying, as well as the terminal part of the SEM electron gun, with the beam directed towards the sample.

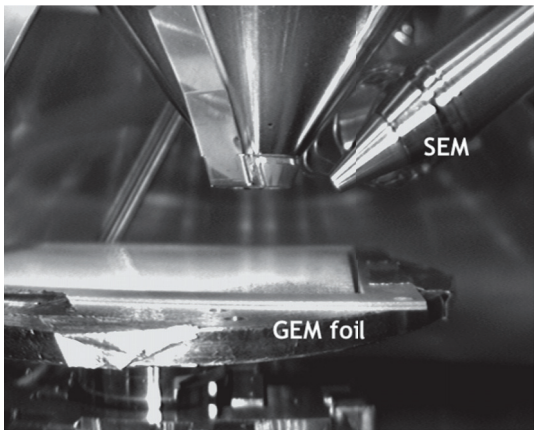

FIGURE 3.25: Picture of the inside of the SEM sample slot, with the GEM foil and the electron gun. [71]

From an amplification factor of about 200, GEM holes can be clearly recognized in the image, in their typical alternate rows pattern. Figure 3.26 reports an example of such image, from which it can be already noticed the main feature that emerges from the comparison between brand new foils and irradiated ones. While on new foils the holes have a good circular shape and a smooth outline, on the tested foils some of the holes were found to have smudged outlines and distorted shapes.

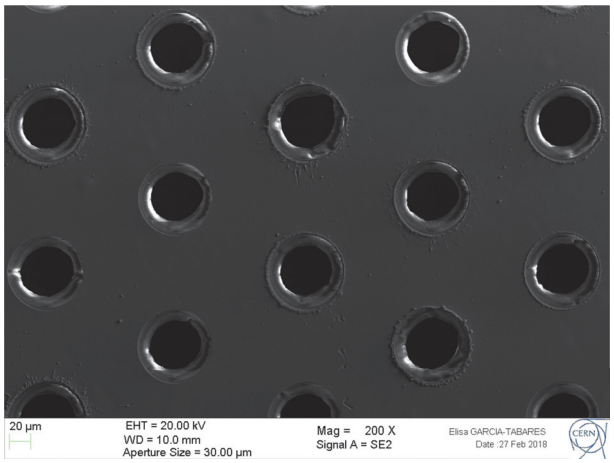

FIGURE 3.26: SEM image of a section of a partly damaged GEM foil, with magnification factor 200. [71]

A bigger magnification factor allowed to obtain images of single holes, reported in

Figure 3.27 (amplification factor 1000). It should be here reminded that GEM holes have a bi-conical shape, so the circular crown of the actual hole that is visible in the reported 2D images corresponds to the conical shape between the foil surface and the central narrowest section of the hole. Measuring the hole diameter with the instrument, it was found that both proper and damaged holes have a diameter of about 46-50 μm, as per foil production requirements. However, it can be clearly seen from the pictures that the outline of the hole at foil surface level looks very different. In the damaged holes, a quantity of deposits can be seen around the external diameter, as if drops of material were present on the foil surface around the hole circumference.

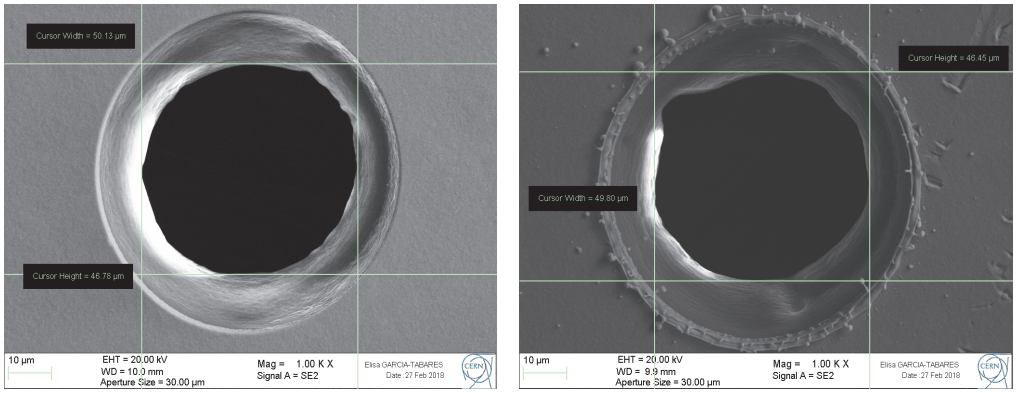

FIGURE 3.27: Comparison of SEM images of single GEM holes, showing a proper hole (left) and a damaged one (right). [71]

An explanation of such morphology could be found looking at the final position of positive ions and electrons when the gas avalanche develops inside the gem holes. Due to the electric field configuration, where many field lines are ending in the circular area around the hole circumference on the surface of the foils (Figure 3.28), the charged particles are accelerated towards that area and their energy could contribute to create discharges that cause the foil material to be deformed and some drops to be deposited along the hole outline. Further simulations studies, including the behavior of the foils material in presence of discharges, could give a better overview on the phenomenon.

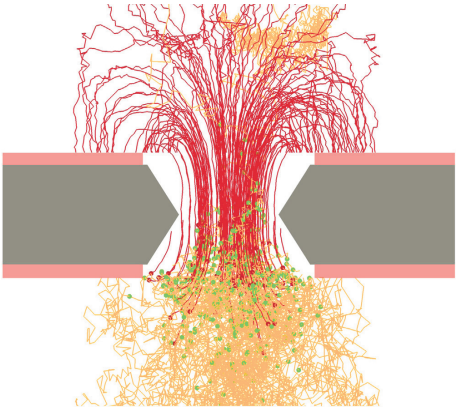

FIGURE 3.28: Graphical representation of the positive ions (red) and electrons tracks (orange) inside the gem hole during the development of the gas avalanche [73].

The conclusion that can be drawn for the analysis of the pictures obtained with the SEM is that even if some of the gem foil holes result to be damaged in shape and morphology, they only represent a fraction of the total number of holes, i.e. multiplication regions, on a single foil, which performance is not affected by this particular kind of aging.

3.5 Muon efficiency in high-rate environment with gas recirculation

Once Triple-GEM detectors operation was validated with gas recirculation in high rate radiation environment, detector performance was studied in relation to Muon detection efficiency. The setup at the GIF++ facility was adapted to be suitable for the participation to one of the Test Beam periods offered by the facility.

3.5.1 Experimental setup and methods

As described in Section 3.1.3, during the Test Beam period the Triple-GEM data acquisition system was substituted with the Scalable Readout System, with APV25 hybrids as front-end. Only one of the two chambers was kept during the test, as only four APV25 were available. The detector was kept at 1 m distance from the ^{137}Cs source, as during the long-term irradiation campaign, but it was raised to have the center of its active area at the height of the Muon beam (160 cm from the ground). The 4×4 cm^2 scintillator was placed at the same height, as close as possible to the chamber. Figure 3.29 shows the geometrical configuration of the bunker setup. A schematic representation of the full setup is reported in Figure 3.30, with the elements located inside the irradiation bunker (detector, electronics), and in the gas area (main gas system, PC and sensors).

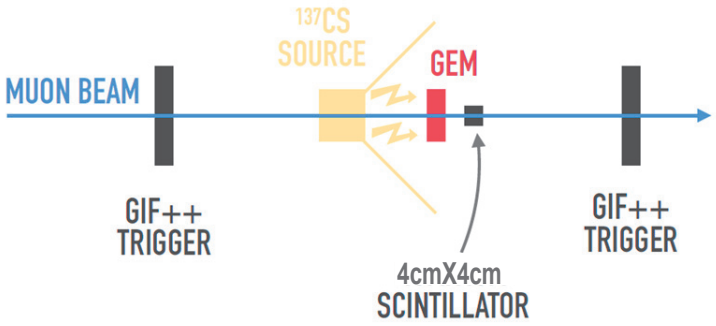

FIGURE 3.29: Geometrical layout of the Test Beam experimental setup.

Triple-GEM detectors efficiency to Muon detection was tested with High Voltage scans in different conditions. Muon events were selected for each step of the scan as the ones with a cluster of consecutive fired strips in the range correspondent to the projection of the small scintillator area over the detector surface (about 100 strips) and the time of maximum deposited charge of such cluster within 5 ns of the trigger time (Figure 3.31). Muon detection efficiency is defined as the ratio between Muon events and total events triggered by the scintillators coincidence. The total charge deposited on the readout plane by the passage of a Muon in the detector volume is measured for each selected event. As the electron avalanche size is proportional

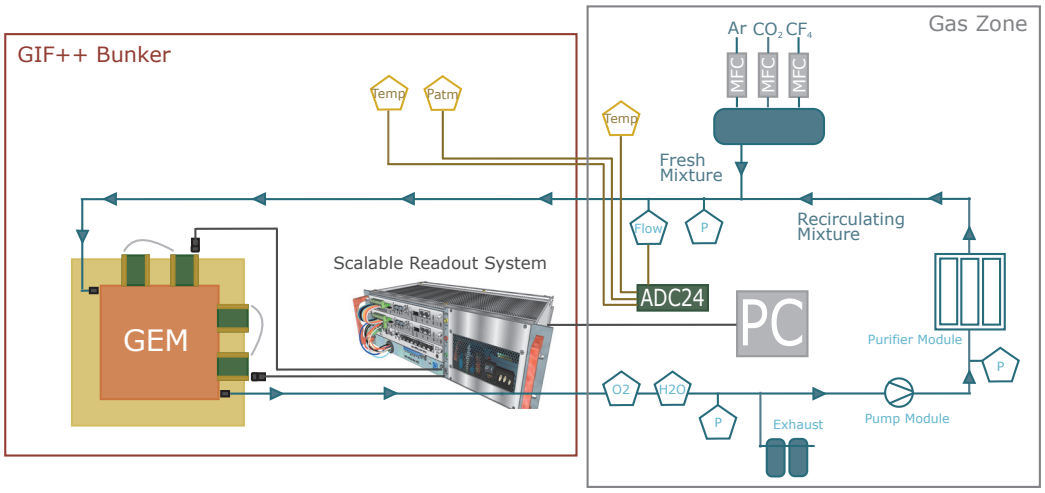

FIGURE 3.30: Schematic representation of the Test Beam experimental setup, with the elements inside the GIF++ bunker and in the gas area.

to the energy lost by the Muon, the distribution of the total deposited charge is a Landau, whose Most Probable Value (MPV) gives an estimation of the amplification gain. Figure 3.31 shows an example of the charge distribution, where a Landau fit is performed to extract the MPV. The amplification gain is then calculated with the conversion factor obtained from the APV25 characterization.

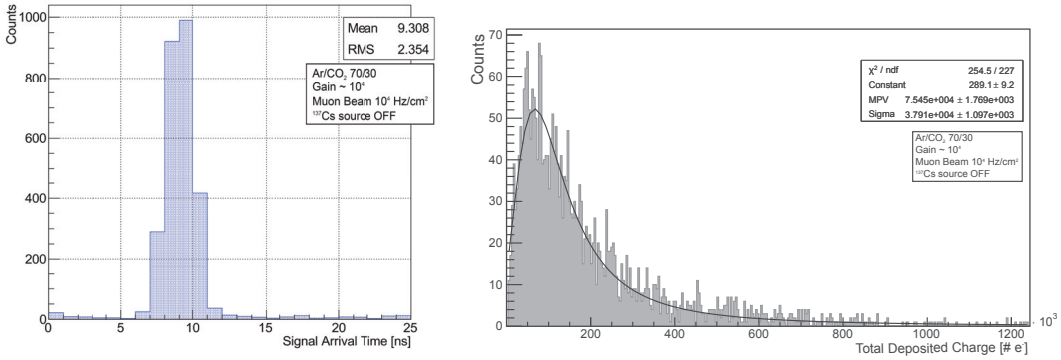

FIGURE 3.31: Distribution of the signal arrival time in the 25 ns acquisition window (left) and distribution of the total measured charge deposited at readout plane (right).

A reference scan was performed with the Muon beam only, in absence of photon irradiation with the gas system in open mode, using the two gas mixtures Ar/CO_2 70/30 and $Ar/CO_2/CF_4$ 45/15/40. Figure 3.32 shows the efficiency curves: Muon detection efficiency reaches almost 100% with both gas mixtures. This scan also allowed to define the working point of the detector, taken 100 V after the point at 90% efficiency. The goodness of the efficiency parameter and working point choice is confirmed by the measurement of amplification gain, calculated to be around 10^4, which is the typical gain value of Triple-GEMs at full efficiency.

To have a complete characterization of the detector behavior and the acquisition electronics, the cluster size distribution was also calculated. Its value was obtained counting the number of strips composing the signal cluster. Figure 3.33 reports the cluster size distribution for the two gas mixtures, from which it is obtained a mean

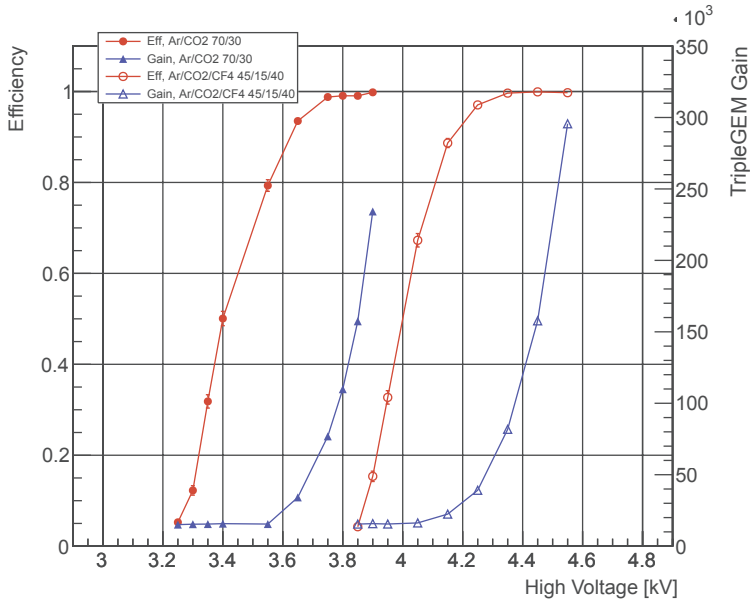

FIGURE 3.32: Efficiency curve and amplification gain trend for the two tested gas mixtures, measured with Muon beam only in open mode.

value of 4.06 strips for the Ar/CO_2 70/30 mixture and of 3.35 for the $Ar/CO_2/CF_4$ 45/15/40 mixture. Considering a strip width of about 0.4 mm, it is obtained a cluster size of 1.6 mm and 1.3 mm respectively.

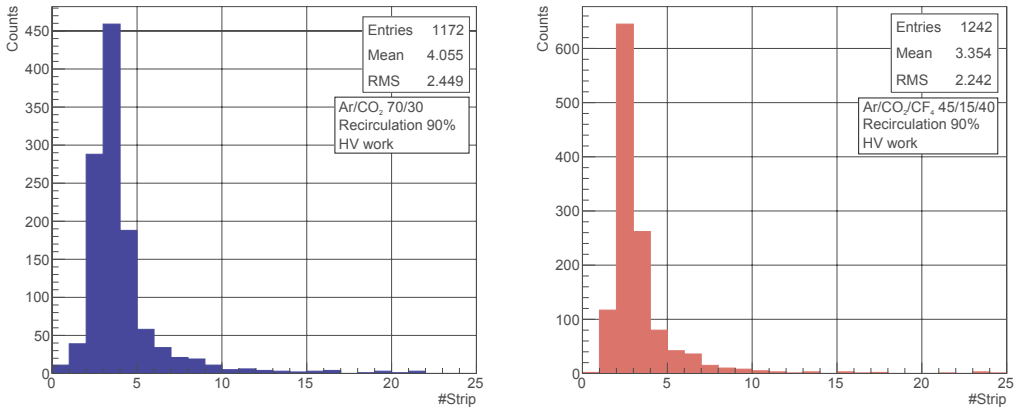

FIGURE 3.33: Cluster size distribution for Ar/CO_2 70/30 (left) and $Ar/CO_2/CF_4$ 45/15/40 (right).

3.5.2 Results

To compare Triple-GEMs performance in open and closed loop, a scan with Muon beam only was realized with the gas system in gas recirculation configuration (90%). In Figure 3.34 the efficiency curve and amplification gain are reported for the scans with $Ar/CO_2/CF_4$ 45/15/40 gas mixture, with open gas system and gas recirculation. It can be seen how the curves are almost superposed, and that in both cases the maximum efficiency is reached. The same result was obtained for the Ar/CO_2 70/30 gas mixture. Moreover, it was seen that also the cluster size value remained constant

for the two operation modes. It can thus be concluded that, as already seen during the long-term irradiation campaign, the presence of the Purifier module allows the removal of impurities before the gas mixture is re-injected in the system, making the operation with gas recirculation as good as in open mode.

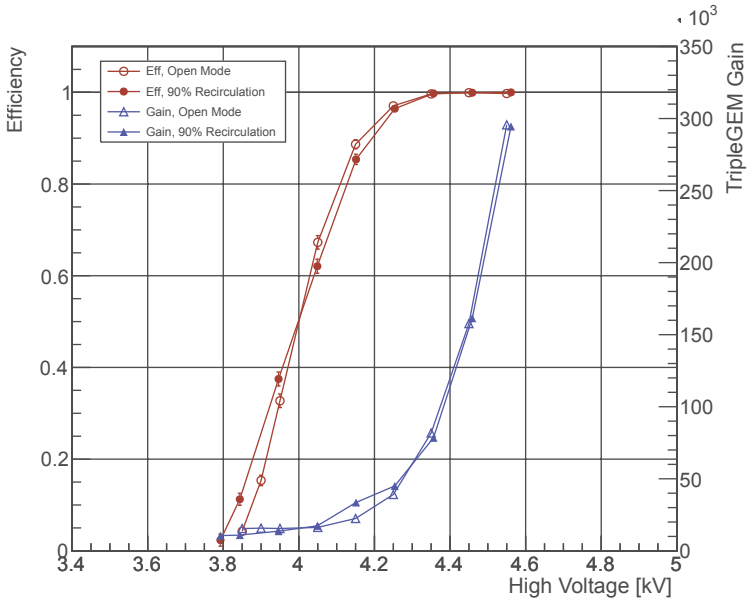

FIGURE 3.34: Efficiency curve and amplification gain trend measured with Muon beam only, for the open mode and 90% gas recirculation operation, with $Ar/CO_2/CF_4$ 45/15/40 gas mixture.

To evaluate the performance of Triple-GEM detectors operated with gas recirculation in presence of high-rate radiation, high-voltage scans were performed with gamma irradiation of increasing intensities. Three different source intensities (ABS 2200, 220, 22) were tested for the Ar/CO_2 mixture (in open and recirculation modes) and for the $Ar/CO_2/CF_4$ mixture in open mode. A wider filter scan was performed for the $Ar/CO_2/CF_4$ mixture with 90% gas recirculation, being the most relevant gas system configuration (ABS 2200, 220, 100, 46, 22, 10).

The source intensity scan results show how Triple-GEM detectors can reach full efficiency even in presence of significantly high radiation background. The efficiency curves for recirculating gas operation with $Ar/CO_2/CF_4$ 45/15/40 gas mixture are reported in Figure 3.35. The reference curve is the one obtained without any gamma background, i.e. with Muon beam only. The other curves are obtained progressively increasing the ^{137}Cs radiation rate, from 3×10^4 Hz/cm^2 (ABS 2200) up to 4.5×10^6 Hz/cm^2 (ABS 10). As an example, the background rate foreseen for the CMS GE1/1 region during the HL-LHC phase corresponds to a gamma background intensity around ABS 220 (10^5 Hz/cm^2 [4]), in which the Triple-GEM detector still shows a Muon efficiency higher than 95%.

Figure 3.36 shows the Triple-GEM detector amplification gain, estimated from the readout deposited charge, measured for different source intensities at the chamber working point. The latter is defined 100 V after the 90% efficiency point of the Muon beam efficiency curve with no background of Figure 3.35, and corresponds to an amplification gain of about 4×10^4. It can be seen how the amplification gain remains

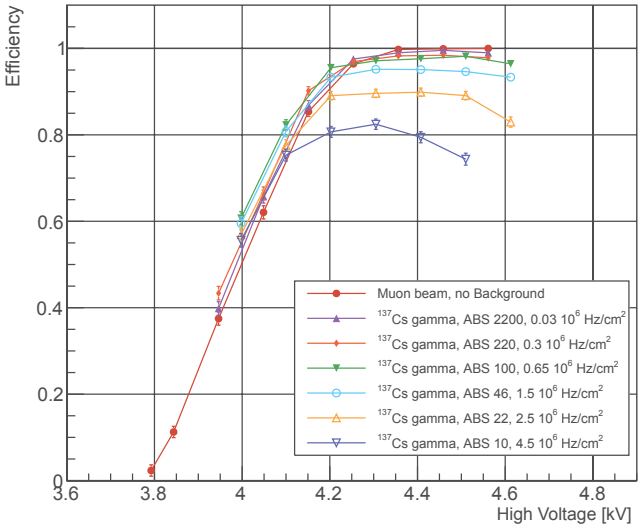

FIGURE 3.35: Efficiency curve measured with the $Ar/CO_2/CF_4$ 45/15/40 gas mixture in 90% gas recirculation, with Muon beam only and in presence of gamma background of different intensities.

stable for increasing background rate. This is indeed coherent with what is found in literature, as Triple-GEM detectors are expected to lose in amplification gain for incoming rates higher than 100 MHz/cm^2 [4]. As the APV25 front-end electronics does not normally suffer of dead-time in the conditions of this study, the loss in efficiency for radiation rate higher than 10^6 Hz/cm^2 (Figure 3.35) could be traced back to an excessive occupancy of the detector. Being the gamma rate much higher than the Muon rate, the probability of detecting a Muon in a given time window (opened by the external trigger) becomes lower and the chamber efficiency is therefore affected.

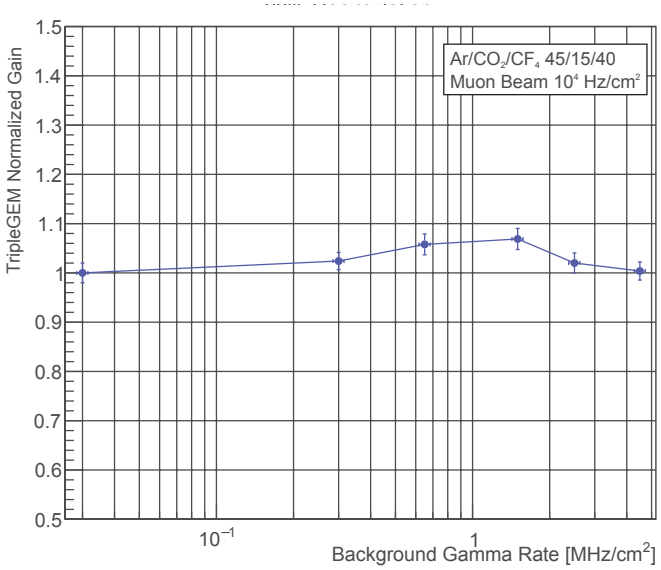

FIGURE 3.36: Amplification gain measured with $Ar/CO_2/CF_4$ 45/15/40 gas mixture in 90% gas recirculation as a function of the background rate.

3.6 Studies on CF_4-based impurities

As already mentioned in the previous sections, gas mixture quality can be undermined by the presence of impurities, some of which could be created in the detector itself. It is the case of Triple-GEM detectors when operated with CF_4-based gas mixture, as CF_4 molecules are subject to break up processes when exposed to high-rate radiation and in presence of high electric field. The release of highly reactive products could be critical as they could either create polymerized deposits or cause material etching, that could compromise detector performance and accelerate aging processes. For example, if H_2O is present in the gas mixture, it can react with Fluoride components forming Hydrofluoric Acid, which could corrode the GEM foils or the readout board material, compromising proper detector performance [74]. The increasingly common operation of gas systems with gas recirculation could worsen the risk of damage due to impurities accumulation.

Fluorine-based impurities production is characterized operating Triple-GEM detectors under high-rate irradiation at the GIF++ facility, in relation to different detector operation conditions, such as gas mixture composition, working voltage, input flow rate and irradiation rates. Moreover, as Triple-GEM detectors were operational in the LHCb Muon System during Run 2, Fluoride impurities measurements were realized in 2018 and the results were afterwards compared with the ones obtained at GIF++.

3.6.1 Experimental Setup and Fluoride Measurement

The test was realized using the two 10×10 cm^2 Triple-GEMs installed at the GIF++ facility with the dedicated gas system (Section 3.1.2). Detectors were operated with the standard CF_4-based gas mixture, and during the test the gas system was operated both with open loop and gas recirculating mode. Triple-GEM detectors performance was monitored through detector current, measured with the standard 10×10 cm^2 readout board, as during the long-term irradiation campaign (Section 3.1.3). It should be noticed that the two chambers, named GEM1 and GEM2 in the following, are placed at a slightly different distance from the source, with GEM1 being 15 cm closer. Such difference results in a higher radiation rate for the chamber closer to the source, in line with the values obtained from the gamma rate current simulation [65]. Figure 3.37 reports a schematics of the setup used during the test, including the Fluoride sampling points.

Fluoride impurities were measured with an Ion Selective Electrode station (ISE, Figure 3.38), specific for the measurement of Fluoride (F^-) in solution. Two different types of Fluoride electrodes were used, the HI4010 electrode with separate reference from HANNA Instruments [75] and the Orion 9409BN combined electrode from ThermoScientific [76]. Measurements were done in parallel with the two electrodes, with the aim to cross check the results with two different instruments. As results were found to be consistent between the two, for simplicity only one set of measurements will be reported in the following.

Gas samples were extracted from the system and bubbled for a given time inside a solution based on distilled water. F^- ions are deposited into the solution, progressively accumulating in the sample volume, while other mixture components are exhausted to air. After the accumulation, the electrode (and the reference, for the

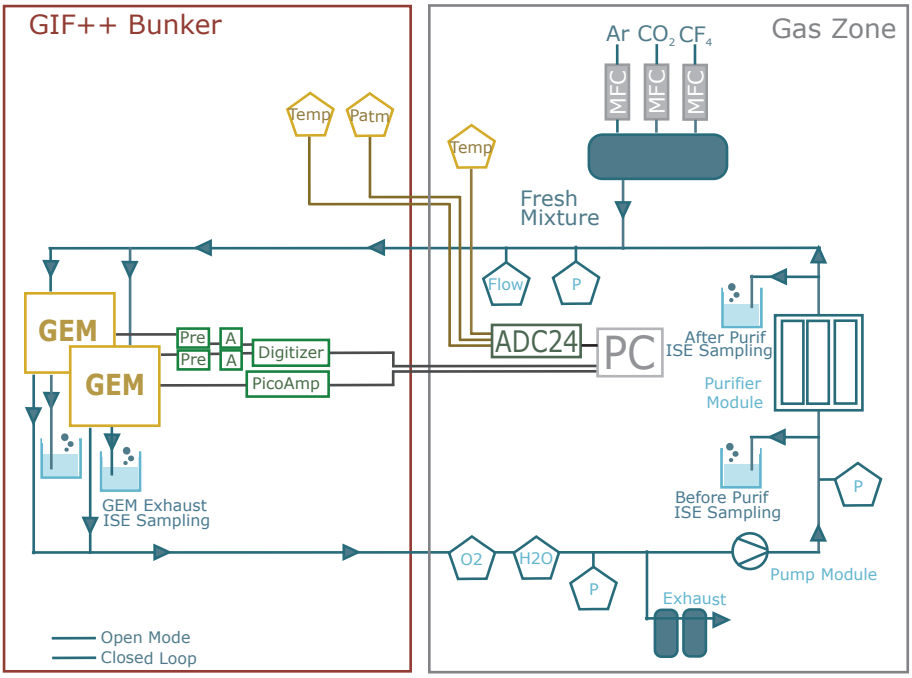

FIGURE 3.37: Schematic representation of the experimental setup, with Fluoride sampling points marked along the gas path.

FIGURE 3.38: Picture of the Orion Fluoride electrode (left) and the ISE measurement station with the HANNA separate electrodes during the sampling (right).

separate HANNA electrode) was immersed in the sample solution, and connected to the station to measure its output. The electrode develops indeed a voltage difference thanks to the exchange of ions happening between the sample solution and the solid state inorganic membrane contained in the electrode body. The voltage response of the electrode is proportional to the concentration of free ions in the sample volume, thanks to the addition of an alkaline solution (TISAB II), that ensures stable pH and ionic strength. The voltage is converted into Fluoride concentration with parameters obtained from periodical calibrations of the electrode, realized with a set of standard solutions containing a fixed Fluoride concentration (from 0.5 ppm to 100 ppm).

It is fundamental to point out that such measurement gives an estimation of the concentration of accumulated F^- inside the sample solution for the duration of the measurement, and not a measurement of concentration or volume of F^- in the gas system or in the chambers at a given instant. As concentration depends on the sample solution volume and on the quantity of bubbling gas, a sample volume of 20 ml was used in all measurements, while bubbling time and gas flow rate were recorded to normalize and compare the results, that will be presented in the following in terms of F^- accumulation rate (ppm/h). Th typical accumulation duration was of 12 hours, obtaining in this way concentrations sensibly higher than the 0.02 ppm detection limit of the electrodes. This allowed more precise and stable electrode measurements, limiting uncertainties on the concentration values.

For completeness, a rough estimation of the possible Fluoride concentration contained in the Triple-GEM chamber volume is given in the following. Assuming that the gas at the chamber exhaust has the same F^- concentration as the gas contained in the chamber volume, it can be obtained that:

$$C^{F^-}_{GEM} = \frac{mg^{F^-}_{GEM}}{V_{GEM}} = \frac{mg^{F^-}_{exh}}{V_{exh}} = \frac{mg^{F^-}_{s}}{V_{exh}} = \frac{C^{F^-}_{s} \times V_s}{V_{exh}}$$

where C is the concentration in ppm, mg the quantity of Fluoride ion in milligrams, V the volume in liters, exh the gas extracted from the sampling point and s is the sample solution. The expression is obtained considering the equivalence between the F^- volume rate in the exhaust flow and the F^- volume deposited in the sample solution. Following this, a measurement of 1 ppm in the sample solution corresponds to about 0.04 ppm concentration in the chamber volume.

Fluoride impurities measurements were first performed operating Triple-GEM detectors with the gas system in open mode. The chambers exhaust gas was directly bubbled into the sample volume, therefore with a gas flow rate equivalent to the detectors input one. The impact of gas mixture composition was tested changing the CF_4 fraction, while the effect of different charge density in the detector volume was tested varying both irradiation rate and High Voltage (i.e. the electric field in the gas volume). Lastly, the input gas flow rate was varied. The gas system was then moved to gas recirculation, with gas recirculating fraction of 90%. In this case, the gas sample was extracted in two different points of the gas system, before and after the Purifier module. The extracted gas flow was sent to the sample volumes through a rotameter, to regulate and measure the bubbling flow rate.

3.6.2 Results

The impact of gas mixture composition was studied varying the CF_4 concentration from 3% to 70%, keeping constant the ratio between Ar and CO_2 as in the standard mixture $Ar/CO_2/CF_4$ 45/15/40, i.e. Ar equal to three times CO_2. Chambers were irradiated with the maximum irradiation rate. As the working point of the chambers depends on the components concentration, at each change of mixture the High Voltage was adjusted to have the same detector current as the one reached at the working point with standard gas mixture, i.e. the same amplification gain of about 10^4. Figure 3.39 reports the measured Fluoride ion accumulation as a function of the CF_4 concentration in the gas mixture. The Fluoride trends oscillates around 0.6 ppm/h

and 0.4 ppm/h for GEM1 and GEM2 respectively, with a slight increase for CF_4 concentration higher than 50%. As previously mentioned, the absolute value of Fluoride ion accumulation differs between the two chambers due to their different distance from the ^{137}Cs source, therefore different irradiation rate. The reported results show how the Fluoride ion production rate remains stable between CF_4 concentrations of 3% and 50%. The lower limit of the concentration was fixed by the mixer module characteristics, and it was not possible to test a lower concentration with the system in use. It can be concluded that the CF_4 concentration contained in the gas mixture is not a main factor influencing the F^- production process, though the obtained result might suggest a limited increase in the impurity production when CF_4 concentration is higher than 50%.

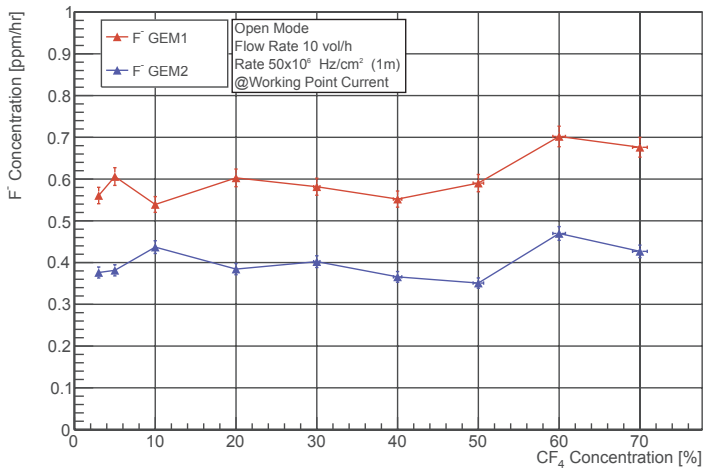

FIGURE 3.39: Trend of accumulated Fluoride ion concentration for increasing CF_4 concentration in the gas mixture. Detectors are kept at working point varying the supply voltage in way to keep detector current constant.

The influence of charge density on the Fluoride production was studied with variations of irradiation intensity and High Voltage, the latter directly defining the electric field intensity in the GEM foils holes. Detectors were operated with $Ar/CO_2/CF_4$ 45/15/40 gas mixture, with fixed input gas flow rate of 10 vol/h, where *vol* refers to the detector volume.

A first set of measurements was taken varying the High Voltage, keeping constant the incoming radiation at the maximum available rate (50×10^6 Hz/cm^2 at 1 m distance). The High Voltage range was chosen around the working point, without exceeding safe values. For lower voltages, detectors are not yet efficient, therefore the charge density in the chamber is lower due to the lower primary ionization. With the voltage increase, the chambers reach efficiency and the amplification gain increases, leading to an exponential increase of detector current. The trend of Fluoride concentration for increasing High Voltage values is showed in Figure 3.40. For both detectors the Fluoride concentration increases with the voltage, therefore with the electric field in the gas volume. The plot also shows the detector current along the scan (right axis), which also increases with the applied voltage as expected.

The second set of measurements was taken varying the irradiation source intensity by applying different absorption filters to the ^{137}Cs source, keeping the chambers at their working point High Voltage. The source intensity was increased from about

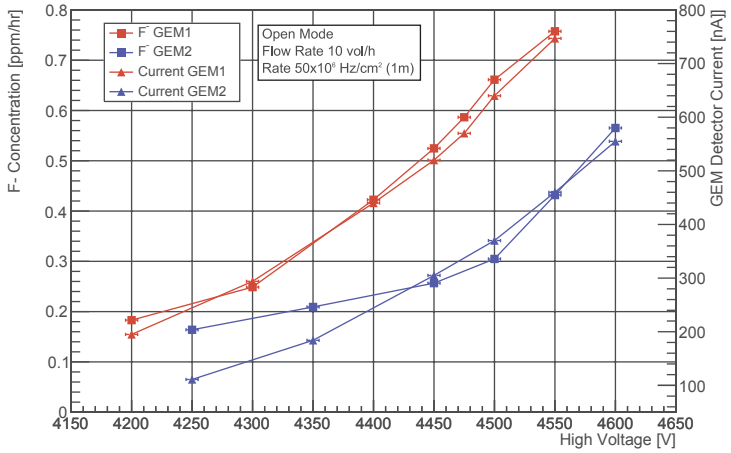

FIGURE 3.40: Trend of accumulated Fluoride ion concentration (left axis) and detector current (right axis) measured during the high voltage scan, with detectors operated in Open mode with fixed input flow rate and radiation intensity.

20×10^6 Hz/cm^2 up to the maximum irradiation rate. As already mentioned, given the different distance of the detectors from the source, the same absorption filter results in a slightly different incoming gamma rates. Figure 3.41 shows the trend of Fluoride concentration in relation to the gamma radiation rate. While the Fluoride concentration linearly increases with the radiation rate for rates lower than about 50 $\times$ 10^6 Hz/cm^2, above such value it shows a plateau around 0.4-0.45 ppm/h. As in the previous plot, detector current is plotted on the right axis and, differently from the Fluoride accumulation, its trend linearly increases with irradiation rate.

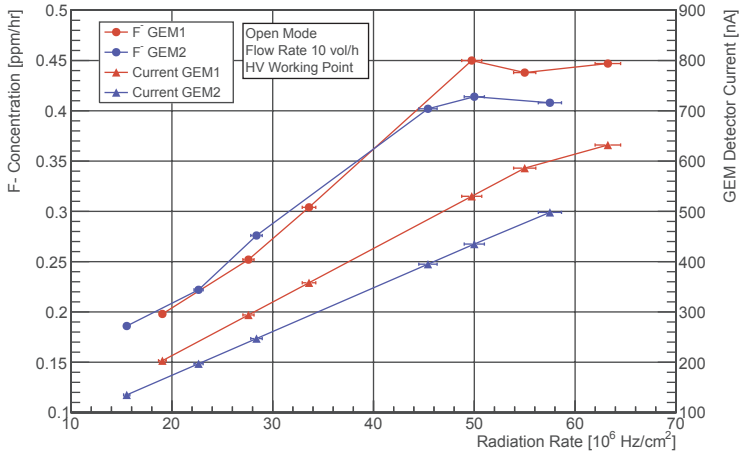

FIGURE 3.41: Trend of accumulated Fluoride ion concentration and detector current measured for irradiation with increasing gamma rate, i.e. with different absorption filters applied at the ^{137}Cs source. Detectors are kept at working point with fixed input gas flow rate.

Comparing the two sets of measurements, a significant difference can be seen in the behavior of Fluoride ion production. When the detector current increment, i.e. total charge density in the detector volume, is caused by an increase of supply voltage it leads to a continuous increase in the Fluoride production. On the other hand, when the current increase is caused by higher irradiation rates, a plateau in the Fluoride

production is found. A possible explanation of such difference could be traced back to the different causes of detector current increase. When High Voltage is incremented, the electric fields is increased and it leads to an exponential increase in the amplification gain, which is proportional to detector current. A higher amplification gain means therefore a bigger electron avalanche, which would in turn proportionally increase the break up of CF_4 molecules. On the other side, the increment in irradiation rates only increases the number of incoming photons, i.e. the probability of primary ionization, which does not correspond to a higher amplification gain but only to a higher number of avalanches. For this reason, the CF_4 break up process is not incremented as avalanches might not be intense enough, though produced in a higher number.

The last part of the characterization consisted in varying the detectors input gas flow rate, keeping constant the radiation rate at 50×10^6 Hz/cm^2 and operating Triple-GEMs at working point with constant detector current. The nominal input flow rate of each chamber was varied from 5 to 70 vol/h, and the effective output flow rate was measured with a rotameter before bubbling it into the sample solution. As the variation of the bubbling flow rate yields to a variation in the accumulation rate in the sample solution, electrode measurements are normalized with the measured flow rate, to obtain comparable results. Such calculation is done assuming a linear relation between bubbled gas flow and Fluoride accumulation, which was indeed demonstrated with previous laboratory tests. Given the measurement procedure and the detector volume, it was impossible to test gas flow rates lower than 5 vol/h, as it would have lead to extremely low concentrations of Fluoride in the sampling solution, below electrodes sensitivity.

Results are reported in Figure 3.42, where the normalized Fluoride concentration is plotted against the input flow. The Fluoride trend is found to be decreasing with the increase of the flow rate, reaching values below 0.1 ppm/h for flow rates higher than 40 vol/h. Very low gas flow rates definitely lead to high Fluoride production in the chambers volume, probably due to the longer permanence of CF_4 in the irradiated area, increasing the probability of breaking the molecule. It was impossible to determine whether an upper limit exists, due to the impossibility of testing very low flows. It is therefore concluded that a higher input gas flow rate could be helpful to reduce the production of Fluoride impurities, diminishing the risk of aging processes.

The presented results from open mode operation clearly show a significant Fluoride production in the detector volume, that is subsequently carried at the detectors gas exhaust. Therefore, moving to Closed Loop operation, the exhaust gas would transit through the Pump and the Purifier module before being re-injected in the system. Impurities produced in the irradiated chamber volume would follow the same path, possibly accumulating more and more in the gas system. The possible effect of the Purifier module on F^- molecules coming from the Triple-GEMs exhaust was studied taking measurements from the two sampling points in the recirculating gas system, before and after the module, with a gas recirculating fraction of 90%. It should be noticed that, in this point of the system, the return lines of the two chambers are already united in a single pipe, therefore the gas sample will contain impurities created in both chambers. The detectors were irradiated with full source (50×10^6 Hz/cm^2), at working point, with fixed input flow rate of 10 vol/h, the same used for open mode operation.

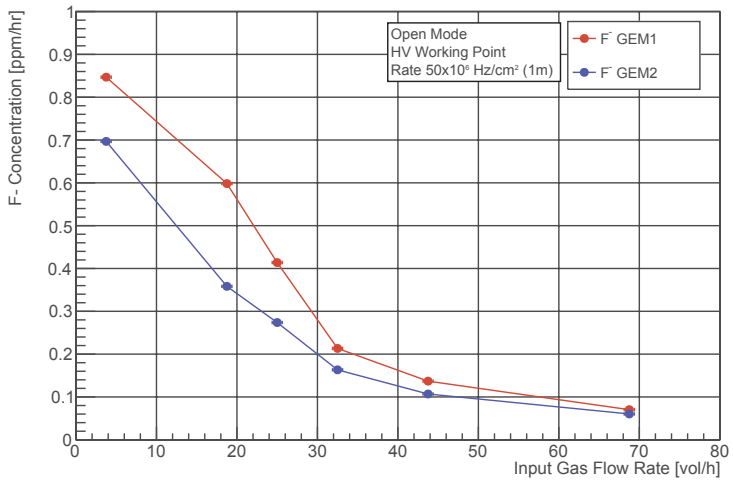

FIGURE 3.42: Accumulated Fluoride ion concentration as a function of the input gas flow rate.

The recirculated gas was sampled along 24 hours of chambers irradiation, extracting from the main gas system line a flow of 0.5 l/h. The sample collected before the Purifier module showed a Fluoride accumulation of about 0.6 ppm/h. On the other hand, samples collected after the Purifier showed a Fluoride concentration close to zero. It is therefore concluded that the material of the Purifier module is capable of trapping F^- molecules from the exhaust gas mixture. Concerning Fluoride impurities accumulation, operating the system with recirculating gas is thus equivalent to running it in open mode, within the possible saturation of the purifier material for higher impurities concentration, as the re-injected mixture is not carrying the Fluoride ions back to the chambers.

On a more general note, it can be acknowledged how the presence of the Purifier module is fundamental in all gas systems operated with Freon-based gas mixtures. The elimination of Fluoride ions from the recirculated gas prevents indeed the critical formation and accumulation of Hydrofluoric Acid (HF) in the chamber volume. HF is the result of the reaction between F^- and H_2O ($F^- + H_2O \rightarrow HF + OH^-$), and it chemically attacks detector and readout plane materials, representing one of the most dangerous pollutants for detectors integrity. As also presented in Section 3.3, the action of the Purifier module successfully reduces H_2O concentration down to about 50 ppm [77], which combined to the almost full removal of Fluoride significantly averts the HF formation.

3.6.3 Fluoride impurities measurement in LHCb GEM Gas System

As described in Chapter 2, the LHCb Muon system hosted Triple-GEM detectors during operation of Run 1 and Run 2. In this case, Triple-GEMs were operated with $Ar/CO_2/CF_4$ 45/15/40 gas mixture, in open mode during Run 1 and with 90% gas recirculation during Run 2, with a reduction of 90% in Greenhouse Gas emission [78]. In the last months of Run 2 (August-December 2018), the ISE station was used to measure the presence of Fluoride-based impurities at the chambers exhaust. Triple-GEM detectors were indeed located close to the beam interaction point, where the radiation reaches its highest rate, with a dose level of about 1.6 kGy/year [79].

The measurement was realized in three different locations of the gas system, on the return lines from detectors exhaust. One was located underground, in the service cavern, after the Pump module, while the others were located in the surface gas building, before and after the Purifier module. All the sampling points were located on the gas return line common to all Triple-GEM detectors installed in the system, therefore merging their exhaust gas flow. A schematic of the recirculation gas system with the ISE station sampling points is reported in Figure 3.43.

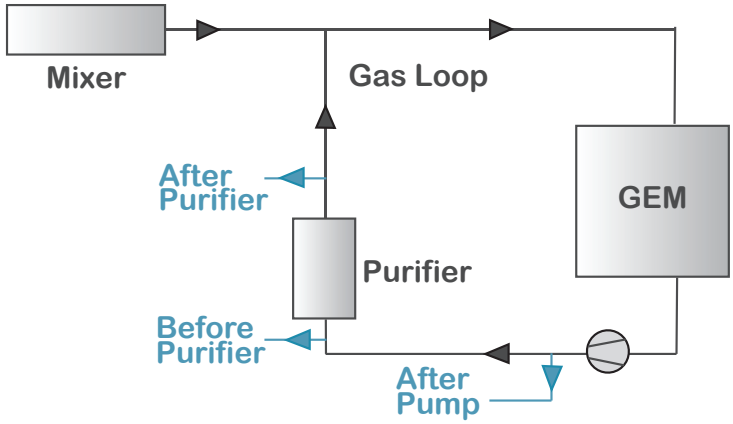

FIGURE 3.43: Schematics of the LHCb GEM gas recirculation system, with the location of the Fluoride sampling points.

The gas sampling was realized with the same method described in the previous section for the GIF++ studies, but in this case the Fluoride accumulation was continuous, with the gas sample permanently bubbled in the sample solution, at a fixed flow rate of 0.5 l/h. The Fluoride concentration measurement in the sample solution was realized every couple of days, monitoring the progressive impurity accumulation. As expected, given that the sampling points After Pump and Before Purifier are located at equivalent points of the gas system, only separated by a hundred meters of inox gas pipe, the obtained results for Fluoride accumulation in the two points are equivalent. Therefore, for simplicity, only the Before Purifier measurements will be reported in the following.

Figure 3.44 and 3.45 report the trend of Fluoride ion accumulation in the Before Purifier sample along the duration of the measurement. It can be seen how, starting from zero, it progressively increases with a linear trend, only discontinued by some flat periods. Looking at the LHC schedule, it was found that such periods of interrupted accumulation correspond to technical stops of the accelerator, therefore periods in which Triple-GEM detectors are switched off and no radiation is present in the Experiment. The LHC schedule also indicates that from the beginning of November the accelerator was operating in the so-called Ion Run, in which the LHC collision in not realized with protons (pp), but with lead ions (pPb or PbPb). In this period, the Fluoride accumulation shows again an increasing trend but with about half the slope of the previous periods. The flat trend of the LHC luminosity is given by the fact that only pp collision data were considered, however the particle flux in such period is much higher than in ordinary runs hence the radiation received by detectors is also higher. Chambers were however operated at lower currents, therefore the different Fluoride accumulation could be explained by a combination of these

two factors. Quantitative information about the different parameters characterizing this period of operation were impossible to retrieve, hence the measurements of this last period are not considered in the considerations below.

To better understand the measured Fluoride accumulation trend in relation to the accelerator and detectors activity, it is compared to the trend of the Triple-GEMs accumulated charge [80] (Figure 3.44) and the trend of LHC integrated Luminosity (Figure 3.45) These two variables give respectively indication of charge density developed inside detectors volume and of the radiation activity inside the Experiment. In particular, the reported accumulated charge takes into account the sum of detector currents of all Triple-GEM chambers installed in the system. The comparison between the trends during normal runs clearly shows how the measured Fluoride accumulation perfectly follows the accumulated charge of Triple-GEMs, coming from the detector current measurement, as well as the LHC Luminosity trend which determines the intensity of the charge developed in the chambers volume. The measurement is therefore found to be in line with what the GIF++ characterization showed, i.e. a clear dependence of the produced quantity of Fluoride impurities on the charge density in the detector volume, determined by both radiation rate end electric field in the gas avalanche area.

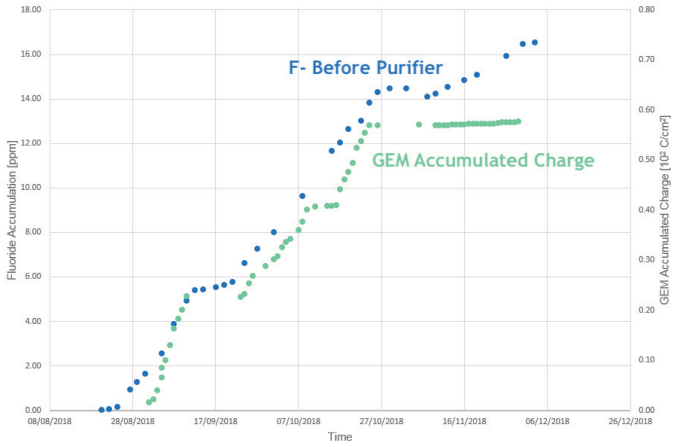

FIGURE 3.44: Trend of Fluoride ion accumulation of the Before Purifier sampling point (left axis), with the trend of LHCb Triple-GEMs accumulated charge ([80], right axis).

Figure 3.46 reports again the trend of Fluoride accumulation of the Before Purifier sampling point, now compared to the trend of the After Purifier sampling point. The plot clearly shows how the Purifier module traps all the Fluoride ions that are present in the gas flow carried back from the detectors, as in the measurement after the module no Fluoride concentration could be detected during the entire duration of the campaign. This result is also in accordance with what was found in the small LHC gas system at GIF++, showing that the capability of the Purifier module to remove Fluoride impurities from the recirculated gas remains valid also when the full system is scaled up to LHC Experiments size.

3.7 Conclusions

Different tests were realized with 10×10 cm^2 Triple-GEM detectors prototype to characterize their performance in relation to gas mixture properties, gas systems

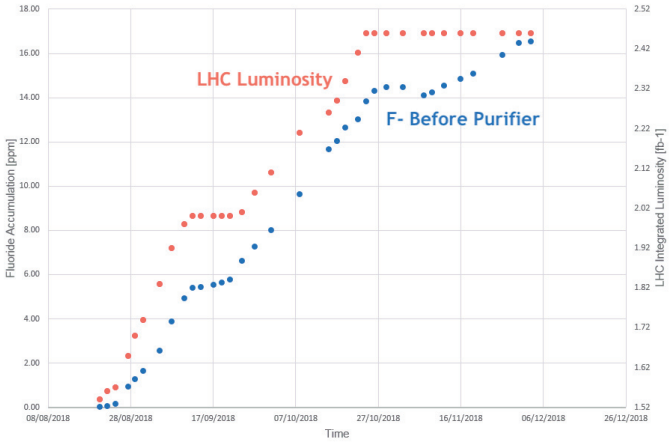

FIGURE 3.45: Trend of Fluoride ion accumulation of the Before Purifier sampling point (left axis), with the trend of LHC Luminosity (right axis).

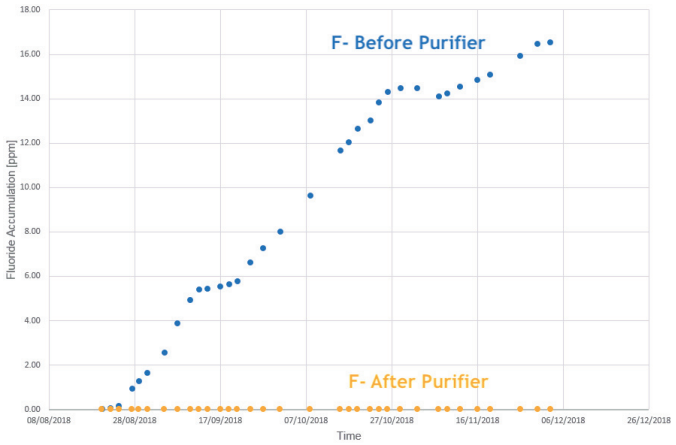

FIGURE 3.46: Trend of Fluoride ion accumulation of the Before Purifier and After Purifier sampling points.

conditions and operation environment.

Triple-GEMs operation was characterized at laboratory level for variations in CF_4 content in the standard gas mixture ($Ar/CO_2/CF_4$ 45/15/40), with parallel simulation to compare the experimental results with the theoretical behavior of the electron avalanches with a given gas mixture. Firstly, it was found that the Garfield++ simulation models quite well the amplification gain of the detector, which is used to quantify the effect of gas mixture variations on detector performance. The simulation and laboratory measurements showed that a significant variation in the gain is obtained per 1% of CF_4 variations, up to 10% with respect to the standard mixture value, confirming the fundamental requirement of an extremely stable gas mixture composition.

Triple-GEM detectors were then operated in a small replica of LHC gas systems at the GIF++ facility, to study their performance in a LHC-like configuration in presence of high-rate radiation. A long-term irradiation campaign was completed exposing Triple-GEM detectors to ^{137}Cs gamma emission, accumulating around 80 mC/cm^2 with detectors operated with recirculating gas fraction higher than 90%.

Detectors response was found to be stable along the entire duration of the test, regardless of the gas recirculating fraction and the background radiation rate. Moreover, during the irradiation campaign the action of the Purifier module for removing and stabilizing H_2O and O_2 concentration in the recirculating gas system was validated. Triple-GEM detectors exposed to radiation when operated in Ar/CO_2 gas mixture were also studied with the SEM technique, observing the GEM foils holes morphology after irradiation. It was found that a fraction of the GEM holes results to be damaged, with smudged outlines and distorted shapes. However, given the results of the long-term irradiation test, the damages to these holes are not sufficient to compromise amplification capabilities of the GEM foil.

Triple-GEMs Muon detection efficiency was also studied at the GIF++ facility, during a Test Beam campaign, operating the gas system both in open mode and with gas recirculation (90% recirculating fraction). The obtained results show how the operation of Triple-GEM detectors is equivalent in the two different gas system modes, thanks to the action of the Purifier module. The detector under study could reach the maximum efficiency for both Ar/CO_2 70/30 and $Ar/CO_2/CF_4$ 45/15/40 gas mixtures with 90% gas recirculation. Furthermore, it was seen how Triple-GEM detectors efficiency is not significantly compromised by high-rate gamma background.

Finally, Fluoride impurities production in CF_4-based mixture was studied for Triple-GEMs operated in high-radiation rate environments, at the GIF++ facility with 10×10 cm^2 detectors prototypes and in the LHCb experiment during Triple-GEMs operation of LHC Run 2. The production process characterization showed how the CF_4 content does not particularly affect the F^- production rate, at least for concentrations below 50%, and how a higher input gas flow rate contributes to the decrease of Fluoride produced in the chamber volume. Moreover, it was showed how both detectors electric field and irradiation intensity contribute to an increase in the Fluoride ion production, finding the same effect also in the LHCb experiment measurements. Lastly, the equivalence of operation with the gas system in open mode and in gas recirculation mode in relation to Fluoride impurities was verified in the GIF++ setup as well as in the LHCb full size gas system. It was found that the standard LHC Purifier module is capable of trapping Fluoride ions produced in the detector volume, that are therefore not carried by the re-injected gas mixture.

Chapter 4

LHC Gas Recuperation Systems

As illustrated in Chapter 2, the operation of LHC Experiments gaseous detectors systems require the use of different gases, some of which are classified as Greenhouse Gases (GHG). Many of the LHC gas systems are operated with gas recirculation, which allows to re-use a great fraction of the gas mixture by re-injecting it in the system, after purification processes (Section 2.3). Nevertheless, recirculating the 100% of the gas mixture is currently not feasible for most of the systems, and the gas recirculating fraction have to be limited around the 90%. In fact, a 10% of the total gas volume needs to be continuously injected from fresh supply, for example to guarantee the required gas mixture purity or to compensate gas system and detectors leaks. Moreover, even in systems that are are operated with higher recirculating fractions, a great amount of gas needs sometimes to be exhaust from the gas system, due to gas mixture changes or detector maintenance works. Taking these factors into account, the main consequence on LHC gas systems operation is that there is in some cases a given volume of gas mixture that has to be exhaust to air, implying the emission of Greenhouse gases in the atmosphere.

One of the possible strategies for reducing GHG emissions is the gas recuperation process, already in use in some LHC gas systems. The process consists in the separation of the gas mixture components, with the purpose of recuperating the most valuable ones at a good purity level. The final product can then be re-used in the gas system, allowing to limit both GHG emissions and the original consumption of fresh gases. Nevertheless, recuperation plants introduce additional complexity in the gas systems and impose the need of a continuous gas mixture monitoring. Moreover, given the diversity of the possible gas mixtures used for LHC gaseous detectors, dedicated R&D studies are necessary to optimize recuperation plants for every specific case. The work presented in this thesis mainly focuses on the recuperation of two Freon gases used in LHC Experiments gaseous detectors, Tetrafluoromethane (CF_4 or R14) and 1,1,1,2-Tetrafluoroethane ($C_2H_2F_4$ or R134a), which are both Greenhouse gases, with a Global Warming Potential of 7390 and 1430 respectively.

Different gaseous detectors at the LHC Experiments make use of CF_4, such as Multi Wire Proportional Chambers (MWPCs), Cathode Strip Chambers (CSCs) and, as illustrated in Chapter 2, Triple-GEM detectors. CF_4 is added in a given fraction to the gas mixture for different purposes, such as the cleaning of wires impurities or the improvement of time resolution. CF_4 is also used as major component in the gas mixture of one of the two Ring Imaging CHerenkov (RICH) detectors installed in the LHCb experiment, thanks to its low dispersion and refractive index. Though these detectors gas systems are operated with gas recirculation, CF_4 recuperation is a key step to further limit its emission in the atmosphere. A good method to separate and recuperate CF_4 is represented by the selective membranes technique, that allows to

separate CF_4 from other gas mixture components, obtaining a product with sufficiently high purity. The selective membranes separation technique is described in the first section of the Chapter, with focus on the specific case of CF_4 separation. The characterization of the separation membranes chosen for the LHC recuperation system is also briefly illustrated.

The LHCb RICH2 detector is operated during physics runs with a gas mixture composed by the 92% of CF_4, while the remaining 8% is CO_2. The mixture fills the 100 m^3 detector volume, and during operation the only gas emission comes from the purifier module regeneration procedure and from the gas system exhaust when detector pressure needs to be adjusted. However, a major gas emission would have occurred during the LHC LS2, when it was planned to fill the detector volume with 100% CO_2 to allow system maintenance, and then to re-fill it with the CF_4/CO_2 92/8 gas mixture before Run 3. A separation membrane module was present in the RICH2 gas system, included in the original design as a N_2 separation module, never put into operation. The module was hence repurposed as a CF_4 recuperation plant, to be used in the emptying procedure during the LHC LS2. This Chapter will illustrate the plant design, the characterization and optimization of the recuperation process realized during the LS2, when all the CF_4 content was replaced by CO_2. An overview of the gas recuperation plant upgrades realized after the emptying procedure is also given, put in place to improve the recuperation performance for the CF_4 filling procedure to be done before Run 3 and also for the future standard operation of the gas system during physics runs.

The selective membrane separation technique is also used in the CF_4 recuperation plant of the CSC detectors system of the CMS Experiment. The CSC gas system is indeed operated with 90% gas recirculation, as it requires a constant injection of 10% of fresh gas mixture to compensate N_2 intake from the detector volume, that would accumulate in the system in too high concentration. Operational since 2012, the recuperation plant allows to separate CF_4 from the other components present in the CSC gas mixture, $Ar/CO_2/CF_4$ in fractions 40/50/10. In this case, the selective membranes are used in combination with others gas purification techniques, obtaining as final product good quality CF_4, only polluted with small quantities of Ar and N_2. The CF_4 recuperation plant is described in the following Chapter, with particular focus on the re-injection of recuperated CF_4 in the CSC gas system, brought to operation at design conditions in 2018. The aim of the plant is indeed to have continuous CF_4 recuperation from the gas system exhaust, and in parallel a continuous injection of half fresh and half recuperated gas over the total CF_4 volume required to keep the system operational with 90% gas recirculation. The CF_4 re-injection process is also described in relation to the Single Wire Proportional Chambers (SWPCs) monitoring system operational on the CSC gas system, which allows to monitor the mixer injection, guaranteeing the quality and stability of the mixture obtained from recuperated CF_4.

The second portion of the Chapter is dedicated to the recuperation of $C_2H_2F_4$, hereafter called R134a. It is used as major component of the gas mixture of Resistive Plate Chambers (RPCs), operational in the Muon Systems of the ALICE, ATLAS and CMS Experiments since Run 1. With slight variations on the precise concentration values, R134a is always present in the RPC gas mixture for at least the 90%, in combination with iC_4H_{10} and SF_6. It is hence fundamental to limit R134a emission, in particular given the high volume of the RPC detectors systems and therefore of the

gas mixture volume needed for the gas system. While R&D studies are ongoing to find more environmental friendly gas mixtures [52], for the RPCs gas systems currently in operation the way of gas recuperation is pursued. A prototype of R134a recuperation system was put in operation in 2018, with the aim of separating R134a from the other components of the exhaust RPC mixture and possible impurities, to be able to re-use it in the mixer module in place of the fresh gas. The Chapter will illustrate the design, working principle and developments of the R134a recuperation plant. The discussion will firstly focus on the characteristics of the mixture itself which presents some major challenges for what concerns the separation process, as the couple R134a/iC_4H_{10} shows an azeotropic point in its vapor-liquid phase transition. The various steps of the plant development will be illustrated, together with the tests preformed on the plant to make it ready for the final commissioning and realization in the different Experiments.

4.1 CF_4 Recuperation with selective membranes

This section will describe the technique of CF_4 separation used for the LHCb RICH2 and CMS CSC recuperation plants. A generic description of separation membranes working principle will be given, followed by specific details on their operation for CF_4 separation. An overview will also be given on the characterization of the UBE separation membranes, the specific type selected for the LHC CF_4 recuperation plants.

4.1.1 Selective membranes separation

The separation of two substances which would spontaneously mix can be accomplished via different methods and with different devices, and it is always based on the consumption of a given amount of some form of energy ([81], [82]). Two substances would spontaneously mix if the free enthalpy of the mixture is smaller than the sum of the free enthalpies of the two single pure substances. Therefore, the separation of the two components would require an amount of energy equal or larger than the free enthalpy of the mix. Different separation techniques require different amounts of energy, in general much larger than the minimum required value. Differently from the processes which involve a phase transition (distillation, freezing), membrane processes such as reverse osmosis and electrodialysis require a lower amount of energy, as no heat or vaporization has to be supplied, and therefore can be more advantageous in terms of technical and economical feasibility. Membrane technology is also particularly convenient as it can be carried out continuously, it can be easily scaled-up, and it can be combined with others separation processes when necessary. On the other hand, membranes lifetime could be relatively short and the up-scaling factor of the process can only be linear. Among others means of membrane classification, a useful one can be to discriminate them depending on their morphology or structure, as it determines the separation mechanism and therefore their application. Considering solid synthetic membranes, the most common ones, they can be classified according to the symmetry of their structure and, as a sub-classification, according to their thickness (10-200 μm) that determines the final resistance to mass transfer of the membrane.

Membrane processes are in general characterized by a feed stream which is then divided into two parts, a retentate steam and a permeate stream, with either the retentate or the permeate being the final product of the separation. Though different

membrane processes exists, the common element is the membrane itself, which represents the selective barrier between two phases. The separation is achieved thanks to the ability of the membrane to transport a given component from the feed mixture more readily than the others, because of differences in the physical or chemical properties between the membrane and the permeating component. A schematic representation of the basic process and the membrane action is reported in Figure 4.1.

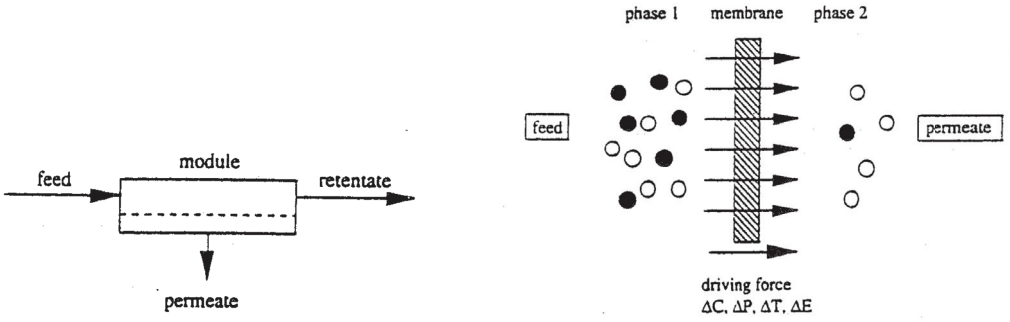

FIGURE 4.1: Schematic representation of the membrane working principle (left) and the membrane element acting on a two-phase mixture (right) [81].

The membrane design and the separation driving force are the main factors determining the flux and the selectivity of the process. The flux, also referred to as permeation rate, is defined as the volume flowing through the membrane per unit area and time, given under standard conditions (STP) when the process involves gas mixtures. The driving force of the separation process could be a gradient in concentration, pressure, temperature or electrical potential, and it is normally proportional to the permeation rate through the membrane. The membrane selectivity can be expressed with the separation (α) factor, normally used for gaseous components and defined as:

$$\alpha = \frac{y_A / y_B}{x_A / x_B}$$

where y_i are the concentrations of the components in the permeate stream and x_i are the concentrations of the components in the feed stream, expressed either in mass concentration or molar concentration. The separation factor hence quantifies the ability of the membrane to separate the species A from the species B, as it reflects the modification of permeate stream concentrations with respect to the feed stream. For α=1 no separation occurs, and the higher is its value the better is the separation result.

The most common separation force used for membrane processes is hydrostatic pressure. Depending on the size of the molecules involved, the separation can be defined as microfiltration (diameter $>$ 100 nm), ultrafiltration (macromolecules with molecular weights in the range 10^4-10^6), nanofiltration and finally reverse osmosis for low molecular weight components of approximately similar sizes. From microfiltration to reverse osmosis, a progressively higher driving force is necessary. However, while better separation can be achieved with a higher pressure gradient, the stream flux through the membrane becomes lower and the size of retained molecules

smaller. For the specific case of gas separation, which will be the topic of the following sections, the membrane process is normally based on dense membranes materials where transport takes place via diffusion. Such processes are commonly used in industry for hydrogen recovery, separation of air (O_2/N_2), methane and carbon dioxide. The following paragraph will discuss the separation mechanism for the type of membrane chosen for CF_4 separation, which is normally not included in standard industrial separation processes.

4.1.2 CF_4 separation with selective membranes

The membrane chosen for the CF_4 separation processes at the LHC recuperation plants is based on selective gas permeation via diffusion, as most of the membranes for gas separation. In particular, the membranes used in the recuperation plants described in the following sections are commercially available separation membranes from UBE Industries [83]. The choice was based on the fact that, in the use cases of LHC gas recuperation plants, CF_4 needs to be extracted from $Ar/CO_2/CF_4$ or CF_4/CO_2 gas mixtures, and the UBE membranes are specifically designed for CO_2 separation. Though Argon can also be present in the gas mixture from which CF_4 needs to be extracted, CO_2 represents the most difficult component to separate as the two molecules have more similar characteristics. CO_2 is by design efficiently separated by the UBE membrane in the permeate stream, with the remaining components flowing in the retentate stream at a good purity level.

The UBE separation membrane is a hollow fiber membrane (HFM) made of capillaries of aromatic polyamide, with an asymmetrical dense-porous structure, achieved thanks to the different length of the polymer chain with variable porosity along the cross-section of the capillary. The separation is in this case driven by hydrostatic pressure difference, as different species would exert different partial pressures at the two sides of the membrane wall. Capillaries are arranged in a bundle, housed in a case module where gas inlet and outlets are located. The arrangement of the membrane material in capillary straws allows to maximize the material surface that can interact with the feed gas mixture, increasing the membrane selectivity. Figure 4.2 reports a picture of the internal section of the membrane and the case module.

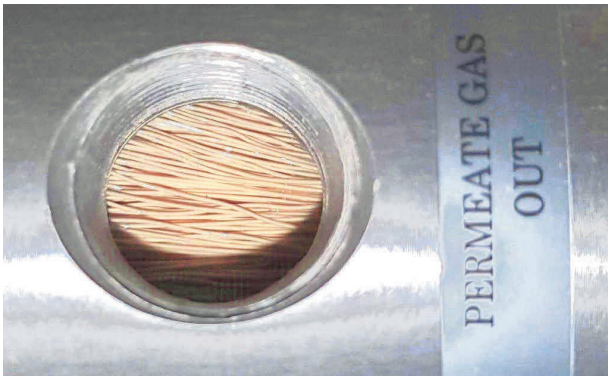

FIGURE 4.2: Picture of the UBE membrane section, with the bundle of straws visible inside the membrane case.

To illustrate the CF_4 separation principle, it will be now discussed for simplicity the two-component separation, i.e. the separation case of CF_4/CO_2 gas mixture. When the gas mixture is introduced into the membrane (feed stream), the CO_2 molecules

easily diffuse through the membrane material, thanks to the partial pressure difference between the two sides of the membrane, helped by a pump which allows to create a higher pressure gradient. The retained component, CF_4, keeps flowing through the straws and is let out of the membrane body. A schematic representation of the process is shown in Figure 4.3.

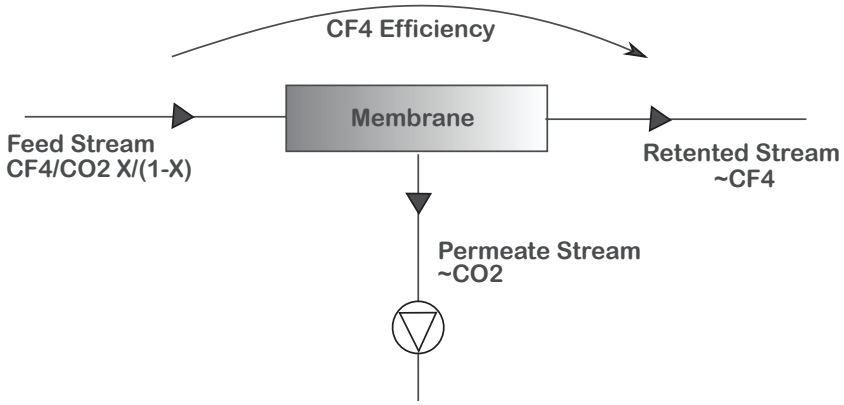

FIGURE 4.3: Separation process for the CF_4/CO_2 gas mixture.

In an ideal separation process, all the CO_2 molecules present in the feed mixture would permeate the membrane walls, while all the CF_4 molecules would flow at the retentate output of the membrane. Given the non-ideal nature of the separation process, separation membranes have limitations in their performance, which can be tuned through the accessible parameters depending on the requirements on the separation product. For this specific case, while on one hand it is crucial that the retained gas contains the highest possible CF_4 fraction, it is also fundamental that the fewer possible CF_4 volume leaves the membrane through the permeated flow. For example, one could have very pure CF_4 in the retented gas fraction, but then such fraction could contain only half of the total CF_4 present in the input, while the other half would be lost in the permeate stream. Therefore, a balance should be found between having very pure recuperated CF_4 and recuperating a gas volume that is high enough to make the process worth the costs and efforts.

To tune the balance of the process requirements, membrane performance is evaluated with two parameters: recovered gas quality and CF_4 separation efficiency. The recuperated gas quality is simply expressed with the CF_4 concentration in the gas volume of the retentate stream. The CF_4 separation efficiency is defined as follows:

$$\epsilon(CF_4) = \frac{volume(CF_4^{Output})}{volume(CF_4^{Input})}$$

where the output is here the retentate gas stream. It should be considered that CF_4 separation efficiency depends on different factors, such as the input gas pressure, the feed flow rate and mixture composition. For example, for the same type of membrane different versions are produced, each specifically developed to work with a given input flow rate, in way to optimize the separation for such flow range. For this reason, different studies were realized to characterize the UBE membranes to maximize their performance in the LHC CF_4 recuperation plants.

4.1.3 Membranes performance characterization

The studies on UBE separation membranes started back in 2010, when the first CF_4 recuperation plant was designed and prototyped for the CMS CSC gas system [84] [85]. More tests were realized in 2019, before the LHCb RICH2 recuperation plant was put into operation, and finally a last characterization was realized in 2020, in view of possible upgrades of the CSC plant. Moreover, in 2019 an upgraded version of the UBE membrane with increased selectivity has become commercially available. This section will illustrate a brief summary of all these studies, to give an overview on the UBE membranes general performance, in relation to different operation parameters.

In all the reported tests, the membrane characterization was realized with the membrane installed in custom-made systems where all the parameters can be tuned and measured. Gas flow rates can be regulated with rotameters or Mass Flow Controllers, and measured with these same devices, or alternatively with Mass Flow Meters or Flow Calibrator devices (MesaLab DryCal [86]). Pressure regulators allow to fix the pressure values of the membrane input and the permeate pump output, and pressure values in different points are measured with pressure sensors. Finally, the gas mixture concentration at the input and outputs of the membrane is measured using a Gas-Chromatograph (Section 2.3.1) that allows to determine the concentration of the different components and impurities (O_2, N_2) in the gas streams.

It is here reported the characterization of five different UBE membranes, which nomenclature and specifications are reported in Table 4.1. The *old test* [84] membrane is one the ones tested back in 2010 for designing the CSC plant, and that was finally chosen among other types available at the time as the most suitable for the purpose. The same type of membrane was therefore installed in the final CSC plant and afterwards also on the LHCb plant. The membranes *old@CMS* [87] and *old@LHCb* are therefore of the same type as the original one, but characterized after some years from their installation, and after some years of active operation for the CMS one. The *new@CMS* [87] is the version of the original membrane that is currently available on the market, which UBE Industries declares having slight modifications on the internal structure with respect to the previous one, and it was tested brand new. Finally, the *high selectivity* [87] membrane is the latest upgrades of the original model, made available in 2019 from UBE, and it should have improved separation power.

Label	Name	Model	Feed gas mixture
A	old test	E type	$Ar/CO_2/CF_4$ 40/50/10
B	old@LHCb	CO-C10A	CO_2/CF_4 40/60
C	old@CMS	CO-C10A	$Ar/CO_2/CF_4$ 40/55/5
D	new@CMS	CO-C10	$Ar/CO_2/CF_4$ 40/55/5
E	high selectivity	CO-C7FS	$Ar/CO_2/CF_4$ 40/55/5

TABLE 4.1: Details of the UBE membranes which characterization is reported in this section.

It should be taken into account that, as indicated in Table 4.1, the tests were realized with different feed gas mixture, depending on the requirements of the system and the mixture available at the time of the test. The results of the characterization will be given in terms of the same parameters for all membranes, but it should

be remembered that they could vary also depending on the feed stream composition. Nevertheless, in all the tests the chosen mixture was always kept constant. The implications of variations in the input gas mixture will be discussed in the Section dedicated to the RICH2 CF_4 recuperation plant, as in that case it becomes relevant for the plant operation.

One of the most relevant parameters that determines separation performance is the volume rate of the membrane feed stream. Figure 4.4 reports the trend of the CF_4 separation efficiency, defined as the ratio between the CF_4 volume in the retentate stream and the total CF_4 volume in the feed stream, as a function of the membrane input gas flow rate. All the membranes are showing an efficiency higher than 90% in separating CF_4 from the rest of the mixture, with membrane A showing a markedly lower efficiency due to its older technology. The membranes C, D and E are tested for lower flows, and they show a very high efficiency for increasing flows, with membrane E keeping basically a constant efficiency of the 100%. Though membrane B shows a slight lower efficiency, it is however well above the acceptable level for the recuperation plant operation.

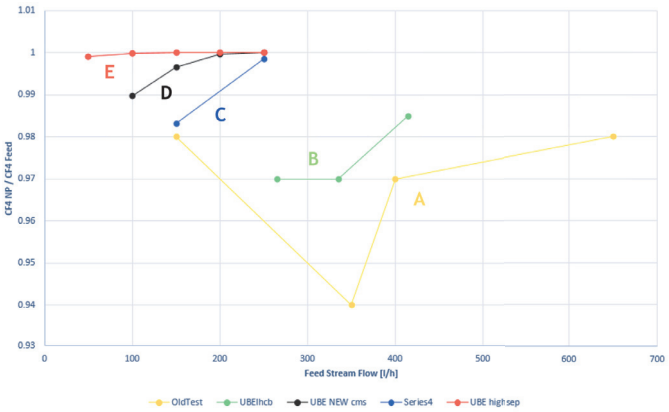

FIGURE 4.4: Trends of the membranes CF_4 separation efficiency, defined as the ratio between the CF_4 volume in the retentate stream and the total CF_4 volume in the feed stream. [84] [87]

Figure 4.5 reports the trends of the CO_2 fraction that is carried into the non permeate stream. The first relevant conclusion is that such value is always assessed below the 5% of the total CO_2 volume in the feed stream, meaning that most of the CO_2 can easily be removed by the membrane in the permeate stream. However, especially for the older membranes operated with higher flows, such value tends to increase, while for the other membranes it stays very close to zero.

The membranes were also tested concerning their performance in removing N_2 from the retented gas stream. Figure 4.6 shows the trend of the fraction of N_2 passed in the retentate stream with respect to the total quantity in the feed stream, as a function of the feed volume stream. What can be concluded from the obtained results is that in general the increase of the feed volume flow causes an increase of the N_2 fraction carried in the retentate stream. It can be noticed that among the tested membranes, the one that shows higher values of transferred N_2 is the membrane E, the high selectivity one. This can be explained taking into account that the design improvement of this membrane was directed towards improving the separation and purity of CO_2 into the permeate stream, therefore losing out on the retentate stream composition.

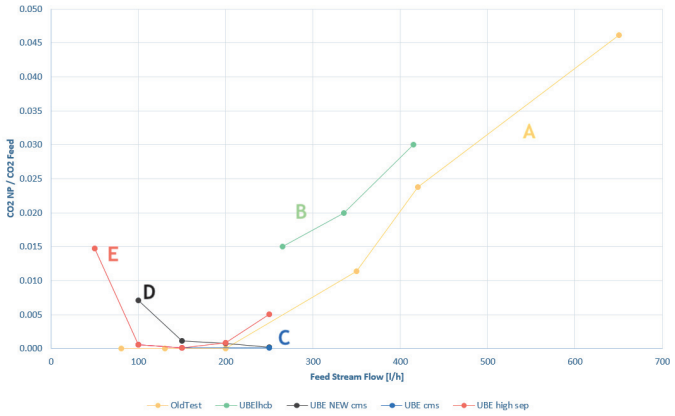

FIGURE 4.5: Trend of the CO_2 fraction carried into the non permeate stream with respect to the CO_2 feed stream content. [84] [87]

Nevertheless, it should be considered that even if only a 60%-70% of N_2 is removed from the retentate stream, the order of magnitude of its concentration is typically around the 1%, therefore already low enough to have an acceptable purity level of the recuperated gas.

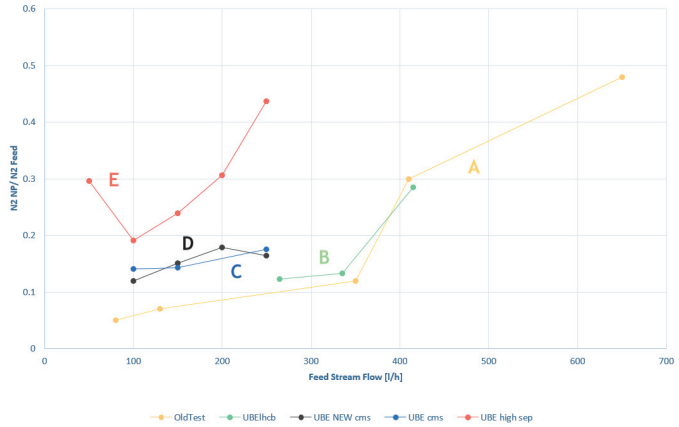

FIGURE 4.6: Trend of the fraction of N_2 passed in the retentate stream with respect to the total quantity in the feed stream, as a function of the feed volume stream. [84] [87]

4.2 LHCb RICH2 CF_4 Recuperation

The LHCb Experiment makes use of Ring Imaging Cherenkov (RICH) detectors to achieve particle identification, in particular to distinguish between pions and kaons in a variety of final states, a fundamental feature to have meaningful CP-violation measurements. The only feasible technique that can cover the required momentum range (1–150 GeV/c) is the detection of Cherenkov light produced by the passage of charged particles through radiators [88]. In particular, the RICH2 section of the LHCb spectrometer, its location visible in Figure 4.7, is designed to analyze the high-momentum tracks which will traverse the magnet. Figure 4.8 reports a

schematic representation of the working principle of RICH detectors and the geometrical layout of the LHCb RICH2 detector, where the presence of a secondary flat mirror allows to reduce the focal length reflecting the spherical mirror image onto the detector plane.

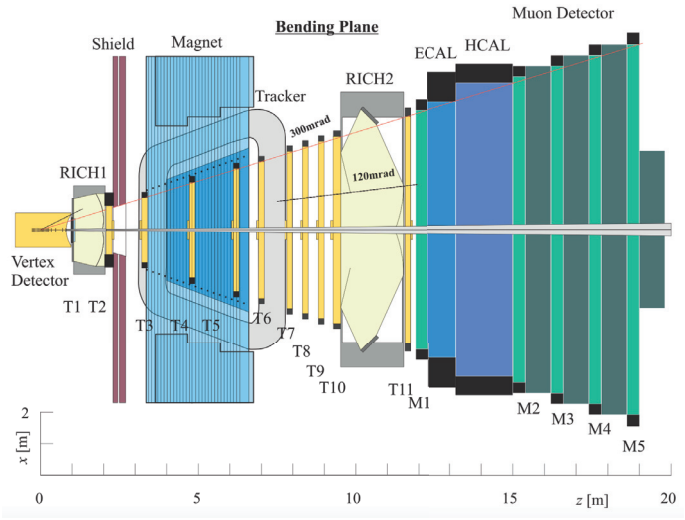

FIGURE 4.7: The LHCb spectrometer seen from above, showing the location of the RICH2 detector. [88]

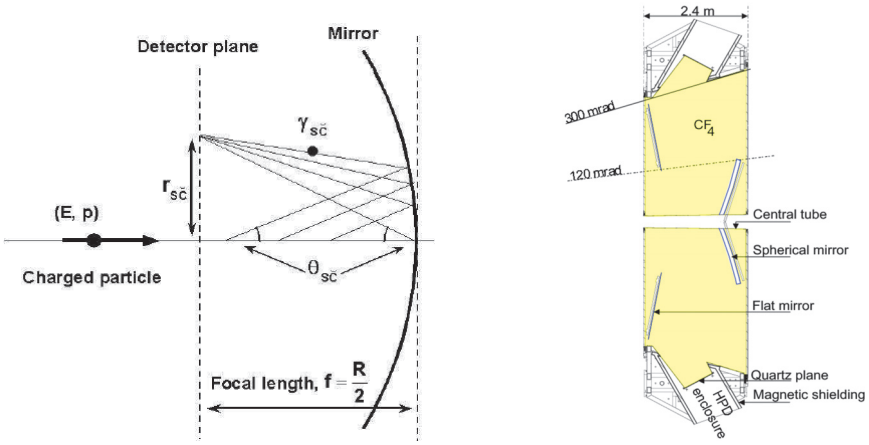

FIGURE 4.8: Schematic representation of the working principle of RICH detectors (left) and layout of the RICH 2 detector (right). [88]

To satisfy the RICH2 detector requirements, it is necessary to fill the volume with a gas with low refractive index, in way to have a reduced yield of Cherenkov photons for a given radiator length. Therefore, CF_4 was chosen as main component of the RICH2 gas mixture, thanks to its low dispersion and refractive index. About 8% of CO_2 was added to CF_4 in order to quench possible scintillation. The detector consists in a vessel with dimensions approximately $7\times7\times2$ m^3, resulting in a total detector volume of approximately 100 m^3, to be filled with CF_4-based gas mixture. Given the high GWP of CF_4 (7390) and its relatively high cost, the gas mixture is recirculated in a closed loop system, with a gas recirculating fraction of almost 100%.

To keep the photon absorption at an acceptable level, the H_2O and O_2 impurities are limited to about 100-200 ppm thanks to the Purifier module.

Since the beginning of Run 1 the RICH2 has been operated with CF_4/CO_2 92/8, but during the LHC LS2 it was filled with 100% CO_2, to allow maintenance operations. It was therefore emptied of CF_4-mixture, and to be sure that the 100 m^3 detector volume was re-filled with the correct gas mixture, it had been necessary to flush the gas system in open mode with a gas volume equivalent to at least four detector volumes exchanges, meaning that a large quantity of CF_4 would be exhausted to the atmosphere. The aim of the CF_4 recovery plant is therefore to intervene on the exhaust gas mixture in way to extract good quality CF_4 to be stored and reused at necessity, avoiding its emission.

4.2.1 Recuperation Setup

The RICH2 CF_4 recuperation system, already present in the original gas system design as N_2 separation module, is added to the standard LHC gas system configuration. It includes a dedicated membrane module, the standard Purifier module and a custom-made compressor module. A schematic drawing of the system is reported in Figure 4.9. The three relevant modules are reported in the context of the entire RICH2 gas system.

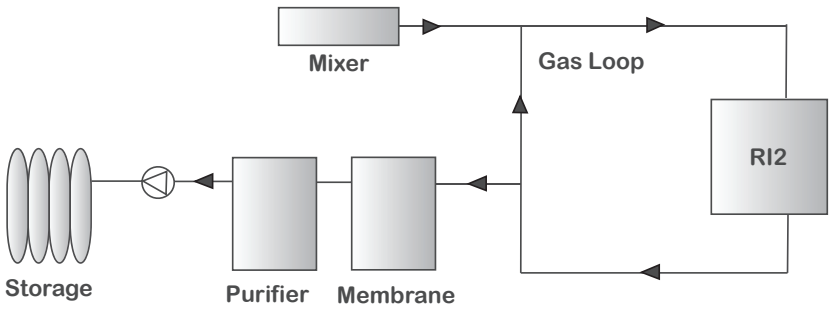

FIGURE 4.9: Schematic view of the CF_4 recovery plant in the context of the LHCb RICH2 closed loop gas system.

The main phase of the CF_4 separation from the CO_2 and the possible N_2 contamination is realized with the membrane module. The membrane module includes two separation membranes (hereafter called M1 and M2). Its design is reported in the schematic representation of Figure 4.10. The membrane module input comes from the closed loop return line, with the same pressure of the gas system (0.4-0.8 mbar) and a total volume flow that can be manually regulated thanks to a bypass of the module itself. The module can be operated in the following configurations:

- *Single membrane*: the feed gas is sent only through M1, the retained fraction is sent to storage while the permeate is sent to exhaust.
- *Double membrane*: the feed is sent to M1, the permeate fraction from M1 is sent as input into M2, which permeate stream is sent to exhaust while the retained fraction is sent to storage together with retained from M1.

- *Double membrane with re-injection*: the feed is sent to M1, the permeate fraction from M1 is sent as input into M2, the M2 permeate fraction is sent to exhaust while the M2 retained fraction is sent back as input of M1 for a further grade of purification.

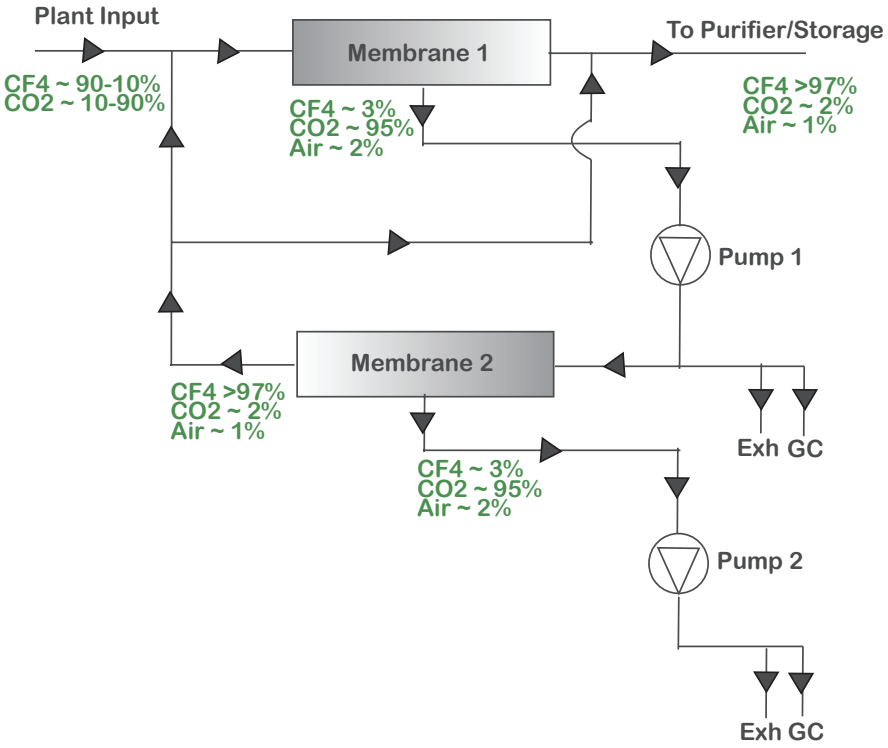

FIGURE 4.10: Schematic drawing of the membrane module configuration. The different operation configurations can be traced following the arrows representing the gas stream direction.

Depending on the operation conditions of the module, the optimal configuration is used. Figure 4.10 also shows the position of the two pumps, to extract the permeate gas flow from each of the two membranes. As knowing the gas mixture composition in each part of the plant is crucial for a good understanding of recuperation efficiency, sampling gas points are placed in relevant locations of the module. The sampled gas is sent to a Gas-Chromatograph (Section 2.3.1), that allows to measure the concentration of each gas component in the mixture.

The Purifier module is normally used within the closed loop for standard operation, to allow the removal of impurities before the re-injection in the system. As the Purifier material (MolSieve 5Å) designed for H_2O adsorption can also trap CO_2 molecules when in low concentration, during recuperation the Purifier can be placed after the membrane module to obtain a further grade of purification of the extracted CF_4. As a matter of fact, the gas mixture at the output of the membrane module has a CF_4 concentration always higher than 97%, meaning that a maximum of 3% of CO_2 is left at that stage. Such CO_2 concentration in low enough to be trapped by the Purifier module without it reaching saturation, yielding to a final CO_2 concentration <0.05%. As last stage, the compressor module serves to compress and put into storage batteries the recuperated gas. In particular, the standard compressor module

configuration was here modified with a loop around the compressor with a buffer volume. The compressor can indeed operate only within a given range of input gas pressure, which is guaranteed by the presence of the loop and the upstream buffer.

A set of sensors completes the setup, allowing continuous remote monitoring of operation. In particular, Mass Flow Meters (MFMs) are installed at the input and outputs of the membranes, allowing to measure the gas flow rate. Pressure sensors are placed at different relevant points of the setup (membranes input/output, before pump, purifier, compressor input/output, storage battery).

4.2.2 CF_4 Recuperation Process at the beginning of LS2

The first phase of operation of the RICH2 CF_4 recuperation plant was realized during the Long Shutdown 2 (LS2). At the end of Run 2 (2018), the RICH2 100 m^3 volume was full of standard gas mixture (CF_4/CO_2 92/8), therefore with 92 m^3 of CF_4 available to be recovered. The aim of this phase was to avoid to empty the detector volume from CF_4 sending it to exhaust in the atmosphere, but to recuperate it and put it in storage for the future detector filling.

Nevertheless, the stop of the gas system during the end-of-year break caused the loss of about 25 m^3 of CF_4 because of the backup mechanism used to keep the detector pressure stable. The gas system is indeed designed to keep constant the detector pressure also when it is not in operation, adapting to the changes in atmospheric pressure. When the atmospheric pressure increases, the gas system pressure decreases, and a regulated CO_2 backup system injects the necessary gas volume to restore the original detector pressure. On the other hand, when the atmospheric pressure decreases, the gas system pressure increases, therefore a bubbler allows the elimination of part of the gas volume contained in the detector to compensate. The continuous alternation of these two processes, with significant changes in the atmospheric pressure due to winter weather, yielded to the emission of more than 25 m^3 of gas mixture (CF_4/CO_2 92/8) from the bubbler, and the injection of an equivalent volume of CO_2. As a result, at the moment of the re-start of the RICH2 gas system in closed loop, the gas mixture composition in the detector volume was measured to be around CF_4/CO_2 60/40, with only 60 m^3 of CF_4 available for recuperation.

The CF_4 recuperation plant operation started in June 2019 and it was carried on until October 2019, after an initial period of tuning of the system parameters to optimize the system operation. Given the working conditions of the membrane module, it was decided to operate in single membrane configuration. During the recuperation period, the plant has been operational for about 500 hours over about four months. The plant could not indeed work in a continuous mode, given the need of attentive monitoring of operation parameters and recuperation efficiency, and it was therefore only put into operation during working hours.

The volume of recuperated CF_4 was monitored with the gas flow rate at the output of the membrane module as well as with the gas volume accumulated in the storage battery, measured with a dedicated pressure sensor. The trend of accumulated CF_4 volume is reported in Figure 4.11 for the two measured variables. It can be noticed that while at the beginning the two values match, after a certain point the gas volume measured in the storage battery is lower than what is measured at the output of the membrane module. Such difference is given by gas leaks developed between the

membrane module and the battery (purifier, gas lines, compressor). This caused a first gap between the two values, which however remains constant in the following period thanks to an almost complete repair of the leaks. The effective recuperated CF_4 available for future usage is the one calculated from the storage battery volume, for a total of 28.5 m^3 at the end of operation, with CO_2/N_2 contamination <1%.

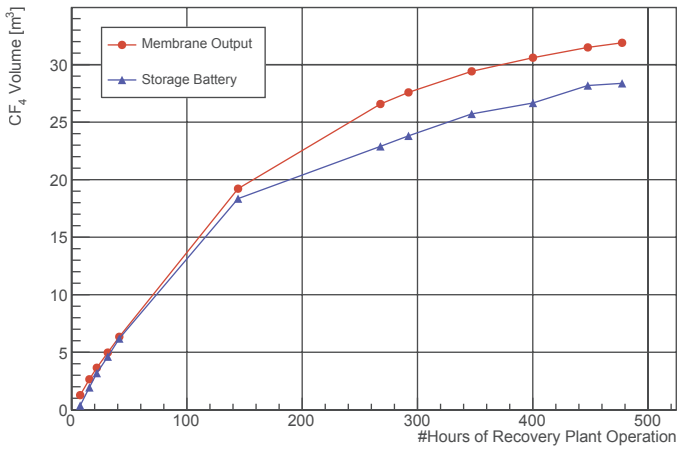

FIGURE 4.11: Recuperated CF_4 volume trend, calculated with membrane output flow and with storage battery pressure.

The average efficiency of the recuperation plant can be calculated as the ratio between the stored CF_4 volume and the total CF_4 available at the start of operation. However, to the total initial volume of CF_4 it should be subtracted the 7% of CF_4 (7 m^3) left in the detector volume at the end of operation, interrupted due to the decrease of separation efficiency, and the 15 m^3 lost during an incident with underground detector pipes. The plant effective efficiency is hence found to be around the 65%, as an average value over the full recuperation process.

Nevertheless, as mentioned in the previous section, separation membrane efficiency depends on different factors, one of these being the input gas mixture composition. Such dependence was clearly seen during the RICH2 recuperation process. As a matter of fact, when the gas mixture is extracted from the detector volume to undergo the recovery process, the detector pressure is compensated injecting pure CO_2 from the mixer module. This progressively modifies the gas composition in the detector volume, increasing the concentration of CO_2, that in turn also increases in concentration at the input of the membrane module. The plot reported in Figure 4.12 shows the trend of the CF_4 membrane efficiency together with the trend of CF_4 concentration at the input of the membrane module along the time period of recuperation. It can be seen how the two are progressing in parallel, as the efficiency decrease is indeed caused by the decrease of input CF_4 concentration, for operation with constant pressure and volume flow rate.

It can be seen how the separation efficiency spans from 90% down to about 50% when the input CF_4 concentration is lower than 20%. The average of these values, weighted by the gas volume accumulated at each point, gives a 70% efficiency for the membrane module. Taking into account the 10% loss reported in Figure 4.11, a 65% efficiency of the overall process is obtained, the same value obtained from the

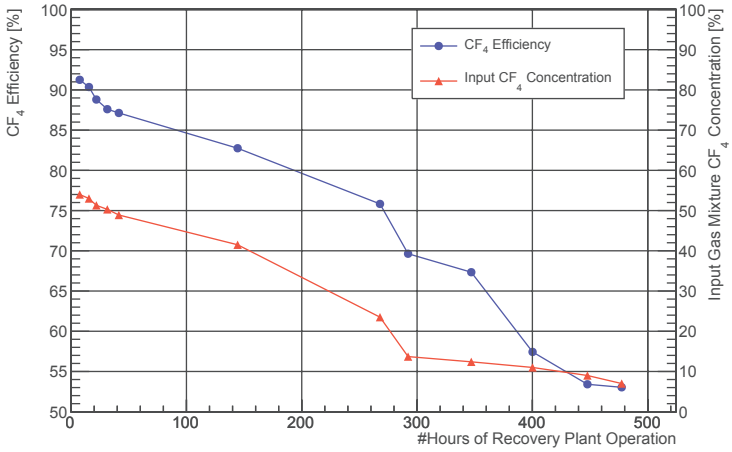

FIGURE 4.12: Trend of CF_4 recuperation efficiency (left axis) and of CF_4 concentration at the input of the membrane module (right axis).

calculation of the previous paragraph based on the CF_4 recuperated volume. What can be concluded from the last plot is that, considering that the recovery operation started with an input gas mixture of CF_4/CO_2 60/40, the gas fraction lost during the end-of-year stop would have been recuperated with very high efficiency (>90%), increasing the overall operation efficiency.

As next step, the recuperated CF_4 volume will be used for the re-fill of the RICH2 before Run 3, limiting the consumption of fresh CF_4. Since to completely change the 100% CO_2 detector volume and reach the correct CF_4/CO_2 92/8 gas mixture it will be necessary to run the gas system in open loop, the recuperation plant will be put back in operation to avoid the emission of the detector exhaust gas flow, which will contain more and more CF_4 until reaching the requested 92%.

4.2.3 CF_4 Recuperation Plant Upgrades

After the recuperation run realized to empty the RICH2 volume after the end of Run 2, a set of upgrades and modifications to the membrane module and the general gas system were planned, thanks to the experience gained with the first operation of the plant. The upgrades have the double aim of improving the CF_4 recuperation process for the detector filling before Run 3, as well as to take advantage of the recuperation setup also during the standard physics run operation.

As mentioned in the previous section, the first recuperation run was realized operating the membrane module in single membrane configuration. The most relevant upgrade to the module was a set of modifications done to efficiently operate it with the double membrane configuration. In particular, at the restart of operation, it could be advantageous to re-inject the M1 permeate flow into M2, which would contain a significant CF_4 volume when the plant input has a high CO_2 concentration, due to the efficiency variations depending on gas mixture composition. To have such configuration operational, the M2 retentate output is merged with the one of M1, and it is therefore necessary to have compatible pressures of the two streams. Such condition is achieved with the installation of new pressure sensors and non-return valves in the critical points of the gas path, plus the installation of a bypass to regulate the

action of the pump on the M2 permeate stream. The modifications on the module and the double membrane operation gas path are reported in the scheme of Figure 4.13. Another key modification of the membrane module was the installation of a flow regulation automatic valve (Emerson ASCO Series [89]) on the bypass line of the module, in place of the previous on/off manual valve. Thanks to this upgrade, it will be possible to precisely regulate and keep stable the gas flow sent to the module.

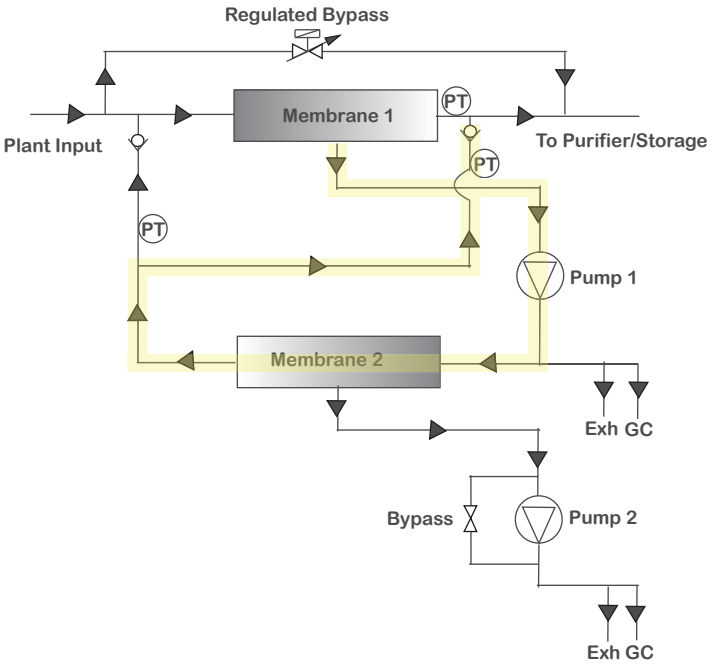

FIGURE 4.13: Schematic drawing of the membrane module, with the newly installed elements and the double membrane configuration gas path highlighted in yellow.

The compressor module realized for the CF_4 recuperation plant is only used during emptying-filling procedures, i.e. when the RICH2 gas system is off during shutdowns. Therefore, it was decided to exploit it during normal operation to limit the emission of CF_4/CO_2 gas mixture from the Purifier module and the gas system exhaust. As in these points the gas mixture comes from the operating chamber, it is already in the correct composition and it is not necessary to use the membrane module as the mixture can directly be re-used as it is. When a purifier cartridge needs to be regenerated, it is normally put under vacuum before flushing and heating it to properly regenerate the material. To create vacuum, an external pump extracts the gas mixture from the column and exhaust it to air. Taking into account a year of run operation, it is calculated that a total of 8 m^3 of CF_4 are emitted in the atmosphere, corresponding to about the 10% of the total CF_4 consumption of the system. A new line was hence built to connect the Purifier module exhaust output to the compressor module, to be opened during the vacuum phase of cartridges recuperation, in way to collect the CF_4/CO_2 gas mixture and directly re-use it in the mixer module. Following the same principle, a line was built from the gas system exhaust to the compressor module, with the addition of a new Mass Flow Meter. In this way it will be possible to measure and collect the detector exhaust mixture, let out from the gas system to compensate for detector pressure variations during the run. To convey the recuperated CF_4/CO_2 mixture into the mixer module, an extra supply line was

added to the two already present (one for CF_4 and one for CO_2). Such line allows to feed the gas system with the recuperated gas mixture when necessary, avoiding to make use of fresh CF_4 and CO_2 from the primary gas supply. A schematic representation of the gas system with such modifications and upgrades is reported in Figure 4.14

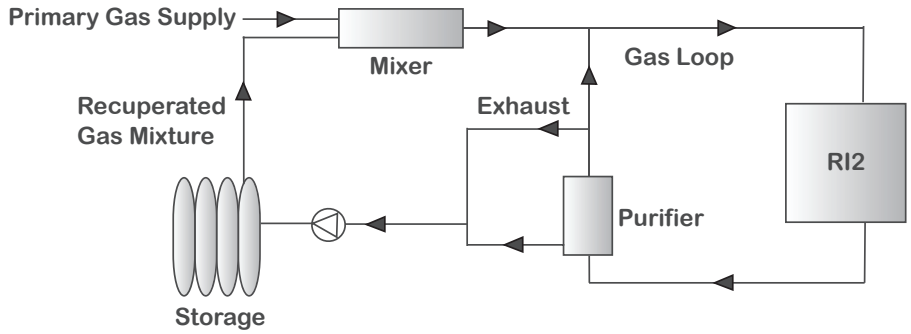

FIGURE 4.14: Schematic drawing of the RICH2 gas system with the upgrades for mixture recuperation from the exhaust and the Purifier module during normal operation.

Finally, to properly control and monitor the operation of the upgraded gas system and recuperation plant, custom modifications were realized on the SCADA software control system (Section 2.3). This will allow to automatize some phases of the recuperation, such as the ones from the Purifier and exhaust, the mixer injection and the compressor module operation. Moreover, it will make possible to fully monitor the CF_4 recuperation plant performance, and remotely control different system components when necessary.

4.3 CMS CSC CF_4 Recuperation

The Cathode Strip Chambers (CSC), operational in the CMS Experiment end-cap regions since Run 1 [90], are multi-wire proportional chambers in which one cathode plane is segmented into strips running across the wires. The choice of CSCs was done to combine precision and trigger functions in one device. They can operate at relatively high rates, in large and non-uniform magnetic fields (1-3 Tesla). The CMS end-cap Muon system consists of 540 CSCs, all of them with trapezoidal shape (Figure 4.15). They are all made of six wire planes interleaved between seven cathode panels, with strips milled on cathode panels that run lengthwise at constant $\Delta\phi$ width to provide a precise measurement of the ϕ-coordinate, while wires run azimuthally and determine the tracks radial coordinate. A typical chamber has about 1000 readout channels.

The overall area covered by CSCs is more than 1000 m^2, divided into four stations (ME1, ME2, ME3, ME4). The chambers are arranged in concentric rings centered on the beam line, separated by the iron disks of the flux return yoke, thick enough to isolate the electrons in showers. The ME1 station has three rings of chambers, at increasing radius, while the other three stations are composed of two rings of chambers. All but the ME1/3 chambers are partly overlapped and therefore they form rings with no dead area in the azimuth. A side view of the CMS Experiment showing part of the end-cap CSCs is reported in Figure 4.15.

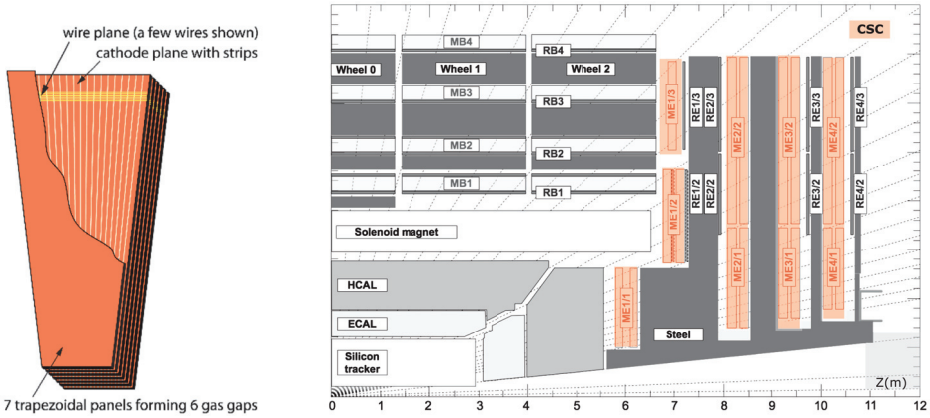

FIGURE 4.15: Example of a set of CSCs (left) and a side-view of the CMS experiment showing the CSC location in the end-cap (right).

To optimize gas gain and working voltage, but also inhibit anode wire aging, CSCs are operated with a gas mixture containing $Ar/CO_2/CF_4$ in fractions 40/50/10 [91]. Beside Ar and CO_2, which are standard operational gases for gaseous chambers, CF_4 was introduced in the CSCs gas mixture thanks to its capacity to prevent polymerization processes that could occur in the gas avalanche and cause premature wire aging due to molecules deposition. Its concentration is however limited to the 10% as on the other hand it could contribute to the etching of chamber and readout components [74]. As already mentioned in the previous sections, CF_4 is both expensive and harmful for the environment. In particular, given the 90 m^3 volume of the CSCs gas system, a great amount of CF_4 is necessary to operate the system regardless the small fraction of it over the total mixture composition.

To limit costs and emission of the CSCs gas system, it is operated in closed loop since the start of its operation. By system design, the gas recirculating fraction should have been above the 95%, but it was reduced to the 90% after some months of operation due to the excessive accumulation of air in the return gas mixture, around the 2% when the 5% of fresh gas was injected. The source of the contamination was identified as a diffusion leak resulting from components used for the construction of the detectors, which was therefore impossible to fix [84]. Operating the system with a 90% recirculating fraction gives acceptable values of air intake, where N_2 accumulation is lower than 1% and O_2 concentration is limited to a few ppm thanks to the Purifier module. In such operating condition, its is necessary to inject the 10% of the total gas volume as fresh gas mixture from the mixer module, of which a 10% is composed by CF_4. The gas system consumption has therefore a total cost of 100-200 kCHF per year of operation, depending on gas market conditions, of which 90% is represented by the cost of CF_4 only. Though the CF_4 concentration is reduced to the 5% ($Ar/CO_2/CF_4$ 40/55/5) in periods such as Long Shutdowns, the effort is not bringing enough gain in terms of reduction of gas system costs and Greenhouse gas emission.

Therefore, in 2011 a CF_4 recuperation system was designed, prototyped and commissioned and it started to be operational in the CSC gas system by 2014 [85]. The design of the recuperation plant will be described in the following sections, as well

as its performance details and the employment of recuperated CF_4 in the CSC mixer module.

4.3.1 Recuperation Setup

The CF_4 recuperation plant is based on the separation of the CSC gas mixture coming from the closed loop exhaust, before the Purifier module. The exhaust of the gas system is sent to the input of the recuperation plant through a Mass Flow Meter, with a total gas volume flow that can be either fixed manually, i.e. during specific plant tests, or automatically regulated to keep stable the system pressure. Figure 4.16 reports a schematic representation of the CSC gas system with the location of the CF_4 recuperation plant.

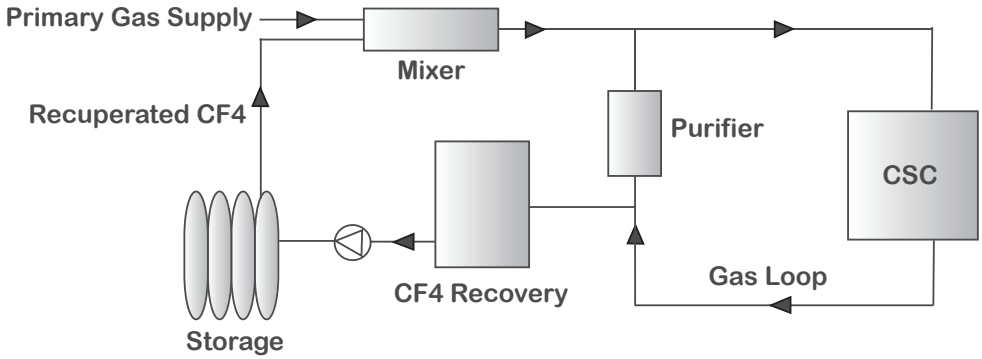

FIGURE 4.16: Schematic representation of the CSC gas system, with the elements of the CF_4 recuperation plant.

Given the composition of the CSC gas mixture, the CF_4 recuperation process is divided into several steps, in which separation membranes are involved, but also molecular sieves for gas adsorption. The different steps are briefly described in the following points [85], and a schematic representation of the process is reported in Figure 4.17.

1. *CO_2 bulk separation with membranes*:
   The first step is realized with the UBE separation membranes described in Section 4.1.2, to reduce the CO_2 concentration of the input gas mixture to a very low level, where the starting point is $Ar/CO_2/CF_4$ 40/50/10. While CO_2 diffused through the membrane walls and is extracted through the permeated stream, Ar and CF_4 keep flowing to the retented output to the following phase of the process. After this step, because of the non-ideal membrane separation efficiency, the CF_4 loss correspond to about the 5% of its input volume, but most of the CO_2 is removed, reaching a concentration of about 1% in the output stream. To manage the full CSC exhaust flow at once, four UBE membranes are installed in parallel: three membranes can be operated with a maximum flow of 300 l/h each, while the forth is designed for a higher flow regime (more than 600 l/h). The gas flow is uniformly distributed to the membranes with manual rotameters.

2. *Molecular sieve 4Å for CO_2 residual adsorption*:
   To reduce the CO_2 concentration in the mixture below the 1%, an adsorption cartridge filled with 4Å molecular sieve is installed as second step. The chosen

material is designed to efficiently adsorb CO_2 without affecting the CF_4 component. In a short time span, the CO_2 molecules are trapped in the cartridge material, allowing to have an output flow in which its concentration is reduced to only a few ppm. Given the nature of the process, the cartridge material has a fixed lifetime, as it is subject to CO_2 saturation. The column expected lifetime is around 90 hours for the nominal design flow (about 600 l/h), after which the column adsorption capacity is recovered through the standard regeneration procedure, with a vacuum-heating cycle reaching 200°C. To have a cartridge always available, two columns are installed in this stage so that when one goes into regeneration the other one can be used. A 1500 liters buffer is installed after this phase, to decouple it from the following one.

3. *Molecular sieve 13X for CF_4 adsorption*:
   In the last separation stage, the remaining Ar/CF_4 (now in concentrations 65/35) and N_2 mixture is sent to a second adsorber module, filled with a 13X molecular sieve with 10Å pore size. This material only traps CF_4, while Ar and N_2 remain free. The process is started with the cartridge under vacuum, and it is filled until slight below atmospheric pressure. The gas in the cartridge is then extracted in three phases, triggered by different values of its pressure. In the first phase, the mixture extracted is basically the same as the input and it is therefore sent back to the buffer. In the second phase mainly Ar is released, which is sent to exhaust, and finally the CF_4 trapped in the molecular sieve is extracted and sent to the storage stage of the recuperation. As in the previous step, two columns are present in this module to allow operation when one of the two needs a regeneration cycle, which basically coincide with every CF_4 extraction. To efficiently perform such regeneration the columns have a particular heating system, allowing to supply heat by a central bar and not only from the outside of the cartridges. At this stage of recuperation, the CF_4 loss is measured to be about the 15 % of the incoming quantity.

4. *CF_4 compression and storage*:
   After the CF_4 has been desorbed from the 13X molecular sieve, it is sent to a buffer volume and then compressed and stored into cylinders suitable for pressurized gas. Two batteries are installed with a total volume of 12x50 liters, which are alternatively used as output of the CF_4 recuperation plant. By design, while one of the batteries is filled with recuperated gas, the other is used as a CF_4 supply for the CSC mixer. The injection process will be described in the following section.

The transition between the phases is managed by software controls, contained in the same infrastructure as the standard gas systems controls (Section 2.3). The software controls the opening/closing of valves and start/stop of pumps, according to the values of specific parameters (i.e. columns pressure, temperature), that can be set by the user.

The correct and efficient operation of the full recuperation plant is mainly monitored through the analyses of the gas composition at different stages of the process. The gas analysis are realized with a Gas Chromatograph (Section 2.3.1), in the same way described for the single membrane characterization (Section 4.1.3). Figure 4.18 reports the chromatograms of the gas mixture analyzed before the input of the recuperation plant (Exhaust from Buffer, green) and the composition of the recuperated gas (Recuperated CF_4, blue). From the GC PPU column results it can be seen how

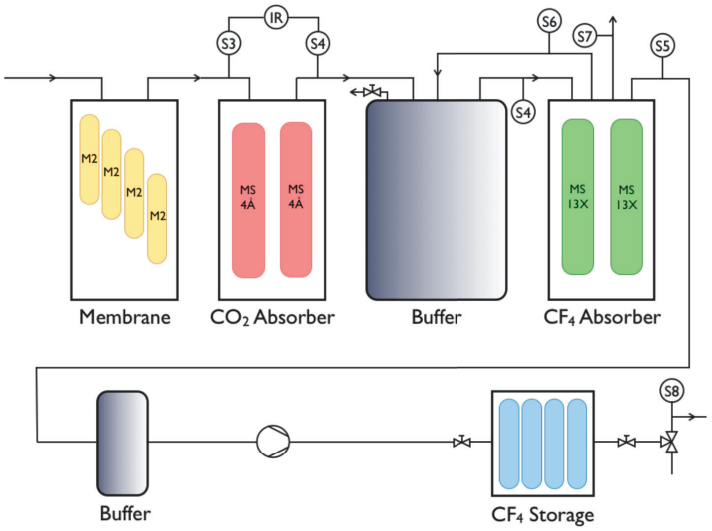

FIGURE 4.17: Diagram of the CF_4 recuperation process, with the different separation modules and the final storage phase. [92]

the CO_2 is completely removed, and the Ar fraction is lowered down to the 5%. The GC MS column chromatogram shows how also the N_2 content is significantly reduced.

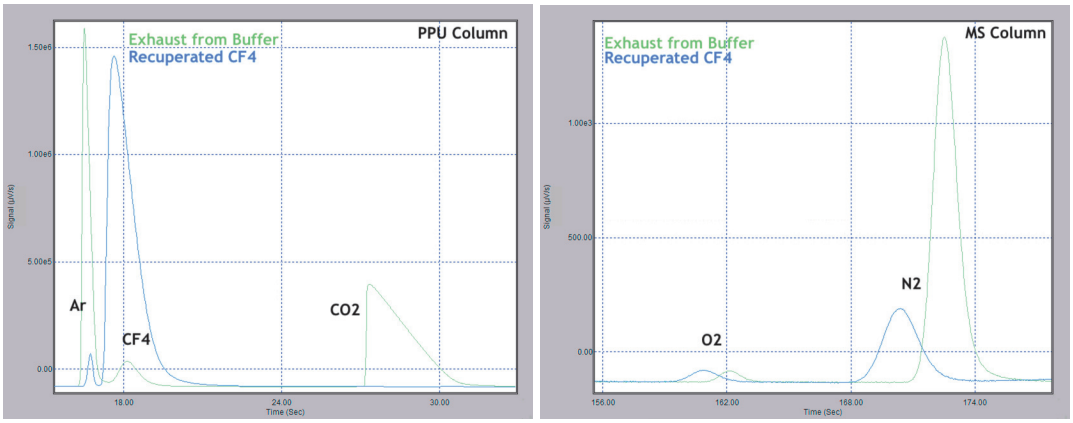

FIGURE 4.18: Gas chromatograms of input (Exhaust from Buffer, green) and output (Recuperated CF_4, blue) of the CF_4 recuperation plant, for the PPU column (left) and MS column (right).

Knowing the gas volumes and mixture concentrations at the different steps, the total CF_4 separation efficiency of the plant is calculated as the ratio between the CF_4 volume recuperated at the storage point and the CF_4 volume at the input of the plant. Such value takes into account the different modules efficiency as well as the CF_4 losses along the steps of the process. Figure 4.19 reports on the right axis the values of recuperation efficiency along the full operation period of the plant. In the first years of commissioning and operation (2012-2015) the overall efficiency was assessed around the 20%, due to the not yet optimal operation parameters, as well

as due to different gas leaks and hardware problems in various parts of the recuperation plant. Thanks to the works realized to improve these factors, recuperation efficiency was brought above the 30% in the following years. Since then, it is found to be oscillating between the 30% and 60%, with a solid stability around the 50% in the last year. The instability of recuperation efficiency depends on many factors, for example the pressure and volume flow of the input of the plant, the parameters of the different separation steps and the possible development of gas leaks in the path of the recuperated gas. While most of the hardware problems have now been fixed, other operational parameters still show room for improvement. In particular, the stability of the input volume flow to the plant, i.e. the exhaust flow from the CSC gas system, is considered to be a key factor determining the final efficiency and recuperated gas quality.

Figure 4.19 also reports on the left axis the trend of recuperated CF_4 accumulation, calculated from the pressure of the storage batteries. Since the construction and commissioning of the plant in 2012, a total of 450 m^3 of CF_4 were recuperated, a volume that corresponds to more than 1 year of CF_4 consumption by the CSC gas system.

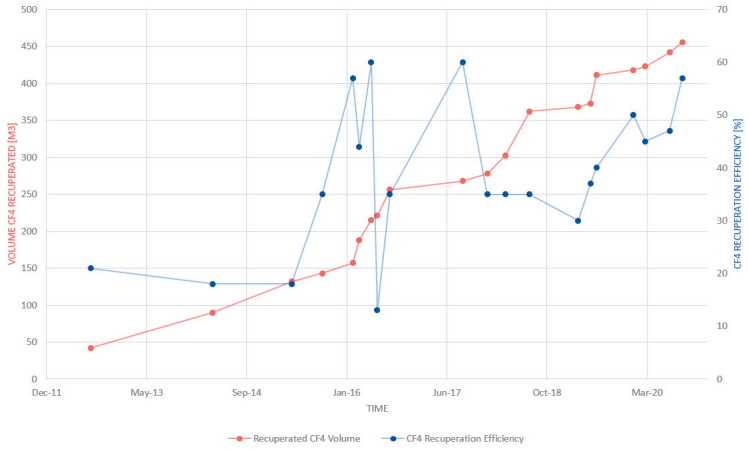

FIGURE 4.19: Trends of the CF_4 recuperated volume (left axis) and CF_4 recuperation efficiency (right axis) along the years of operation of the CSC recuperation plant.

4.3.2 CMS CSC Monitoring

Before illustrating the procedure employed to inject the recuperated CF_4 in the CSC gas system through the mixer module, in this Section it will be given a brief description of the gas monitoring system realized with Single Wire Proportional Chambers (SWPCs) [39]. As it will be explained in the next Section, it represents indeed a fundamental step during the mixer tuning of the CF_4 injection procedure.

The CSC gas monitoring system consists of two SWPCs, installed in two strategic points of the gas system: after the mixer module (After Mixer), to monitor the freshly injected mixture, and after the Purifier module (Exhaust to Distribution), to monitor the quality of the exhaust mixture that is going back to the detectors. The response of

the SWPCs can therefore give information about the quality of the gas mixture prepared by the mixer and the possible variations after the mixture has passed through the CSC detectors and all the elements of the gas system. The position of the two chambers in the CSC gas system is showed in Figure 4.20.

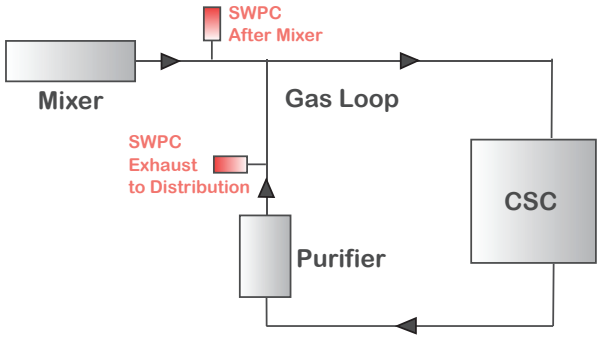

FIGURE 4.20: Schematic representation of the CSC gas system with the location of the SWPCs used for the gas monitoring.

The two SWPCs are irradiated with a 15 MBq ^{55}Fe source, and their performance is monitored measuring their amplification gain, estimated with the mean value of the main peak position of the typical ^{55}Fe spectrum. The X-ray induced signal is collected through a basic acquisition electronic chain, composed by a pre-amplifier, amplifier and multi channel digitizer. Data are registered on a computer and automatically analyzed to obtain a real-time trend of the SWPCs amplification gain. Figure 4.21 reports the schematic drawing of the SWPCs setup and data acquisition chain, while Figure 4.22 reports the typical detector signal shape and the signal height spectrum obtained from ^{55}Fe irradiation. With such system, thanks to the high sensitivity of SWPCs to changes in their gas mixture, any possible variation in the mixture can be spotted before it affects CSC detectors operation.

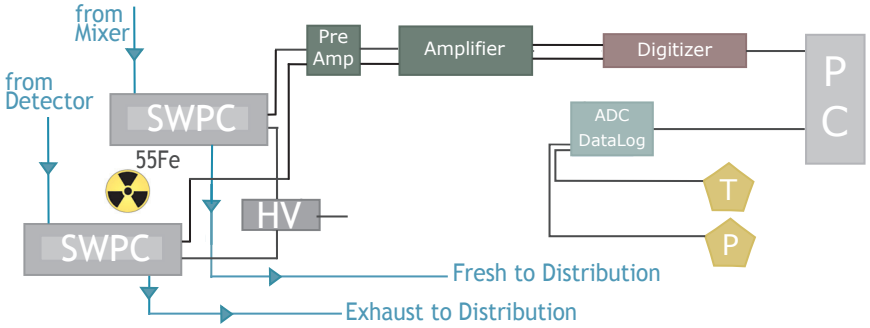

FIGURE 4.21: Schematic representation of the SWPCs monitoring system setup, with the layout of the detectors and elements of the data acquisition chain.

The monitoring system is operational in an online mode since 2016 [93], with the SWPCs amplification gain trend published on a webpage as well as to the CMS technical network and DIP service [94], accessible to the gas system and CSC detectors users. Figure 4.23 reports the trend of the SWPCs gain for their full operation period. It can

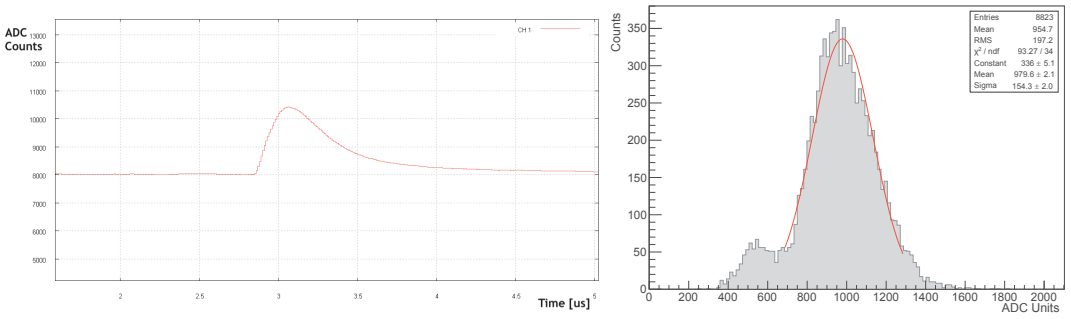

FIGURE 4.22: Waveform shape obtained from X-ray induced signals (left) and ^{55}Fe signal height spectrum (right).

be seen how it results to have an overall good stability, aside from specific moments in which its variation gave hint of gas system issues, as the last period of 2020 which will be discussed in details below.

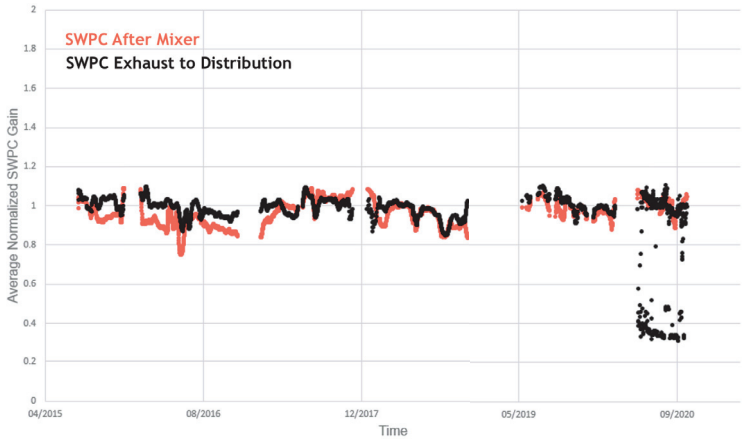

FIGURE 4.23: SWPCs amplification gain trend, from the start of operation of the monitoring system.

The monitoring system proved useful in different situations when it was possible to detect gas system problems through the response of the SWPCs. As an example, it is reported in Figure 4.24 the trend of the Exhaust to Distribution chamber amplification gain in the period June-October 2020, when the CSC gas system was put back in operation after the safe mode imposed by the CERN closure due to Covid-19. In these months, the Exhaust to Distribution SWPC shows and overall stable trend, but interspersed by short intervals when the gain drops below the 50% of its original value. After a first period in which such drops looks quite irregular, they occur about every five days. Thanks to the gain drops pattern, the cause of the issue could be traced back to a malfunctioning of one of the two columns of the Purifier module. As known from previous performance characterizations [92], SWPCs amplification gain undergoes a significant decrease when the gas mixture is polluted by Air, N_2 or O_2. As a matter of fact, the problem on the purifier column caused a premature saturation of the column material, which should trap all the O_2 accumulated in the mixture along the passage in the CSC detectors. In this way, O_2 concentration, normally kept to a few ppm, raised to about 700-800 ppm at half of the cycle of one of

the columns, i.e. about every five days. Figure 4.24 also reports the trend of the O_2 concentration measured by the Analysis module on the Exhaust to Distribution analysis line, and it can be clearly seen that the periods in which the O_2 reached higher concentrations correspond to the ones of low amplification gain of the SWPC.

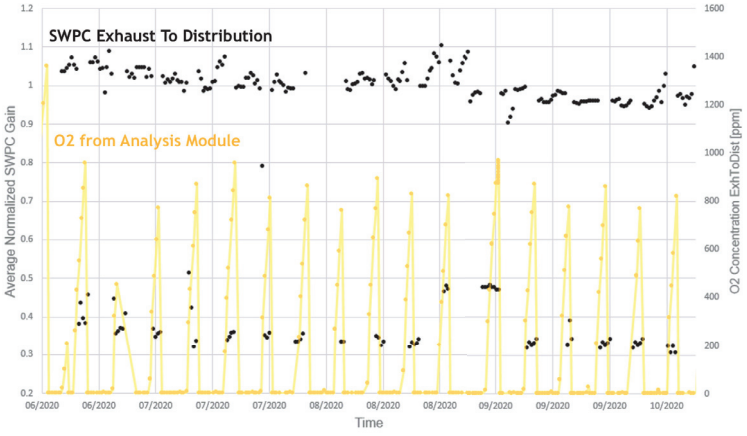

FIGURE 4.24: Trend of the normalized amplification gain of the Exhaust to Distribution SWPC (black, left axis) with the trend of the O_2 concentration in the same gas system point from the gas Analysis module (yellow, right axis), in the period June-October 2020.

4.3.3 Recuperated CF_4 injection

By the original design of the recuperation plant, the system should continuously operate and feed the CSC mixer module, with recuperated CF_4 accounting for half of the total CF_4 required. The requirement of having half of fresh CF_4 from the primary gas supply comes from the fact that recuperated CF_4 could still contain a certain degree of N_2 pollution, which must be kept very low to avoid consequences on the CSC operation. Due to the not yet optimal operation of the recovery plant, such half-half CF_4 supply to the mixer could not be achieved until 2018, when it was first put into operation.

To be sure that the injection of recuperated CF_4 does not compromise the correct composition of the mixture supplied to the CSC system, the setting of the injection parameters needs to be performed following a precise procedure and monitoring in real time the quality of the mixture. In fact, recuperated CF_4 normally contains a certain amount of Ar, which needs to be taken into account when setting the Mass Flow Controller of the mixer. Figure 4.25 reports the schematic drawing of the mixer module, with the three lines for Ar, CO_2 and CF_4 from the primary gas supply and the fourth one connected to the storage of recuperated CF_4.

The first step of the procedure is to analyze with the Gas Chromatograph the exact composition of the recuperated CF_4. In this way, knowing the precise quantity of extra Ar that will be injected in the fourth mixer line, the adjusted concentrations of Ar and fresh CF_4 can be calculated and used as a starting point for injection. Right before starting the injection, the mixer output is also analyzed with the GC, to have the correct mixture reference. Once injection is started setting the mixer with the calculated parameters, GC analysis of the mixture are continuously monitored as well

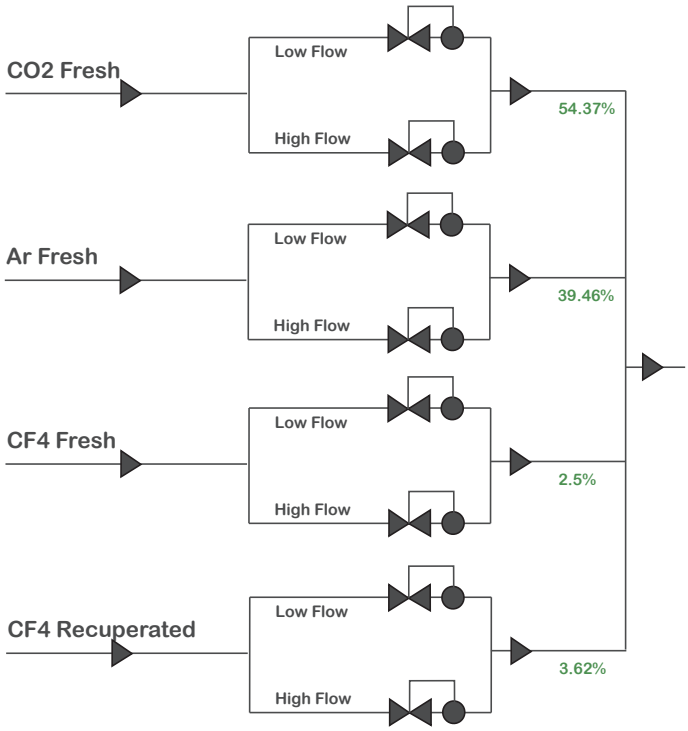

FIGURE 4.25: Schematics of the CSC gas system mixer module, with the standard three lines from primary gas supply (CO_2, Ar, CF_4) and the fourth line for recuperated CF_4.

as the response of the After Mixer SWPC. Indeed, after possible initial instabilities, the SWPC gain should settle back to its previous value if the new gas mixture is equivalent to the one before injection. Moreover, the SWPC could give indication of an excessive content of N_2 in the mixture, as its presence would significantly drop the amplification gain.

If the SWPC and GC give hint that the gas mixture does not have the required concentrations, the GC analysis values are used to perform a further calculation to fine tune the mixer parameters. Such procedure can be repeated as many times as needed to reach a precise mixture composition, though normally a couple of iterations are sufficient to obtain the correct values. It should be noticed that, while Ar pollution can be compensated by tuning the mixer, if N_2 is present in the recuperated CF_4 its injection in the CSC system cannot be avoided. Nevertheless, thanks to the good performance of the recovery system and the injection of only half of recuperated gas, N_2 value is normally kept at concentrations compatible with the requirements of CSC detectors operation.

Figure 4.26 reports an example of the SWPCs monitoring during the injection. It can be seen how the After Mixer chamber presents a fast decrease in the amplification gain (about -5%) as it is immediately reached by the new gas mixture, which in this case contained about 200 ppm of N_2. Figure 4.27 reports the gas chromatograms of the gas mixture injected by the mixer for 100% fresh CF_4 and for operation with recuperated CF_4. It can be seen how, though the main components concentration is maintained the same, the mixture with recuperated CF_4 show a significant increase in the N_2 concentration. On the other hand, the Exhaust to Distribution chamber

trend has a much slower and less important decrease, as the new mixture takes some days to flow through the full gas system and reach the re-injection point, and the N_2 concentration is diluted with the gas already in the system.

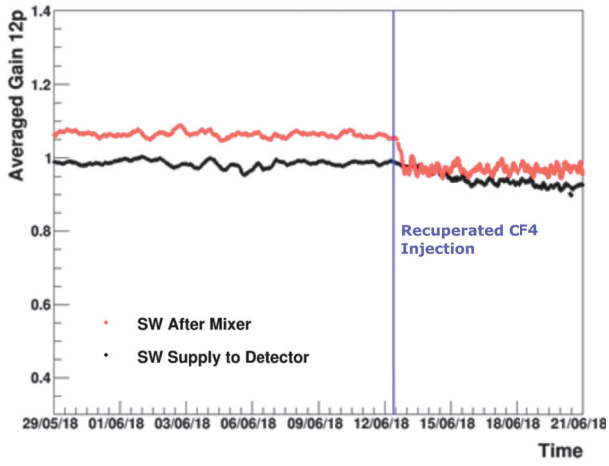

FIGURE 4.26: Example of the trend of the SWPC monitoring during the injection of recuperated CF_4.

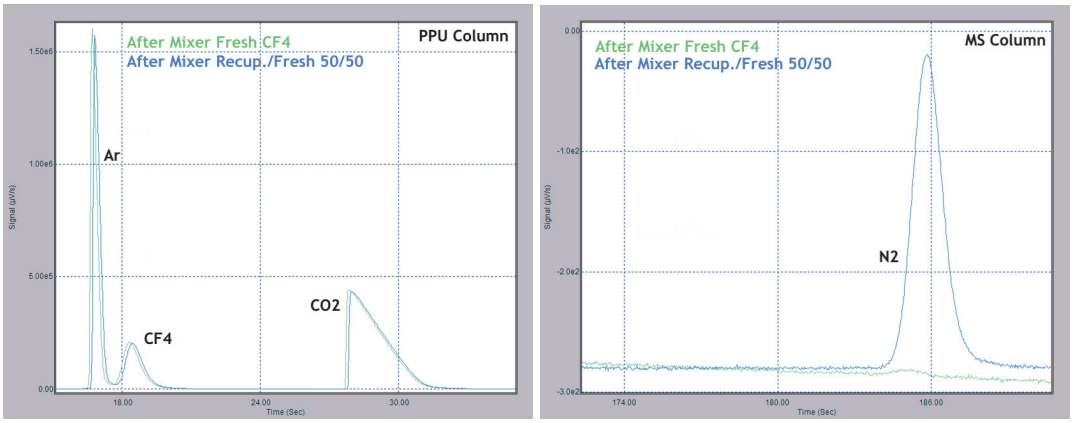

FIGURE 4.27: Gas chromatograph analysis of the After Mixer analysis line, for operation with 100% fresh CF_4 (green) and for operation with fresh and recuperated CF_4 50/50 (blue). Results are reported for both the PPU column (left) and MS column (right).

4.4 RPCs R134a Recuperation

Resistive Plate Chambers (RPCs) are operational in the Muon Systems of the ALICE, ATLAS and CMS Experiments since Run 1. RPCs operation is based on the detection of the gas ionization produced by charged particles when traversing the active area of the detector, under a strong uniform electric field applied by resistive electrodes. In the ALICE Experiment, RPCs are present in two different detector systems, the Muon TRigger system (MTR) [95], that will soon become Muon IDentifier (MID), and the Time Of Flight (TOF) detector [96]. In the ATLAS and CMS Experiments,

RPCs are present as a key part of their Muon systems, providing in both cases first-level trigger information (Figure 4.28) [32] [37].

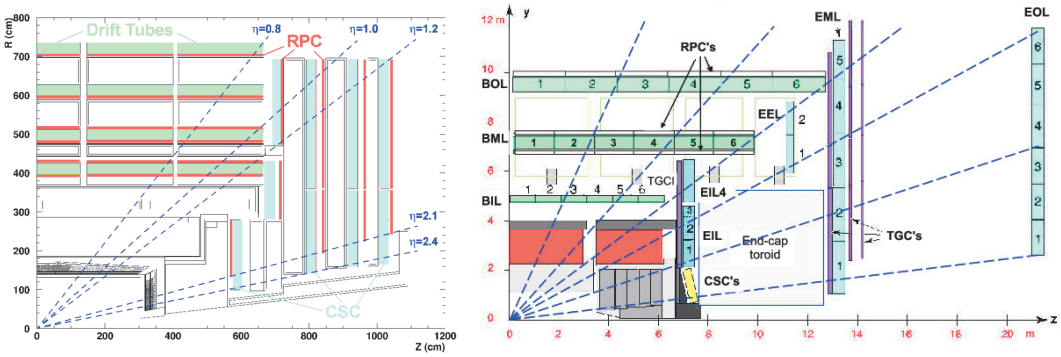

FIGURE 4.28: Side-cut of the CMS (left) and ATLAS (right) Experiments, with the position of the RPCs detector stations.

RPCs design can vary depending on the detector requirements, but their basic structure remains the same, with a pair of electrodes at a fixed distance and the gap in between filled with gas mixture (Figure 4.29). The electrodes are commonly made of an high-pressure laminate with phenolic resin, the bakelite, which has a volume resistivity between 10^9 and 10^{12} Ωcm. The most common configuration has 2 mm gas gaps, but the gap and the thickness of the plates can vary. RPCs in use in LHC Experiments are operated in avalanche mode, following the typical Townsend mechanism, i.e. with the avalanche multiplication due to the drifting electrons colliding with the gas molecule and producing further ionization.

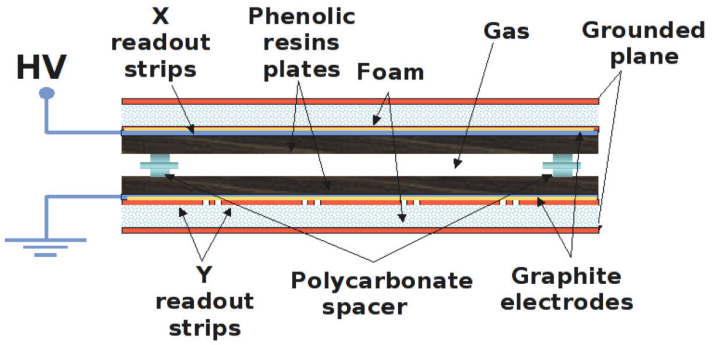

FIGURE 4.29: Schematic drawing of the RPC detector structure, in the specific case of the ATLAS chambers.

In way to be able to work in avalanche mode, the RPCs gas mixture have to contain as main component an electronegative gas, with high enough primary ionization production but with low free path for electron capture. The gas of choice is 1,1,1,2-Tetrafluorethane (R134a), which has a high enough electronegative attachment coefficient. In all the LHC Experiments RPC detectors, R134a accounts for the most part of their gas mixture, in concentration around the 90%. Another component that can be present in the RPCs gas mixture is iC_4H_{10}, a polyatomic gas which has a high

absorption probability for ultra violet photons produced in electron-ion recombinations. This component allows to dissipate the photon energy by roto-vibrational energy levels. Finally, SF_6 can be introduced as a quencher gas, that further suppresses streamer formation allowing to work in a pure avalanche mode. Concentrations of these components can have slight variations and the precise composition of the gas mixture of each RPC detector system can be found in Table 4.2.

Detector	R134a [%]	iC_4H_{10} [%]	SF_6 [%]
ATLAS RPC	94.7	5	0.3
CMS RPC	95.2	4.5	0.3
ALICE MTR	89.7	10	0.3
ALICE TOF	93	0	7

TABLE 4.2: Gas mixture composition of the RPC detectors operated in the LHC Experiments.

R134a and the SF6 are both known to be Greenhouse Gases (GHG) with a GWP of 1430 and 22800 respectively. This brings the RPC gas mixture in the focus for what concerns the CERN measures to comply with the European regulations [97] aiming to reduce the GHG emissions from fluorinated gases. As a first step, all the RPC gas systems are operating in closed loop mode since 2015. The ALICE TOF, ATLAS and CMS systems (respectively with a volume of 18 m^3, 15 m^3 and 15 m^3) are operating with a recirculating fraction around the 90% and the ALICE MTR system between 50% and 70%, but only with a 0.3 m^3 total volume. Thanks to the almost non-existent leaks at detector level, the operation of the ALICE TOF and ALICE MTR gas systems basically has a very low contribution to GHG emissions. On the other hand, the ATLAS and CMS RPC systems account for about the 80% of the CERN GHG emissions, mainly due to significant leaks in the detectors [51]. Works are currently ongoing during the LS2 to fix as much as possible the present leaks, but the low accessibility of the chambers in the experimental cavern makes it a hard mission to complete. Moreover, even if most of the leaks were to be fixed, RPC gas system would probably keep working in closed loop with a given fresh gas fraction, which would therefore mean to always have a given volume of RPC mixture exhaust to the atmosphere.

While R&D studies are ongoing to find more environmentally friendly gas mixtures [52] for the ATLAS and CMS RPC design, steps need to be taken to limit the emissions of the gas systems that will probably be operational with the current RPC mixture for a few more years. Even if SF_6 has an exceptionally high GWP, it only accounts for the 0.3% over the total mixture, and therefore it was decided to focus the efforts for Greenhouse gases reductions on R134a. Though its GWP is about 15 times lower than the SF_6, its concentration is 300 times higher and it hence contributes the most to the total GWP of the mixture.

After considering different possibilities to treat the R134a of the RPC gas mixture, it was concluded that the most useful and cost-effective way would be to recuperate it, with the aim of avoiding its emission in the atmosphere and at the same time being able to re-use it in the RPC gas system. The design and prototyping of an R134a recuperation plant started in 2018, and its final developments and commissioning are currently ongoing, to have the plant possibly operational on both the ATLAS and CMS RPC gas systems in next LHC Runs. The following Sections will describe

the R134a recuperation plant, starting from the challenges presented by the properties of the RPC gas mixtures, the design and progressive upgrades realized on the system, the tests realized to characterize and optimize the recuperation process and the results obtained in terms of R134a recuperation efficiency.

4.5 Separation of the RPC gas mixture

Given the nature of the components of the RPC gas mixture, differently from the CF_4 case described in the previous Section, membrane separation does not represent a viable technique to achieve the separation of R134a from the other mixture components. Though preliminary studies are being conducted to treat refrigerants with separation membranes [98], the technology is not yet developed enough to be efficiently applied and be cost effective for most of the use cases. Therefore, to design the R134a recuperation plant it was decided to work with the more widespread and well known technique of separation by phase transition. The following section will illustrate the different phases of the thermodynamic process exploited to separate the RPC gas mixture. Different assumption will be made through the explanation, to try to best describe the involved phenomena and discuss them in a theoretical fashion.

In the case of an ideal mixture of real fluids, the liquid-vapor equilibrium of a mixture can be described with the Raoult's law [99], which links the pressure of the fluids, their temperature and their concentrations. The equation describes the interaction between the molecules of the two components of the mixture: in the ideal case, the intramolecular forces have roughly the same intensity for the attraction between the two species and the same-component attraction. The system equilibrium is therefore described by three free parameters: pressure, temperature and the fraction of one of the components x_i. As a first assumption, the processes described in the following will be considered to be isobaric, i.e. happening at constant pressure. The approximation is done due to the fact that the full system is kept at atmospheric pressure, and the introduced variations in pressure are negligible in the bigger picture of the process. The key variable of the separation process will be the gas mixture temperature, and as it will specifically concern temperature variations it will be expressed in Celsius degrees, though the equations governing the phenomena are normally defined for Kelvin degrees.

The Raoult's law can be used to obtain the phase diagram of the mixture, also called boiling point diagram, when either the pressure or temperature of the mixture is fixed. The phase diagram describes the phase equilibrium phenomenon of the liquid and vapor phases of a binary mixture of components A and B through the dew point curve and bubble point curve. The temperature of the mixture for the two phases is expressed as a function of the fraction x_A, where the fraction x_B will simply be equal to 1-x_A. An example of the T(x_A) diagram of an ideal binary mixture is reported in Figure 4.30. A is here the less volatile component, i.e. the one with the higher boiling point (T_A), while B is the more volatile component, i.e. the one with the lower boiling point (T_B). The plot is normally expressed as a function of the molar fraction of the less volatile component of the mixture, in this case x_A. The curves on the plot express the trend of the vapor (top) and liquid (bottom) phases, for different values of the temperature. A point on the plot, (x_A^0, T^0), will indicate a binary mixture at temperature T^0 with the component A in concentration x_A^0 and

component B in concentration 1-x_A^0. If the point is located above the curves, the binary mixture is fully in vapor phase, while if the point is located below the curves, the mixture is fully in liquid phase. If the point is located in the area within the curves, part of the mixture is in vapor phase with the component A in concentration x_A^V, i.e. the concentration point on the isotherm line of the vapor curve. The other part of the mixture is in liquid phase with the component A in concentration x_A^L, i.e. the concentration point on the isotherm line of the liquid curve.

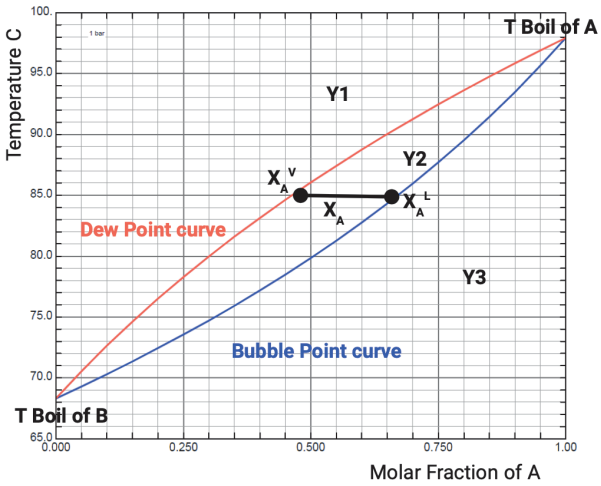

FIGURE 4.30: Phase diagram of an ideal binary mixture of components A and B obtained from REFPROP [100], where the Y1 region indicates a fully vapor mixture, Y3 a fully liquid mixture, and Y2 the phase transition mixture with x_A^V concentration of A in the vapor fraction and x_A^L concentration of A in the liquid fraction.

The quantity of mixture that sets in each of the two phases is determined by the lever rule: the ratio between the mass of the two phases is equal to the inverse of the ratio of the distances of the point (x_A^0, T^0) from the relative phase curve.

$$\frac{M_{liquid}}{M_{vapor}} = \frac{|x_A^0 - x_V|}{|x_A^0 - x_L|} = \frac{l}{v}$$

where l and v are the segment marked in Figure 4.31. In other words, the closer is a given point to the bubble curve the higher will be the liquid phase fraction, and vice versa.

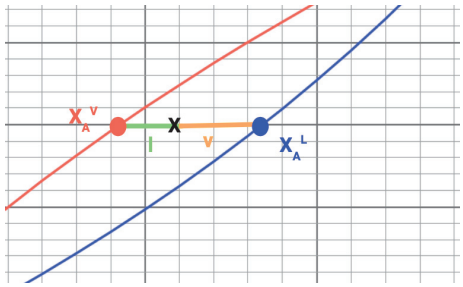

FIGURE 4.31: Zoom of Figure 4.30, where the distribution between vapor and liquid phase is marked through the graphic representation of the lever rule.

To determine the optimal way of separating the RPC mixture, its specific features should be considered. In Table 4.3 the components of the mixture (R134a, iC_4H_{10} and SF_6) are reported with their concentration at the starting point of the separation process and their boiling points at atmospheric pressure. N_2 is also included because the RPC gas mixture is fed to the recuperation module from the gas system after the Purifier module, and therefore it contains a certain concentration of N_2, accumulated in the system and impossible to remove with the purifier material. Though the RPC mixture is often humidified with H_2O concentrations of the order of thousands of ppm, the presence of H_2O is neglected as the Purifier module is capable of reducing it to few ppm. The reported concentrations specifically refer to the CMS RPC gas mixture, as the plant characterization described in the following discussion was fully realized on the CMS RPC gas system. At the moment of extraction from the gas system, the mixture is in vapor phase at a temperature of about 20 °C.

Component	Concentration	Boiling point @PAtm
iC_4H_{10}	4.5 %	-12 °C
R134a	95.2 %	-26.3 °C
SF_6	0.3 %	-64 °C
N_2	0.05 %	-196 °C

TABLE 4.3: Components of the RPC gas mixture, with their concentrations and boiling points at atmospheric pressure.

It is here reminded that the final aim of the separation procedure is the recuperation of the R134a component, with the highest possible purity and efficiency. For doing so, the mixture separation is approached through two main phases. The first phase concerns the separation of N_2 and SF_6 from the rest of the mixture (R134a and iC_4H_{10}), somehow considering them as low-concentration impurities to eliminate from the bulk of the mixture. In the second phase, the separation of iC_4H_{10} from R134a is considered, which represents the more challenging part of the separation as the two components present a non-ideal behavior.

To simplify the discussion of the first separation phase, it will be described as the separation of a binary mixture, where the component α is the mix of R134a and iC_4H_{10} and the component β is either SF_6 or N_2. For both these components, given that the difference in their boiling point with respect to the α component is greater than 25 °C , their separation can be successfully realized with a simple distillation process. Considering the example of SF_6, its boiling temperature is -64 °C and therefore it is the more volatile component of the mixture α/β. Lowering the mixture temperature just below the vapor curve of α (T_α), a separation in a vapor and liquid phase is obtained, where the vapor phase is enriched of the more volatile component, i.e. SF_6, and the liquid phase is enriched in the less volatile component, i.e. α. Given the very small concentration of SF_6 in the original mixture, one distillation step is sufficient, in good approximation, to get rid of all the SF_6 from the liquid phase. The same process will happen for N_2, with even better purification of the liquid phase as the difference in boiling temperature is greater and the N_2 fraction in the original mixture is smaller.

At the end of the first separation phase, the RPC mixture is separated into a vapor phase containing SF_6 and N_2, that can be easily exhausted to air, and a liquid phase containing the component α, i.e. R134a and iC_4H_{10}. The latter has a concentration of approximately 95/5, and it remains fully in liquid phase if it is kept at the final

temperature of the previous phase.

The second separation phase focuses therefore on the separation of the liquid mixture R134a/iC_4H_{10} 95/5. In this case, the mixture does not behave following the ideal model of liquid-vapor equilibrium, but presents a so-called azeotropic point. The R134a/iC_4H_{10} mixture falls into a deviation of the Raoult's law, as the intramolecular attraction between same-species molecules is significantly higher than the one between the different species, presenting a so-called disaffinity between the species. Such behavior is defined as a positive deviation from the Raoult's law. The main consequence of this phenomenon is that in the T(x_A) phase diagram of the mixture a minimum boiling point is present (the azeotropic point), at a temperature lower than the boiling points of both mixture components. Figure 4.32 reports the T(x_A) phase diagram of the mixture R134a/iC_4H_{10}, which presents a minimum boiling point at a temperature of about -32.5°C for the concentration 65/35. At this concentration values, the azeotropic mixture will change of phase without changes in the concentration. The specific phase diagram of the two component was obtained with the software REFPROP [100], which allows to compute the thermodynamic properties of many gases and their mixtures.

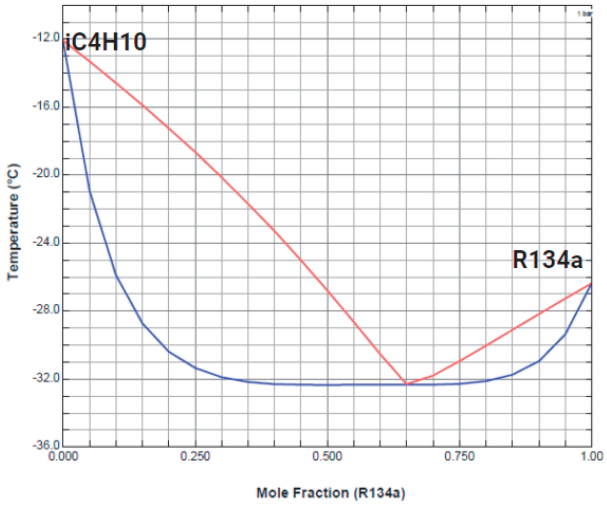

FIGURE 4.32: Phase diagram of the non-ideal binary mixture R134a/iC_4H_{10}, which presents a point of minimum azeotrope at the concentration 65/35.

Before describing the separation process, it is here pointed out that the properties just described yield to the choice of the temperature T_α of the first phase of the separation process. Indeed, to be sure not to be in the region of the liquid-vapor equilibrium of R134a/iC_4H_{10}, a temperature lower than then minimum boiling point of the mixture has to be chosen, i.e. lower than -32.5 °C.

Considering a possible separation by distillation of a minimum azeotrope mixture, the vapor phase will always tend to the azeotrope point, while the liquid phase will be enriched of the component that is at the starting point in excess with respect to the azeotrope concentration, i.e. to the component which boiling point is at the same side of the plot as the starting point composition. In our case, being the starting point mixture R134a/iC_4H_{10} 95/5, the process will happen in the right lobe of the phase

diagram, and the distillation process can be treated as the ideal case but with the binary mixture composed of R134a as less volatile component and the azeotrope mixture as more volatile component ($T_{boil}^{R134a} > T_{boil}^{azeoMix}$). Figure 4.33 reports the right lobe of the phase diagram. As mentioned above, the starting point is a liquid mixture, i.e. at a temperature located below the bubble point curve, at the x_{R134a} concentration of 95%.

The separation can be realized through a slow and continuous increase in the temperature of the mixture, in a quasi-static process where the temperature steps are infinitesimal. The aim of the process is to move on the bubble point curve from the 95% concentration up to the 100% concentration. To illustrate the process in a more clear way, it will here be considered as a sequence of finite steps in temperature increase (Figure 4.33). The mixture is first brought from a temperature T_0 to a temperature T_1, in way to be above the bubble point curve at the starting point concentration X_0. At that point, it is obtained a liquid phase enriched in R134a (concentration $X_1 > X_0$), and a vapor phase enriched in the azeotrope mixture. The vapor phase is then removed from the system, for example through a gas exhaust, and therefore the system is brought to the point of temperature T_1 on the bubble point curve, i.e. with only a liquid phase with R134a concentration X_1 (pink arrows on the plot). The temperature is then raised of another step, reaching T_2 and creating again a liquid phase enriched in R134a (concentration $X_2 > X_1$), and a vapor phase enriched in the azeotrope mixture. The same process is then iterated until the temperature T_{R134a} is reached. Keeping into account the lever rule, it can be noticed that given the shape of the curve the liquid phase is always favored and the vapor phase that is eliminated is always a very small fraction of the total. The process can also be described as if the binary system was basically moving along the boiling point curve (blue dotted line in Figure 4.33), with a continuous and slow removal of the vapor phase progressively formed. The final result of the process, once T_{R134a} is reached, is a liquid phase which is 100% R134a, and a total removed vapor phase which contains all the iC_4H_{10} volume of the starting point mixture plus the R134a progressively eliminated due to the enrichment of the vapor phase in the azeotrope mixture.

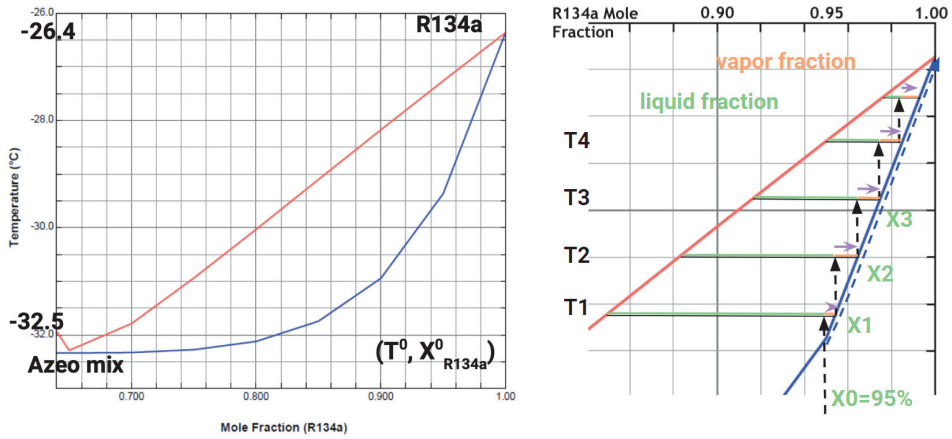

FIGURE 4.33: Right lobe of the phase diagram of the R134a/iC_4H_{10} mixture (left), and graphic representation of the step-separation of the mixture on the relative portion of the phase diagram (right).

As a conclusion, it should be remembered that the full separation process described in this section is based on ideal assumptions and, even when non-ideal cases are considered, the overall discussion mainly takes into account theoretical behaviors. The described separation process represents therefore a basis on which the actual separation plant is designed, but the precise value of temperature, volumes and efficiencies are subject to modifications given by the fact that the system is built and operated in real conditions.

4.6 R134a Recuperation Plant

The design and construction of the prototype of the R134a recuperation plant started in 2018, when the first setup was built on the RPC gas system of the ATLAS Experiment. After some months of tests, it was dismounted and moved on to the RPC gas system of the CMS Experiment, as the ATLAS RPC system was put off due to the LS2 maintenance. Since late 2019 the recuperation setup is hence on the CMS RPC system, where most of the tests were realized.

The final version of the R134a recuperation plant will be built on the ATLAS and CMS RPC gas systems, and possibly also in other locations where RPCs are tested with great volumes of gas mixture consumed, for example at the GIF++ facility. The recuperation plant, regardless its final location, will need to fulfill the following requirements:

- *Repeatability of the recuperation process*:
  The recuperation setup should give the same results if the process is repeated in the same condition, i.e. all the parameter influencing the recuperation outcome should ideally be controlled by the user.

- *Quality of recuperated R134a*:
  As the final aim of the recuperation plant is to store R134a to be re-used in the RPC mixer module, the purity of the recuperated gas should be high enough to guarantee the correct composition of the RPC mixture.

- *High R134a recuperation efficiency*:
  Within the limits of theoretical processes efficiency and real-system limitations, the overall efficiency of the recuperation plant should be high enough to compensate the cost and effort of the plant operation, i.e. the loss of R134a in the recuperation process should be limited as much as possible.

- *High input volume flow rate*:
  The input of the recuperation plant would be the exhaust of the RPC gas system, which could potentially reach 1000 l/h. The plant should therefore be able to handle such volume flow rate.

In this Section the design and characterization of the R134a recuperation plant prototype will be described, focusing on the tests realized on the plant operation and the relative variations on the plant layout. Indeed, various versions of the recuperation setup were tested, progressively modifying the elements that could help improve the overall performance of the plant.

4.6.1 R134a Recuperation plant setup

Though the final aim for the R134a recuperation plant operation on RPCs gas systems is to be working continuously, the recuperation prototype was designed to work with gas batches. Therefore, in the following description and characterization of the prototype plant, it will always be assumed to have a given volume flow of RPC mixture reaching the input of the plant, filling the plant with a certain amount of mixture and stopping the input flow at necessity. Having a single recuperation module with continuous input flow would introduce significant challenges for the recuperation process design if not a concrete impossibility of having an efficient separation of the mixture components. To overcome this issue, the final R134a recuperation plant will be designed to have two separate modules that could work alternatively to cope with the continuous volume flow rate coming from the RPCs gas system exhaust.

Figure 4.34 reports a schematic representation of the basic elements of the R134a separation setup, therefore without the storage part of the plant. The plant mainly consists in a heat exchanger and two buffer volumes. The heat exchanger and the first volume (A) are connected to a cooling unit, that provides the refrigerant liquid to the heat exchanger and keeps the volume A at the desired temperature. The two are thermally insulated with a layer of extruded elastomeric foam, a strongly insulating material (ArmaFlex [101]). The second volume (B) is kept at room temperature (+20 °C), at least in the first phases of the characterization of the plant.

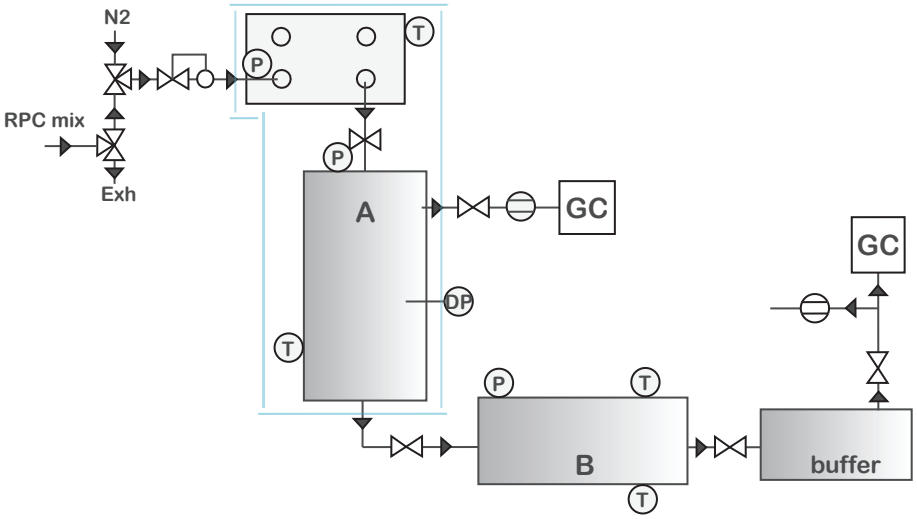

FIGURE 4.34: Schematic representation of the basic prototype of the R134a separation plant.

The input of the plant is connected to the RPC exhaust after the Purifier module, with a three-way valve that allows to send the gas volume flow either to the plant, with a flow rate regulated through a Mass Flow Controller, or to air exhaust when necessary. With a second three-way valves, it is also possible to chose between RPC mixture and N_2 as plant input, the latter to be used when the system needs for example to be flushed and cleaned between tests, or when it needs to be opened for hardware maintenance.

An output of the plant is located on volume A, in the form of a gas exhaust placed at

the top of the volume, and a second one is located at the output of volume B, where liquid is taken out from the plant. For the characterization tests, the two outputs were connected to two Gas Chromatographs (Section 2.3.1). For the gas output of volume A, the gas is directly sent to the instrument, with a regulated flow. For the liquid output of volume B, as liquid cannot be sent to the GC, an intermediate buffer is installed to evaporate the liquid before the analysis. Two flowmeters are installed on the outputs to register the gas volume flow rate.

Temperature sensors are installed in various location of the plant, to monitor the correct operation of the cooling unit as well as the gas mixture temperature in relevant moments of its separation. Pressure sensors are also installed in relevant locations, as well as a back-pressure regulator on the gas exhaust of volume A. Moreover, a differential pressure sensor installed on volume A allows to measure the level of the liquid filling the volume. Manual and pneumatic valves regulate the connection between the various parts of the plant. The full plant module, connected to a PLC, is also present on the WinCC-OA infrastructure for control and monitoring purpose.

4.6.2 Validation of the RPC mixture separation process

The first part of the characterization of the plant consisted in verifying the principle of operation of the plant, i.e. the correct separation of the mixture components, as well as tuning the temperature of the cooling unit. The test was realized analyzing the composition of the mixture at its equilibrium at different temperatures. The first aim of this test is to verify the first separation phase, i.e. the separation of SF_6 and N_2 lowering the mixture temperature. Once this phase is reached, a following temperature increase was realized with the purpose of verifying the behavior of the azeotrope mixture R134a/iC_4H_{10}.

Given the theoretical consideration of Section 4.5, the initial temperature of the cooling unit was set to -36 °C, to be at a temperature low enough to separate SF_6 and N_2 and below the boiling point of the R134a/iC_4H_{10} mixture. The input flow rate of the plant was set to 100 l/h, and the gas was let flow through the heat exchanger to the volume A, keeping its output towards volume B closed. As the feed stream started to reach the output of the heat exchanger, part of the stream flowed through the gas exhaust (measured with the flowmeter) while the rest started accumulating in liquid phase in the volume A (measured with the differential pressure sensor). The input flow rate was stopped once the volume A was filled. During the process, the gas exhaust was analyzed with the GC. Once the measured exhaust gas flow was stable at zero, i.e. the gas mixture in the volume A reached its equilibrium, the cooling unit temperature was increased of a step of 1 °C. As the mixture started again to partly evaporate, the gas exhaust volume rate was registered and its concentration measured with the GC. The process was then repeated for subsequent 1 °C steps of temperature increase.

Table 4.4 reports the results obtained from the Gas Chromatograph analysis of the gas exhaust, for the different temperature steps of the test. The first temperature setting shows how the SF_6/N_2 separation already happens at a good level at -36 °C, as their concentration in gas phase are much higher than the ones of the starting point gas mixture. Therefore, the vapor phase of this phase equilibrium is enriched in these two more volatile components, and while some of them remained in the liquid phase, most of their volume is now removed from the mixture. This step confirms

the correct theoretical assumption of a simple distillation process for the separation of SF_6/N_2 from the R134a/iC_4H_{10} mixture. Nevertheless, what is also clear from the gas exhaust analysis at -36 °C is that already at this temperature the R134a/iC_4H_{10} mixture starts separating into a vapor phase (enriched in the Azeotrope mixture 65/35) and a liquid phase (enriched in R134a). The following steps of temperature increase, when all of the SF_6/N_2 are removed, show how the composition of the vapor phase exhaust follows the expected trend of the dew point curve of the R134a/iC_4H_{10} phase diagram, as reported in Figure 4.35, up to the point where the vapor fraction is composed of 100% R134a. The experimental points are found to be shifted in temperature with respect to the theoretical curve, but this can be explained considering that the temperature used for the experimental points is the set-point of the cooling unit, that is the same as the one measured on the outside surface of the volume A but not the actual temperature of the liquid inside. The difference between curves is hence corrected with a constant shift to match the temperature measurement uncertainty.

Comp / Temp	N_2 [%]	SF_6 [%]	R134a [%]	iC_4H_{10} [%]
+20 °C (input)	0.05	0.30	95.15	4.50
-36 °C	2.62	5.66	73.18	18.62
-35 °C	0.02	0.51	79.59	19.88
-34 °C	0.00	0.01	84.53	15.46
-33 °C	0.00	0.00	87.63	12.37
-32 °C	0.00	0.00	92.69	7.31
-31 °C	0.00	0.00	95.37	4.63
-30 °C	0.00	0.00	99.94	0.06

TABLE 4.4: Summary of the GC results obtained from the analysis of the vapor exhaust in relation to the temperature setting.

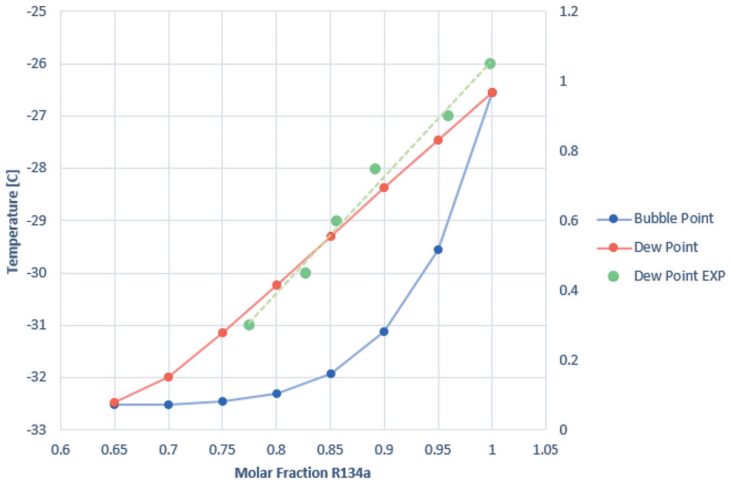

FIGURE 4.35: Comparison between the dew point curve obtained from experimental point and from the theoretical model of REFPROP.

The obtained results allow to validate the first phase of the separation process, for which a temperature around -36 °C can be chosen. Moreover, they confirm the non-ideal behavior of the R134a/iC_4H_{10} mixture, showing a phase equilibrium that follows the one foreseen by the theoretical phase-diagram. Nonetheless, the realized

test with finite steps in the temperature increase does not yet give enough information about the successful separation of pure R134a in the liquid phase.

The second phase of the mixture separation is tested with a different procedure, the one that would be in fact followed for the overall separation process. The test is started again, with the empty plant and the cooling unit with a set-point temperature of -36 °C. The 100 l/h input flow is opened, and let through the heat exchanger to complete the first separation phase, with SF_6/N_2 removed from the gas exhaust and the R134a/iC_4H_{10} liquid mixture accumulating in volume A with the valve between volume A and volume B open, letting the liquid mixture slowly flowing through it. Once the volume A is filled, the input flow is stopped and after a while the gas phase is fully exhausted. When the liquid mixture reaches volume B, which is kept at room temperature, its temperature starts to increase without modifying its composition, until it reaches the boiling point curve of the mixture phase diagram (Figure 4.33). From this moment, the slow and continuous heat exchange between the mixture and the environment starts, realizing the quasi-static equilibrium that allows to separate the R134a in liquid phase as described in Section 4.5. The vapor phase, enriched in the azeotropic mixture component, goes back towards the connection of the two volumes and exhausts through the gas output on top volume A. During the process, the output of volume B is opened and the liquid sent to the Gas Chromatograph, obtaining an analysis of the composition of the liquid mixture. While in the very first set of analysis (about half an hour) some ppm of iC_4H_{10} are detected, it progressively decreases until it completely disappears from the mixture. This result confirms the validity of the second phase of the separation process, also giving hint of the fact that a certain amount of time is necessary to complete the separation process before extracting pure R134a in liquid phase. The validity of the quasi-static separation process is hence confirmed.

A further conclusion that can be drawn from the results of this test concerns the vapor-liquid fraction separation. In particular, measuring the gas flow rate at the vapor exhaust of volume A, it could be calculated the total quantity of mixture that is removed from the system, i.e. the total loss in vapor phase. Figure 4.36 reports an example of the trend of the vapor fraction exhausted with respect to the total volume of the feed mixture, both values calculated for the mixture in vapor state. It can be seen how the vapor is slowly released in time, until the moment when the mixture reaches an equilibrium and only liquid is left. The total vapor fraction exhausted is around the 15%, confirming the fact that the lever rule favors the liquid phase in the separation.

4.6.3 Variation of the input/output flow rate

Once the separation process in the prototype setup was validated, its performance was tested for different rates of the input volume flow. As anticipated in the recuperation plant requirements, the system will need to be operational with input flows potentially up to 1000 l/h, but such value will mainly depend on the RPC gas system performance and it will not be possible to specifically tune it for the plant operation. It is therefore fundamental for the recuperation process to be independent of the volume flow at the input of the plant.

Different volume flow rates were tested, up to values of 400 l/h as such was the capability of the RPC system exhaust at the time of the characterization of the prototype.

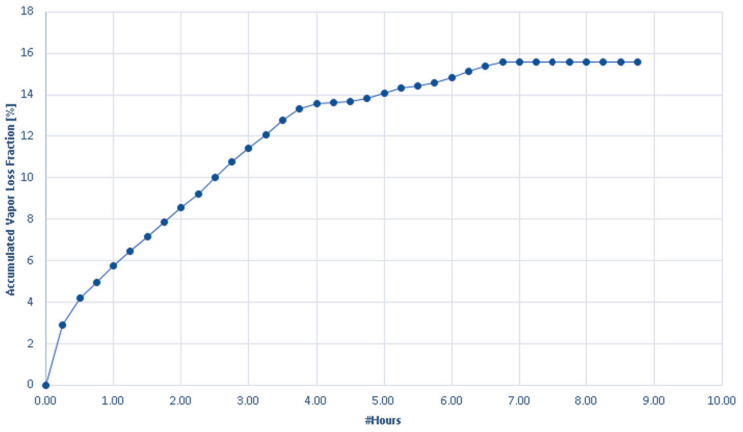

FIGURE 4.36: Trend of the accumulated exhaust vapor phase volume, with respect to the total feed stream volume sent to the plant.

The test showed how, regardless of the input flow rate, the quality of the mixture at the liquid exhaust of volume B remained the same, i.e. with mostly R134a, with only a few ppm of iC_4H_{10} in the first analysis. However, the rate of the incoming gas mixture determines the speed at which the volume A is filled of liquid. It was found that the relation between the input flow rate and the increase of the differential pressure measured in volume A is linear, meaning that the first phase of the separation is not affected by the rate of the mixture flowing through the heat exchanger. Further tests will be necessary to confirm this result for higher input flows.

The impact of the rate of the output flow of the recuperation plant was also tested. The output gas flow on top of volume A, i.e. the vapor exhaust, despite being measured with a flowmeter, is not controlled by a flow regulator, but just let out of the system to the atmosphere thanks to the slight over-pressure set on the volume A. On the other hand, the output flow of volume B, i.e. of the separated liquid R134a, is controlled with a rotameter after part of it is sent to the Gas Chromatograph. In fact, considering that after the characterization tests the liquid output should be connected to a compressor for the storage phase, a flow regulation could be introduced before this last step if necessary.

Output flows between 100 l/h and 250 l/h were tested, and it was seen that the flow variation does not have an effect on the purity of the extracted gas. Nonetheless, it clearly affects the rate at which volume A is emptied from the liquid, i.e. the rate at which the mixture is transferred to volume B and then sent to analysis. However, in between the actual separation process and the moment in which the liquid is sent to the next step in vapor phase there is the phase transformation of R134a from liquid to vapor, which concerns very small amounts of liquid at a time and it happens in the buffer volume after volume B. This allows to decouple the separation process from the transfer to the following steps, therefore the volume rate of the latter does not affect the separation result, i.e. the R134a purity.

4.6.4 Optimization of the R134a/iC_4H_{10} separation conditions

Given that the actual separation between R134a and iC_4H_{10} mostly happens in the transition from volume A to volume B, efforts were concentrated on the tuning of the

parameters of these two parts of the plant. For volume A, the temperature is easily chosen through the cooling unit settings and its good value was already assessed -36 °C. On the other hand, in the original plant design, volume B is simply left at room temperature, and it is physically in contact with the steel floor of the rack containing the setup. Thanks to the temperature sensors located on the top and bottom of such volume, it was noticed that these values were very oscillating along the separation process and, more importantly, their trend was not the same in the different tests. Such condition was probably given by the fact that there was no control on the temperature around the volume, therefore subject to changes in room temperature and heat exchanges between the volume and the steel floor.

It was hence decided to thermostat the surrounding environment of volume B, to stabilize the temperature around it and possibly tune it to potentially improve the separation conditions. A first test was realized with volume B placed into a steel container filled with water, but the separation did not look optimal, as many of the GC analysis of the liquid phase showed iC_4H_{10} concentration up to 2-3%. This could be explained considering that the water was changing in temperature, therefore with not such an effect on the stability of the temperature surrounding volume B. The setup was therefore modified as reported in the scheme of Figure 4.37, with the water filling the steel tank continuously flushed through a heat exchanger. In this way, the temperature around volume B could be kept uniform and stable thanks to the constant temperature of the water around it. Such stability is indeed maintained with the action of the heat exchanger, connected to a small cooling unit. Repeating the test with such modification, the effect of temperature stability was clearly seen on the quality of the separated phase, as no iC_4H_{10} was detected in the GC analysis. Figure 4.38 reports the trend in time of the iC_4H_{10} obtained with the GC in the two different conditions.

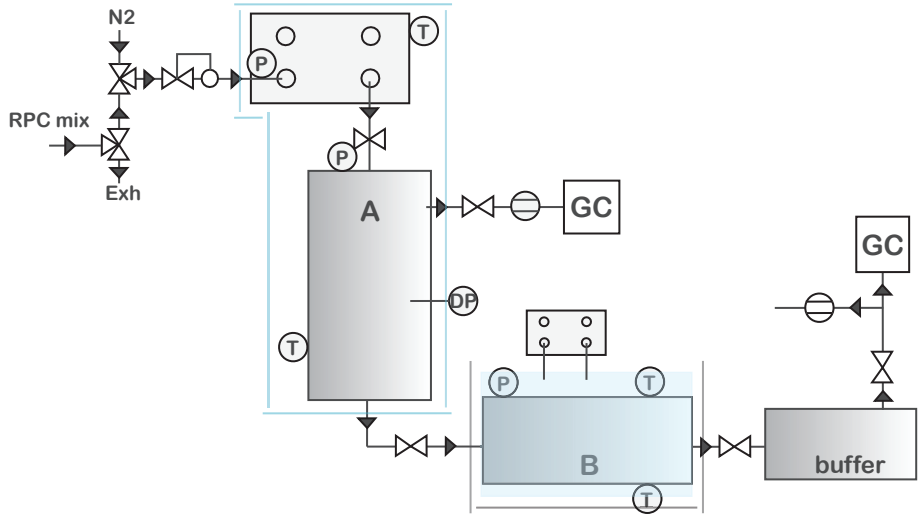

FIGURE 4.37: Schematic representation of the R134a recuperation plant prototype with the modifications around volume B.

The effectiveness of this modification can be traced back to the fact that, to be close to the ideal model of quasi-static separation described in Section 4.5, the heat exchange between the original mixture and the environment around needs to happen very slowly, and such condition can be achieved having a very stable environment with which the mixture at -36 °C exchanges heat. Further improvements of this part of

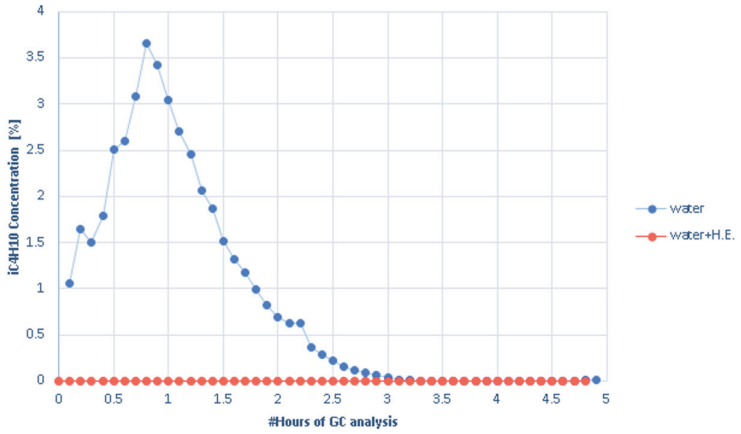

FIGURE 4.38: iC_4H_{10} concentration in the extracted liquid phase after separation, for the test with water around volume B with controlled (red) and non-controlled (blue) temperature. [102]

the setup could include the tuning of the settings of the heat exchanger controlling the temperature of the water, that could be eventually set to an optimum value.

4.6.5 R134a recuperation efficiency

A key parameter of the recuperation plant is its final efficiency in obtaining high quality R134a. As mentioned in Section 4.5, the theoretical separation process of the RPC mixture is already characterized by a certain inefficiency, as a fraction of the initial mixture has to be exhausted from the system in vapor phase and such fraction does contain R134a in a significant concentration (minimum 65%, the azeotrope mixture fraction). The advantage of the overall process sits in the fact that the exhausted vapor phase is much lower in volume than the one of recuperated liquid. Looking at the experimental result of Figure 4.36, the lost fraction of the total mixture in the real setup is assessed around the 15%. It should however be considered that such fraction does not contain 100% R134a, but also N_2, SF_6 and iC_4H_{10} in variable fractions, as reported in Table 4.4, therefore the 15% does not represent the R134a loss.

In addition to the theoretical inefficiency of the separation process, different other factors should be considered. For example, temperatures are known with a given uncertainty and they are never the real temperatures of the mixture at a certain point of the plant, but the temperatures that can be measured with real sensors placed outside the volumes and pipes. Therefore, though the aim of tuning the plant parameters is to optimize the separation process, the parameters setting will only tend to optimization but the theoretical ideal configuration is doubtlessly very difficult to achieve. Moreover, the various elements of the plant such as valves and pipe connectors could always introduce leaks, leaks-through and a list of real-system characteristics such as permeability and rigidity.

To keep into account all these factors, the R134a recuperation efficiency is calculated considering the total mass of R134a obtained at the liquid output of the plant (after

volume B) and the total mass of R134a sent to the plant input.

$$\epsilon(R134a) = \frac{mass(R134a^{Output})}{mass(R134a^{Input})}$$

Figure 4.39 reports the R134a recuperation efficiency value, calculated for all the tests performed since the prototype plant was installed on the CMS RPC gas system. Apart from some spare tests when the efficiency showed values below 70%, for most of the tests its value is found to be stable in the range 80% - 95%. Such result is strongly encouraging for the future developments and application of the plant as, even if further inefficiencies were to be introduced, the basis of the recuperation process has a very good performance to begin with.

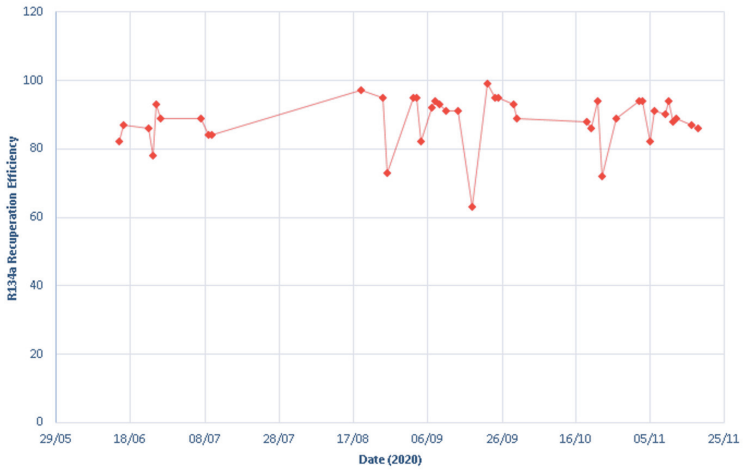

FIGURE 4.39: Trend of the R134a recuperation efficiency along the full plant characterization period.

To cross check the efficiency calculation, the R134a loss was estimated looking at the exhaust vapor of the plant and comparing it to the R134a loss defined as 1-$\epsilon(R134a)$. The R134a loss was calculated as the ratio between the R134a present in the total volume of exhaust vapor and the R134a volume at the recuperation plant input. In particular, the calculation was done considering the average R134a concentration in the exhaust vapor, as to have the precise value it should have been necessary to know in every instant the exhaust mixture composition, which is not possible due to the relatively long time it takes the GC to perform an analysis run (about six minutes). It was therefore considered the average R134a concentration in the vapor phase analysis, which corresponds to 65%.

Figure 4.40 reports the R134a loss along the plant characterization period, calculated with the two different methods. It can be seen how the two values are most of the times coherent, with an average difference of the 4%, left out some tests when the R134a loss calculated as 1-$\epsilon(R134a)$ results to be particularly high. Though in theory the two values should be the same, the fact that they are different but still very close suggests that one or both of them are calculated from variables that are measured with some uncertainty (GC concentrations, volume flow rates). Nonetheless, the overall characterization of the process can be considered correct as it was cross checked with the results of both plant outputs.

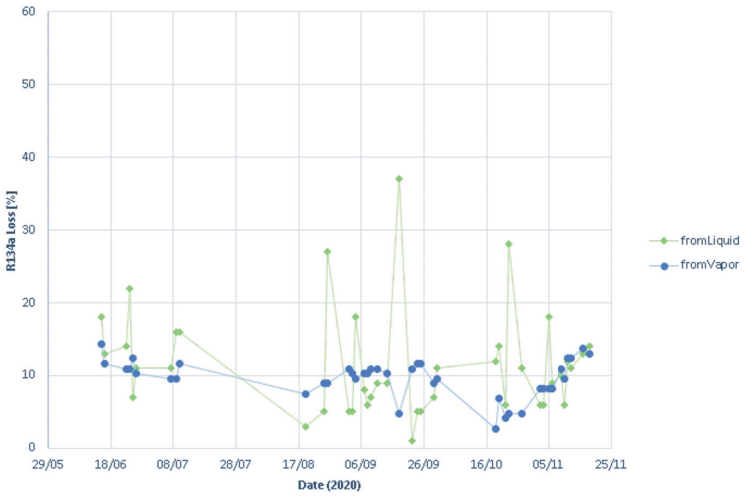

FIGURE 4.40: Trend of the R134a loss along the plant characterization period, calculated from the liquid output (green) and the vapor output (blue).

4.6.6 Storage of recuperated R134a

As a final step of the recuperation plant operation, the storage phase was designed and tested. The aim of this last phase is to collect the high quality recuperated R134a and compress it into storage, in way to be able to re-use it. The R134a can be easily put into storage with a compressor, which in this case is capable of compressing either liquid or gas. However, the action of the compressor would introduce a pressure difference that could affect its input stream, in particular because its functioning is controlled by an oscillating membrane which modifies the fluid volume, therefore generating oscillations in the input pressure. As the last volume of the recuperation plant is volume B, introducing pressure perturbations could strongly affect the successful realization of the R134a/iC_4H_{10} separation.

Therefore, it was necessary to decouple the action of the compressor from the separation process. The schematics of Figure 4.41 shows the additions to the recuperation plants to finalize the storage of recuperated R134a. A storage volume (C) is added after the output of volume B, with a second heat exchanger to have R134a in liquid phase so to store a greater quantity in the new volume. Both the second heat exchanger and volume C are thermally insulated and connected to the same cooling unit of the first part of the plant, therefore both kept at the same temperature of -36 ° C. The compressor is placed between the buffer volume and the storage tank. The storage tank has specific connectors and regulators, which allow to put as input a compressed fluid, i.e. liquid, and a secondary output for taking out its content in gas phase. With such configuration, the R134a separated in volume B can flow trough the heat exchanger, be liquefied again and stored in volume C. Once volume C is full, the connection with the separation part of the plant can be closed, and the liquid R134a can be sent to the buffer volume where it can expand and reach a vapor phase at uniform pressure, which will be the input of the compressor. After the compressor output the high pressure R134a can be put into the storage tank, and its composition can be analyzed with the GC thanks to the vapor output of the tank.

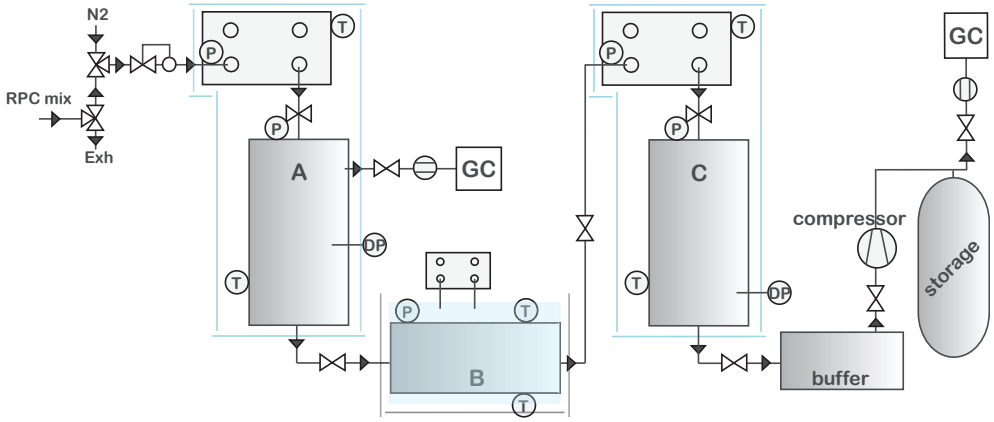

FIGURE 4.41: Schematic drawing of the full R134a recuperation plant prototype, including the separation phase and the storage phase.

The test of the storage phase was realized filling volume C with batches of recuperated R134a, as volume C is bigger than volume A and multiple runs of accumulation and separation can be realized before filling volume C and activating the compressor. Such solution is chosen to minimize the activity of the compressor, which is hence used only when a significant quantity of R134a is recuperated. After filling the storage tank, GC analysis were realized to check the final purity of the recuperated R134a. The results of the analysis showed how SF_6 is completely removed from the mixture, as its concentration is found to be constant at zero. The concentration of iC_4H_{10} is instead found to be around 0.035% in the first analysis (350 ppm), but it slowly decrease after some time. Such value of iC_4H_{10} is considered acceptable with respect of the high purity requirement of the recuperated R134a. Figure 4.42 reports the trend of iC_4H_{10} concentration obtained with the GC analysis for an example run of recuperation. The trend of air concentration is also reported, as it was found to be present in the recuperated gas in concentrations around 0.015% (150 ppm). The presence of such amount of air can be traced back to the action of the compressor, which might not be fully air-tight and introduce a certain air intake. Tough this aspect could surely be improved with upgrades in the compressor, the level of air contamination is considered acceptable.

4.6.7 Future developments

Though the current level of performance of the R134a recuperation prototype plant can be considered fully acceptable, different improvements could be still realized on the plant. In particular, a better tuning of the plant working temperatures could help improving the plant performance. A range of temperatures of the R134a/iC_4H_{10} separation phase could be tested, modifying the settings of the small cooling unit controlling the water temperature, to identify its optimal value in terms of separated R134a purity. The effects of changes in the main cooling units could also be tested, possibly leading to an improvement in the separation efficiency. Moreover, before having the plant ready for commissioning, input volume flow rates should be tested up to 1000 l/h, to be sure that the plant can efficiently operate for any operational flow condition of the RPC gas system. Finally, the R134a re-injection process should be tested and validated. In fact, in the original design of the plant a connection is foreseen between the storage unit and the RPC mixer module, to directly re-inject the recuperated R134a when enough volume is available.

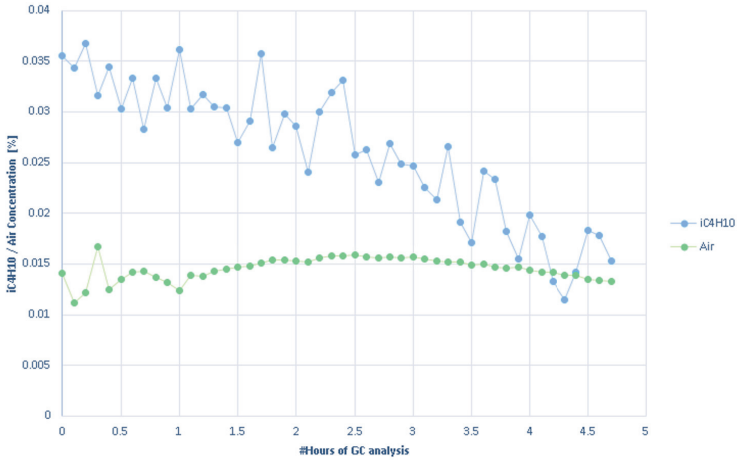

FIGURE 4.42: Results of the GC analysis for an example run of R134a recuperation, in terms of iC_4H_{10} and air concentrations found in the storage tank. [102]

4.7 Conclusions

Given the need of reducing the consumption and emission of Greenhouse gases used in LHC Experiments, different gas recuperation systems have been developed in the last years. Three of these systems were either designed or upgraded as part of the work of this thesis, and their key achievements will be illustrated as a conclusion of this Chapter.

Among other Greenhouse gases, CF_4 is widely used by LHC gaseous detectors, in combination with Ar and CO_2. Membrane separation technology proved efficient in separating CF_4 from the others mixture components, though with limitations linked to its variable performance in relation to operation parameters such as the input flow rate. Moreover, it was proved that membrane efficiency strongly depends on the input gas mixture composition, favoring CF_4 separation when its concentration is higher. The good knowledge developed on separation membranes allowed to design two different CF_4 recuperation plants making use of such technology.

A CF_4 recuperation plant was commissioned and put into operation in the LHCb RICH2 gas system, in which 100 m^3 of CF_4/CO_2 92/8 gas mixture are used. During the LS2, the RICH2 volume was emptied from its standard mixture and filled with CO_2, recuperating the exhaust mixture to extract and store good quality CF_4. The recuperation plant reached an average efficiency of the 60%, recuperating a total of about 450 m^3 of CF_4, with Air/CO_2 contamination <1%. The knowledge acquired during the first plant operation allowed to design and realize different modifications to improve the CF_4 recuperation system, that will be again used during the filling phase before Run 3, and to develop a new recuperation process for the CF_4/CO_2 gas mixture to be used during physics run operation.

The separation membrane technology has also been exploited for the CMS CSC CF_4 recuperation plant, already operational since Run 1. Membranes are used in combination with others separation methods, allowing to recuperate CF_4 from the CSC gas mixture ($Ar/CO_2/CF_4$ 40/50/10), with an average purity level of the 95%.

The plant is nowadays continuously operational, and it reached in 2018 the design operation configuration: CF_4 is continuously recuperated from the gas system and continuously re-injected in the mixer module. The injection is realized with 50% recuperated CF_4 and 50% fresh CF_4 supply, obtaining a good quality CSC gas mixture but with a significantly decreased supply gas consumption. The injected mixture quality is controlled thanks to a gas analysis system that allows a precise tuning of the mixer parameters through Gas Chromatograph analysis and real-time check on the gas mixture quality with a Single Wire Chambers monitoring system. Operational since 2016, the latter also allow to continuously monitor the CSC gas mixture quality during normal operation, at the mixer output as well as at the return of the closed loop system, to verify the good quality of the recirculated gas.

Together with CF_4, another widely consumed Greenhouse gas is R134a, as it is the main component of the gas mixture of RPC detectors, operational in the ALICE, ATLAS and CMS Muon systems. Therefore, the design and development of an R134a recuperation plant was started in 2018, with the aim of separating R134a from the others mixture components (iC_4H_{10}, SF_6), to be able to re-use it in the RPC mixer module. The gas mixture thermodynamic properties were determined and the separation process was designed to work through subsequent distillation processes, recuperating good quality R134a. Many tests and modifications of the prototype plant were realized, and its characterization showed very high separation efficiency (80% - 95%). In the final configuration, the recuperated R134a has pollution levels around hundreds of ppm in iC_4H_{10} and Air.

Conclusion

To fulfill the requirements of the future Physics Program of the LHC, the accelerator is currently facing a set of upgrades to increase its performance before the next Run 3, as well as to bring it closer to the future HL-LHC phase. The increase in the LHC accelerator performance sets important challenges to all detector systems. The work presented in this thesis focused on the improvements and upgrades related to Muon detector systems and the operation main infrastructure, the gas distribution systems.

Together with the requirements imposed by the accelerator upgrades, gaseous detectors operation will have to keep into account the latest CERN requirements in terms of reduction of Greenhouse gases (GHGs) emission and gas systems costs, as GHGs are fundamental for the operation of different detector systems. This thesis delineates the development and upgrades of two different research lines put in place to cope with gas systems requirements: the operation of gas systems with gas recirculation, in particular for the Triple-GEM detectors case, and the recuperation of valuable gas components after their usage in the gas systems, with focus on the recuperation process of CF_4 and R134a.

The main strategy actuated since the beginning of gas systems operation is the gas recirculation, i.e. re-using the gas mixture by collecting the exhaust gas flow and re-injecting it in the system after a purification process. The first part of this work aimed to validate the operation of Triple-GEM detectors, part of the latest MPGD technologies, in gas recirculating systems and in a high rate radiation environment, as the one they will have to face in the future phases of the LHC. The key points of the performance validation, realized with 10×10 cm^2 Triple-GEM detectors prototypes in a small replica of LHC gas systems at the GIF++ facility, are the following:

- Triple-GEMs operation was characterized at laboratory level for variations of CF_4 concentrations in the gas mixture $Ar/CO_2/CF_4$, with parallel simulation (GEANT4, Garfield++) to compare the experimental results with the theoretical behavior of the electron avalanches in a given gas mixture. Firstly, it was found that the simulation could model quite well the amplification gain of the detector, which is used to quantify the effect of gas mixture variations on detector performance. Concerning the characterization results, it was found that a significant variation in the gain is obtained for CF_4 content variations, up to 10% for 1% of CF_4 concentration, confirming the fundamental requirement of an extremely stable gas mixture composition.

- A long-term irradiation campaign was completed exposing Triple-GEM detectors to ^{137}Cs gamma emission, accumulating around 80 mC/cm^2 with detectors operated with recirculating gas fraction higher than 90% in $Ar/CO_2/CF_4$ gas mixture. Detectors response was found to be stable along the entire duration of the test, regardless of the gas recirculating fraction and the background

radiation rate. Moreover, during the irradiation campaign the action of the purifier module for removing and stabilizing H_2O and O_2 concentration in the recirculating gas system was validated.

- Triple-GEM detectors exposed to radiation when operating in Ar/CO_2 gas mixture were studied with the SEM imaging technique. Observing the GEM foils holes morphology it was found that a fraction of the GEM holes results to be damaged, with smudged outlines and distorted shapes. However, given the results of the long-term irradiation test, the observed damages to these holes are not sufficient to compromise amplification capabilities of the GEM foil.

- Muon detection efficiency was studied at the GIF++ facility, during a Test Beam campaign, operating the gas system in open mode and with gas recirculation (90% recirculating fraction). The obtained results show how the operation of Triple-GEM detectors is equivalent in the two different gas system modes, thanks to the action of the Purifier module. The detector under study could reach the maximum efficiency for both Ar/CO_2 and $Ar/CO_2/CF_4$ gas mixtures with 90% gas recirculation. Furthermore, it was seen how Triple-GEM detectors efficiency is not compromised by high-rate gamma background up to 1.5×10^6 Hz/cm^2

- Fluoride impurities production in CF_4-based mixture was studied at the GIF++ as well as in the LHCb Experiment on the GEM detector system in the last months of Run 2. At GIF++ the Fluoride production process characterization showed how the CF_4 content does not particularly affect the Fluoride production rate, at least for concentrations below 50%, and how a higher input gas flow rate contributes to the decrease of Fluoride produced in the chamber volume. Moreover, it was showed how both detectors electric field and irradiation intensity contribute to an increase in the Fluoride ion production. In the LHCb GEM studies, such behavior was found through the proportionality between the accumulated Fluoride ion and the integrated luminosity of the Experiment. Finally, both at GIF++ and in the LHCb GEM gas system in was verified the equivalence of operation with the gas system in open mode and with gas recirculation, finding that the standard LHC Purifier module is capable of trapping Fluoride ions produced in the detector volume.

Though many of the LHC gas systems are operated with gas recirculation, recirculating the 100% of the gas mixture is currently not feasible for many of those, and a set of other causes could yield to the emission of a significant amount of GHGs. A possible strategy to further limit gas emission is to put in operation gas recuperation plants, separating the most valuable mixture component with the aim of re-using it in the gas system. The work presented in the second part of this thesis discusses the operation and upgrades of three different gas recuperation systems, the CF_4 recuperation for the LHCb RICH2 and CMS CSC gas systems, and the R134a recuperation prototype for RPCs gas systems.

CF_4 Recuperation in LHCb RICH2 and CMS CSC gas systems

- Membrane separation technology was characterized in relation to CF_4 separation from the others mixture components. It proved efficient in obtaining good quality CF_4, though with limitations linked to its variable performance in relation to operation parameters such as the input flow rate. Moreover, it was

proved that membrane efficiency strongly depends on the input gas mixture composition, favoring CF_4 separation when its concentration is higher.

- A CF_4 recuperation plant based on separation membranes was commissioned and put into operation in the LHCb RICH2 gas system. During the LS2, the RICH2 volume was emptied from CF_4/CO_2 92/8 mixture and filled with CO_2, recuperating from the exhaust mixture good quality CF_4. The recuperation process allowed to store about 450 m^3 of CF_4, with Air/CO_2 contamination <1%, with a total recuperation efficiency around the 60%. Moreover, different modifications to the plant were designed to improve the CF_4 recuperation process, that will be again used during the filling phase before Run 3, and to develop a new recuperation process for the CF_4/CO_2 gas mixture to be used during physics run operation.

- In the CMS CSC CF_4 recuperation plant, operational since Run 1, membranes are used in combination with others separation methods to obtain CF_4 from the $Ar/CO_2/CF_4$ (purity level of about 95%). Though with oscillating performance in terms of efficiency, the plant is nowadays continuously operational. In 2018 the design operation configuration was reached, with CF_4 continuously recuperated from the gas system exhaust and, in parallel, re-injected in the mixer module. Recuperated CF_4 is injected in combination with fresh CF_4 (50/50), in way to guarantee a significantly decreased supply gas consumption while maintaining the CSC mixture at a good quality level.

R134a Recuperation for RPC gas mixture

- The design and development of an R134a recuperation plant was started in 2018, with the aim of separating R134a from the others mixture components (iC_4H_{10}, SF_6), to be able to re-use it in the RPC mixer module. Thanks to the experience gained through many tests and modifications of the prototype plant, the gas mixture thermodynamic properties were determined and an effective separation process could be designed, recuperating R134a through subsequent distillation processes. The characterization of the prototype plant showed very high separation efficiency (80% - 95%) and an extremely good quality of the recuperated R134a, with pollution levels around hundreds of ppm in iC_4H_{10} and Air. The obtained results are encouraging in view of further possible upgrades and a successful final commissioning of the recuperation plant.

Bibliography

[1] I. Béjar Alonso et Al. "High-Luminosity Large Hadron Collider (HL-LHC): Technical design report". In: (Dec. 2020). DOI: https://doi.org/10.23731/CYRM-2020-0010.

[2] R. Guida, M. Capeans, and B. Mandelli. "Gas Systems for Particle Detectors at the LHC Experiments: Overview and Perspectives". In: *Springer Proc. Phys.* 212 (2018), pp. 91–96. DOI: 10.1007/978-981-13-1313-4_19.

[3] Christiane Lefèvre. *The CERN accelerator complex*. DOI: Dec2008, CERN-DI-081201.

[4] *The Phase-2 Upgrade of the CMS Muon Detectors*. Tech. rep. CERN-LHCC-2017-012. CMS-TDR-016. This is the final version, approved by the LHCC. Geneva: CERN, 2017. URL: https://cds.cern.ch/record/2283189.

[5] G. Aad et al. "Observation of a new particle in the search for the Standard Model Higgs boson with the ATLAS detector at the LHC". In: *Physics Letters B* 716.1 (2012), pp. 1 –29. ISSN: 0370-2693. DOI: https://doi.org/10.1016/j.physletb.2012.08.020. URL: http://www.sciencedirect.com/science/article/pii/S037026931200857X.

[6] S. Chatrchyan et al. "Observation of a new boson at a mass of 125 GeV with the CMS experiment at the LHC". In: *Physics Letters B* 716.1 (2012), pp. 30 –61. ISSN: 0370-2693. DOI: https://doi.org/10.1016/j.physletb.2012.08.021. URL: http://www.sciencedirect.com/science/article/pii/S0370269312008581.

[7] R. Aaij et al. "Measurement of the $B_s^0 \to \mu^+\mu^-$ Branching Fraction and Effective Lifetime and Search for $B^0 \to \mu^+\mu^-$ - Decays". In: *Physical Review Letters* 118.19 (2017). ISSN: 1079-7114. DOI: 10.1103/physrevlett.118.191801. URL: http://dx.doi.org/10.1103/PhysRevLett.118.191801.

[8] R. Aaij et al. "Evidence for CP Violation in Time-Integrated $D^0 \to h^+h^-$ Decay Rates". In: *Physical Review Letters* 108.11 (2012). ISSN: 1079-7114. DOI: 10.1103/physrevlett.108.111602. URL: http://dx.doi.org/10.1103/PhysRevLett.108.111602.

[9] Rende Steerenberg et al. "Operation and performance of the CERN Large Hadron Collider during proton Run 2". In: *10th International Particle Accelerator Conference*. 2019, MOPMP031. DOI: 10.18429/JACoW-IPAC2019-MOPMP031.

[10] J. T. Boyd. *LHC Run-2 and Future Prospects*. 2020. arXiv: 2001.04370 [hep-ex].

[11] R. Aaij et al. "Observation of CP Violation in Charm Decays". In: *Physical Review Letters* 122.21 (2019). ISSN: 1079-7114. DOI: 10.1103/physrevlett.122.211803. URL: http://dx.doi.org/10.1103/PhysRevLett.122.211803.

[12] R. Aaij et al. "Observation of a Narrow Pentaquark State, Pc(4312)+ , and of the Two-Peak Structure of the Pc(4450)+". In: *Physical Review Letters* 122.22 (2019). ISSN: 1079-7114. DOI: 10.1103/physrevlett.122.222001. URL: http://dx.doi.org/10.1103/PhysRevLett.122.222001.

[13] Dukhishyam Mallick. "Mesonic Resonance Production in pPb, PbPb and XeXe Collisions with ALICE at the LHC". In: *MDPI Proc.* 10.1 (2019), 23. 5 p. DOI: 10.3390/proceedings2019010023. URL: https://cds.cern.ch/record/2727104.

[14] Francesco Noferini. "ALICE results from Run-1 and Run-2 and perspectives for Run-3 and Run-4". In: *Journal of Physics: Conference Series* 1014 (May 2018), p. 012010. DOI: 10.1088/1742-6596/1014/1/012010.

[15] G. Arduini et al. "High Luminosity LHC: challenges and plans". In: *Journal of Instrumentation* (2016). DOI: 10.1088/1748-0221/11/12/c12081. URL: https://doi.org/10.1088%2F1748-0221%2F11%2F12%2Fc12081.

[16] Klaus Hanke et al. "The LHC Injectors Upgrade (LIU) Project at CERN: Proton Injector Chain". In: *8th International Particle Accelerator Conference*. 2017, WEPVA036. DOI: 10.18429/JACoW-IPAC2017-WEPVA036.

[17] *Long Term LHC schedule*. URL: https://lhc-commissioning.web.cern.ch/schedule/LHC-long-term.htm.

[18] D. Contardo. *Highlights of LHC, ATLAS, CMS and LHCb upgrades*. 2020. URL: https://indico.in2p3.fr/event/19802/contributions/79162/attachments/57949/77571/ProspectiveIN2P3_1203GT01F_2020.pdf.

[19] ALICE Collaboration. *Upgrade of the ALICE Time Projection Chamber*. Tech. rep. CERN-LHCC-2015-002. URL: https://cds.cern.ch/record/1984329/files/ALICE-TDR-016-ADD-1.pdf.

[20] Marco Valente. *The ATLAS Trigger and Data Acquisition Upgrades for the High Luminosity LHC (HL-LHC)*. Tech. rep. ATL-DAQ-PROC-2019-020. Geneva: CERN, 2019. URL: https://cds.cern.ch/record/2692161.

[21] Djamel Eddine Boumediene. "ATLAS Calorimeter: Run 2 performance and Phase-II upgrades". In: *PoS* EPS-HEP2017 (2017). Ed. by Paolo Checchia et al., p. 485. DOI: 10.22323/1.314.0485.

[22] T Kawamoto et al. *New Small Wheel Technical Design Report*. Tech. rep. CERN-LHCC-2013-006. ATLAS-TDR-020. 2013. URL: https://cds.cern.ch/record/1552862.

[23] *Technical Design Report: A High-Granularity Timing Detector for the ATLAS Phase-II Upgrade*. Tech. rep. CERN-LHCC-2020-007. ATLAS-TDR-031. Geneva: CERN, 2020. URL: https://cds.cern.ch/record/2719855.

[24] *The Phase-2 Upgrade of the CMS Barrel Calorimeters*. Tech. rep. CERN-LHCC-2017-011. CMS-TDR-015. This is the final version, approved by the LHCC. Geneva: CERN, 2017. URL: https://cds.cern.ch/record/2283187.

[25] A Colaleo et al. *CMS Technical Design Report for the Muon Endcap GEM Upgrade*. Tech. rep. CERN-LHCC-2015-012. CMS-TDR-013. 2015. URL: https://cds.cern.ch/record/2021453.

[26] Simone Paoletti. *The CMS Tracker Upgrade for the High Luminosity LHC*. Tech. rep. CMS-CR-2019-253. Geneva: CERN, 2019. URL: https://cds.cern.ch/record/2723307.

[27] F.P. Albicocco et al. "Long-term operation of the multi-wire-proportional-chambers of the LHCb muon system". In: *Journal of Instrumentation* 14.11 (2019), P11031–P11031. DOI: 10.1088/1748-0221/14/11/p11031. URL: https://doi.org/10.1088/1748-0221/14/11/p11031.

[28] Lukas Gruber. "LHCb SciFi — Upgrading LHCb with a scintillating fibre tracker". In: *Nucl. Instrum. Methods Phys. Res., A* 958 (2020), 162025. 4 p. DOI: 10.1016/j.nima.2019.03.080. URL: https://cds.cern.ch/record/2712243.

[29] LHCb Collaboration. *LHCb VELO Upgrade Technical Design Report*. Tech. rep. CERN-LHCC-2013-021. LHCB-TDR-013. 2013. URL: https://cds.cern.ch/record/1624070.

[30] Ginés Martinez. "The Muon Spectrometer of the ALICE experiment". In: *Nuclear Physics A* 749 (2005), pp. 313–319. ISSN: 0375-9474. DOI: 10.1016/j.nuclphysa.2004.12.059. URL: http://dx.doi.org/10.1016/j.nuclphysa.2004.12.059.

[31] *The ALICE Dimuon spectrometer*. URL: http://aliceinfo.cern.ch/Public/en/Chapter2/Chap2_dim_spec.html.

[32] G Aad The ATLAS Collaboration and et al. "The ATLAS Experiment at the CERN Large Hadron Collider". In: *Journal of Instrumentation* 3.08 (2008), S08003–S08003. DOI: 10.1088/1748-0221/3/08/s08003. URL: https://doi.org/10.1088/1748-0221/3/08/s08003.

[33] Pierluigi Paolucci. *The CMS Muon system*. Tech. rep. CMS-CR-2006-006. Geneva: CERN, 2005. DOI: 10.1142/9789812773678_0096. URL: https://cds.cern.ch/record/927394.

[34] Sergey Chatrchyan and et al. "Performance of the CMS Drift-Tube Local Trigger with Cosmic Rays". In: *Journal of Instrumentation* 5 (Mar. 2010), T03003.

[35] A. A. Alves Jr. et al. "Performance of the LHCb muon system". In: *JINST* 8 (2013), P02022. DOI: 10.1088/1748-0221/8/02/P02022. arXiv: 1211.1346 [physics.ins-det].

[36] G Morello et al. "The micro-Resistive WELL detector for the phase-2 upgrade of the LHCb muon detector". In: *Nucl. Instrum. Methods Phys. Res., A* 936 (2019), 497–498. 2 p. DOI: 10.1016/j.nima.2018.11.078. URL: https://cds.cern.ch/record/2717434.

[37] *The Phase-2 Upgrade of the CMS Muon Detectors*. Tech. rep. CERN-LHCC-2017-012. CMS-TDR-016. This is the final version, approved by the LHCC. Geneva: CERN, 2017. URL: https://cds.cern.ch/record/2283189.

[38] Glenn F Knoll. *Radiation detection and measurement; 4th ed.* New York, NY: Wiley, 2010. URL: https://cds.cern.ch/record/1300754.

[39] M Capeans, Roberto Guida, and Beatrice Mandelli. "Gas Mixture Monitoring Techniques for the LHC Detector Muon Systems". In: *Springer Proc. Phys.* 212 (2018), 97–101. 5 p. DOI: 10.1007/978-981-13-1313-4_20. URL: https://cds.cern.ch/record/2643547.

[40] Fabio Sauli. "The gas electron multiplier (GEM): Operating principles and applications". In: *Nuclear Instruments and Methods in Physics Research Section A: Accelerators, Spectrometers, Detectors and Associated Equipment* 805 (2016). Special Issue in memory of Glenn F. Knoll, pp. 2 –24. ISSN: 0168-9002. DOI: https://doi.org/10.1016/j.nima.2015.07.060. URL: http://www.sciencedirect.com/science/article/pii/S0168900215008980.

[41] Andrey Marinov. "Feasibility study of a GEM based muon system for the CMS detector at the Large Hadron Collider". eng. PhD thesis. Ghent University, 2012, pp. XIII, 210.

[42] Mara Corbetta. "Studies on Gas Mixture and Gas Recirculation Effects on GEM Detectors Operation at the CERN GIF++ Facility". 2018. URL: https://cds.cern.ch/record/2653175.

[43] T. Zhao et al. "A study of electron drift velocity in Ar/CO2 and Ar/CO2/CF4 gas mixtures". In: *Nuclear Instruments and Methods in Physics Research Section A: Accelerators, Spectrometers, Detectors and Associated Equipment* 340.3 (1994), pp. 485 –490. ISSN: 0168-9002. DOI: https://doi.org/10.1016/0168-9002(94)90129-5. URL: http://www.sciencedirect.com/science/article/pii/0168900294901295.

[44] *PROFIBUS and PROFINET International (PI)*. URL: https://www.profibus.com.

[45] E Altuntas et al. *Long-term study of optimal gas purifiers for the RPC systems at LHC*. Tech. rep. PH-EP-Tech-Note-2012-001. Geneva: CERN, 2012. URL: https://cds.cern.ch/record/1415996.

[46] Agilent Technologies. "Fundamentals of Gas Chromatography". In: (). URL: https://www.agilent.com/cs/library/usermanuals/public/G1176-90000_034327.pdf.

[47] Agilent Technologies. "Agilent 490 Micro Gas Chromatograph, User Manual". In: (). URL: https://www.agilent.com/cs/library/usermanuals/Public/G3581-90001.pdf.

[48] The European Parliament and the Council of the European Union. *Regulation (EU) No 517/2014 of 16 April 2014 on fluorinated greenhouse gases*. Tech. rep. EU, 2014.

[49] M. Capeans, R. Guida, and B. Mandelli. "Strategies for reducing the environmental impact of gaseous detector operation at the CERN LHC experiments". In: *Nuclear Instruments and Methods in Physics Research Section A: Accelerators, Spectrometers, Detectors and Associated Equipment* 845 (2017). Proceedings of the Vienna Conference on Instrumentation 2016, pp. 253 –256. ISSN: 0168-9002. DOI: https://doi.org/10.1016/j.nima.2016.04.067. URL: http://www.sciencedirect.com/science/article/pii/S0168900216302807.

[50] R. Guida and B. Mandelli. "R&D strategies for optimizing greenhouse gases usage in the LHC particle detection systems". In: *Nuclear Instruments and Methods in Physics Research Section A: Accelerators, Spectrometers, Detectors and Associated Equipment* 958 (Apr. 2019). DOI: 10.1016/j.nima.2019.04.089.

[51] G. Rigoletti, B. Mandelli, and R. Guida. "Performance studies of RPC detectors with new environmentally friendly gas mixtures in presence of LHC-like radiation background". In: *Journal of Instrumentation* 15.05 (2020), pp. C05004–C05004. DOI: 10.1088/1748-0221/15/05/c05004. URL: https://doi.org/10.1088/1748-0221/15/05/c05004.

[52] Gianluca Rigoletti et al. "Studies of RPC detector operation with eco-friendly gas mixtures under irradiation at the CERN Gamma Irradiation Facility". In: *PoS* EPS-HEP2019 (2020), p. 164. DOI: 10.22323/1.364.0164.

[53] F. Murtas et al. "Applications in beam diagnostics with triple GEM detectors". In: *Nuclear Instruments and Methods in Physics Research Section A: Accelerators, Spectrometers, Detectors and Associated Equipment* 617.1 (2010). 11th Pisa Meeting on Advanced Detectors, pp. 237–241. ISSN: 0168-9002. DOI: https://doi.org/10.1016/j.nima.2009.10.039. URL: https://www.sciencedirect.com/science/article/pii/S0168900209019445.

[54] F Murtas. "Applications of triple GEM detectors beyond particle and nuclear physics". In: *Journal of Instrumentation* 9.01 (2014), pp. C01058–C01058. DOI: 10.1088/1748-0221/9/01/c01058. URL: https://doi.org/10.1088%2F1748-0221%2F9%2F01%2Fc01058.

[55] H. Schindler. *Garfield++*. 2016. URL: http://garfieldpp.web.cern.ch/garfieldpp/.

[56] R. Guida and B. Mandelli. "A portable gas recirculation unit for gaseous detectors". In: *Journal of Instrumentation* 12.10 (2017), T10002–T10002. DOI: 10.1088/1748-0221/12/10/t10002. URL: https://doi.org/10.1088%2F1748-0221%2F12%2F10%2Ft10002.

[57] Rajendra Nath Patra et al. "Measurement of basic characteristics and gain uniformity of a triple GEM detector". In: *Nuclear Instruments and Methods in Physics Research Section A: Accelerators, Spectrometers, Detectors and Associated Equipment* 862 (2017), pp. 25 –30. ISSN: 0168-9002. DOI: https://doi.org/10.1016/j.nima.2017.05.011. URL: http://www.sciencedirect.com/science/article/pii/S0168900217305405.

[58] M. Capeans et al. "Studies of purification of the Resistive Plate Chamber gas mixture for the Large Hadron Collider experiments". In: *2008 IEEE Nuclear Science Symposium Conference Record*. 2008, pp. 934–938. DOI: 10.1109/NSSMIC.2008.4774548.

[59] A Bressan et al. "Two-dimensional readout of GEM detectors". In: *Nuclear Instruments and Methods in Physics Research Section A: Accelerators, Spectrometers, Detectors and Associated Equipment* 425.1 (1999), pp. 254 –261. ISSN: 0168-9002. DOI: https://doi.org/10.1016/S0168-9002(98)01405-3. URL: http://www.sciencedirect.com/science/article/pii/S0168900298014053.

[60] S. Martoiu, H. Muller, and J. Toledo. "Front-end electronics for the Scalable Readout System of RD51". In: *2011 IEEE Nuclear Science Symposium Conference Record*. 2011, pp. 2036–2038. DOI: 10.1109/NSSMIC.2011.6154414.

[61] M.J. French et al. "Design and results from the APV25, a deep sub-micron CMOS front-end chip for the CMS tracker". In: *Nuclear Instruments and Methods in Physics Research Section A: Accelerators, Spectrometers, Detectors and Associated Equipment* 466.2 (2001). 4th Int. Symp. on Development and Application of Semiconductor Tracking Detectors, pp. 359 –365. ISSN: 0168-9002. DOI: https://doi.org/10.1016/S0168-9002(01)00589-7. URL: http://www.sciencedirect.com/science/article/pii/S0168900201005897.

[62] Rene Brun and Fons Rademakers. "ROOT - An Object Oriented Data Analysis Framework". In: *AIHENP'96 Workshop, Lausanne*. Vol. 389. 1996, pp. 81–86.

[63] Roberto Guida. "GIF++: A new CERN Irradiation Facility to test large-area detectors for the HL-LHC program". In: *PoS* ICHEP2016 (2016), p. 260. DOI: 10.22323/1.282.0260.

[64] Dorothea Pfeiffer et al. "The radiation field in the Gamma Irradiation Facility GIF++ at CERN". In: *Nuclear Instruments and Methods in Physics Research Section A: Accelerators, Spectrometers, Detectors and Associated Equipment* 866 (2017), pp. 91–103. ISSN: 0168-9002. DOI: 10.1016/j.nima.2017.05.045. URL: http://dx.doi.org/10.1016/j.nima.2017.05.045.

[65] M R Jakel et al. "CERN GIF++ : A new irradiation facility to test large-area particle detectors for the high-luminosity LHC program". In: *PoS* TIPP2014.AIDA-CONF-2014-018 (2014), p. 102. URL: https://cds.cern.ch/record/1977147.

[66] S. Agostinelli et Al. "Geant4—a simulation toolkit". In: *Nuclear Instruments and Methods in Physics Research Section A: Accelerators, Spectrometers, Detectors and Associated Equipment* 506.3 (2003), pp. 250 –303. ISSN: 0168-9002. DOI: https://doi.org/10.1016/S0168-9002(03)01368-8. URL: http://www.sciencedirect.com/science/article/pii/S0168900203013688.

[67] Mary Thompson John Thompson. *ANSYS Mechanical APDL for Finite Elements Analysis*. 2017.

[68] T Aoyama. "Generalized gas gain formula for proportional counters". In: *Nuclear Instruments and Methods in Physics Research Section A: Accelerators, Spectrometers, Detectors and Associated Equipment* 234.1 (1985), pp. 125 –131. ISSN: 0168-9002. DOI: https://doi.org/10.1016/0168-9002(85)90817-4. URL: http://www.sciencedirect.com/science/article/pii/0168900285908174.

[69] R. Guida et al. "Development of a common gas analysis approach for the gas systems of all the experiments at the CERN Large Hadron Collider". In: *2012 IEEE Nuclear Science Symposium and Medical Imaging Conference Record (NSS/MIC)*. 2012, pp. 1156–1159.

[70] M Corbetta. "Studies on Gas Mixture and Gas Recirculation Effects on GEM Detectors Operation". In: *JRJC 2018 Book of proceedings* (2019), pp. 103–106. URL: https://hal.archives-ouvertes.fr/hal-02271401.

[71] E. García-Tabarés and A. T. Pérez Fontenla. *Scanning Electron Microscope (SEM) and Focus Ion Beam (FIB) observation of a Gas Electron Multiplier (GEM)*.

[72] R. Beanland P. J. Goodhew J. Humphreys. *Electron and Microscopy Analysis*. 2001. ISBN: ISBN 07484 0968 8.

[73] F.V. Böhmer et al. "Simulation of Space-Charge Effects in an Ungated GEM-based TPC". In: *Nucl. Instrum. Meth. A* 719 (2013), pp. 101–108. DOI: 10.1016/j.nima.2013.04.020. arXiv: 1209.0482 [physics.ins-det].

[74] M Hohlmann et al. "Aging phenomena in gaseous detectors - perspectives from the 2001 workshop". In: *Nuclear Instruments and Methods in Physics Research Section A: Accelerators, Spectrometers, Detectors and Associated Equipment* 494.1 (2002). Proceedings of the 8th International Conference on Instrumentation for Colliding Beam Physics, pp. 179 –193. ISSN: 0168-9002. DOI: https://doi.org/10.1016/S0168-9002(02)01463-8. URL: http://www.sciencedirect.com/science/article/pii/S0168900202014638.

[75] *HI 4110/HI 4010 Fluoride Ion Selective Electrode*. URL: https://hanna.it/downloads/dl/file/id/1028/hi4110r3.pdf.

[76] *Thermo Scientific™ Orion™ Fluoride Electrodes*. URL: https://www.thermofisher.com/order/catalog/product/9409BN#/9409BN.

[77] Mara Corbetta, Roberto Guida, and Beatrice Mandelli. "Triple-GEM detectors operation under gas recirculation in high-rate radiation environment". In: *Nuclear Instruments and Methods in Physics Research Section A: Accelerators, Spectrometers, Detectors and Associated Equipment* 984 (2020), p. 164627. ISSN: 0168-9002. DOI: https://doi.org/10.1016/j.nima.2020.164627. URL: http://www.sciencedirect.com/science/article/pii/S016890022031024X.

[78] "LHCb muon system: second addendum to the Technical Design Report". In: Technical Design Report LHCb (2005). URL: http://cds.cern.ch/record/831955.

[79] V Talanov. *Radiation environment at the LHCb inner tracker area*. Tech. rep. LHCb-2000-013. Geneva: CERN, 2000. URL: http://cds.cern.ch/record/691603.

[80] D. Brundu and A. Cardini. *LHCb Muon Group, Private communication*. 2020.

[81] M. Mulder. *Basic Principles of Membrane Technology*. Kluwer Accademic Publisher, 2003.

[82] R T Yang. *"Gas separation by adsorption processes"*. 1986.

[83] *UBE Separation Membranes*. URL: http://www.ube.co.th/picture/file/CO2%20Separation%20Membrane.pdf.

[84] M. Capeans et al. "Development of a CF4 recuperation plant for the Cathode Strip Chambers detector at the CERN Compact Muon Solenoid experiment". In: *IEEE Nuclear Science Symposium Conference Record* (Oct. 2010). DOI: 10.1109/NSSMIC.2010.5874009.

[85] M. Capeans et al. "Commissioning of the CF4 recuperation plant for the Cathode Strip Chambers detector at the CERN Compact Muon Solenoid experiment". In: *IEEE Nuclear Science Symposium Conference Record* (Oct. 2011). DOI: 10.1109/NSSMIC.2011.6154690.

[86] *DryCal Highly Accurate Portable Gas Flow Calibrator*. URL: https://drycal.mesalabs.com/flexcal-series/.

[87] M. C. Arena and R. Guida. *CERN EP-DT-FS, Private communication*. 2020.

[88] S et al Amato. "LHCb RICH: Technical Design Report". In: Technical Design Report LHCb (2000). URL: https://cds.cern.ch/record/494263.

[89] *Emerson ASCO Series V022 Flow Control Valves*. URL: https://www.emerson.com/en-us/catalog/asco-v022.

[90] D Acosta et al. "Large CMS cathode strip chambers: design and performance". In: *Nuclear Instruments and Methods in Physics Research Section A: Accelerators, Spectrometers, Detectors and Associated Equipment* 453.1 (2000). Proc. 7th Int. Conf on Instrumentation for colliding Beam Physics, pp. 182 –187. ISSN: 0168-9002. DOI: https://doi.org/10.1016/S0168-9002(00)00627-6. URL: http://www.sciencedirect.com/science/article/pii/S0168900200006276.

[91] C Anderson et al. *Effect of Gas Composition on the Performance of Cathode Strip Chambers for the CMS Endcap Muon System*. Tech. rep. CMS-NOTE-2004-033. Geneva: CERN, 2004. URL: http://cds.cern.ch/record/837542.

[92] B Mandelli. *The CF4 Recuperation Plant for the Cathode Strip Chamber detectors at the CMS experiment*. Scuola Superiore IUSS, Pavia. 2012.

[93] Beatrice Mandelli. "Detector and System Developments for LHC Detector Upgrades". Presented 12 May 2015. 2015. URL: https://cds.cern.ch/record/2016792.

[94] *CERN DIP Service*. URL: https://readthedocs.web.cern.ch/display/ICKB/DIP+and+DIM.

[95] L Terlizzi. "The ALICE Muon IDentifier". In: *JINST* 15 (2020). Proceeding of the 15th Workshop on Resistive Plate Chambers and Related Detectors (RPC2020), 10-14 February 2020, University of Roma Tor Vergata, Italy, C10031. 8 p. DOI: 10.1088/1748-0221/15/10/C10031. URL: https://cds.cern.ch/record/2717117.

[96] *ALICE Time-Of-Flight system (TOF): Technical Design Report*. Technical Design Report ALICE. Geneva: CERN, 2000. URL: https://cds.cern.ch/record/430132.

[97] M. Schulz and D. Kourkoulas. *Regulation (eu) no 517/2014 of the european parliament and of the council of 16 april 2014 on fluorinated greenhouse gases and repealing regulation (ec) no 842/2006*. URL: https://eur-lex.europa.eu/legal-content/EN/TXT/?uri=uriserv:OJ.L_.2014.150.01.0195.01.ENG.

[98] Fernando Pardo, Gabriel Zarca, and Ane Urtiaga. "Separation of Refrigerant Gas Mixtures Containing R32, R134a, and R1234yf through Poly(ether-block-amide) Membranes". In: *ACS Sustainable Chemistry and Engineering* 8.6 (2020), pp. 2548–2556. DOI: 10.1021/acssuschemeng.9b07195. eprint: https://doi.org/10.1021/acssuschemeng.9b07195. URL: https://doi.org/10.1021/acssuschemeng.9b07195.

[99] Ente nazionale idrocarburi (ENI). *Encyclopaedia of hydrocarbons, Volume V*. Istituto della Enciclopedia italiana, 2005.

[100] *NIST Reference Fluid Thermodynamic and Transport Properties Database (REFPROP): Version 10*. URL: https://www.nist.gov/srd/refprop.

[101] *ArmaFlex® LTD*. URL: https://local.armacell.com/fileadmin/cms/uk/products/en/ArmaflexLTDRangeUKROI.pdf.

[102] F. Cambiè and R. Guida. *CERN EP-DT-FS, Private communication*. 2020.